Theory of nonlinear and amplified surface plasmon polaritons

Marini, Andrea

Award date:
2011

Awarding institution:
University of Bath

Theory of nonlinear and amplified surface plasmon polaritons

Andrea Marini

Department of Physics

University of Bath

A thesis submitted for the degree of

Doctor of Philosophy

September 2011

Acknowledgements

I would like to thank my supervisor Dmitry Skryabin for his support and guidance and Andrey Gorbach for patiently answering many questions.

Abstract

This thesis presents a study of Surface Plasmon Polaritons (SPPs) in hybrid metal-dielectric waveguides. The embedding of metal in nanostructured photonic components allows for manipulating and guiding light at the subwavelength scale. Such an extreme confinement enhances the nonlinear response of the dielectric medium, which is important for applications in optical processing of information, but is paid in terms of considerable ohmic loss in the metal. It is, however, possible to embed externally pumped active inclusions in the dielectric in order to compensate for the metal loss. A novel perturbative theory for Maxwell equations is introduced and applied to various nonlinear metal-dielectric structures, deriving the propagation equation for the optical field. The nonlinear dispersion law for amplified SPPs, filamentation and dissipative plasmon-soliton formation have been studied, revealing intrinsic core and tail instabilities that prevent solitons to propagate over long distances. Stable propagation of plasmon-solitons can be achieved in insulator-metal-insulator structures with active and passive interfaces. The active SPP is coupled with the passive SPP, which absorbs the perturbations destabilising the zero background of the soliton. Theoretical modelling of optical propagation in metal-dielectric stacks predicts a modified two-band structure, allowing for gap/discrete plasmon-soliton formation. Loss and nonlinear parameters in subwavelength nanowire waveguides are evaluated and compared to the results obtained by other research groups. In all calculations, particular attention is paid in considering boundary conditions accounting for loss and nonlinear corrections, which contribute to the propagation equation with a *surface term* that becomes significant in the subwavelength regime.

Contents

Chapter 1

Introduction

Recent advances in nanotechnology have enabled possibilities for the fabrication and characterisation of nano-sized photonic components, which can be used for controlling and manipulating light at the nano-scale. This thesis is fundamentally about *nano-optics*, a newly emerging research area that aims at understanding optical phenomena in the subwavelength regime, i.e. near or beyond the diffraction limit of light [Novotny and Hect, 2006]. *Plasmonics* is a subfield of nanophotonics that has received considerable attention by the scientific community in recent years, mainly motivated by its striking nanometric applications in sensing [Homola, 2006], optical circuits [Bozhevolnyi, 2008] and active devices [Shalaev and Kawata, 2007].

Basically, the main ingredient exploited in plasmonics is the use of metallic components in the design of photonic structures. Common experience through everyday life tells us that light does not propagate in metals, but is reflected from the surface. Thus, using metals to handle light it may look weird in the eyes of the reader. However, it will be shown that, close to the metal surface, the light can couple with free electrons oscillating in the metal and can be confined across the interface with an external dielectric; the resulting electromagnetic surface wave is commonly named *Surface Plasmon Polariton* (SPP) [Maier, 2007]. SPPs exhibit the intrinsic property of being exponentially localised across the metal-dielectric interface, and under certain conditions depending on geometric and optical properties of the structure, they can get tightly bound to the surface.

Early description of Surface Plasmon Polaritons (SPPs) has been theoretically established in the context of radio waves [Sommerfeld, 1899; Zenneck, 1907]. Initial measurements of reflection/absorption spectra of visible light incident on metallic gratings reported an anomalous behaviour [Wood, 1902], which was later explained in terms of SPP excitation in Ref. [Fano, 1941]. From then on, the investigation of SPPs has rapidly increased, becoming of great interest in the last decade with the development of the nanofabrication techniques [Barnes et al., 2003; Bozhevolnyi et al., 2006b; Ozbay, 2006].

The tight confinement of SPPs is entirely due to the metal components and is paid in terms of considerable ohmic loss, which quenches off the peculiarly striking SPP properties. In turn, scientists put effort in trying to overcome the metal loss by embedding externally pumped gain materials in plasmonic components [Ambati et al., 2008; Noginov et al., 2008a; Zheludev et al., 2008]. In this context, relevant applications in optical processing of information have been developed, e.g., ultrafast all-optical modulation of SPPs [MacDonald et al., 2009; Pacifici et al., 2007].

The very unique benefit provided by SPPs resides in the strong field enhancement close to the metal surface, which is responsible for relevant surface-enhanced optical phenomena such as Raman Scattering (SERS) [LeRu and Etchegoin, 2009] and Second Harmonic Generation (SHG) [Zayats and Richards, 2009]. In general, the high intensity of SPPs boosts all nonlinear effects, which can be exploited, e.g., in plasmonic all-optical switching active devices [Wurtz et al., 2006]. In turn, the research area of *nonlinear plasmonics* has become of great interest both from experimental and theoretical perspectives. Theoretical modelling of SPP propagation in nonlinear nanostructures is still lacking of a shared unified understanding. One of the open questions concerns the physical origin of the extremely high optical nonlinearity of metals measured in experiments [Nie and Emory, 1997; Ricard et al., 1985]; recent approaches taking account of nonlocal ponderomotive nonlinearity [Ginzburg et al., 2010] predict an enhancement of nonlinear effects. Undoubtedly, the electromagnetic field enhancement at the metal surface plays a major role in this context. Imperfections and roughness of the metal surface lead to a further increasing of nonlinearity, constituting the leading contribution in SERS [LeRu and Etchegoin, 2009].

Light propagation in nonlinear systems is subject to peculiar physical mechanisms, such as self-focusing/self-defocusing [Boyd, 2003]. In particular, the focusing nonlinearity is able to compensate for diffraction, enabling the possibility to achieve localised non-diffracting light beams, named *spatial solitons* [Kivshar and Agrawal, 2003]. The occurrence of *plasmon soliton* formation in plasmonic systems has been reported recently [Feigenbaum and Orenstein, 2007; Ye et al., 2010]. Plasmon-solitons are receiving attention by the scientific community for their localised self-sustained nature, which can be used to obtain miniaturised optical channels.

Besides, fundamental research in plasmonics is directly linked to a novel class of hydrid metal-dielectric nanostructured materials, commonly named *metamaterials*, which exhibit unusual optical properties [Engheta and Ziolkowski, 2006; Ramakrishna and Grzegorczyk, 2009]. One of the most peculiar features of metamaterials is negative refraction [Veselago, 1968], which is responsible for superlensing [Pendry, 2000] and cloaking [Schurig et al., 2006] applications. In this context, plasmonic Negative Index Materials (NIMs), allowing for negative refraction [Dionne et al., 2008], can be exploited for super-imaging applications [Shalaev, 2007].

In conclusion, the embedding of metals in photonic components gives rise to a completely new phenomenology, which is creating space for several nano-scaled applications. In this context, the study of fundamental physics plays an important role in supporting and suggesting novel potential applications. Further, in order to describe electromagnetic fields highly confined in the subwavelength scale, the devolopment of adequate theoretical tools is needed. In this thesis, a novel perturbative theory for Maxwell equations is derived and applied to various nonlinear and active plasmonic structures. Such an analytical technique, accounting for nonlinear corrections at the boundaries between metal and dielectric structures, predicts a nonlinearity enhancement coming from surface effects. The dispersion law of nonlinear SPPs and plasmon-soliton formation at a single interface between a metal and a nonlinear active dielectric are investigated, revealing that intrinsic instabilities prevent the solitons to propagate over long distances. In turn, a method to stabilise solitons by exploiting the coupling

with a passive SPP is proposed and described. Theoretical modelling of nonlinear propagation in one dimensional SPP arrays predicts a modified two-band structure due to the negative coupling in the metallic stripes and the existence of gap/discrete plasmon-solitons. The bifurcation of the discrete soliton family from the antisymmetric branch is also predicted, finding confirmation in a numerical study done by another research group and published in a recent paper [Salgueiro and Kivshar, 2010]. Theoretical modelling of light propagation in cylindrical silver nanowires allows calculating the loss and nonlinearity enhancement around the surface plasmon frequency. We demonstrate that the enhancement of loss and nonlinearity is due to surface-induced effects, which become relevant in the subwavelength regime.

1.1 Outline

This thesis is specifically focused on the theoretical modelling of light propagation in gaining and nonlinear plasmonic nanostructures. This chapter introduces the general concepts and background theories of nonlinear optics that are used in the following chapters. Section 1.2 reviews the basic concepts of light propagation in dielectric structures. After introducing the macroscopic Maxwell equations and the constitutive relations, paraxial optics in dielectric bulks is briefly discussed and light propagation in optical fibres, silicon on insulator (SOI) waveguides and photonic crystals is introduced. Nonlinearity, generalised constitutive relations, paraxial propagation of light in nonlinear dielectrics and soliton formation are described in section 1.3.

Chapter 2 is aimed at reviewing SPPs and their properties in the linear regime, where nonlinear effects are neglected. In section 2.1, the basic optical properties of metals are briefly described: dielectric susceptibility, plasma frequency and volume plasmons. In sections 2.2, 2.3, the propagation of SPPs in single metal-dielectric interfaces and in Insulator-Metal-Insulator (IMI) waveguides are considered, respectively. The possibility to excite long-range SPPs in IMI waveguides and the inherent trade-off between confinement and loss are discussed in these sections. The experimental methods to excite SPPs are briefly reviewed in section 2.4, while applications of SPPs for optical interconnection in miniaturised

photonic circuitry are discussed in section 2.5. Section 2.6 reviews SPP amplification in various settings, describing the electromagnetic energy transfer and the possibility to use SPPs for miniaturised active devices.

The nonlinear propagation of amplified SPPs is theoretically modelled in chapter 3. In section 3.1, we derive a semi-analytical expression for the dispersion law of nonlinear SPP waves neglecting the metal loss. In section 3.2, the lossy case is considered and the dispersion law for stationary amplified and nonlinear SPPs is derived by a perturbative expansion of Maxwell equations. In section 3.3, we derive the Ginzburg-Landau equation for SPPs propagating along a single active interface and use it to describe filamentation and dissipative plasmon-soliton formation. We demonstrate that plasmon-solitons suffer from intrinsic core and tail instabilities, which prevent them to propagate over long distances. The dispersion law for stationary SPPs and the Ginzburg-Landau propagation equation are achieved through the direct calculation of the electric field corrections due to linear and nonlinear perturbations and the imposition of boundary conditions. The perturbative expansion is performed around the gain threshold where the metal loss is exactly compensated by the amplifying medium. Hence, in this approach the metal loss and the dielectric gain are not assumed small.

In chapter 4, we develop an alternative theory to model optical propagation of SPPs in one-dimensional subwavelength structures. In first place, in this alternative approach the metal loss is considered as a small perturbation of the same order of nonlinearity. Further, the propagation equation is obtained as a scalar product solvability condition for the perturbative expansion, without calculating the field corrections. Such an approach is more flexible and allows modelling optical propagation in more complex structures. The accounting of linear and nonlinear corrections in the boundary conditions affects the propagation equation with the surface term η. In this chapter we demonstrate that such a term is responsible for the enhancement of loss and nonlinearity in the subwavelength regime observed in Refs. [Afshar and Monro, 2009; Afshar et al., 2009]. The traditional *averaging approach* [Agrawal, 2001b; Davoyan et al., 2010b; Feigenbaum and Orenstein, 2007], neglects the linear and nonlinear corrections to the boundary conditions, which become significant in the subwavelength regime.

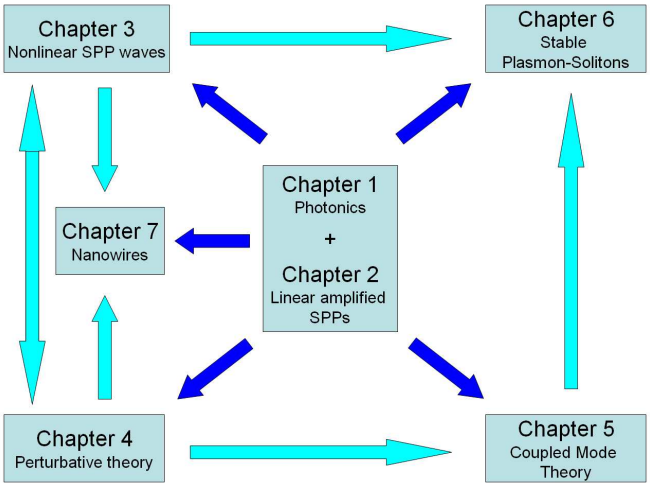

Figure 1.1: Schematic map of the thesis outline.

In chapter 5, we introduce the general concepts of optical propagation in waveguide arrays and apply the multiple-scale expansion derived in the previous chapter to model optical propagation of SPPs along a metal-dielectric stack. A system of *discrete nonlinear Schrödinger equations* (DNLSEs) for the SPP amplitudes is derived assuming that the coupling between SPPs propagating along the single metal-dielectric interfaces is small. We observe alternate positive and negative coupling in dielectric and metallic regions, respectively. The alternate couplings are responsible for the modified two-band dispersion, allowing for the formation of *gap* and *discrete* plasmon-soliton families.

A method to stabilise plasmon-solitons is described in chapter 6. Here, we consider an insulator-metal-insulator (IMI) structure, composed of a gain material, a metal and a dielectric. If the coupling between the active and passive interfaces is small, Maxwell equations can be reduced to a system of two coupled Ginzburg-Landau (GL) equations for the SPP amplitudes. The coupling of the active SPP with the passive interface affects the bifurcation of the homogeneous nonlinear modes with the trivial zero background. Indeed, such a bifurcation becomes *subcritical* and we demonstrate the possibility to achieve stable plasmon-solitons in the subcritical region.

Loss and nonlinearity enhancement in metallic and dielectric nanowires are evaluated in chapter 7. We generalise the one-dimensional perturbative theory developed in chapter 4 to the two-dimensional case of cylindrical waveguides, obtaining a *nonlinear Schrödinger equation* (NLSE) for the SPP amplitude. In this chapter, we also describe the *Reciprocity Theorem Approach* (LRT), showing that it perfectly coincides with our results. Hence, analogously to the one-dimensional case developed in chapter 4, we are able to identify the enhancement of nonlinearity observed in Refs. [Afshar and Monro, 2009; Afshar et al., 2009] as a surface-induced effect that becomes dominant in the subwavelength regime. A schematic map of the thesis outline and of the links between the chapters is illustrated in Fig. 1.1.

1.2 Propagation of light in dielectrics

In this section, some basic concepts of light propagation in dielectrics are briefly reviewed. Macroscopic Maxwell equations and linear constitutive relation for the polarisation and the electric field are introduced in section 1.2.1. Section 1.2.2 is focused on the standard modelling of optical diffraction in the paraxial approximation. Such a well known theoretical approach is based on the scalar approximation, which is valid in the limit of weak confinement [Yariv, 1985], and is used to derive the propagation equation for an optical fibre with small index step in section 1.2.3. However, in order to describe optical propagation in subwavelength photonic structures in the following chapters of this thesis, a vectorial approach is required [Daniel and Agrawal, 2010; Feigenbaum and Orenstein, 2007], since the scalar approximation is not adequate in this regime. Subwavelength confinement can be achieved in silicon on insulator (SOI) waveguides, which are characterised by the high index step and are briefly reviewed in section 1.2.4. Finally, section 1.2.5 introduces some basic concepts of photonic crystal theory, which will be used in chapter 5 to describe optical propagation in arrays of SPPs. Although the theoretical background presented in this section is known to an expert reader, it is necessary to introduce such general concepts in order to provide a complete insight of the topic and to highlight the peculiarites concerning surface plasmon polaritons.

1.2.1 Macroscopic Maxwell equations

At optical frequencies, the propagation of light in dielectrics is well described in the framework of macroscopic Maxwell equations in the absence of external charges and currents [Jackson, 1999]:

$$\nabla \cdot \vec{\mathcal{D}} = 0, \tag{1.1}$$

$$\nabla \cdot \vec{\mathcal{B}} = 0, \tag{1.2}$$

$$\nabla \times \vec{\mathcal{E}} = -\partial_t \vec{\mathcal{B}}, \tag{1.3}$$

$$\nabla \times \vec{\mathcal{H}} = \partial_t \vec{\mathcal{D}}. \tag{1.4}$$

For non-magnetic materials, electric displacement $\vec{\mathcal{D}}$ and magnetic induction $\vec{\mathcal{B}}$ depend on electric $\vec{\mathcal{E}}$ and magnetic $\vec{\mathcal{H}}$ fields through the relations

$$\vec{\mathcal{D}} = \epsilon_0 \vec{\mathcal{E}} + \vec{\mathcal{P}}, \tag{1.5}$$

$$\vec{\mathcal{B}} = \mu_0 \vec{\mathcal{H}}, \tag{1.6}$$

where $\vec{\mathcal{P}}$ is the induced polarisation, and ϵ_0, μ_0 are the electric permittivity and magnetic permeability of vacuum, respectively. Within the framework of linear response, for homogeneous isotropic materials the induced polarisation $\vec{\mathcal{P}}$ is modelled as

$$\vec{\mathcal{P}}(\vec{r}, t) = \epsilon_0 \int_{-\infty}^{+\infty} dt' \chi(t - t') \vec{\mathcal{E}}(\vec{r}, t'), \tag{1.7}$$

where $\chi(t - t')$ is the temporal response function of the system [Stratton, 1941]. In this expression, spatially local response is assumed, i.e. the induced polarisation $\vec{\mathcal{P}}(\vec{r}, t)$ depends only on the electric field $\vec{\mathcal{E}}(\vec{r}, t')$ at the position $\vec{r}$; non-local contributions to the induced polarisation $\vec{\mathcal{P}}(\vec{r}, t)$ from electric fields $\vec{\mathcal{E}}(\vec{r}', t')$ in different positions $\vec{r}' \neq \vec{r}$ are not taken into account. Since the material is also assumed homogeneous and isotropic, the temporal response function $\chi(t - t')$ is position independent.

Expressing the quantities $\mathcal{F}(\tau) = \vec{\mathcal{P}}(\tau), \vec{\mathcal{E}}(\tau), \chi(\tau)$ in terms of their correspondent Fourier integrals

$$\mathcal{F}(\tau) = \frac{1}{2\pi} \int_{-\infty}^{+\infty} d\omega F(\omega) exp(-i\omega t), \tag{1.8}$$

and applying the convolution theorem [Folland, 1992], one gets

$$\vec{P}(\vec{r},\omega) = \epsilon_0 \chi(\omega) \vec{E}(\vec{r},\omega), \tag{1.9}$$

which inserted in Eq. (1.5) provides the constitutive relation

$$\vec{D}(\vec{r},\omega) = \epsilon_0 \epsilon(\omega) \vec{E}(\vec{r},\omega). \tag{1.10}$$

$\chi(\omega)$ is the electrical susceptibility and $\epsilon(\omega) = 1 + \chi(\omega)$ is the relative dielectric constant of the medium. From the reality condition of the electric displacement $\vec{\mathcal{D}}$ and of the electric field $\vec{\mathcal{E}}$, it follows that $\epsilon^*(-\omega) = \epsilon(\omega)$, meaning that $\epsilon'(\omega), \epsilon''(\omega)$ are even and odd functions of ω, respectively. Note that the integral in Eq. (1.7) runs from $-\infty$ to $+\infty$. In turn, it is necessary that $\chi(t - t') = 0$ for $t' > t$ in order to fulfil the causality connection between the polarisation and the electric field; such a requirement is responsible for some peculiar properties of the electric susceptibility $\chi(\omega)$, which are commonly known as Kramers-Kronig relations [Jackson, 1999]. In general, $\chi(\omega) = \chi'(\omega) + i\chi''(\omega)$ is a complex function of the angular frequency ω, which provides useful information on the dispersion and loss/gain properties of the medium. Kramers-Kronig relations directly link real $\chi'(\omega)$ and imaginary $\chi''(\omega)$ parts of the dielectric susceptibility

$$\chi'(\omega) = \frac{1}{\pi} P \int_{-\infty}^{+\infty} d\omega' \frac{\chi''(\omega')}{\omega' - \omega}, \tag{1.11}$$

$$\chi''(\omega) = \frac{1}{\pi} P \int_{-\infty}^{+\infty} d\omega' \frac{\chi'(\omega')}{\omega - \omega'}, \tag{1.12}$$

where P represents the Cauchy principal value of the integral [Arfken and Weber, 2001]. For monochromatic fields $\vec{\mathcal{E}}(\vec{r},t) = \vec{E}(\vec{r}) e^{-i\omega t}$, it is possible to demonstrate that ϵ'' is responsible for dissipation or gain [Landau and Lifshitz, 1984]; indeed, the energy absorbed by the medium per unit volume and time is

$$Q = \frac{1}{2} \omega \epsilon_0 \epsilon'' |\vec{E}|^2. \tag{1.13}$$

Within the framework of macroscopical Maxwell equations, dissipative media are described by a complex dielectric constant $\epsilon(\omega) = \epsilon'(\omega) + i\epsilon''(\omega)$ with positive imaginary part ϵ''; on the other hand, gaining media are characterised by a negative imaginary part ϵ''. A remarkable application of Kramers-Kronig relation is found in absorption spectroscopy, where the measurement of $\epsilon''(\omega)$ allows for a direct calculation of $\epsilon'(\omega)$ by using Eq. (1.11).

1.2.2 Paraxial optics and diffraction

In this paragraph, the standard paraxial approximation for optical beams propagating in a lossless homogeneous medium is briefly reviewed. For a generic monochromatic field $\vec{\mathcal{E}}(\vec{r},t) = \vec{E}(\vec{r})e^{-i\omega t}$, it is possible to derive a scalar wave equation directly from Maxwell equations. Taking the curl of both sides of Eqs. (1.3,1.4) and combining them, one reaches the Hemholtz equation for the electric field $\vec{E}(\vec{r})$

$$\nabla^2\vec{E} + \frac{\omega^2}{c^2}\epsilon(\omega)\vec{E} = 0. \tag{1.14}$$

Elementary solutions of the Hemholtz equation are plane waves $\vec{E}(\vec{k})e^{i\vec{k}\cdot\vec{r}}$, where $k^2 = \omega^2\epsilon(\omega)/c^2$; the general solution, which is a direct consequence of the superposition principle [Jackson, 1999], is given by the Fourier envelope

$$\vec{E}(\vec{r}) = \int_S d^2k\vec{E}(\vec{k})e^{i\vec{k}\cdot\vec{r}}, \tag{1.15}$$

where the integral is performed over the iso-frequency surface $k^2 = \omega^2\epsilon(\omega)/c^2$. In general, for a given field distribution $\vec{E}(\vec{r})$, the electromagnetic field propagates in all directions with wavevector $\vec{k}$. For a very collimated optical beam propagating in the z-direction, it is possible to perform the Slowly Varying Envelope Approximation (SVEA), where the electric field is expressed as the product

$$\vec{E}(\vec{r}) = A(\vec{r}_\perp, z)e^{ikz}\hat{n}. \tag{1.16}$$

$\vec{r}_\perp = (x,y)$ is the transverse position vector, $\hat{n}$ is the polarisation unit vector lying in the $x-y$ plane and the envelope $A(\vec{r}_\perp, z)$ slowly depends on z compared to $\lambda = 2\pi/k$. Inserting the ansatz above into Eq. (1.14) and neglecting $\partial_z^2 A$ ($|\partial_z^2 A| << |2ik\partial_z A|$) one reaches

$$2ik\partial_z A + \nabla_\perp^2 A = 0, \tag{1.17}$$

where $\nabla_\perp^2 = \partial_x^2 + \partial_y^2$ is the transverse Laplace operator. Such a scalar equation is often referred to as *parabolic equation* because of its mathematical structure [Boyce and DiPrima, 1997] and describes with good accuracy *paraxial optics* [Yariv, 1985]. The polarisation $\hat{n}$ is arbitrary in the transverse plane perpendicular to $\hat{z}$, meaning that the electric field has no longitudinal component. Trivial

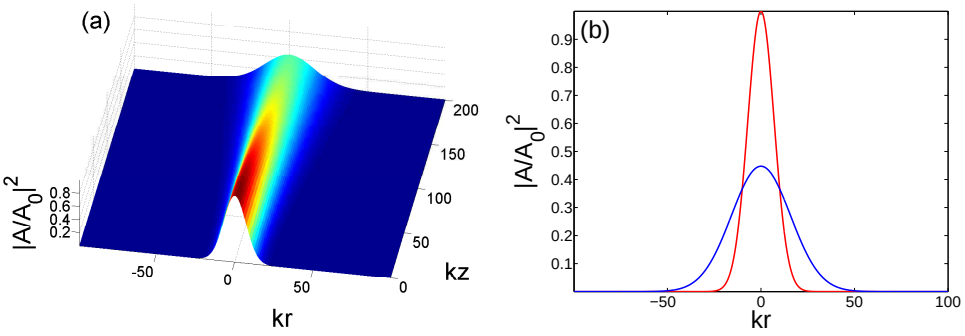

Figure 1.2: Diffraction of a gaussian beam.

solutions are plane waves $A = A_0$ propagating in the $\hat{z}$ direction; however, it is impossible to excite plane waves since they have infinite energy. For confined optical beams, the parabolic equation describes the phenomenon of *diffraction*: for every given field distribution $A(x, y)$ at $z = 0$, the electromagnetic field spreads out in propagation with a characteristic length-scale, called *diffraction length* L_D, which depends on the wavelength and on the size of the optical beam.

For an input Gaussian beam

$$A(r, 0) = A_0 e^{-r^2/2w_0^2}, \tag{1.18}$$

where $r = \sqrt{x^2 + y^2}$, it is possible to solve exactly Eq. (1.17) [Saleh and Teich, 2007], which provides us with the result

$$A(r, z) = A_0 \frac{kw_0^2}{iq(z)} exp\left(ik\frac{r^2}{2q(z)}\right), \tag{1.19}$$

where $q(z) = z - ikw_0^2$. For the squared modulus of the amplitude one gets

$$|A(r, z)|^2 = |A_0|^2 \frac{w_0^2}{w^2(z)} exp\left(-\frac{r^2}{w^2(z)}\right), \tag{1.20}$$

which is a Gaussian of half width at half maximum $HWHM = \sqrt{ln2}w(z)$, where $w^2(z) = w_0^2 + z^2/(k^2w_0^2)$. It is possible to define the *diffraction length* $L_D = kw_0^2$, as the distance of propagation where $w(L_D) = \sqrt{2}w_0$; L_D provides us with the typical length-scale where diffraction occurs. Such a parameter is important

in the theoretical modelling of soliton formation, which is described in section 1.3.2, and will be exploited in the following chapters, where plasmon-solitons are derived. Note that L_D is inversely proportional to the wavelength and directly proportional to the square of the beam width w_0. In Figs. 1.2a,b, it is plotted the spreading of an input Gaussian beam of width $kw_0 = 10$ (kL_D=100); in Fig. 1.2b, red and blue curves correspond to the Gaussian input ($kz = 0$) and output ($kz = 200$), respectively.

1.2.3 Confining light in dielectric structures

As pointed out in the preceding paragraph, the confinement of light is substantially limited by diffraction. However, it is possible to engineer and structure the dielectric geometry in order to suppress diffraction. Indeed, for an inhomogeneous dielectric structure, a region with high dielectric constant is an attractive basin of light [Yariv, 1985]. In what follows, we assume that the dielectric inhomogeneity $\delta\epsilon(\vec{r}_\perp)$ occurs only in the transverse $x - y$ plane and is small compared to the background dielectric susceptibility ϵ_b. For a monochromatic field in the paraxial approximation

$$\vec{\mathcal{E}}(\vec{r}, t) = A(\vec{r}_\perp, z)\hat{n}e^{ikz-i\omega t}, \tag{1.21}$$

optical propagation is determined by the scalar equation

$$2ik\partial_z A + \nabla_\perp^2 A + \delta\epsilon(\vec{r}_\perp)A = 0, \tag{1.22}$$

where $k^2 = \omega^2\epsilon_b/c^2$. In order to understand the effect of dielectric inhomogeneities on the propagation of light, a simple analogue with quantum mechanics can be exploited. Indeed, if one substitutes the longitudinal position z with time t ($z \to t$), the field amplitude A with the wavefunction ψ ($A \to \psi$) and the dielectric inhomogeneity $\delta\epsilon$ with the potential energy opposite in sign $-V$ ($\delta\epsilon \to -V$), then the parabolic equation is thoroughly equivalent to the Schrödinger equation.

In turn, traditional quantum mechanical concepts such as energy eigenvalues and wavefunction eigenvectors can be directly bridged to optics. The optical analogue of hamiltonian eigenvectors and eigenvalues is represented by modes and propagation constants.

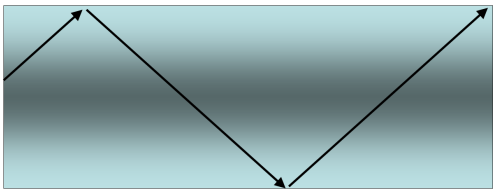

Figure 1.3: Light rays trapped in an optical fibre.

A mode of a dielectric structure is an electromagnetic field pattern that changes only its global phase ϕ as it propagates; the spatial phase change rate $\beta = d\phi/dz$ is called propagation constant of the mode.

Hence, a minimum of $-\delta\epsilon$ plays the role of an effective potential, which attracts light and can trap it under some conditions. In this context, within the limits of the paraxial approximation, the problem of light propagation in a cylindrical waveguide [Marcuse, 1982] is completely equivalent to the finite potential well problem in quantum mechanics [Cohen-Tannoudji et al., 1977].

Light trapping can also be explained qualitatively in the framework of geometrical optics, resulting from total internal reflection of rays striking at the interface between the core and the cladding, as depicted in Fig. 1.3. Only a small number of discrete modes can be excited, depending on the geometry of the dielectric structure; if only one mode exists, the optical fibre is known as single mode. Fibre optic communication has become of practical reality in the last decade; the main advantage provided by optical fibres lies in the high frequency of light ($\nu \approx 10^2 - 10^3$THz), which enables modulation at high rates ($\approx$ 100Gbit/sec). Practical optical fibres have a geometry that is more complex than the cylindrical dielectric wire: the silica core is typically cladded with another dielectric medium, surrounded by a buffer and a jacket.

Within the paraxial approximation, the longitudinal component of the electric field E_z is neglected. Such an approximation works well for optical fibres with small dielectric step $\Delta\epsilon \approx 10^{-3} - 10^{-2}$ and with a core diameter much larger than wavelength and is exact for plane waves in homogeneous media. However, as confinement increases, the longitudinal electric field component E_z increases accordingly and non-paraxial effects need to be included for an adequate description

of light propagation. For an optical fibre, Maxwell equations for a monochromatic field $\vec{\mathcal{E}}(\vec{r},t) = \vec{E}(\vec{r})e^{-i\omega t}$ in the linear response regime provide

$$\nabla \cdot [\epsilon \vec{E}] = 0, \tag{1.23}$$

$$\nabla \times \nabla \times \vec{E} = \frac{\omega^2}{c^2}\epsilon(\vec{r})\vec{E}. \tag{1.24}$$

If one wants to include non-paraxial effects, the vectorial identity

$$\nabla \times \nabla \times \vec{E} = -\nabla^2 \vec{E} + \nabla(\nabla \cdot \vec{E}) \tag{1.25}$$

can not be reduced to $-\nabla^2\vec{E}$. Indeed, the dielectric profile $\epsilon(\vec{r})$ is not homogeneous and

$$\nabla \cdot \vec{E} = -\vec{E} \cdot \nabla(ln\epsilon) \neq 0. \tag{1.26}$$

Nevertheless, the linear modes of Eq. (1.24) can be directly calculated by performing the ansatz $\vec{E}(\vec{r}) = \vec{A}(\vec{r}_\perp)e^{i\beta z}$. Eq. (1.24) can be solved exactly in both media, and after imposing boundary conditions of tangential electric field $\vec{E}_{//}$ continuity and normal electric displacement $\vec{D}_\perp$ continuity at the boundaries [Jackson, 1999], one achieves the mode dispersion $\beta = \beta(\omega)$. From a mathematical perspective, the optical problem of calculating the modes and the corresponding dispersion law is a part of the general theory of partial differential equations, commonly called Boundary Value Problem (or Sturm Liouville problem) [Arfken and Weber, 2001]. In chapter 7, the modes of a cylindrical wire, made either of metallic or dielectric core, are calculated exactly and such a mathematical procedure is explained with more detail.

The mode dispersion $\beta = \beta(\omega)$ basically depends on two contributions: material $\epsilon(\omega)$ and geometric dispersion. The material dispersion is due to the frequency dependent dielectric response of the media. On the other hand, the geometric dispersion ensues from the spatial characteristics of the dielectric structure, and in principle it can be tailored and engineered. The dispersion affects the mode phase velocity $\omega/\beta(\omega)$, which depends on the angular frequency ω. Thus, for a temporal pulse propagating in the fibre, every frequency contribution travels with a different velocity; as a result, the pulse is dispersed during propagation, with a characteristic length-scale called *dispersion length*. The pulse dispersion is the temporal analogue of diffraction and limits the modulation rate achievable in

optical communications. Theoretical modelling of ultrashort pulse propagation, taking account of the interplay between the dispersion and various nonlinear effects, is an interesting research area that has been extensively studied in recent years [Agrawal, 2001b; Boyd, 2003]; however, an accurate description of temporal effects on the propagation of electromagnetic pulses goes beyond the scope of this introduction and will not be examined in this dissertation.

1.2.4 Silicon on insulator (SOI) waveguides

Silicon on insulator (SOI) waveguides are photonic components made of a silicon wire sitting on the top of a silica base. Typically, they operate in the transparency region of silicon in the infrared, at wavelengths around $1.55\mu m$. SOI waveguides are receiving great interest by the scientific community because of the tight confinement they can provide, which can be exploited to fabricate miniaturised all-optical circuits [Almeida et al., 2004a]. Indeed, silicon is characterised by a high refractive index, approximately $n_{Si} \simeq 3.5$ in the band of interest [Edwards, 1985]. The high index step between silicon and air provides a much stronger confinement with respect to standard optical waveguides. Further, the strong geometric dispersion resulting from the tight confinement allows for dispersion tailoring by altering the geometry of the waveguide. An important advantage of embedding nano-sized silicon components in dielectric structures lies in the well-developed manifacturing techniques, which are based on the silicon technology, e.g., deep ultraviolet (DUV) and electron beam (EBM) lithography [DeLaRue et al., 2006].

However, SOI photonic devices suffer from considerable loss; the leading contribution to loss is provided by the roughness of silicon edges and can be limited by smoothing the surface [Lee et al., 2001]. Other contributions come from the coupling to the substrate [Grillot et al., 2006] and the two-photon absorption (TPA) [Baehr-Jones et al., 2005]. It is possible to reduce the effective TPA by engineering the geometry of the waveguide; an example is represented by the slot waveguide, depicted in Fig. 1.4. Such a geometry consists of two parallel silicon wires separated by a small gap of $50nm$ surrounded by silica [Almeida et al., 2004b]. In this case, the electromagnetic intensity is peaked within the silica glass between the two silicon wires; hence, only the small intensity tales residing

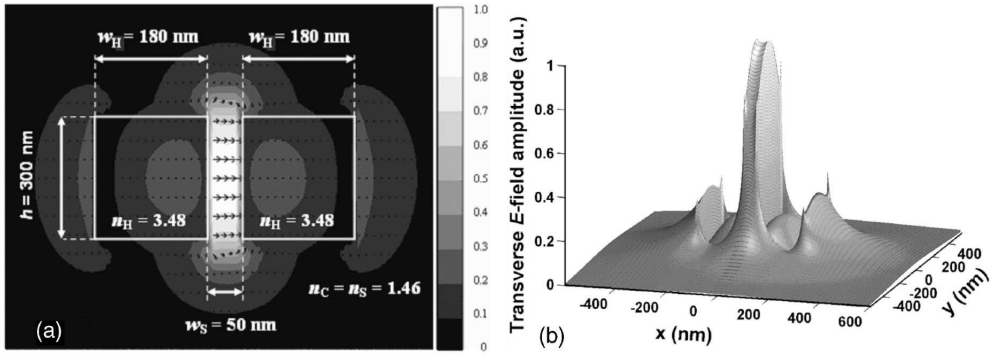

Figure 1.4: Transverse component of the electric field for the TM mode of a slot SOI waveguide. Image from [Almeida et al., 2004b].

in the silicon wires suffer from the high TPA and the effective nonlinear loss is reduced.

Further, the tight confinement of the electromagnetic field within the slot enhances the optical nonlinear processes, which are described in the following section. Novel geometries embedding a highly nonlinear polymer between the two silicon wires have been proposed and realised, demonstrating the possibility to exploit SOI slot waveguides for miniaturised ultrafast all-optical switching applications [Koos et al., 2009]. Theoretical modelling of light propagation in nonlinear SOI slot waveguides and silicon nanowires is described in chapters 4 and 7, respectively.

1.2.5 Photonic crystals

For optical fibres, the physical mechanism leading to the electromagnetic field confinement is the dielectric step between core and cladding media, as discussed in the previous paragraphs. However, the light confinement in dielectric structures can be achieved by means of different optical processes. Indeed, in the last two decades, the research in optical fibres has been revolutionised by the advent of photonic crystals [Russell, 2003].

Atoms or molecules constituting a crystal are arranged in highly ordered periodical patterns, called *lattices*. The optical, conductive and thermodynamic

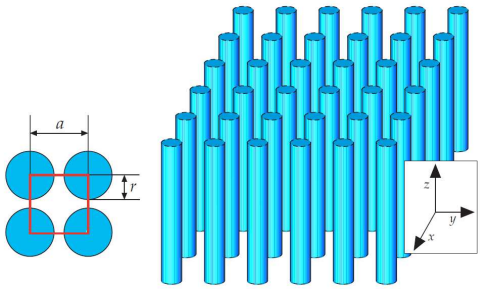

Figure 1.5: Two-dimensional photonic crystal with square lattice and cylindrical unit cell. Image from [Joannopoulos et al., 2008].

properties of solids stem from the lattice structure and from the *unit cell*, which is the atom or molecule corresponding to a single lattice point. Indeed, an electron bound or free to propagate through a crystal is subject to a periodic potential, determined both by the lattice pattern and by the unit cell constituent. In this context, it is known from solid state physics that energy bands and gaps are formed, and the conductive properties of the medium depend on the Fermi energy level [Kittel, 1996].

Photonic crystals are the optical analogues of crystals in solid state physics [Joannopoulos et al., 2008]. Important concepts such as the unit cell, the Bravais and the reciprocal lattices are naturally bridged to optics, where the counterpart of the molecular lattice periodic potential is represented by a periodic dielectric profile $\epsilon(\vec{r})$. Practical photonic crystals are made by arranging media with different dielectric constants in periodic patterns, as depicted in Fig. 1.5.

Remarkable phenomena occurring in solid state physics such as, e.g., Bloch oscillations and Zener tunnelling, have been reported also for photonic crystals [Sapienza et al., 2003; Trompeter et al., 2006a]. Important theoretical tools such as the Bloch theorem and group theory [Ashcroft and Mermin, 1976] have an optical counterpart. The *Bloch theorem* in solid state physics states that the wavefunction ψ of a particle in a periodic potential can be expressed as the product of a plane wave and a periodic function that has the same periodicity of the potential

$$\psi_{n\vec{k}} = e^{i\vec{k}\cdot\vec{r}} u_{n\vec{k}}(\vec{r}), \tag{1.27}$$

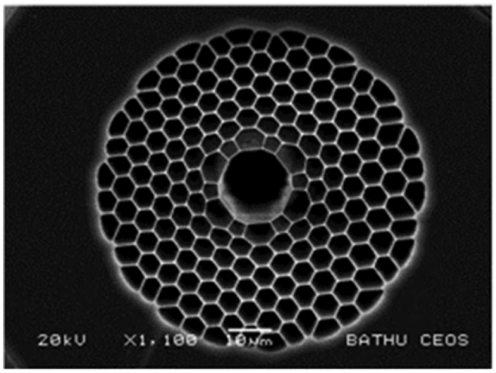

Figure 1.6: Scanning electron micrograph of a state-of-the-art HCPCF. Image from [Welch et al., 2009].

where $u_{n\vec{k}}(\vec{r}) = u_{n\vec{k}}(\vec{r}+\vec{R})$ is the unit cell wavefunction and $\vec{R}$ is a generic vector spanning the Bravais lattice points. The corresponding energy eigenvalues are periodic $E_n(\vec{k}) = E_n(\vec{k}+\vec{K})$, where $\vec{K}$ is a generic reciprocal lattice vector. Thus, for a complete analysis of Bloch modes, it is sufficient to limit the $\vec{k}$ values within the first Brillouin zone of the reciprocal lattice, which depends on the real lattice structure [Kittel, 1996].

In the same way, the electromagnetic modes of a photonic crystal are Bloch modes

$$\vec{E}_{n\vec{k}} = e^{i\vec{k}\cdot\vec{r}}\vec{e}_{n\vec{k}}(\vec{r}), \tag{1.28}$$

where the unit cell electric field $\vec{e}_{n\vec{k}}(\vec{r}) = \vec{e}_{n\vec{k}}(\vec{r}+\vec{R})$ and the mode dispersion $\omega_n(\vec{k}) = \omega_n(\vec{k}+\vec{K})$ are periodic. Like in solid state physics, also for photonic crystals bands and gaps are formed and the band structure can be engineered by tailoring the dielectric pattern.

Within a complete photonic bandgap [Joannopoulos et al., 2008], in analogy with solid state physics, light is not allowed to propagate since destructive interference by Bragg reflection occurs. Thus, monochromatic light impinging on a photonic crystal penetrates very short distances and is reflected back if its frequency lies within a complete photonic bandgap. Such a mechanism can be exploited for confining light in *lattice defects*, and is commonly called *bandgap guidance*.

Hollow Core Photonic Crystal Fibres (HCPCFs) rely on bandgap guidance to confine light in a hollow fibre core surrounded by a glass lattice, a mechanism that is completely different from the refractive index step guidance. The large index contrast and complex structure of HCPCFs make it difficult to treat mathematically, and most of theoretical modelling is done numerically. An important advantage provided by HCPCFs, relies on its flexibility in engineering the dispersion $\beta(\omega)$ by tailoring the dielectric pattern. A micrograph of a state-of-the-art HCPCF is depicted in Fig. 1.6.

Research in photonic crystals is still receiving a lot of interest, which overlaps with plasmonics if the photonic structure of the lattice is hybrid metal-dielectric. In chapter 5, the optical propagation in nonlinear *surface-plasmon-polaritonic crystals* is examined and general concepts coming from the theory of photonic crystals are exploited.

1.3 Nonlinear optical processes in dielectrics

In this paragraph, we briefly review some basic concepts of *nonlinear optics*, which are used in the following chapters of this thesis. In the linear regime, the electric polarisation $\vec{P}(\omega)$ is assumed proportional to the electric field $\vec{E}(\omega)$ in the Fourier domain. In this limit, the *superposition principle* holds, meaning that a superposition of different electromagnetic waves $\int_{-\infty}^{+\infty} d^3k \vec{E}(\vec{k},\omega)e^{i\vec{k}\cdot\vec{r}-i\omega(k)t}$ does not affect the propagation of each singular wave $\vec{E}(\vec{k},\omega)e^{i\vec{k}\cdot\vec{r}-i\omega(k)t}$. In this context, as described in paragraph 1.2.1, the presence of bound oscillating charges within the dielectric medium is taken into account by the dielectric constant $\epsilon(\omega)$. From a classical perspective, neglecting the damping, the motion of bound electrons of mass m and charge $-e$ in the linear response regime is described by the equation

$$\ddot{\vec{r}}(t) + \omega_0^2 \vec{r}(t) = -(e/m)\vec{E}(t), \tag{1.29}$$

where $\vec{E}(t)$ is an externally applied electric field and $\vec{r}, \omega_0$ are the position and the natural oscillation frequency of a single electron, respectively [Shen, 1984]. In this model, it is assumed the linear restoring force $\vec{F} = -m\omega_0^2\vec{r}$ corresponding to the harmonic potential $V = (1/2)m\omega_0^2 r^2$, which is an approximation of the molecular potential. In general, the potential V is a complex function of $\vec{r}$; however, for

small electromagnetic field amplitudes $|\vec{E}|$, the harmonic approximation works well and Eq. (1.29) can be solved straightforwardly in the Fourier domain:

$$\vec{r}(\omega) = \frac{e/m}{\omega^2 - \omega_0^2}\vec{E}(\omega). \tag{1.30}$$

In turn, the electric polarisation is proportional to the electric field: $\vec{P}(\omega) = -ne\vec{r}(\omega) \propto \vec{E}(\omega)$, where n is the electron density.

If the electromagnetic field intensity increases, the motion of electrons experiences anharmonic terms of the molecular potential $V(\vec{r})$; thus, the electric polarisation $\vec{P}(\omega)$ becomes a nonlinear function of the electric field $\vec{E}(\omega)$ depending on the molecular structure details. Such a classical argument was used to grasp the physical origin of optical nonlinearity; however, for an accurate description of nonlinear processes, one needs to resort to a quantum-mechanical approach [Boyd, 2003; Shen, 1984].

When the optical nonlinearity is taken into account, the superposition principle does not hold and the electromagnetic waves can mix or self-interact. Remarkable nonlinear phenomena include *second harmonic generation* [Franken et al., 1961], *four wave mixing* [Inoue, 1992] and *stimulated Raman scattering* [Eckhardt et al., 1962]. The family of optical nonlinear effects can be split in two sub-groups, namely *parametric* and *non-parametric* processes, which involve electronic transitions to *virtual* and *real* states, respectively. In other words, for parametric processes, the electrons oscillating in response to the optical field experience only virtual transitions. Conversely, for non-parametric processes, the external electromagnetic field is resonant with the electronic transitions, which involve emission or absorption of photons.

In this thesis, we describe the effect of the *nonresonant electronic* and *two-level atom* nonlinearities on light propagation in plasmonic waveguides. The two-level atom nonlinearity is a non-parametric process arising from the resonant absorption or emission of a photon by the dielectric medium [Boyd, 2003], as depicted in Fig. 1.7; such an effect is considered in the theoretical modelling of amplified surface plasmons in chapters 3 and 6. In this case, the electric polarisation is

$$\vec{P} = \epsilon_0 \alpha \frac{\delta - i}{1 + \delta^2 + |E/E_S|^2}\vec{E}, \tag{1.31}$$

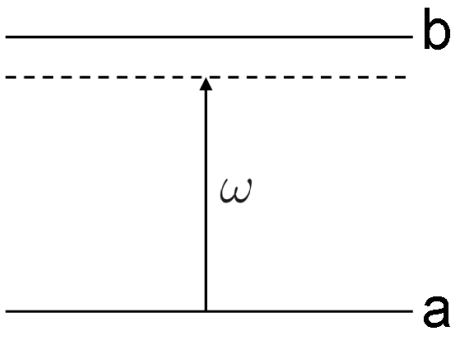

Figure 1.7: Electromagnetic excitation of electrons in a two-level system close to resonance.

where α is a dimensionless parameter describing gain ($\alpha > 0$) or loss ($\alpha < 0$), δ is the renormalized detuning with respect to the resonance frequency and E_S is the resonance saturation field; the derivation of the two-level nonlinearity is reported in appendix A. Such a saturated nonlinearity can be expanded in Taylor series only if $|\vec{E}| << E_S$:

$$\vec{P} \simeq \epsilon_0 \alpha \frac{\delta - i}{1 + \delta^2} \left[1 - (1 + \delta^2)^{-2} |E/E_S|^2 + o\left(|E/E_S|\right)^4\right] \vec{E}. \tag{1.32}$$

The nonresonant electronic nonlinearity is a parametric process resulting from two mechanisms: one-photon and two-photon processes [Boyd, 2003], which are depicted in the energy level diagrams a,b of Fig. 1.8. The electric polarisation can be expressed as the sum of two terms $\vec{P}(\omega) = \vec{P}_L(\omega) + \vec{P}_{NL}(\omega)$, where $\vec{P}_L(\omega) = \epsilon_0 \chi(\omega) \vec{E}(\omega)$ is the linear contribution and $\vec{P}_{NL}(\omega)$ is the nonlinear counterpart. For an isotropic nonresonant electronic process (Kerr nonlinearity), the nonlinear polarisation is provided by

$$\vec{P}_{NL} = \frac{1}{2} \epsilon_0 \chi_3 \left[|\vec{E}|^2 \vec{E} + \frac{1}{2} (\vec{E} \cdot \vec{E}) \vec{E}^* \right]. \tag{1.33}$$

It can be demonstrated that the one-photon processes contribute only to the first term $|\vec{E}|^2 \vec{E}$, while the two-photon processes contribute to both terms [Boyd, 2003]. Phenomenologically, the effect of the nonlinear polarisation $\vec{P}_{NL}$ is described by an intensity-dependence of the refractive index $n = n_0 + n_2 I$, where $n_2 = \dfrac{3\chi_3}{4\epsilon_0 c n_0^2}$, and is commonly referred to as *optical Kerr effect*.

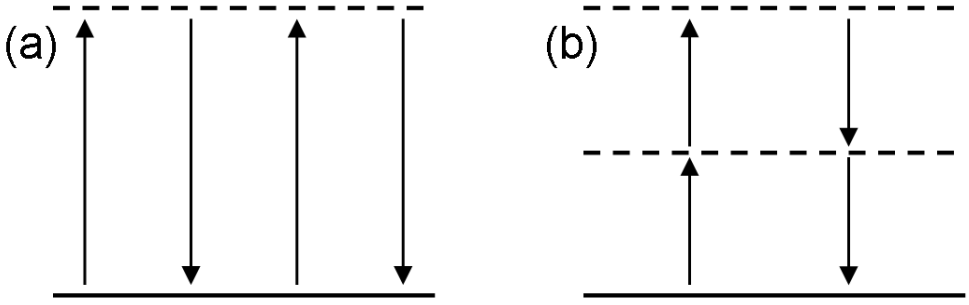

Figure 1.8: Energy level diagram for (a) one-photon and (b) two-photon nonlinear processes.

Typical values of Kerr nonlinear susceptibilities range from $\chi_3 \simeq 2\times10^{-22}m^2V^{-2}$ for silica glass to $\chi_3 \simeq 2\times10^{-19}m^2V^{-2}$ for highly nonlinear polymers (DDMEBT) [Michinobu et al., 2005; Vallaitis et al., 2009].

1.3.1 Nonlinear Schrödinger equation (NLSE)

For a monochromatic electromagnetic wave $\vec{\mathcal{E}}(\vec{r},t) = \vec{E}(\vec{r},\omega)e^{-i\omega t}$ propagating in a nonlinear medium, Maxwell equations are

$$\nabla \cdot \left[\epsilon_0\epsilon(\omega)\vec{E}(\vec{r},\omega) + \vec{P}_{NL}(\vec{r},\omega)\right] = 0, \tag{1.34}$$

$$\nabla \cdot \vec{H}(\vec{r},\omega) = 0, \tag{1.35}$$

$$\nabla \times \vec{E}(\vec{r},\omega) = i\mu_0\omega\vec{H}(\vec{r},\omega), \tag{1.36}$$

$$\nabla \times \vec{H}(\vec{r},\omega) = -i\omega\epsilon_0\epsilon(\omega)\vec{E}(\vec{r},\omega) - i\omega\vec{P}_{NL}(\vec{r},\omega). \tag{1.37}$$

Combining the curl equations and using Eq. (1.34) one gets a vectorial equation for the electric field $\vec{E}$ and the nonlinear part of the polarisation $\vec{P}_{NL}$

$$\nabla^2\vec{E} + \frac{\omega^2}{c^2}\epsilon(\omega)\vec{E} + \mu_0\omega^2\vec{P}_{NL} + \frac{1}{\epsilon_0\epsilon(\omega)}\nabla(\nabla\cdot\vec{P}_{NL}) = 0, \tag{1.38}$$

where $\vec{P}_{NL}$ is a nonlinear function of $\vec{E}$. Here, we consider the specific case of isotropic nonresonant electronic nonlinearity described in the previous paragraph, where $\vec{P}_{NL}$ is given by Eq. (1.33). In the framework of paraxial optics, the electric field is given by the product of a slowly-varying field envelope and a plane wave

$\vec{E}(\vec{r},\omega) = \vec{A}(\vec{r}_\perp, z)e^{ikz}\hat{n}$, where $k^2(\omega) = \omega^2\epsilon(\omega)/c^2$ and $\hat{n}$ is the polarisation unit vector. In the limit where $|\vec{P}_{NL}/\epsilon_0|$ is a small quantity of the same order of $|k^{-1}\partial_z A|, |k^{-2}\nabla_\perp^2 A|$, the term $\nabla(\nabla\cdot\vec{P}_{NL})$ can be neglected. In turn, for a linearly polarised electromagnetic wave, one gets the scalar propagation equation

$$2ik\partial_z A + \nabla_\perp^2 A + \frac{3}{4}k^2\chi_3|A|^2A = 0, \tag{1.39}$$

which is commonly referred to as *nonlinear Schrödinger equation* (NLSE) [Sulem and Sulem, 1999]. Such a scalar equation is very useful to grasp nonlinear phenomena like *self-action*, but its application is limited by the paraxial approximation. In the two-dimensional case, renormalizing the field amplitude to $(3|\chi_3|/8)^{-1/2}$, one reaches

$$i\partial_z A + \frac{1}{2k}\partial_x^2 A + k\gamma|A|^2A = 0, \tag{1.40}$$

where $\gamma = sign(\chi_3)$. Plane wave solutions are readily found by substituting the ansatz

$$A = A_0 e^{ipz+iqx} \tag{1.41}$$

in Eq. (1.40), obtaining the *nonlinear dispersion*:

$$p + \frac{q^2}{2k} = k\gamma|A_0|^2. \tag{1.42}$$

The nonlinear dispersion is a typical property of nonlinear systems, where the phase shift p depends on the field intensity $|A_0|^2$ and the transverse momentum q. Hence, conversely to linear optics where the field amplitude remains arbitrary, here plane waves with different optical amplitudes propagate with modified propagation constants. Note that Eq. (1.40) is left invariant by an arbitrary phase shift $A \to Ae^{i\phi}$. Such a symmetry of the NLSE is reflected onto its solutions $A_0 \to A_0e^{i\phi}$, which global phase is left arbitrary.

The nonlinear propagation of a generic input profile $A(x,z)$ is involved and is generally modelled by resorting to computational methods, like, e.g., the split-step beam propagation method, which is reported in appendix C. However, it is possible to grasp the role played by nonlinearity from a simple analogue with quantum-mechanics. Indeed, by substituting

$$V(kx) = \gamma|A(kx)|^2, \tag{1.43}$$

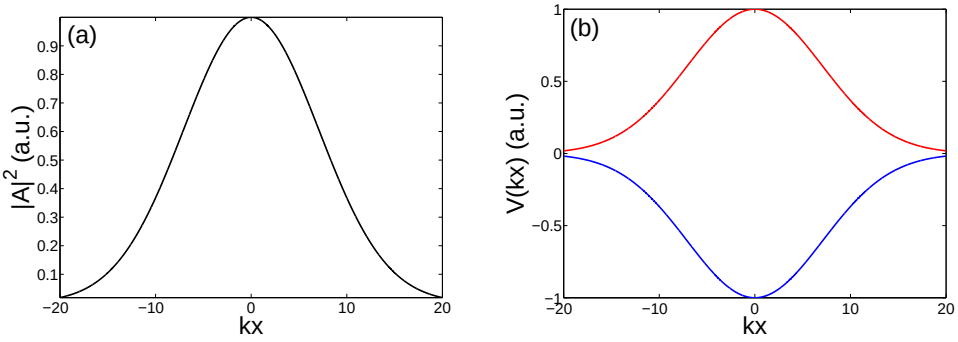

Figure 1.9: (a) One-dimensional optical beam squared amplitude experiencing an effective potential (b) for focusing (blue line) and defocusing (red line) nonlinearities.

the NLSE resembles the Schrödinger equation. In turn, the nonlinearity represents an effective potential acting on the optical field, which depends on the optical field itself; for this reason, such a mechanism is named *self-action* and can lead to different effects, the most remarkable being *self-focusing* and *self-defocusing* [Boyd et al., 2009]. Focusing (defocusing) nonlinearity is characterised by a positive (negative) nonlinear susceptibility χ_3. A one-dimensional optical beam propagating in a nonlinear medium, see Fig. 1.9a, generates an effective potential that depends on the transverse beam profile, see Fig. 1.9b. For focusing nonlinearity (blue curve), such a potential attracts the beam tails towards the centre, countering diffraction; conversely, for defocusing nonlinearity, the effective potential repels light from the beam centre towards the tails, together with diffraction. From the stability analysis, it can be demonstrated that plane-wave solutions $A = A_0 e^{ipz+iqx}$ are absolutely stable for defocusing nonlinearity ($\gamma = -1, \chi_3 < 0$), and unstable for focusing nonlinear media ($\gamma = 1, \chi_3 > 0$) [Kivshar and Agrawal, 2003]. The instability occurs only if the transverse momentum is smaller than a particular threshold, $|q| < 2k|A_0|$; such an effect is commonly named *modulation instability*, since it breaks up plane-waves in periodic patterns [Agrawal, 2001b]. The NLSE is a general model that has found application in other ambits of nonlinear optics, like, e.g., optical propagation in nonlinear lattices, which is modelled by a discrete NLSE [Christodoulides and

Joseph, 1988]. In chapter 5, the propagation of light in nonlinear arrays of SPPs is considered and the discrete NLSE is described with more detail. Another relevant application of the NLSE is found in ultrashort pulse propagation in optical fibres [Hasegawa and Tappert, 1973]; here, however, higher order dispersion and different nonlinear effects such as self-steepening, Raman scattering and Stokes losses play an important role [Mamyshev and Chernikov, 1990].

1.3.2 Solitons

A soliton is a non-diffracting self-sustaining wave that can arise in numerous nonlinear systems. From a historical perspective, a remarkable example of solitary wave is the "wave of translation" observed by John Scott Russell in 1834. He observed that if a boat moving along a canal suddenly stopped, the surge of water at its bow continued to move, and "assumed the form of a large solitary elevation, a rounded, smooth and well-defined heap of water, which continued its course along the channel apparently without change of form or diminution of speed" [Russell, 1844].

Optical spatial solitons are self-trapped non-diffractive beams of finite spatial cross section [Chiao et al., 1964; Segev and Stegeman, 1998]. The occurrence of soliton formation ensues from the nonlinear self-action of light, which basically creates its own waveguide. The striking peculiarity of soliton dynamics manifests when different solitons are made to interact [Stegeman and Segev, 1999]. In this context, solitons exhibit a unique particle-like behaviour, exerting attractive or repulsive forces on each other, depending on their relative phase [Gordon, 1983]. Further, soliton collisions are elastic, i.e. power and momentum are conserved, since nonlinear dynamics restores the initial soliton profiles after the collision [Zabusky and Kruskal, 1965]. From a relativistic quantum field theory perspective, solitons possess many of the basic attributes of particles, such as mass, charge and spin [Manton, 2008]. In this paragraph, *bright* and *dark* soliton formation in a Kerr medium is reviewed, preparing a solid background for the description of *plasmon solitons*, which is developed in chapters 3 and 6.

In analogy with linear modes, a *nonlinear mode* of the NLSE is a solution that changes only its global phase ϕ as it propagates; the spatial phase change rate

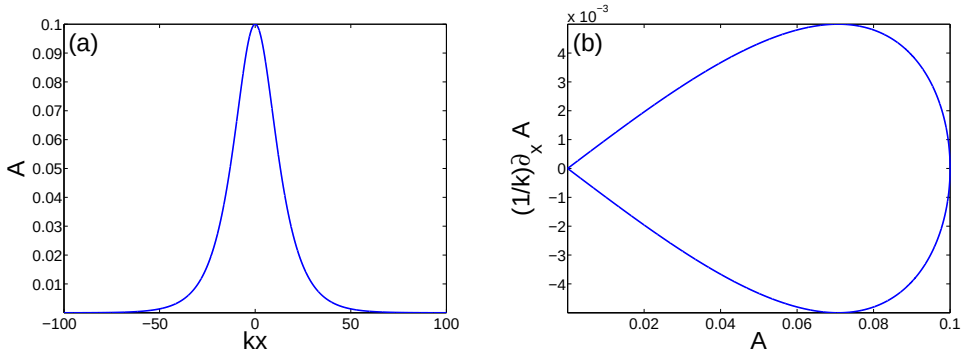

Figure 1.10: (a) Kerr bright soliton profile for $\alpha = 0.1$ and (b) its homoclinic trajectory in the phase space portrait.

$d\phi/dz$ is the propagation constant of the nonlinear mode. Kerr bright solitons are a family of nonlinear modes of the NLSE that remain confined and preserve their shape. The soliton existence is strictly related to the occurrence of modulational instability [Hasegawa, 1984]. Indeed, the NLSE is exactly integrable through the inverse scattering transform [Zakharov and Shabat, 1972], providing an exact analytical expression for the bright soliton solution ($\gamma = 1$)

$$A(x,z) = \alpha \mathrm{sech}(\alpha k x) exp\left(ik\alpha^2 z/2\right). \tag{1.44}$$

As for the case of the homogeneous Kerr nonlinear solutions, the soliton propagation constant $\mu = k\alpha^2/2$ depends on the amplitude α. Thus, Eq. (1.44) describes a soliton family, parametrized by the amplitude α. In the phase space, bright solitons are characterised by a homoclinic trajectory [Boyce and DiPrima, 1997], as depicted in Fig. 1.10.

For defocusing Kerr nonlinearity ($\gamma = -1$), the homogeneous nonlinear plane waves $A = A_0 e^{ipz+iqx}$ are always stable against small perturbations; in turn, solitons can exist only in the form of localised dark spots emerging from a plane-wave background [Luther-Davies and Kivshar, 1998]. In this case, the inverse scattering method with boundary conditions $|A(kx)| \to A_0$ for $kx \to \pm\infty$, provides us with the analytical expression for dark solitons

$$A(x,z) = \alpha \tanh(\alpha k x) exp\left(-ik\alpha^2 z\right). \tag{1.45}$$

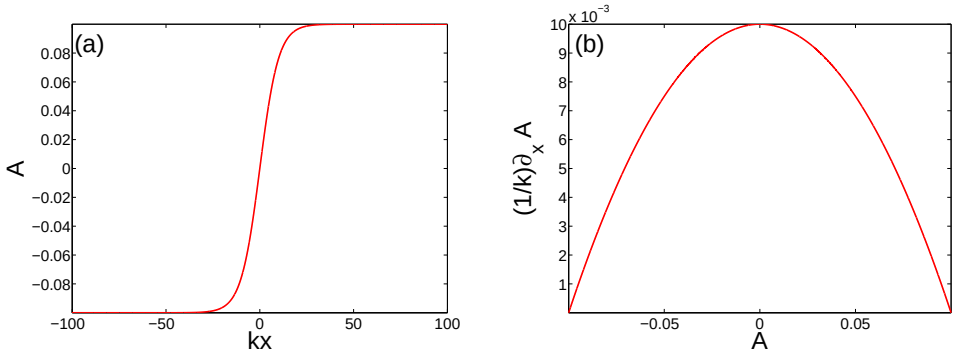

Figure 1.11: (a) Kerr dark soliton profile for $\alpha = 0.1$ and (b) its heteroclinic trajectory in the phase space portrait.

The dark soliton field profile and its trajectory in the phase space are depicted in Fig. 1.11. Note that the dark solitons undergo a π phase change at $x = 0$ where the field amplitude is null, mathematically described by the odd function $\tanh(\alpha k x)$.

The stability analysis reveals that both bright and dark solitons are stable solutions of the NLSE [Kivshar and Agrawal, 2003]. However, it can be demonstrated that even relatively small perturbations due to non-Kerr nonlinearities generate instabilities [Pelinovsky et al., 1996]. The description of non-Kerr nonlinearities goes beyond the aim of this introduction, and only the cubic nonlinearity is considered in this thesis.

1.4 Concluding remarks

In this introductory chapter, some basic concepts of optical propagation in photonic devices have been briefly described. Light diffraction becomes relevant when the size of the optical beam is comparable with the wavelength, but can be suppressed by using optical fibres, silicon on insulator waveguides or bandgap guidance in photonic crystal defects. Alternatively to structuring the dielectric properties of the medium, it is possible to use the nonlinear self-focusing to compensate for the diffraction and achieve a localised self-sustaining wave: the optical

soliton. Important quantities like the diffraction length and the nonlinear length will be used in the following chapters.

The mechanisms presented in this chapter are not sufficient to achieve localisation at the nanoscale. In the next chapter we introduce some basic properties of surface plasmon polaritons (SPPs), which provide a much tighter confinement and constitute the most promising candidate to confine light in the subwavelength scale.

Chapter 2

Surface plasmon polaritons

A *Surface Plasmon Polariton* (SPP) is an exponentially localised electromagnetic wave propagating along a planar interface between a metal and a dielectric medium [Agranovich and Mills, 1982; Boardman, 1982; Raether, 1988]. Such a confined surface wave arises via the coupling of the optical field with free electrons oscillating in the metal, allowing for tight localisation and enhanced electromagnetic field intensity close to the metal surface. From a quantum-mechanical perspective, a SPP is a quasi-particle ensuing from the coupling of *plasmons*, plasma oscillation quanta, and photons. Despite their quantum mechanical nature, SPPs in common plasmonic structures can be described in the framework of classical electrodynamics. Because of their intrinsic surface nature, SPPs are very sensitive to the dielectric properties of the media at the interface and have been extensively used in biosensor devices [Anker et al., 2008; Homola, 2006; Raschke et al., 2003]. Further, the electromagnetic field enhancement close to the metal surface can be exploited for optical detection and spectroscopy of single molecules and single nanoparticles [Kneipp et al., 1997; Lal et al., 2007; Nie and Emory, 1997]. Besides, the subwavelength confinement achievable with SPPs can be exploited to scale down optical devices to nanometric dimensions. Such a tight localisation promises advanced control of light in miniaturised photonic circuits [Bozhevolnyi et al., 2006a; Maier et al., 2001; Shalaev and Kawata, 2007] and SPP-based optical interconnects have been proposed and realised [Ebbesen et al., 2008; Ozbay, 2006].

Propagation of SPPs is fundamentally limited by ohmic loss in the metal. SPP attenuation lengths range from $L_A = 10 - 100\mu m$, for visible light, to $L_A \approx 1mm$ in the near-infrared light spectrum [Barnes et al., 2003]. In the terahertz region, the attenuation length increases considerably $L_A \approx 1km$; however, such a reduced attenuation is paid in terms of much weaker confinement [Jeon and Grischkowsky, 2006]. Optical propagation in resonant metallic nanoparticle chains, where light is transmitted by electrodynamic interparticle coupling [Citrin, 2004; Maier et al., 2003], has been proposed in order to increase the attenuation length L_A. The reduced use of metal lowers the losses due to metal absorption; however, the coupling to radiative modes due to scattering from the nanoparticles increases the effective loss [Quinten et al., 1998].

In turn, several methods have been proposed in order to reduce the metal loss and to optimise the SPP propagation length. A remarkable and successful method relies on the excitation of long-range SPPs in thin metallic films [Berini, 2009; Burke et al., 1986; Quail et al., 1983; Sarid, 1981], where the field penetration in the metal stripe is reduced, lowering the effective loss. However, the smaller penetration within the metal stripe implies weaker localisation in the dielectric medium and the reduced loss is paid in terms of the smaller confinement [Berini, 2001]. Hence, the inherent trade-off between confinement and loss in plasmonic guiding structures can be completely overcome only by embedding gaining dielectrics [Ambati et al., 2008; Bergman and Stockman, 2003; Noginov et al., 2008a; Seidel et al., 2005].

In this chapter, the SPP formation in various settings is reviewed. In section 2.1 we describe the dielectric response of metals to optical fields: metallic susceptibility, volume plasmons and light dispersion in metals are briefly discussed. Dispersion and loss for SPPs excited at a single metal-dielectric interface and in Insulator-Metal-Insulator (IMI) waveguides are described in sections 2.2, 2.3, respectively. Here, the propagation of long-range SPPs is reviewed and the intrinsic trade-off between confinement and loss is pointed out. Experimental methods for exciting SPPs are described in section 2.4, while the application of SPPs as optical interconnects in miniaturised photonic circuitry is discussed in section 2.5. Finally, in section 2.6, the SPP amplification in various settings is reviewed and

the power flow at a single interface between a metal and a gaining dielectric is described.

2.1 Optical properties of metals

The optical properties of metals have been studied extensively in the turning of the last century [Drude, 1900] and are discussed in most of the solid state physics textbooks [Ashcroft and Mermin, 1976]. In this section, we provide a brief review of the relevant aspects of optics in metals. To grasp the basic behaviour of the metal response to electromagnetic fields at optical frequencies, we can rely on classical electrodynamics, without the need to resort to quantum mechanics. Metals have a high density of *free* electrons in the conduction band, which can be considered as a continuum of states [Kittel, 1996]; indeed, at room temperature, the thermal energy of electrons is much higher than the separation of the energy levels in the conduction band and the electrons are *free* to move within the energy band.

From a phenomenological perspective, it is well known that in the electrostatic regime, for low electromagnetic frequencies ranging from microwaves to far-infrared, metals are opaque and highly reflective. In this limit, only a negligible part of the electromagnetic field penetrates into the metal and the resulting ohmic dissipation is small. For visible frequencies, the field penetration and dissipation increase significantly. Finally, for ultraviolet frequencies (or higher), metals become almost transparent except for some particular frequencies resonant with the electronic interband transitions. Accurate measurements of $\epsilon(\omega)$ via reflection experiments have been carried out for noble metals [Johnson and Christy, 1972; Palik, 1998; Rakic et al., 1998].

The basic properties of the dielectric constant $\epsilon(\omega)$ for metals can be derived within the *plasma* approximation [Fox, 2001], which assumes the metal as a gas of *free* electrons moving against a fixed background of positive ion cores, as illustrated in Fig. 2.1. The electrons with effective mass m [Kittel, 1996] oscillate in response to the optical field propagating within the medium. Their motion is damped by the collisions occurring with the characteristic frequency $\gamma = 1/\tau$,

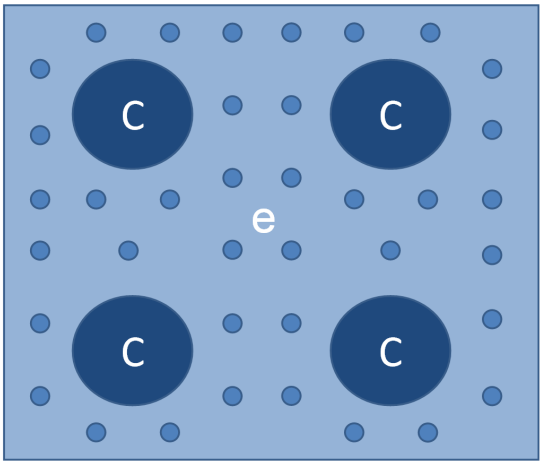

Figure 2.1: Gas of free electrons e oscillating on a fixed background of positive ion cores C.

where τ is the relaxation time of the electron gas. The Newton equation of motion for a generic electron is given by

$$m\ddot{\vec{r}}(t) + m\gamma\dot{\vec{r}}(t) = -e\vec{E}(t), \tag{2.1}$$

where $e, \vec{r}(t)$ are the electron charge and position and $\vec{E}(t)$ is the electric field of light propagating in the medium. The Lorentz force on the electron charge is neglected in the non-relativistic regime [Jackson, 1999]. For a monochromatic plane wave, the temporal dependence is harmonic $\vec{E}(t) = \vec{E}_0 e^{-i\omega t}$ and Eq. (2.1) can be solved by assuming $\vec{r}(t) = \vec{r}_0 e^{-i\omega t}$, which yields

$$\vec{r}(t) = \frac{e}{m}\frac{1}{\omega^2 + i\gamma\omega}\vec{E}(t). \tag{2.2}$$

The macroscopic polarisation $\vec{P}$ induced by the displacements of the electrons can be directly calculated by $\vec{P} = -ne\vec{r}$, where n is the density of free electrons of the medium. In turn, the electric displacement $\vec{D}$ is given by

$$\vec{D} = \epsilon_0 \left(1 - \frac{\omega_p^2}{\omega^2 + i\gamma\omega}\right)\vec{E}, \tag{2.3}$$

where $\omega_p = \sqrt{ne^2/\epsilon_0 m}$ is called the *plasma frequency* of the free electron gas, which is usually in the ultraviolet ($\omega_p \approx 1.45 \times 10^{16} rad/sec, \lambda_p \approx 130nm$ for

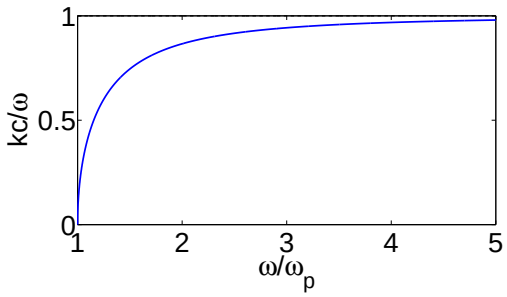

Figure 2.2: Plane-wave dispersion of light propagating in the metal bulk.

silver). As a result, the dielectric constant of the medium is

$$\epsilon(\omega) = 1 - \frac{\omega_p^2}{\omega^2 + i\gamma\omega}. \tag{2.4}$$

For $\omega = \omega_p$, the longitudinal collective oscillations of electrons, commonly named *volume plasmons*, are excited [Kittel, 1996]. Indeed, if we neglect the damping γ, for $\omega = \omega_p$ the induced polarisation $\vec{P}$ is equal in modulus and opposite in sign to $\epsilon_0\vec{E}$. In turn, the electric displacement $\vec{D} = 0$ does not respond to the external electric field $\vec{E}$ and the transverse oscillations are quenched off. Further, such collective oscillations of electrons are called *electrostatic modes*, since no magnetic field is produced ($\nabla \times \vec{B} = -(i\omega/c^2)\vec{D} = 0$). From a quantum mechanical perspective, a volume plasmon is a quantum of plasma oscillation: it can not be excited by an electromagnetic wave because the mode is purely longitudinal, but it may be excited by particle impact.

In this simplified model, metals are opaque for $\omega < \omega_p$ and transparent for $\omega > \omega_p$, where plane waves $\vec{E}(\vec{r},t) = \vec{E}_0 e^{i\vec{k}\cdot\vec{r}-i\omega t}$ can propagate through the medium. Combining Eqs. (1.3,1.4) and substituting the expression for $\vec{E}(\vec{r},t)$, one gets the dispersion of plane waves propagating within the metal

$$\omega^2 = \omega_p^2 + k^2c^2, \tag{2.5}$$

where $c = 1/\sqrt{\epsilon_0\mu_0}$ is the speed of light in vacuum. For $\omega < \omega_p$, the wave vector k is purely imaginary and plane waves do not propagate. Conversely, for $\omega \geq \omega_p$, the transverse plane waves propagate through the metal (loss is neglected) and

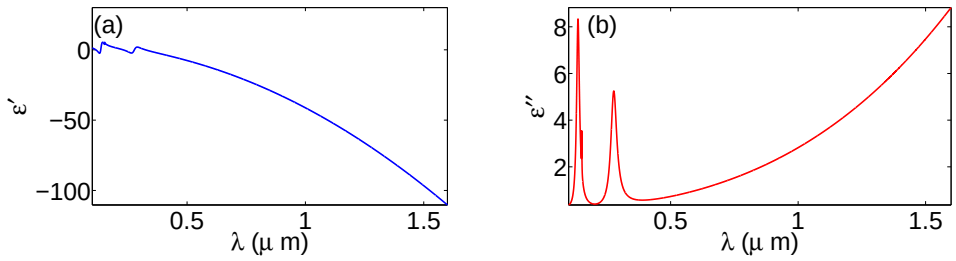

Figure 2.3: (a) Real and (b) imaginary parts of the dielectric constant of silver.

their dispersion is plotted in Fig. 2.2. Note that for $\omega >> \omega_p$, the dispersion of plane-waves tends to the lightline $\omega = ck$, which corresponds to the dispersion of light in vacuum. This simplified model helps to grasp the basic properties of the optical response of metals. However, it completely disregards the effect of interband transitions, which can be included by modelling the dielectric constant as a weighted sum of multiple oscillators

$$\epsilon(\omega) = \epsilon_\infty + \sum_{n=0}^{N} \frac{f_n \omega_p^2}{\omega_n^2 - \omega^2 + i\gamma_n \omega}. \tag{2.6}$$

ϵ_∞ is the background dielectric constant of the ion cores, ω_n, γ_n are the angular frequency and the damping coefficient of the nth interband resonance and f_n is a dimensionless weight. Such parameters can be computed by fitting the experimental data [Rakic et al., 1998] with Eq. (2.6) [Ung and Sheng, 2007]. The dielectric constant of silver computed by this procedure is depicted in Fig. 2.3. Note that the plasma resonance is $\lambda_p = 320nm$ (the free-electron model provides $\lambda_p = 130nm$). Within the wavelength range $\lambda = 100nm - 1.5\mu m$, the real part ϵ' changes by two orders of magnitude and the imaginary part ϵ'' is peaked for the wavelengths resonant with the interband transitions. Such a model for the dielectric constant of metals is often referred to as *Lorentz-Drude model* and will be used in the numerical computations of plasmonic modes.

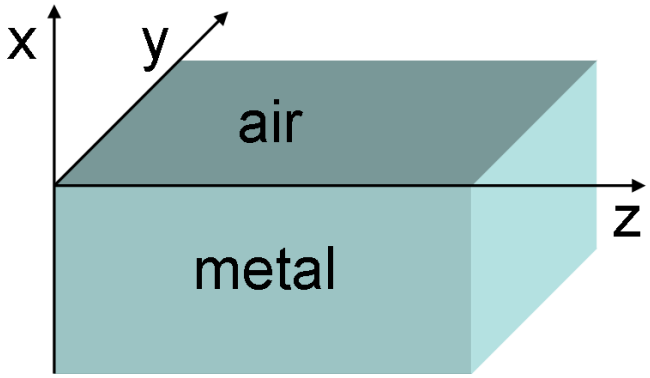

Figure 2.4: Single interface between a metal and air.

2.2 SPPs at a single metal-dielectric interface

In this section, we derive the plasmonic linear modes of a single metal-air interface, depicted in Fig. 2.4. The dielectric response of the metal is described by the frequency dependent dielectric constant $\epsilon_m(\omega)$ in the Lorentz-Drude model, as discussed in the previous section, while the dielectric constant of air is $\epsilon_d = 1$. Here, we assume that the structure is infinitely extended in the y-direction. Hence, the dielectric profile $\epsilon = \epsilon(x, \omega)$ is a function of x and ω only. In the monochromatic case, the electric and magnetic fields are harmonic functions of time

$$\vec{\mathcal{E}}(x, z, t) = \vec{E}(x, z)e^{-i\omega t}, \tag{2.7}$$

$$\vec{\mathcal{H}}(x, z, t) = \vec{H}(x, z)e^{-i\omega t}. \tag{2.8}$$

The time-independent curl Maxwell equations for the fields $\vec{E}, \vec{H}$ are

$$\nabla \times \vec{E} = ic\mu_0\vec{H}, \tag{2.9}$$

$$\nabla \times \vec{H} = -ic\epsilon_0\epsilon\vec{E}, \tag{2.10}$$

where $\partial_x, \partial_y, \partial_z$ derivatives are taken with respect to the dimensionless spatial variables x, y, z, rescaled to $1/k$ ($k = \omega/c$). For the single interface geometry, the dielectric profile is provided by

$$\epsilon(x, \omega) = \epsilon_m(\omega)\theta(-x) + \epsilon_d\theta(x), \tag{2.11}$$

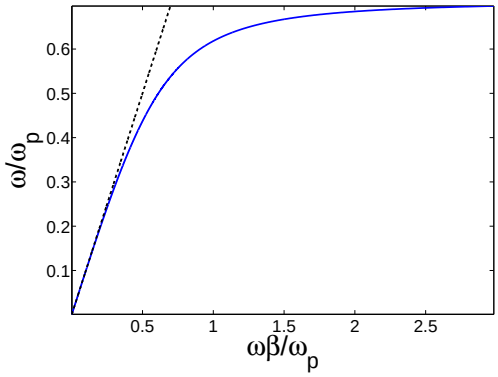

Figure 2.5: SPP dispersion for an ideal metal described by the free electron gas model in the absence of damping.

where $\theta(x)$ is the Heaviside step function [Arfken and Weber, 2001]. The linear modes are derived by assuming the harmonic z-dependence

$$\vec{E}(x,z) = \vec{e}(x)e^{i\beta z}, \tag{2.12}$$

$$\vec{H}(x,z) = \vec{h}(x)e^{i\beta z}, \tag{2.13}$$

where β is the dimensionless mode propagation constant, rescaled to $k = \omega/c$. In general, for one-dimensional geometries, Maxwell equations provide two independent sets of solutions, namely transverse magnetic (TM) and transverse electric (TE) modes [Jackson, 1999].

SPP modes are TM-polarised waves: the magnetic field $\vec{h}$ is purely transverse polarised in the y-direction and the electric field $\vec{e}$ lies in the x-z plane. From a mathematical perspective, the determination of plasmonic modes is a Boundary Value Problem (BVP) [Boyce and DiPrima, 1997]. The modes can be determined by solving Maxwell equations in both sides of the interface $x > 0, x < 0$ and applying Boundary Conditions (BCs) for the continuity of the longitudinal electric field E_z and of the normal electric displacement $D_x = \epsilon E_x$ at x=0. Note that the discontinuity of the dielectric profile $\epsilon(x)$ at $x = 0$ implies that the transverse component of the electric field E_x is also discontinuous. Inserting Eqs. (2.12,2.13) into Maxwell equations and combining them, one reaches

$$\partial_{xx}^2 e_z + (\epsilon_j - \beta^2)e_z = 0, \tag{2.14}$$

$$e_x = -\frac{i\beta}{\beta^2 - \epsilon_j}\partial_x e_z, \tag{2.15}$$

$$h_y = \frac{i}{c\mu_0}(\partial_x e_z - i\beta e_x), \tag{2.16}$$

where the index $j = d, m$ labels the dielectric and metal regions, respectively. For confined modes, it is implied that electric and magnetic fields $\vec{e}, \vec{h} \to 0$ as $x \to \pm\infty$. Hence, the plasmonic mode solutions are provided by the exponential functions

$$e_z = A\left[e^{q_m x}\theta(-x) + e^{-q_d x}\theta(x)\right], \tag{2.17}$$

$$e_x = -i\beta A\left[\frac{1}{q_m}e^{q_m x}\theta(-x) - \frac{1}{q_d}e^{-q_d x}\theta(x)\right], \tag{2.18}$$

$$h_y = \frac{1}{ic\mu_0}A\left[\frac{\epsilon_m}{q_m}e^{q_m x}\theta(-x) - \frac{\epsilon_d}{q_d}e^{-q_d x}\theta(x)\right], \tag{2.19}$$

where $q_{d,m}^2 = \beta^2 - \epsilon_{d,m}$ and A is an arbitrary constant representing the longitudinal field amplitude at $x = 0$. The propagation constant β can be readily calculated from the BCs

$$e_z(0^-) = e_z(0^+), \tag{2.20}$$

$$\epsilon_m e_x(0^-) = \epsilon_d e_x(0^+), \tag{2.21}$$

$$h_y(0^-) = h_y(0^+). \tag{2.22}$$

Note that the BCs for e_x, e_z, h_y are not independent. Indeed, the continuity of the magnetic field h_y is ensured by the continuity of $\epsilon e_x, e_z$ [Jackson, 1999]. Thus, inserting the expressions for the electric fields e_x, e_z in Eqs. (2.20,2.21), one reaches the mode dispersion

$$\beta(\omega) = \sqrt{\frac{\epsilon_d \epsilon_m(\omega)}{\epsilon_d + \epsilon_m(\omega)}}. \tag{2.23}$$

It is worthwhile noting that such a derivation is generally valid for the complex dielectric susceptibility $\epsilon_m = \epsilon_m' + i\epsilon_m''$. If the metal loss ϵ_m'' is neglected, the metal dielectric susceptibility ϵ_m is approximated by the real part ϵ_m' and the propagation constant β is purely real.

The plasmonic mode dispersion $\beta(\omega)$ is plotted in Fig. 2.5, where we have used the Lorentz model for the dielectric response of the metal $\epsilon_m(\omega) = 1 - \omega_p^2/\omega^2$

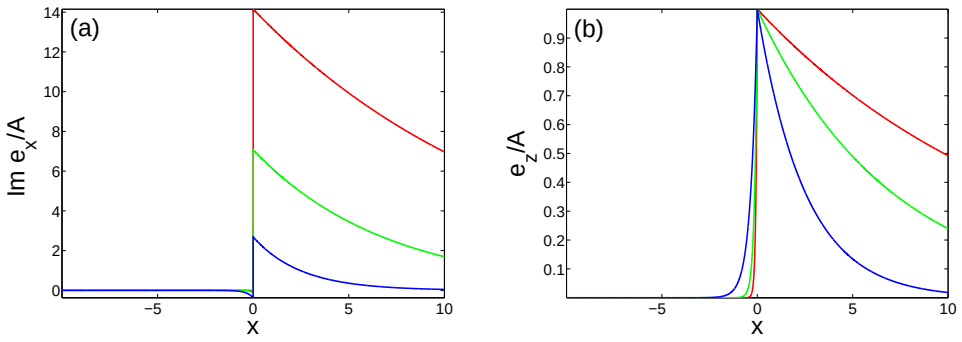

Figure 2.6: SPP mode profiles for (a) transverse e_x and (b) longitudinal e_z electric field components. Red, green and blue curves correspond to $\omega/\omega_p = 0.1, 0.2, 0.5$, respectively. The field amplitudes are rescaled to the arbitrary longitudinal field amplitude A.

(the damping γ is neglected). In such a plot, the angular frequency ω is rescaled to the plasma frequency ω_p and the dimensional propagation constant $\omega\beta/c$ is rescaled to ω_p/c. The blue curve corresponds to the SPP dispersion, while the black dashed line corresponds to the lightline $\beta = \sqrt{\epsilon_d}$. In the low frequency regime, SPPs are weakly localised and assume the shape of grazing light field (in this regime SPPs are also known as Sommerfeld-Zenneck waves [Goubau, 1950; Maier, 2007]). The localisation increases with frequency, diverging at the *surface plasmon resonance*

$$\omega_{sp} = \frac{\omega_p}{\sqrt{1+\epsilon_d}}, \tag{2.24}$$

where $\epsilon_m(\omega_{sp}) = -\epsilon_d$ and $\beta \to \infty$. Note that, in the limit $\beta \to +\infty$, the SPP field is completely squeezed at the interface since $q_d, q_m \to +\infty$. Besides, as the angular frequency ω increases, the group velocity $v_g = d\omega/d\tilde{\beta}$ lowers ($\tilde{\beta} = \omega\beta/c$) and tends to zero in the limiting case $\omega \to \omega_{sp}$, where SPPs acquire an electrostatic behaviour and are known as Surface Plasmons (SPs) [Maier, 2007]. The amplitude $A = e_z(0)$ is arbitrary in modulus and phase and can be set as a real quantity. Hence, the longitudinal electric field component e_z is purely real while the transverse component e_x is purely imaginary. The mode profiles e_x, e_z are plotted in Fig. 2.6 for several ratios ω/ω_p. Note that, for low frequency $\omega/\omega_p = 0.1$,

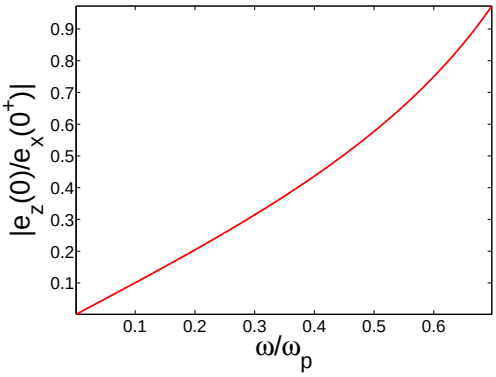

Figure 2.7: Field amplitudes ratio $|e_z(0)/e_x(0^+)|$ as function of rescaled frequency ω/ω_p.

the electromagnetic field basically resides only in the dielectric medium, while for higher frequencies $\omega/\omega_p = 0.2, 0.5$ the field penetration within the metal increases and the SPP mode gets more localised.

Note also that the ratio $|e_z(0)/e_x(0^+)| = q_d/\beta$ increases with the frequency, see Figs. 2.6, 2.7. For low frequencies, the plasmonic dispersion $\beta(\omega)$ tends to the lightline $\beta = \epsilon_d$. Hence, in this limit $q_d \to 0$ and plane waves propagating in the dielectric medium are perturbed only slightly by the presence of the metal surface. Thus, $|e_z(0)/e_x(0^+)| \to 0$ and the plasmonic mode is practically transverse polarised. As the frequency increases, the longitudinal field component e_z becomes more significant, becoming equal in modulus to the transverse component e_x at the surface plasmon frequency ω_{sp}, where $|e_z(0)/e_x(0^+)| \to 1$.

Up to now, the optical response of the metal was approximated by the free electron model in the absence of damping. However, the realistic dielectric properties of metals are more involved, as discussed in section 2.1, being described by a complex dielectric constant $\epsilon_m = \epsilon_m' + i\epsilon_m''$. If the metal loss is considered, then the mode dispersion becomes complex $\beta(\omega) = \beta'(\omega) + i\beta''(\omega)$. The real part β' represents the phase shift rate due to mode propagation, while the imaginary part β'' accounts for absorption. The spectral behaviour of β', β'' is plotted in Fig. 2.8 for a silver-air single interface. The dielectric properties of silver are modelled by the Lorentz-Drude model, a multiple oscillator fit of experimental

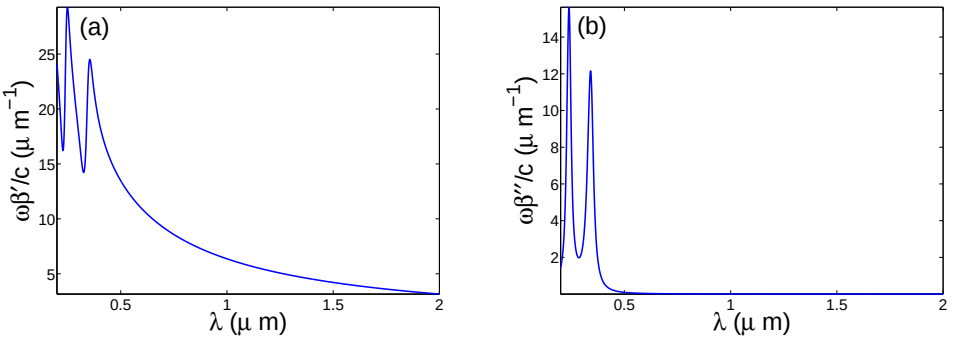

Figure 2.8: (a) SPP dispersion $\omega\beta'/c$ and (b) loss $\omega\beta''/c$ as functions of vacuum wavelength λ for silver.

data [Ung and Sheng, 2007], as discussed in section 2.1.

For long wavelengths λ, the imaginary part of the propagation constant β'' stays relatively small with respect to the real part β' since the silver is highly reflective and the electromagnetic field propagates mostly in the dielectric medium. As the wavelength λ is reduced, the field penetration within the metal increases and the ohmic losses become more significant. In particular, for wavelengths around the surface plasmon resonance, the metal loss becomes dominant. The transverse confinement of the plasmonic mode is determined by the coefficients q_d, q_m and can be estimated by

$$L_C = k^{-1}\left(1/2q_d' + 1/2q_m'\right). \tag{2.25}$$

Besides, the characteristic attenuation length where travelling SPPs are damped off, is defined as

$$L_A = k^{-1}/2\beta''. \tag{2.26}$$

The dependence of L_C, L_A on the vacuum wavelength λ is depicted in Fig. 2.9. Note that, at $\lambda = 500nm$, the subwavelength mode confinement is $L_C \simeq 100nm$ and the attenuation length is $L_A \simeq 10\mu m$. The tight confinement provided by SPPs does not come at zero price, but is paid in terms of enhanced losses, which quench off the functionality of SPPs as nano-scaled waveguides. The time-dependent Poynting vector

$$\vec{\mathcal{S}}(x,z,t) = Re\vec{\mathcal{E}} \times Re\vec{\mathcal{H}} = \frac{1}{2}Re\left[\vec{e}\times\vec{h}e^{2i\beta z - 2i\omega t}\right] + \frac{1}{2}Re\left[\vec{e}\times\vec{h}^{*}\right]e^{-2\beta'' z} \tag{2.27}$$

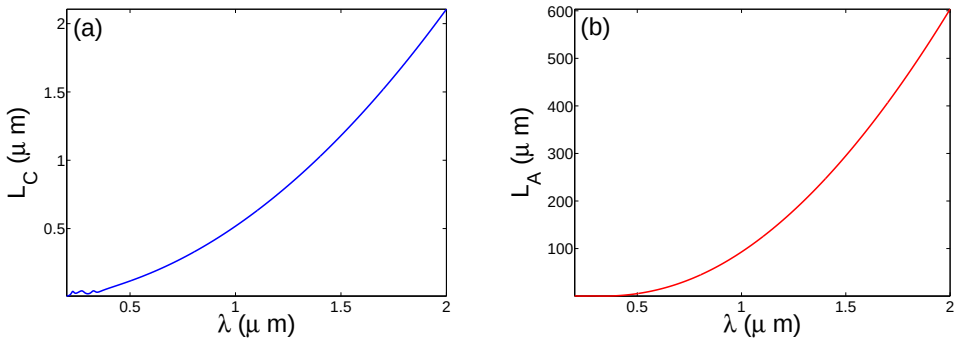

Figure 2.9: (a) SPP mode confinement L_C and (b) attenuation length L_A as functions of vacuum wavelength λ.

provides a remarkable physical insight in the SPP energy flow and dynamics. The first term is a harmonic time-dependent contribution, while the second term is time-independent. An analytical expression for $\vec{\mathcal{S}}$ can be obtained by substituting the mode fields e_x, e_z, h_y in Eq. (2.27); however, such a cumbersome expression is not included here. A qualitative schematic of the spatial orientation of $\vec{\mathcal{S}}$ at a fixed instant of time $t = t_0$ is depicted in Fig. 2.10. The SPP propagation occurs in the form of energy vortices travelling along the z-direction [Wuenschell and Kim, 2006], resulting from the tight coupling of the radiation with the electrons oscillating in the metal. Note that the time-averaged Poynting vector is directed onwards ($\hat{z}$) in the dielectric medium ($x > 0$) and backwards ($-\hat{z}$) in the metal ($x < 0$).

The energy transfer properties can be understood by calculating the power densities

$$P_x = \frac{1}{k}\int_{-\infty}^{+\infty} dx \langle \mathcal{S}_x \rangle_t = \frac{|A|^2}{4\omega\mu_0}\left(\frac{q_m''\epsilon_m' - q_m'\epsilon_m''}{q_m'|q_m|^2} - \frac{q_d''\epsilon_d}{q_d'|q_d|^2}\right) e^{-2\beta'' z}, \quad (2.28)$$

$$P_z = \frac{1}{k}\int_{-\infty}^{+\infty} dx \langle \mathcal{S}_z \rangle_t = \frac{|A|^2}{4\omega\mu_0}\left(\frac{\beta'\epsilon_m' + \beta''\epsilon_m''}{q_m'|q_m|^2} + \frac{\beta'\epsilon_d}{q_d'|q_d|^2}\right) e^{-2\beta'' z}, \quad (2.29)$$

where $\langle \mathcal{S}_x \rangle_t, \langle \mathcal{S}_z \rangle_t$ are the temporal averaged Poynting vector components. In such equations, the prime and double prime superscripts of parameters correspond to their real and imaginary parts, respectively. In general, if the metal loss $\epsilon_m'' \neq 0$ is not neglected, the electromagnetic field energy is attenuated with the exponential

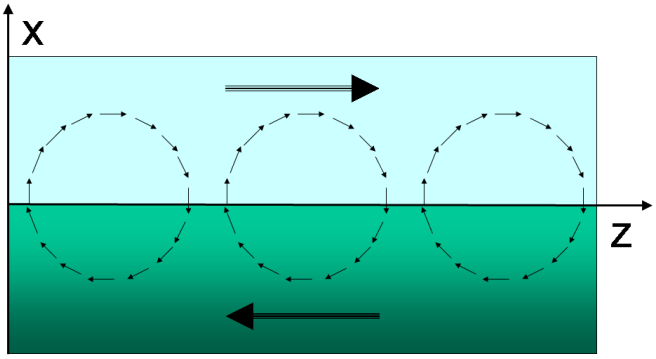

Figure 2.10: Schematic of SPP mode Poynting vector $\vec{S}$ spatial orientation at a fixed instant of time.

law $e^{-2\beta_z''}$. In this case, the non-zero transverse power density $P_x \neq 0$ bridges the electromagnetic energy within the metal, which absorbs it and convert it into heat by Joule effect. Conversely, in the ideal case where $\epsilon_m'' = 0$, all quantities are real and $P_x = 0$. Hence, in this limit the electromagnetic field propagates in the z-direction without attenuation and P_z is a conserved quantity.

2.3 SPPs in IMI photonic structures

In this section, we describe the optical propagation of SPPs in Insulator-Metal-Insulator (IMI) photonic structures. In general, a multilayer structure consisting of alternating metallic and dielectric films sustains SPPs propagating at every interface. If the separation between the adjacent interfaces is comparable with the penetration depth, the SPPs at different metal surfaces interact tightly with each other [Prade et al., 1991]. In this case, it is not possible to distinguish the SPPs of the single interfaces and the optical propagation is well described in terms of the *supermodes* of the entire photonic structure [Yariv, 1985], which can be considered as a waveguide on its own. A generic IMI structure is composed of a metal stripe surrounded by two different dielectric media [Boardman, 1982; Economou, 1969]. For the purpose of this section, we consider only the symmetric case where the dielectric media surrounding the metal stripe are identical, as depicted in Fig. 2.11.

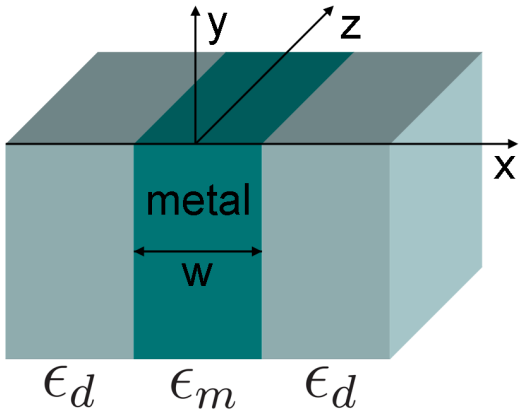

Figure 2.11: Symmetric IMI photonic structure composed of a metal stripe surrounded by a dielectric medium.

As for the case of the single interface described in the previous section, the TM modes propagating in the z-direction are solutions of Eqs. (2.14-2.16) in every medium of the photonic structure. Here, however, the calculation of the SPP modes is more involved, since there exist two solutions with different symmetries. The analytical expressions for the electric and magnetic field components e_x, e_z, h_y of the two SPP modes are provided by

$$\begin{aligned} e_{z,\alpha} &= A\left[e^{q_d(x+w/2)}\theta(-w/2-x)+\alpha e^{-q_d(x-w/2)}\theta(x-w/2)\right]+ \\ &\quad +B\left[e^{-q_m x}+\alpha e^{q_m x}\right]\left[\theta(x+w/2)-\theta(x-w/2)\right], \qquad (2.30) \\ e_{x,\alpha} &= -\frac{i\beta}{q_d}A\left[e^{q_d(x+w/2)}\theta(-w/2-x)-\alpha e^{-q_d(x-w/2)}\theta(x-w/2)\right]+ \\ &\quad +\frac{i\beta}{q_m}B\left[e^{-q_m x}-\alpha e^{q_m x}\right]\left[\theta(x+w/2)-\theta(x-w/2)\right], \qquad (2.31) \\ h_{y,\alpha} &= -\frac{i\epsilon_d}{c\mu_0 q_d}A\left[e^{q_d(x+w/2)}\theta(-w/2-x)-\alpha e^{-q_d(x-w/2)}\theta(x-w/2)\right]+ \\ &\quad +\frac{i\epsilon_m}{c\mu_0 q_m}B\left[e^{-q_m x}-\alpha e^{q_m x}\right]\left[\theta(x+w/2)-\theta(x-w/2)\right], \qquad (2.32) \end{aligned}$$

where $q_{d,m}^2 = \beta^2 - \epsilon_{d,m}$, $\theta(x)$ is the Heaviside step function and $\alpha = \pm 1$ is a dimensionless parameter. For $\alpha = 1$, Eqs. (2.30-2.32) provide the electromagnetic field pattern for TM modes with symmetric longitudinal electric field component e_z. Conversely, for $\alpha = -1$, Eqs. (2.30-2.32) correspond to the TM modes

with antisymmetric longitudinal component e_z. Note that the symmetry of h_y, e_x fields is opposite to the symmetry of e_z. In this dissertation, the denomination *symmetric/antisymmetric* mode is referred to the longitudinal component e_z. The BCs for the continuity of the transverse electric displacement $D_x = \epsilon(x)E_x$ and of the longitudinal electric field E_z at the interfaces $x = \pm w/2$ yield a system of four algebraic equations

$$\epsilon_d e_x(-w^-/2) = \epsilon_m e_x(-w^+/2), \tag{2.33}$$

$$e_z(-w^-/2) = e_z(-w^+/2), \tag{2.34}$$

$$\epsilon_m e_x(w^-/2) = \epsilon_d e_x(w^+/2), \tag{2.35}$$

$$e_z(w^-/2) = e_z(w^+/2). \tag{2.36}$$

As described in the previous paragraph, the BCs for the continuity of the magnetic field h_y are automatically satisfied if the BCs for e_x, e_z are imposed. Inserting the expressions of the mode profiles e_x, e_z into Eqs. (2.33,2.36), one reaches

$$e^{-q_m w} + \alpha \frac{q_m\epsilon_d + q_d\epsilon_m}{q_m\epsilon_d - q_d\epsilon_m} = 0, \tag{2.37}$$

$$B = \frac{1}{2q_d\epsilon_m}(q_d\epsilon_m - q_m\epsilon_d)Ae^{-q_m w/2}. \tag{2.38}$$

Eq. (2.37) is the mode dispersion for symmetric ($\alpha = 1$) and antisymmetric ($\alpha = -1$) modes. The constants B, A are not independent, but are related each other through Eq. (2.38). The amplitude A is left arbitrary and represents the electric field component e_z at $x = -w/2$ ($A = e_z(-w/2)$). It is worthwhile noting that, because of the symmetry of the linear modes, it is sufficient to impose the BCs only at one of the two boundaries $x = \pm w/2$ in order to reach Eqs. (2.37,2.38). Indeed, the BCs at the remaining interface are automatically satisfied by the requirement that SPP modes are either symmetric or antisymmetric.

Fig. 2.12a plots the mode dispersion for a silver stripe of dimensional width $d = 50nm$ embedded in air ($\epsilon_d = 1$). Note that the dimensionless stripe width $w = \omega d/c$ is frequency dependent. The dielectric constant of silver is modelled through the Lorentz-Drude model, neglecting the imaginary part. Red and blue curves correspond to antisymmetric and symmetric (e_z) modes respectively, see Fig. 2.12b. The dispersion of the symmetric mode (blue curve) appears qualitatively pretty similar to the single interface dispersion. For small frequencies, the

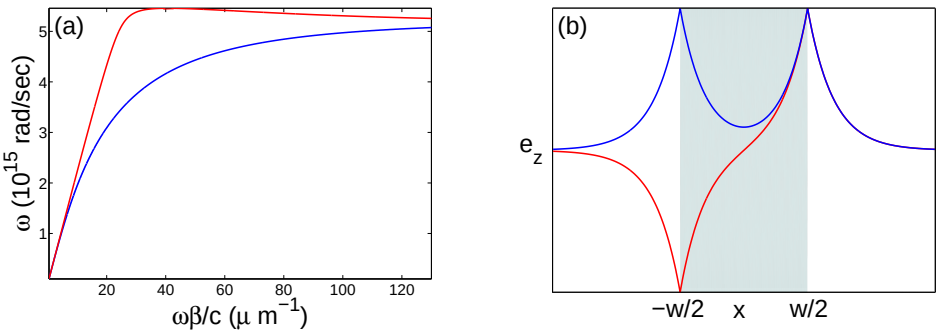

Figure 2.12: (a) Mode dispersion and (b) schematic representation of e_z for symmetric (blue lines) and antisymmetric (red lines) modes. The structure considered is a silver stripe of width $d = 50nm$ embedded in air.

light propagates mainly in the dielectric medium and the confinement is weak. For frequencies around the surface plasmon resonance ω_{sp}, the mode profile gets squeezed across the metal-dielectric interfaces and the confinement increases.

Conversely, the antisymmetric mode dispersion (red curve) presents qualitatively new features with respect to the single interface case. In particular, the mode dispersion is not monotonic: maximum and minimum points of zero group-velocity $v_g = d\omega/d\tilde{\beta} = 0$ ($\tilde{\beta} = \omega\beta/c$) and a range of negative group velocity $v_g < 0$ arise [Dionne et al., 2008; Fedyanin et al., 2010; Rosenblatt et al., 2010]. A similar scenario occurs in Metal-Insulator-Metal (MIM) plasmonic waveguides [Davoyan et al., 2010a, 2008]. Materials having group velocity v_g and phase velocity $v_f = c/\beta$ with opposite signs are named *negative index materials* (NIMs). Negative refraction in the $y - z$ plane has been observed in MIM waveguides [Dionne et al., 2008].

Maximum and minimum points in the mode dispersion for antisymmetric modes arise only if the stripe width w is smaller than a certain threshold. Indeed, if the separation between the two metal-dielectric interfaces is large, the coupling between SPPs propagating at every metal surface is small. Hence, the mode dispersion tends to the single-interface dispersion if $w >> 1$ [Maier, 2007]. For symmetric and antisymmetric modes, the function

$$F_\alpha\left[\beta, \omega(\beta)\right] = e^{-q_m w} + \alpha \frac{q_m \epsilon_d + q_d \epsilon_m}{q_m \epsilon_d - q_d \epsilon_m} \tag{2.39}$$

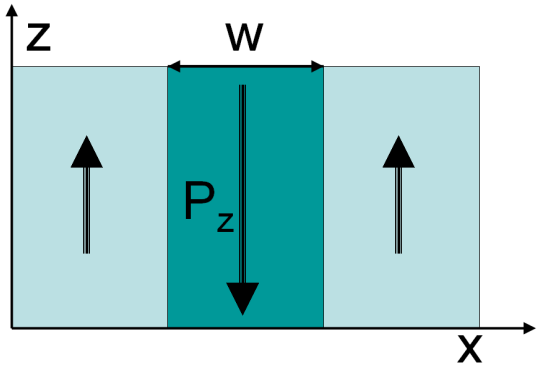

Figure 2.13: Schematic plot of power flow in an IMI structure.

is identically null at every point of the mode dispersion curve, identified by the pair $\beta, \omega(\beta)$. An analytical expression for the group velocity of symmetric and antisymmetric modes can be obtained by calculating the derivative $dF_\alpha/d\beta$

$$\frac{dF_\alpha}{d\beta} = \partial_\beta F_\alpha + \omega^{-1} w \partial_w F_\alpha \frac{d\omega}{d\beta} + \partial_{\epsilon_m} F_\alpha \frac{d\epsilon_m}{d\omega}\frac{d\omega}{d\beta}, \tag{2.40}$$

which is exactly null, since $F_\alpha = 0$ for every pair $\beta, \omega(\beta)$. Thus, the group velocity $v_g = d\omega/d\tilde{\beta}$ ($\tilde{\beta} = \omega\beta/c$) is

$$v_g = \frac{\dfrac{d\omega}{d\beta}}{\dfrac{\beta}{c}\dfrac{d\omega}{d\beta} + \dfrac{\omega\beta}{c}}, \tag{2.41}$$

where

$$\frac{d\omega}{d\beta} = -\frac{\partial_\beta F_\alpha}{\omega^{-1} w \partial_w F_\alpha + \partial_{\epsilon_m} F_\alpha \dfrac{d\epsilon_m}{d\omega}}. \tag{2.42}$$

The term $\omega^{-1} w \partial_w F_\alpha$ accounts for the geometric dispersion of the photonic structure, while the term $\partial_{\epsilon_m} F_\alpha \frac{d\epsilon_m}{d\omega}$ accounts for the metal dispersion $\epsilon_m(\omega)$. In such a calculation, the dielectric medium was assumed non-dispersive. The explicit calculation of v_g shows that for symmetric modes ($\alpha = 1$), $v_g \to 0$ only if $\beta \to +\infty$. Conversely, for antisymmetric modes ($\alpha = -1$), the group velocity can become null also for a finite propagation constant $\bar{\beta}$, identified by the condition $\partial_\beta F_{-1} = 0$, explicitly given by

$$w(q_m \epsilon_d + q_d \epsilon_m) + \frac{2\epsilon_d \epsilon_m (\epsilon_d - \epsilon_m)}{q_d (q_m \epsilon_d - q_d \epsilon_m)} = 0. \tag{2.43}$$

A better understanding of the physical mechanisms occurring at the zero group-velocity points can be grasped by calculating the time-averaged Poynting vector

$$\vec{S} = \frac{1}{2} Re(\vec{\mathcal{E}} \times \vec{\mathcal{H}}^*) \tag{2.44}$$

and the power density

$$P_z = k^{-1} \int_{-\infty}^{+\infty} dx S_z. \tag{2.45}$$

The explicit expression for the Poynting vector is cumbersome and is not reported. Neglecting the metal loss, the power density of symmetric and antisymmetric modes is given by

$$P_{z,\alpha} = \frac{\beta}{2\mu_0 \omega q_d^2} |A|^2 \left[\frac{\epsilon_d}{q_d} + \frac{q_m^2 \epsilon_d^2 - q_d^2 \epsilon_m^2}{2 q_m^3 \epsilon_m} \left[q_m w - \alpha sinh(q_m w) \right] \right]. \tag{2.46}$$

For antisymmetric modes, corresponding to $\alpha = -1$, it can be demonstrated that the total power density P_z is null at the zero group velocity points. Here, the forward power density bridged in the dielectric media is exactly compensated by the backward power density carried within the metal stripe, as depicted in Fig. 2.13, yielding a null total power density P_z. Such an effect is identified by the condition $P_z = 0$:

$$\frac{\epsilon_d}{q_d} + \frac{q_m^2 \epsilon_d^2 - q_d^2 \epsilon_m^2}{2 q_m^3 \epsilon_m} \left[q_m w + sinh(q_m w) \right] = 0, \tag{2.47}$$

which coincides with the zero group-velocity condition expressed in Eq. (2.43). Indeed, if one substitutes in the hyperbolic sine $\sinh(q_m w) = (1/2)(e^{q_m w} - e^{-q_m w})$ the dispersion relation $e^{-q_m w} = (q_m \epsilon_d + q_d \epsilon_m)/(q_m \epsilon_d - q_d \epsilon_m)$, Eq. (2.47) coincides to Eq. (2.43).

The dispersion is so strong that the group velocity becomes negative in a particular range of angular frequencies, see Fig. 2.12a. However, such a description completely disregards the metal loss, which changes substantially the scenario. Indeed, in the region where $v_g/c << 1$, the metal loss is not negligible and it can not be disregarded. In absorptive materials the group velocity is not an adequate quantity to describe the velocity of energy [Loudon, 1970], which is defined by

$$v_E = \frac{S}{u}, \tag{2.48}$$

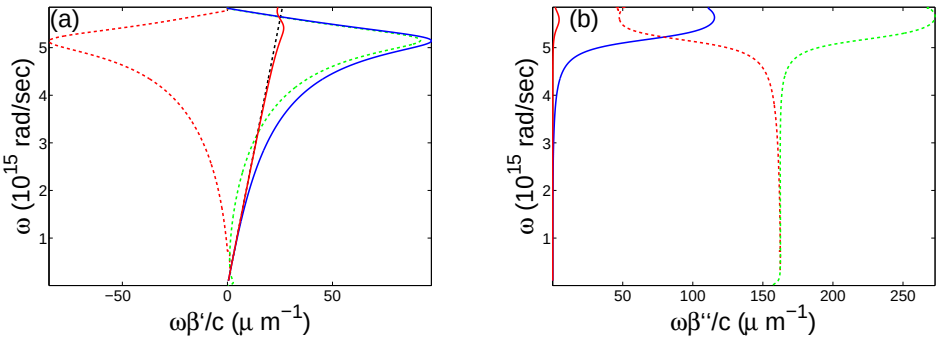

Figure 2.14: (a) Phase shift rate $\omega\beta'/c$ and (b) absorption rate $\omega\beta'/c$ for lossy modes of a silver stripe of $50nm$ embedded in air ($\epsilon_d = 1$).

where S is the time-averaged power flow in the waveguide and u is the time-averaged energy density [Ruppin, 2002]. If one takes into account the metal loss, the dispersion relation expressed in Eq. (2.37) becomes complex. Hence, as described in the previous section for the single interface geometry, also the propagation constant $\beta = \beta' + i\beta''$ is complex. The sign of the velocity of energy is basically determined by the imaginary part of the propagation constant β''.

In Fig. 2.14, the phase shift rate $\omega\beta'/c$ and the absorption rate $\omega\beta''/c$ are plotted for lossy modes of an IMI structure composed of a silver stripe ($d = 50nm$) embedded in air ($\epsilon_d = 1$). The Lorentz-Drude model is used for the dielectric constant of silver $\epsilon_m(\omega)$, as described in section 2.1. Blue curves correspond to the symmetric mode (e_z), while dashed green and full/dashed red curves correspond to three antisymmetric modes (e_z). Note that the non-monotonic behaviour of the antisymmetric modes observed in the lossless case is reflected on the splitting in three separate antisymmetric modes in the lossy case. In particular, the mode labelled by the red dashed line resembles the range of negative group velocity. Indeed, the sign of the velocity of energy, determined by $\beta'' > 0$, is opposite to the sign of phase velocity, determined by $\beta' < 0$. On the other hand, the dashed green line corresponds to the positive group velocity region of the lossless dispersion of antisymmetric modes occuring for large β. Such modes exhibit huge loss and are not helpful to deliver electromagnetic energy in miniaturised optical channels.

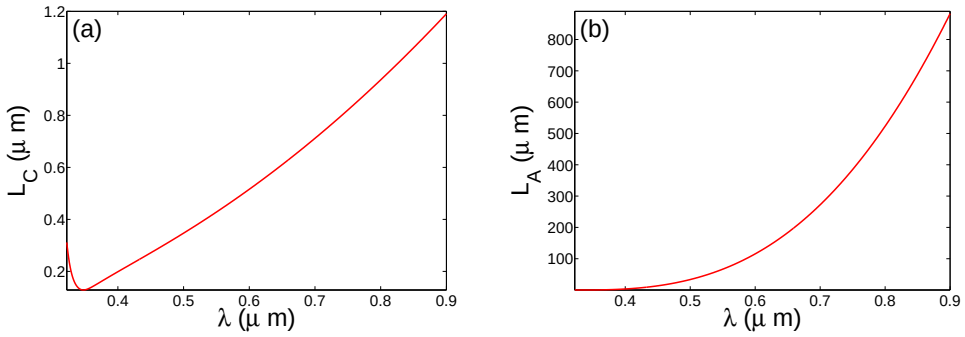

Figure 2.15: (a) Confinement length L_C and (b) attenuation length L_A as functions of λ for Long-Range SPPs.

Conversely, the antisymmetric branch labelled by the red curve is characterised by a very small absorption rate β''. For this reason, such SPP antisymmetric modes are named *Long-Range Surface Plasmon Polaritons* (LRSPPs) [Berini, 2009; Burke et al., 1986; Quail et al., 1983; Sarid, 1981]. The transverse confinement of the linear modes of an IMI structure can be estimated by

$$L_C = d + 1/kq'_d, \tag{2.49}$$

where d is the width of the metal stripe. On the other hand, the attenuation length is defined by

$$L_A = 1/2k\beta''. \tag{2.50}$$

In Fig. 2.15a,b the confinement length L_C and the attenuation length L_A are plotted as functions of the vacuum wavelength λ for a silver stripe of $50nm$ embedded in air $\epsilon_d = 1$. Note that, at $\lambda = 500nm$, $L_C \approx 350nm$ and $L_A \approx 50\mu m$. Thus, the propagation length increases considerably with respect to the single interface geometry. However, such a reduced effective loss is paid in terms of the weaker confinement ($\approx 350nm$ instead of $\approx 100nm$).

Estimates of the attenuation and confinement lengths in several configurations have been calculated in Refs. [Berini, 2009; Quail et al., 1983], suggesting that LRSPPs can propagate over long distances (compared to the single-interface SPPs). Such theoretical predictions have also been confirmed experimentally [Charbonneau et al., 2000, 2005a; Lamprecht et al., 2001]. Detailed studies of

LRSPPs in two-dimensional IMI structures were also conducted [Berini, 1999, 2000, 2001; Leosson et al., 2006; Veronis and Fan, 2005], revealing the possibility to use LRSPPs in miniaturised photonic devices. At telecom wavelengths $\lambda \simeq 1.55\mu m$, achievable propagation lengths are of the order of centimetres.

2.4 Excitation of SPPs

An important feature of SPPs is that, for every given angular frequency ω, their wave vector β_{SPP} is always larger than the wave vector of light in free space β_{Light}, if losses are neglected. Such a circumstance results from the intrinsic bound nature of SPPs, since the physical reason for the increased SPP momentum lies in the strong coupling between light and surface charges.

In general, a TM polarised electromagnetic plane wave impinging on a metal surface from an external dielectric medium does not excite SPPs. Indeed, for the excitation to occur, the wavevector of the incident light needs to match the wavevector of the single interface SPP mode. Such an occurrence is verified only for $\omega \to 0$, see Fig. 2.5, since the SPP dispersion asymptotically approaches the light line only for small angular frequencies. Thus, SPPs on a single interface can not be excited by light of any frequency that propagates in the bulk dielectric unless special phase-matching techniques, such as prism or grating coupling, are adopted [Boardman, 1982; Kretschmann and Raether, 1968; Otto, 1968; Raether, 1988]. Other methods used to excite SPPs are based on the end-fire coupling [Stegeman et al., 1983], which relies on the spatial-mode matching instead of the phase-matching. It is also worthwhile to mention that, from an historical perspective, first attempts to excite SPPs involved the collision of low energy electron beams into thin metallic films [Pettit et al., 1975; Ritchie, 1957; Vincent and Silcox, 1973].

2.4.1 Prism coupling

The most common approach used to excite SPPs is based on the attenuated total reflection method (ATR). Mainly, there are two configurations of the ATR

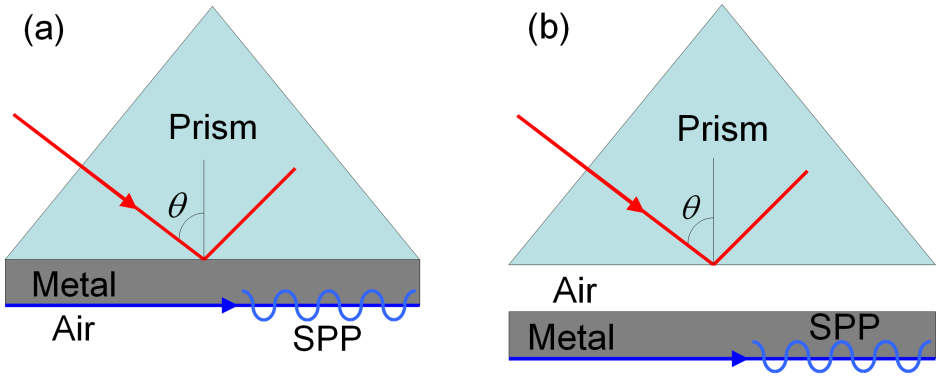

Figure 2.16: Excitation of SPPs: (a) Kretschmann and (b) Otto configurations.

method: the Kretschmann geometry [Kretschmann and Raether, 1968] and the Otto geometry [Otto, 1968], depicted in Figs. 2.16a,b, respectively.

In the Kretschmann geometry of the ATR method (Fig. 2.16a), a prism with high dielectric constant ϵ_p lies on an interface with a metal-dielectric waveguide consisting of a thin metal film and air, characterised by the dielectric constants ϵ_m, ϵ_d ($\epsilon_d < \epsilon_p$). When an electromagnetic wave propagating in the prism impinges on the metal film, it is reflected back. At optical frequencies, the light partially penetrates the metal film in the form of an evanescent electromagnetic wave [Stratton, 1941], exponentially decaying in the direction of propagation. If the metal film is sufficiently thin ($\approx 100nm$) with respect to the optical wavelength, the evanescent tails are coupled with the SPP mode at the other boundary.

Fig. 2.17 plots the SPP dispersions for the two single metal-air (blue curve) and metal-prism (red curve) interfaces. The dielectric response of the metal is modelled by the free electron model in the absence of damping $\epsilon_m = 1 - \omega_p^2/\omega^2$, as described in section 2.1. For the dielectric constant of the prism we assumed $\epsilon_p = 2.25$. Dashed blue and red lines represent the light dispersion in air and prism bulk, respectively. Note that the dashed red line intersects the dispersion of the metal-air SPP mode (blue curve), allowing for the SPP excitation. Conversely, the SPP mode at the prism-metal interface (red curve) can not be excited since its dispersion lies outside the prism light cone (See Fig. 2.17). The phase-matching

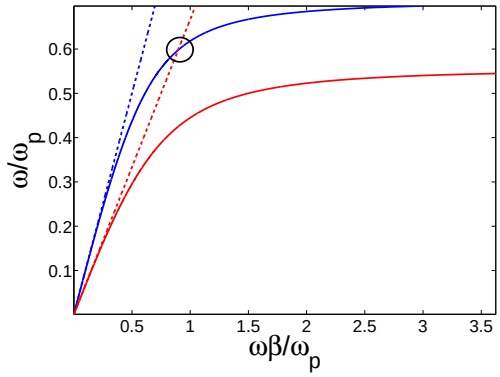

Figure 2.17: SPP dispersion for metal-air (blue curve) and metal-prism (red curve) interfaces.

condition is expressed by

$$\sqrt{\epsilon_p} sin\theta = \beta_{SPP}, \tag{2.51}$$

where

$$\beta_{SPP} = \sqrt{\epsilon_d \epsilon_m / (\epsilon_d + \epsilon_m)}, \tag{2.52}$$

and θ is the angle of incidence. In Fig. 2.17, the phase matching is achieved for $\theta = \pi/2$, which provides the maximum angular frequency ω_{MAX} that can be excited in this configuration. By varying the angle of incidence θ and the angular frequency ω of the impinging electromagnetic wave, it is possible to excite SPP modes with lower frequencies $\omega < \omega_{MAX}$.

Typically, in experiments using the ATR configuration, the signature of the SPP excitation is found by measuring the metal reflectivity R as a function of the angle of incidence θ. For most angles θ, the metal is highly reflective since the phase-matching condition is not satisfied and $R \simeq 1$. The reflectivity suddenly drops for the particular angle $\theta = \bar{\theta}$, where the SPPs are excited [Novotny and Hect, 2006]. An accurate estimate of the reflectivity R as a function of θ can be calculated by using the Fresnel theory for multilayer structures [Jackson, 1999], but is not presented here.

In the Otto geometry, depicted in Fig. 2.16b, a prism with dielectric constant ϵ_p lies on the top of a dielectric-metal waveguide consisting of a thin dielectric

layer and a metal, characterised by the dielectric constants ϵ_d, ϵ_m ($\epsilon_d < \epsilon_p$). Here, an electromagnetic wave propagating inside the prism impinges on the interface with the air layer and is totally reflected back if the angle of incidence is larger than the critical angle of total internal reflection [Stratton, 1941]. Hence, if the thickness of the air layer is comparable with the optical wavelength, the evanescent field produced by the impinging electromagnetic wave penetrates in the underlying metal. Efficient coupling with SPP modes occurs if the phase-matching between the evanescent field and the SPP holds: $\sqrt{\epsilon_p} sin\theta = \beta_{SPP}$, as explained above. By tuning the angle of incidence, the matching of the parallel wave vector components can be achieved and SPPs can be excited. As for the case of Kretschmann geometry, the signature of SPP excitation is manifested in a dip of the reflectivity curve $R - \theta$. If the thickness of the air layer is very small with respect to the wavelength, the resonance is broadened and shifted owing to the radiation damping of SPPs [Novotny and Hect, 2006]. Such an effect ensues from the coupling of SPPs with the radiative modes in the prism. On the other hand, if the thickness of the air layer is too large, SPPs are not excited efficiently. For such reasons, the Otto configuration is experimentally inconvenient and the Kretschmann configuration is desirable. The Otto configuration is preferable only in two cases: for the excitation of SPPs in thick metal slabs where the Kretschmann geometry is not suitable and when the direct contact with the metal surface is undesired.

In the mentioned prism coupling geometries, the excited SPPs are inherently leaky waves: the light impinging from the prism is coupled with the SPP mode and viceversa. Hence, in addition to the intrinsic metal loss, the radiative modes also contribute to the effective loss by the leakage of power into the prism. In turn, the dip in the reflection curve $R - \theta$ arise from two separate mechanisms: the coupling to SPP modes and the destructive interference resulting from the leakage of SPP modes.

2.4.2 Grating coupling

Another technique used to compensate the momentum mismatch between the impinging radiation and SPP modes, relies on diffraction effects due to a grating

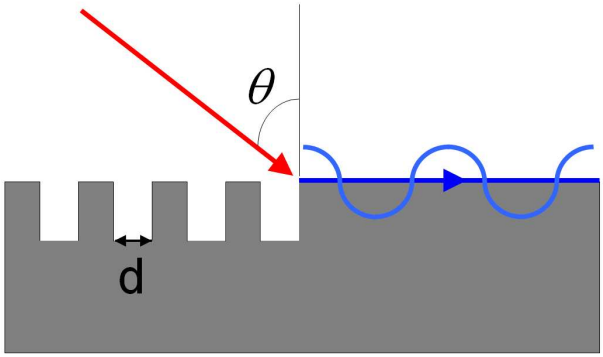

Figure 2.18: Phase-matching of incident light to SPPs by grating coupling.

pattern in the metallic surface [Offerhaus et al., 2005; Park et al., 2003]. However, as a drawback, the use of gratings for exciting SPP modes introduces perturbations on the flat interface that can change significantly the dispersion [Hooper and Sambles, 2004].

As an example, in Fig. 2.18 is depicted a grating structure made of grooves on a metal surface with period d. The phase-matching occurs if the condition

$$\beta_{SPP} = \sqrt{\epsilon_d} sin\theta + nD \tag{2.53}$$

is satisfied. In such an expression, $\beta_{SPP} = \sqrt{\epsilon_d \epsilon_m/(\epsilon_d + \epsilon_m)}$ is the dimensionless SPP propagation constant (rescaled to ω/c), θ is the angle of incidence, $D = 2\pi c/\omega d$ is the step of the reciprocal lattice rescaled to ω/c and $|n|$ is an arbitrary integer number. As described in the previous paragraph, the signature of the SPP excitation is characterised by a dip in the reflectivity curve $R-\theta$. Note that also the inverse process of out-coupling occurs [Devaux et al., 2003], where SPPs are coupled with radiative modes through the grating. The coupling efficiency can be estimated by measuring the radiation leaked [Ditlbacher et al., 2002]. In general, SPPs can be excited by nonresonant scattering from a rough surface or a localised defect. In addition, similarly to grating coupling mechanisms, excitation of SPP modes can be achieved also by light diffraction from periodic patterns [Salomon et al., 2002].

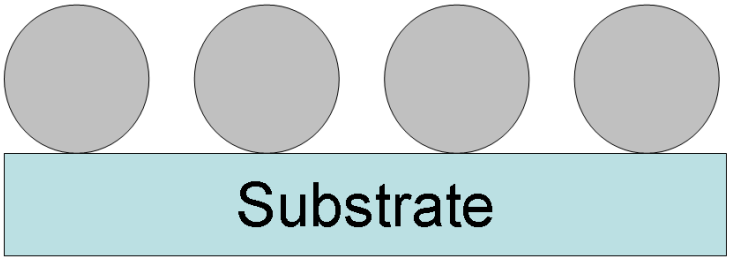

Figure 2.19: Schematic representation of a metallic nanoparticle chain.

2.5 SPP-based optical circuitry

The delivery of energy at the nano-scale is one of the primary tasks for the research in nanophotonics. The transmission of high-capacity digital information by means of optical interconnection is considered as a promising technology to overcome the transport limit of 2.5 *Gbps* for copper lines on integrated circuits [Haurylau et al., 2006]. In this context, SPPs are identified as the best candidates for the fabrication of nano-scaled optical interconnects [Ebbesen et al., 2008; Ozbay, 2006]. Indeed, the integration of optical components in electronic circuits is mostly limited by their respective sizes. While the fabrication of electronic circuits with dimensions below $100nm$ is achievable, the wavelength of light for telecom applications ($\approx 1\mu m$) limits the scaling down of photonic components. As discussed in section 1.2.2, when the dimensions of an optical component become close to the wavelength of light, the optical propagation is limited by the diffraction, which poses a threshold for the minimum size of optical integrated circuits.

The subwavelength confinement provided by SPPs constitutes an ideal solution for such a problem. Indeed, in materials with a negative real part of the dielectric constant, such as metals, there is no cut-off length scale, since the transverse wavevector components become imaginary. In recent years, SPP optical components of various geometries have been proposed and realised experimentally [Maier and Atwater, 2005]. As discussed in the previous paragraphs, the ohmic losses of the metal limit the potentially striking applications provided

by SPP excitation. Light transport along plasmonic nanowires occurs over a distance of a few micrometers ($\lambda = 800nm$) [Ditlbacher et al., 2005; Krenn, 2003; Krenn et al., 2002; Takahara et al., 1997]. Long-Range SPPs, discussed in section 2.3, provide a partial solution to this problem. They offer the longest propagation for plasmon-based waveguides ($L_A \approx 10mm$ at $\lambda = 1550nm$), with localisation of the order of few micrometers [Charbonneau et al., 2005b], allowing for high speed signal transmission ($\approx 40\ Gbit/s$) [Ju et al., 2007].

In order to reduce the ohmic losses, the optical propagation in nanoparticle chains by the resonant electrodynamic interparticle coupling, schematically depicted in Fig. 2.19, has been theoretically [Brongersma et al., 2000; Citrin, 2004; Quinten et al., 1998] and experimentally [Maier et al., 2002, 2003] investigated. In order to reduce the radiative losses, the excitation near the plasmon resonance is necessary for the achievement of tight confinement to the submicron nanoparticles. The reduced metallic volume of the nanoparticle chain with respect to the metallic nanowires implies a reduction of the effective absorption from the metal. However, the coupling to radiative modes arising via the scattering from the metallic nanoparticle enhances the effective loss, which remains of the same order of the loss in metallic nanowires $\approx 1\mu m^{-1}$. Scattering processes can be limited by embedding the metal nanoparticle chain in a periodic plasmonic structure [Maier et al., 2004], where radiative losses are limited by the destructive interference and the resonant inter-particle coupling is not required. Here, the energy attenuation is mainly determined by the ohmic losses in the metal ($L_A \approx 300\mu m$ at $\lambda = 1.6\mu m$).

Novel plasmonic structures such as wedge [Eguiluz and Maradudin, 1976; Yatsui et al., 2001] and groove [Bozhevolnyi et al., 2005; Novikov and Maradudin, 2002; Pile et al., 2005] waveguides, schematically depicted in Fig. 2.20, have been proposed and realised experimentaly. Here, guidance occurs only if the angle of the wedge/V groove with respect to the normal to the surface is smaller than a certain critical angle. In particular, silver V-groove plasmonic waveguides exhibit tight subwavelength localisation ($L_C \approx 300\mu m$), relatively low dissipation ($L_A \approx 2\mu m$ at $\lambda = 633nm$), 100% transmission through sharp bends and high tolerance to structural imperfections [Pile and Gramotnev, 2004]. Improvement on propagation distance with V groove waveguides has been extended to $L_A \approx$

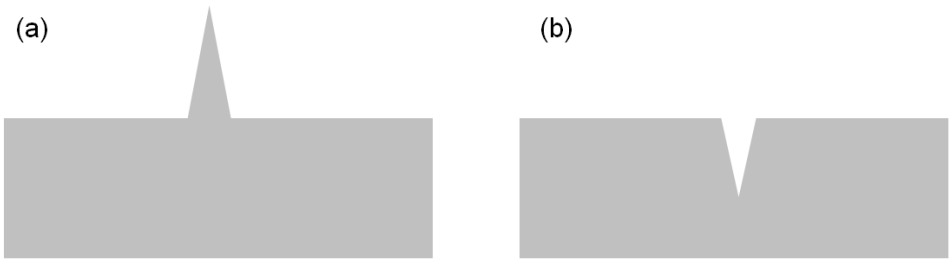

Figure 2.20: Schematic representation of plasmonic (a) wedge and (b) groove waveguides.

$250\mu m$, with a lateral confinement of $L_C \approx 1\mu m$ (at $\lambda = 1620nm$) [Bozhevolnyi et al., 2005].

Remarkable progress in active control of SPPs has been reported for plasmonic signals propagating in a gold-on-silica waveguide containing a few microns long gallium section [Krasavin et al., 2004, 2005]. Here, the transmission properties can be effectively controlled by switching the structural phase of gallium. The gallium phase transition occurs by either an induced change of temperature or by electron-hole excitation. The signal modulation depth is of the order of 80% and the switching times are in the picosecond time-scale.

2.6 Amplified SPPs and active plasmonics

As described in the previous sections, SPPs provide interesting tools for numerous applications ranging from spectroscopy to highly integrated photonic circuitry, which exploitation is limited by ohmic losses of metals. Excitation of long range SPPs provides a significant reduction of effective losses, but is paid in terms of weaker localisation. In turn, in order to take full advantage of the striking sub-wavelength SPP features, the inherent trade-off between confinement and loss can be overcome only by embedding gaining media in plasmonic structures [Sudarkin and Demkovich, 1989]. Besides, the use of plasmonic components as optical interconnects in miniaturised optoelectronic circuits requires the ability to manipulate and control SPPs at the nanoscale. The general term *active plasmonics* has been

coined to collect all of the mechanisms under study to achieve active control of SPPs, ranging from signal switching and modulation to amplification.

Early study of amplified SPPs dates back in 1979, when Plotz and coworkers investigated the enhanced total internal reflection arising in a homogeneous amplifying medium in contact with a thin silver film, evaporated on a high-index prism [Plotz et al., 1979]. Here, the thickness of the gaining medium was assumed infinite. At the specific angle of incidence resonant with SPP excitation, the reflectance was found considerably enhanced to values higher than unity if the gain of the amplifying medium exceeded a certain threshold value, basically determined by the absorption of the metallic film. The authors suggested that the threshold condition might have been overcome in the near infrared $\lambda \approx 1\mu m$, where the silver absorption is small and gaining dyes providing sufficient amplification were available [Hansch et al., 1971].

From then on, the study of amplified SPPs did not receive much attention until 1998, when Sirtori and coworkers came up with the idea of exploiting plasmonic modes to confine the radiation emitted in semiconductor lasers [Sirtori et al., 1998]. The possibility to realize laser waveguides based on SPPs at a metal-semiconductor interface was experimentally demonstrated by using quantum cascade (QC) lasers emitting in the $8 - 11.5\mu m$ wavelength range. Such a structure, exhibited high confinement factor in the laser-active region and strong coupling to the active material with respect to a conventional layered semiconductor waveguide. A peak output power exceeding $25mW$ at the temperature $90K$ was measured for a QC laser with an emission wavelength $\lambda \approx 8\mu m$. Such an approach in realizing SPP-based semiconductor lasers was later assumed also by Tredicucci et al., who demonstrated the possibility of achieving single-wavelength emission at $\lambda \approx 17\mu m$ [Tredicucci et al., 2000a]. Record-breakingly laser action at long wavelength $\lambda \approx 19\mu m$ was also demonstrated [Tredicucci et al., 2000b].

The study of localised surface plasmons [Maier, 2007], which are not described with detail in this thesis, has also received considerable attention in the field of active plasmonics. Surface Plasmon Stimulated Emission of Radiation (SPASER) from a gaining medium surrounding a metal nanoparticle was described from a quantum perspective [Bergman and Stockman, 2003]. Here, the authors found

that two-level emitters surrounding a metallic nanoparticle can undergo radiationless transitions transferring their excitation energy into the quasistatic electric field energy of localised surface plasmons. Later on, it was discovered that the localised surface plasmon resonance of metallic nanostructures exhibits a singularity when the amplification provided by the surrounding medium is equal to a certain critical gain threshold [Lawandy, 2004]. In the presence of gain saturation such a singularity is suppressed, but is still manifested in high local fields. Dipole lasing of metallic nanoparticles coupled with quantum dots was also investigated [Protsenko et al., 2005]. Such a nanolaser exploited near field coupling between a resonant transition of an active particle and the plasmon resonance of a metallic nanoparticle. Indeed, under certain conditions, metallic nanoparticles can act as optical antennas for active atoms [Taminiau et al., 2008], leading to an amplification enhancement. Enhanced scattering induced by the excitation of surface plasmons in random lasers [Popov et al., 2006], and nanoscaled laser cavities with subwavelength confinement have also been claimed [Hill et al., 2009; Noginov et al., 2009; Oulton et al., 2009]. A further development of the SPASER was achieved in the context of metamaterials [Zheludev et al., 2008]; here, a two dimensional array of particular plasmonic resonators supports coherent current excitations that can act as a planar source of spatially and temporally coherent radiation [Stockman, 2008].

Preliminary demonstration of active control on SPP propagation was found in the realisation of an active plasmonic device consisting of a thin silver film sandwiched between two polymer layers [Andrew and Barnes, 2004]. The two polymer layers contained donor chromophore and acceptor fluorophore molecules, respectively. It was demonstrated that SPPs can mediate an effective transfer of excitation energy from donor to acceptor molecules on the opposite sides of a $120nm$ thick metallic film. Further developments in active plasmonics were focused on the use of nanoscale structural phase transformation in gallium plasmon waveguides [Krasavin and Zheludev, 2004] for all-optical modulation of SPPs [Krasavin et al., 2005]. Here, SPP signals in a metal-dielectric waveguide, containing a gallium section a few microns long, were effectively controlled by switching the structural phase of gallium. The switching was achieved by either changing the waveguide temperature or by external optical excitation with a controlling beam. The signal

modulation depth exceeded 80% and picosecond switching times were predicted. Active control of SPP signals was also demonstrated by using reversible changes in waveguide media caused by heating [Lereu et al., 2005; Nikolajsen et al., 2004], optical excitation of photochromic molecules [Pala et al., 2008] and interactions mediated by quantum dots [Pacifici et al., 2007]. Ultrafast all-optical modulation has also been achieved in arrays of subwavelength holes [Dintinger et al., 2006; Hendry et al., 2008], metallic films [Wiederrecht et al., 2007] and gold gratings [Rotenberg et al., 2008] by means of Enhanced Optical Transmission (EOT) and induced shifting of Wood anomalies. Devices with switching times of the order of femtoseconds were ultimately demonstrated by means of direct ultrafast nonlinear optical excitation of the metal [MacDonald et al., 2009].

The theoretical modelling of gain-assisted SPP modes on planar metallic waveguides was established by Nezhad et al., who perturbatively derived the gain threshold condition for SPPs propagating on a single interface and on metal-insulator-metal (MIM)/insulator-metal-insulator (IMI) plasmonic waveguides [Nezhad et al., 2004]. In principle, such a derivation does not require a perturbative approach. As described in section 2.2, the dimensionless propagation constant (rescaled to the wavevector $k = \omega/c$) of SPPs propagating at a single interface is provided by

$$\beta = \sqrt{\frac{\epsilon_d \epsilon_m}{\epsilon_d + \epsilon_m}}, \tag{2.54}$$

where ϵ_m, ϵ_d are the dielectric responses of the metal and of the dielectric media composing the interface, respectively. Such an expression is generally valid for lossy metals and gaining dielectrics, described by complex dielectric constants

$$\epsilon_m = \epsilon_m' + i\epsilon_m'', \tag{2.55}$$

$$\epsilon_d = \epsilon_d' + i\epsilon_d''. \tag{2.56}$$

In turn, also the propagation constant $\beta = \beta' + i\beta''$ is complex, where the real part β' accounts for the SPP phase shift and the imaginary part β'' for the SPP attenuation. Note that, in the formalism used in this thesis, the plasmonic mode dependence is set proportional to $e^{i\beta z - i\omega t}$. Hence, $\epsilon_m'' > 0$ corresponds to the metal loss and $\epsilon_d'' < 0$ to the dielectric gain (signs are inverted if the mode is set proportional to $e^{i\omega t - i\beta z}$). The gain threshold condition is easily found by setting

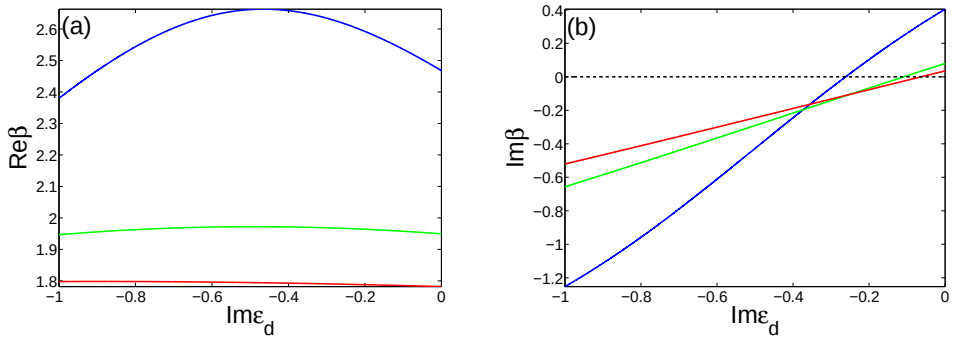

Figure 2.21: Real (a) and imaginary (b) parts of the propagation constant β as functions of dielectric gain ϵ_d''. Blue, green and red curves correspond to $\lambda = 400, 450, 500nm$, respectively. The dashed black line corresponds to the threshold condition $\beta'' = 0$. The dielectric constant of silver is calculated by Drude-Lorentz model, while for the dielectric constant of the gaining medium it is assumed $\epsilon_d' = 2.25$.

the imaginary part of the propagation constant to zero $\beta'' = 0$, which yields the condition

$$\epsilon_m''(\epsilon_d'')^2 + |\epsilon_m|^2(\epsilon_d'') + (\epsilon_d')^2\epsilon_m'' = 0. \tag{2.57}$$

Such a second order algebraic equation for ϵ_d'' provides two solutions for the gain threshold $\epsilon_d'' = T$, but one of them corresponds to the unphysical limit $T \to +\infty$ as $\epsilon_m'' \to 0$. Conversely, the other solution tends to the physically correct limit $T \to 0$ as $\epsilon_m'' \to 0$, and represents the gain threshold T, explicitly provided by

$$T = \frac{|\epsilon_m|^2}{2\epsilon_m''}\left[-1 + \sqrt{1 - 4\frac{(\epsilon_d'\epsilon_m'')^2}{|\epsilon_m|^4}}\right]. \tag{2.58}$$

For $\epsilon_d'' > T$, the metal losses are compensated only partially by the amplifying medium and the SPPs are damped with a reduced rate $\beta'' > 0$. On the other hand, for $\epsilon_d'' < T$, the metal losses are over-compensated and the SPPs are amplified $\beta'' < 0$ (note, that $\epsilon_d'', T < 0$). The gain threshold $\epsilon_d'' = T$, where the metal losses are thoroughly compensated by the gain in the adjacent medium, depends on the dielectric and dissipation properties of the plasmonic structure $\epsilon_m'(\omega), \epsilon_m''(\omega), \epsilon_d'$, which are frequency dependent. In Figs. 2.21a,b, (a) real and (b) imaginary

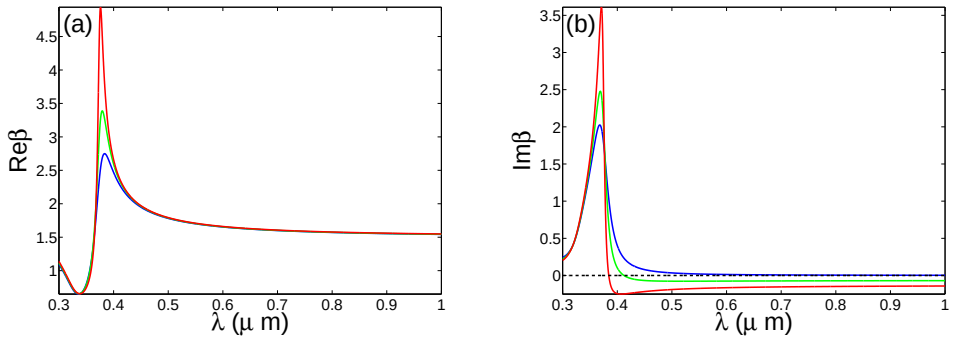

Figure 2.22: Spectral behaviour of real (a) and imaginary (b) parts of the propagation constant β. Blue, green and red curves correspond to $\epsilon_d' = -0.001, -0.2, -0.4$, respectively. The dashed black line corresponds to the threshold condition $\beta'' = 0$. The dielectric constant of silver is calculated by Drude-Lorentz model, while for the dielectric constant of the gaining medium it is assumed $\epsilon_d' = 2.25$.

parts of the propagation constant β are plotted as functions of dielectric gain ϵ_d'' for SPPs propagating at a single interface between silver and a gaining dielectric. Blue, green and red curves correspond to $\lambda = 400, 450, 500\ nm$, respectively. The dashed black line corresponds to the threshold condition $\beta'' = 0$, where the metal loss is exactly compensated by the gain material. The dielectric susceptibility of silver is modelled by the Drude-Lorentz fit of experimental data, as described in section 2.1, while for the dielectric constant of the gaining medium it is assumed $\epsilon_d = 2.25$. Such a simplified picture helps to grasp the physical mechanisms leading to SPP amplification, although in principle a change in the imaginary part of the dielectric constant ϵ_d'' implies a change of the real part ϵ_d' (as a consequence of Kramers-Kronig relations) [Jackson, 1999]. In addition, for emitters close to a metal surface, it is an approximation to consider the resulting dielectric gain ϵ_d'' as a position independent optical constant. Indeed, for amplified SPPs, the presence of the metal surface modifies the gain properties of the amplifying medium [DeLeon and Berini, 2008, 2009]. In this respect, two factors affect the amplification process close to a metal surface: the position-dependent lifetime of the emitter and the irradiance distribution of the pump signal. Basically,

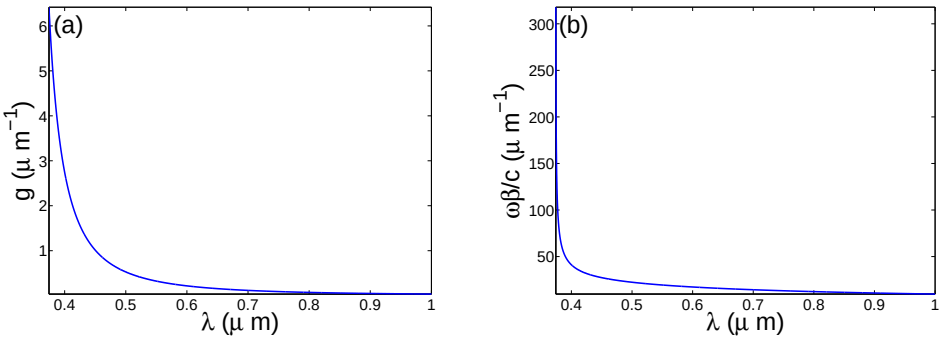

Figure 2.23: (a) Intensity gain threshold g and the corresponding (b) dimensional propagation constant $\tilde{\beta} = \omega\beta/c$ as functions of wavelength λ.

pump and emission processes suffer from interference effects due to the radiation reflected from the metal surface [Barnes, 1998; Ford and Weber, 1984]. As a result, a uniform gain picture is not sufficient to thoroughly describe the amplification in the vicinity of a metallic surface. Such an effect will not be considered in this thesis for the theoretical modelling of amplified SPPs since the simplified picture of uniform gain is useful to describe the fundamental energy transport phenomena occurring in plasmonic structures and will be used to model soliton propagation.

Figs. 2.22a,b plot the spectral dependence of the real (a) and the imaginary (b) parts of the propagation constant β. Here, blue, green and red curves correspond to $\epsilon_d' = -0.001, -0.2, -0.4$, respectively, while other parameters coincide with Fig. 2.21. The dashed black line corresponds to the threshold condition $\beta'' = 0$, where the metal loss is exactly compensated by the dielectric gain. For different fixed values of ϵ_d'', there exist different wavelength thresholds λ_{th}. Long-wavelength modes ($\lambda > \lambda_{th}$) are amplified ($\beta'' < 0$), while short-wavelength modes ($\lambda < \lambda_{th}$) are attenuated ($\beta'' > 0$), see Fig. 2.22b.

The spectral dependence of the gain threshold is plotted in Fig. 2.23a. Here, the gain coefficient (measured in μm^{-1}) is defined by

$$g = -\frac{\omega}{c}\frac{\epsilon_d''}{\sqrt{\epsilon_d'}}. \tag{2.59}$$

g represents the increase rate of the Poynting vector flow for plane waves propagating in the bulk gaining dielectric $I = I_0 e^{gz}$ in the approximation $|\epsilon_d''| << |\epsilon_d'|$. In

Fig. 2.23b, the purely real propagation constant at the gain threshold $\tilde{\beta} = \omega\beta/c$ (rescaled back to physical units) is plotted as a function of the vacuum wavelength λ. At the wavelength $\lambda \approx 400nm$, very close to the surface plasmon resonance, the gain threshold is of the order $g \approx 1\mu m^{-1}$ and the confinement length L_C, defined in section 2.2, is $L_C \approx 10nm$.

The achievement of *lossless* propagation with such an extreme confinement ($L_C \approx 10nm$) requires a considerably high gain ($g \approx 1\mu m^{-1}$), which can not be provided by the present active materials. Quantum dots exhibit a maximum gain $g \approx 0.05\mu m^{-1}$ [Klimov et al., 2000], while rhodamine 6G dyes in PMMA provide $g \approx 0.04\mu m^{-1}$ [Noginov et al., 2006a,b], which was used to demonstrate loss compensation [Noginov et al., 2008a] and stimulated emission of SPPs at $\lambda = 594nm$ [Noginov et al., 2008b] and $\lambda = 633nm$ [Seidel et al., 2005]. Besides, SPP-based lasing has been demonstrated at $\lambda = 594nm$ by using Dielectric-Metal-Dielectric (DMD) waveguides [Kumar et al., 2008]. Here, by introducing optical gain on one side of the dielectric layers, provided by R6G doped polymer, amplification of SPP modes was obtained. Further, by embedding scatter inclusions in the opposite side of the waveguide, random lasing action was achieved [Kumar et al., 2009]. A structure to compensate SPP loss by using multiple quantum wells as gain medium has also been proposed [Alam et al., 2007]; AlGaInAs quantum wells with gain $g \approx 0.2\mu m^{-1}$ at wavelength $\lambda = 1.55\mu m$ [Akram et al., 2004] were suggested to overcome the losses in plasmonic structures with the current technology. Finally, amplified spontaneous emission using erbium ions [Ambati et al., 2008], PbS (Lead sulfide) quantum dots [Bolger et al., 2010; Grandidier et al., 2009] and hybrid organic-inorganic polymer [Gather et al., 2011, 2010] have recently been reported at $\lambda \approx 600nm$.

SPP energy flow in the presence of dielectric gain and metallic loss can be understood from the time averaged Poynting vector $\langle \vec{S} \rangle_t = \frac{1}{2} Re \left[\vec{\mathcal{E}} \times \vec{\mathcal{H}}^* \right]$. In the following, we calculate the Poynting vector for a single interface between a lossy metal and a gaining dielectric. Plasmonic modes for such a geometry are provided by Eqs. (2.17-2.19), with the only difference that here $\epsilon_d = \epsilon_d' + i\epsilon_d''$ is a complex optical constant. Explicit expressions for time averaged Poynting vector

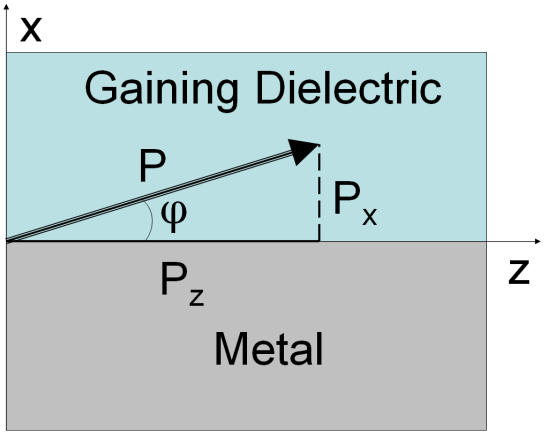

Figure 2.24: Schematical representation of the power flow for SPPs propagating at a single interface between a gaining dielectric and a metal.

x, z components $\langle S_x \rangle_t$, $\langle S_z \rangle_t$ are given by

$$\begin{aligned}
\langle S_x \rangle_t &= -\frac{|A|^2}{2c\mu_0}\left[\frac{q'_m\epsilon''_m - q''_m\epsilon'_m}{|q_m|^2}e^{2q'_m x}\theta(-x) + \frac{q''_d\epsilon'_d - q'_d\epsilon''_d}{|q_d|^2}e^{-2q'_d x}\theta(x)\right]e^{-2\beta'' z}, \\
\langle S_z \rangle_t &= \frac{|A|^2}{2c\mu_0}\left[\frac{\beta'\epsilon'_m + \beta''\epsilon''_m}{|q_m|^2}e^{2q'_m x}\theta(-x) + \frac{\beta'\epsilon'_d + \beta''\epsilon''_d}{|q_d|^2}e^{-2q'_d x}\theta(x)\right]e^{-2\beta'' z}.
\end{aligned}$$

Here, the prime and double prime superscripts indicate real and imaginary parts, respectively. The complex propagation constant β is provided by Eq. (2.57), $q^2_{d,m} = \beta^2 - \epsilon_{d,m}$, $\theta(x)$ represents the Heaviside step function and A is an arbitrary complex constant, representing the electric field z-component amplitude at $x = 0$ ($A = e_z(0)$). As described in section 2.2, in the absence of gain and loss ($\epsilon''_m = \epsilon''_d = 0$), the Poynting vector x-component is null $\langle S_x \rangle_t = 0$ and the SPPs propagate in the z-direction without attenuation. On the other hand, for an interface between a lossy metal and a gaining dielectric, the transverse power flow is non null $\langle S_x \rangle_t \neq 0$ and the propagation is tilted. The power density components $P_{x,z} = k^{-1}\int_{-\infty}^{+\infty} dx \langle S_{x,z} \rangle_t$ are explicitly provided by

$$P_x = -\frac{|A|^2}{4\mu_0\omega}\left[\frac{q'_m\epsilon''_m - q''_m\epsilon'_m}{q'_m|q_m|^2} + \frac{q''_d\epsilon'_d - q'_d\epsilon''_d}{q'_d|q_d|^2}\right]e^{-2\beta'' z}, \tag{2.60}$$

$$P_z = \frac{|A|^2}{4\mu_0\omega}\left[\frac{\beta'\epsilon''_m + \beta''\epsilon''_m}{q'_m|q_m|^2} + \frac{\beta'\epsilon'_d + \beta''\epsilon''_d}{q'_d|q_d|^2}\right]e^{-2\beta'' z}. \tag{2.61}$$

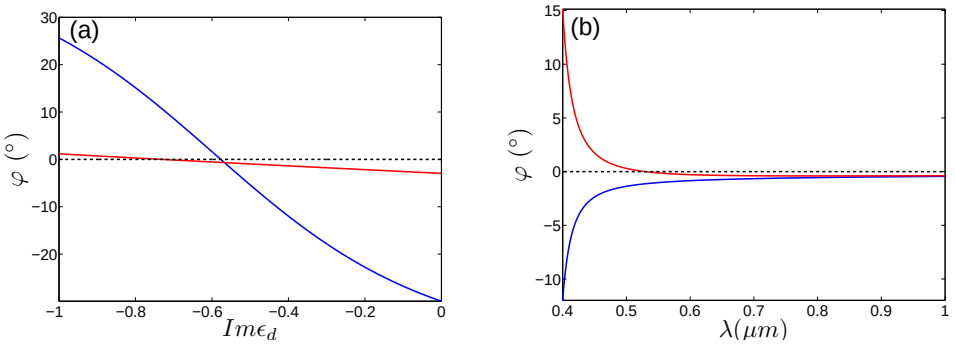

Figure 2.25: (a) Tilt angle φ of the power flow as a function of dielectric gain ϵ_d''. Blue and red curves correspond to $\lambda = 400, 500nm$, respectively. (b) Tilt angle φ of the power flow as a function of wavelength λ. Blue and red curves correspond to $\epsilon_d'' = -0.4, -0.8$, respectively. In both figures, the dielectric properties of silver are calculated by the Lorentz-Drude model, while for the gaining dielectric it is assumed $\epsilon_d' = 2.25$.

The time-averaged optical energy is absorbed/amplified at rate $2\beta''$ and travels with a tilted angle φ (see Fig. 2.24), which is provided by

$$\tan\varphi = \frac{P_x}{P_z}. \tag{2.62}$$

The tilt angle φ depends on the dielectric properties of the media $\epsilon_m(\omega), \epsilon_d$. In Fig. 2.25a, φ is plotted as a function of the dielectric gain ϵ_d'' for two fixed wavelengths $\lambda = 400, 500nm$, corresponding to blue and red curves, respectively. For the calculation of φ, we considered a single interface between silver and a gaining dielectric with $\epsilon_d' = 2.25$. The dielectric properties of silver are modelled by the Drude-Lorentz fit of experimental data, as described in section 2.2. For small values (in modulus) of gain ϵ_d'', the SPPs are attenuated and the optical propagation is tilted towards the metal ($\varphi < 0$). As gain increases (in modulus), overcoming the gain threshold determined by Eq. (2.58), the SPPs are amplified and the optical propagation is tilted towards the metal. The tilt direction changes at the point $\epsilon_d'' = -\epsilon_m''$, where $P_x = 0$. For higher values of gain $|\epsilon_d''| > \epsilon_m''$, the transverse power P_x becomes positive and the energy flows towards the dielectric medium with a positive tilt angle $\phi > 0$. In Fig. 2.25b, the tilt angle φ is

plotted as a function of the vacuum wavelength λ for two fixed gain values $\epsilon_d'' = -0.4, -0.8$, identified by blue and red curves, respectively. For the blue curve, corresponding to $\epsilon_d'' = -0.4$, the power flow is always tilted towards the metal; conversely, for the red curve corresponding to $\epsilon_d'' = -0.8$, the tilt direction changes at the particular wavelength $\bar{\lambda}$ where $\epsilon_m''(\bar{\lambda}) = 0.4$.

2.7 Concluding remarks

In this chapter we have reviewed the scientific literature concerning surface plasmon polaritons (SPPs) in the linear regime. SPPs propagating at a single interface and in an Insulator-Metal-Insulator (IMI) structure have been described and the dispersion curve has been derived for such geometries. The tight subwavelength confinement of SPPs around the surface plasmon resonance is paid in terms of enhanced loss, which limits their use as miniaturised optical channels. In turn, the embedding of gain materials is needed in order to lengthen the propagation of SPPs and overcome the inherent trade-off between loss and localisation. The amplification of SPPs has been reviewed, discussing the results of some recent experiments that report the amplified spontaneous emission of SPPs using erbium ions [Ambati et al., 2008], PbS (Lead sulfide) quantum dots [Bolger et al., 2010; Grandidier et al., 2009] and hybrid organic-inorganic polymer [Gather et al., 2011, 2010].

Chapter 3

Nonlinear plasmonic waves at a single interface

The enhancement of nonlinear optical phenomena mediated by a metallic surface has been a matter of study and research in the turn of the century [Ponath and Stegeman, 1991; Zayats et al., 2005]. Nonlinear effects are boosted by the electromagnetic field enhancement on the metal surface. The main responsible for the field enhancement is the localisation of electromagnetic energy in small gaps and voids. If the effects of metal imperfections are neglected, the electromagnetic field enhancement is due to the excitation of surface plasmon polaritons (SPPs) in ideal surfaces and of localised surface plasmons in metallic nanoparticles. Relevant examples of surface-enhanced nonlinear processes include Surface Enhanced Raman Scattering (SERS) [LeRu and Etchegoin, 2009], Kerr nonlinearity [Agranovich et al., 1980; Stegeman et al., 1985], Second Harmonic Generation (SHG) [Antoine et al., 1998; Davoyan et al., 2009a; Kroo et al., 2008], Third-Harmonic Generation (THG) [Lamprecht et al., 1999] and Four Wave Mixing (FWM) [Palomba and Novotny, 2008].

In this chapter, we introduce a perturbative theory to model amplification of SPPs propagating on a single interface between a metal and a gain material. Gain is modelled through the two-level atom model [Boyd, 2003], described in appendix A, which is characterised by the cubic nonlinear polarisation $\vec{P}_{NL} \propto |\vec{E}|^2\vec{E}$ for field intensities I much smaller than the saturation intensity: $I << I_S$. The chapter is organised as follows: section 3.1 reviews the principal achievements in

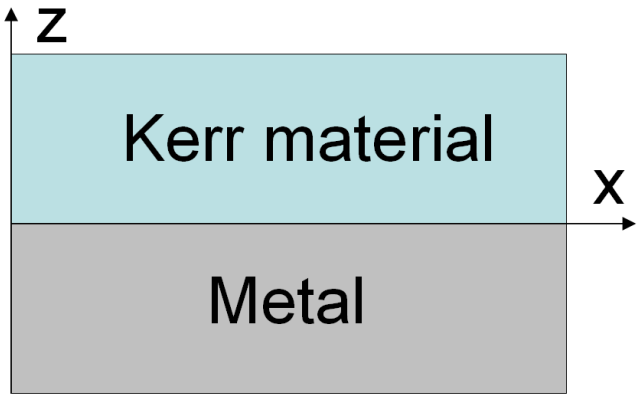

Figure 3.1: Schematic representation of the single interface between a metal and a nonlinear dielectric, which is considered in Ref. [Mihalache et al., 1987].

the theoretical modelling of nonlinear SPPs; in section 3.2, we derive the dispersion relation for a single interface between a metal and a nonlinear amplifying medium and section 3.3 describes the plasmon-soliton formation at an active metal-dielectric interface and the inherent instabilities arising in such a system.

3.1 Nonlinear propagation of SPPs

Early study of nonlinear plasmonic waves was focused on the reflectivity properties of a silver film adjacent to a Kerr material in the Kretschmann configuration [Wysin et al., 1981]. The nonlinear optical properties of the Kerr material lead to an intensity-dependent reflection coefficient R, which exhibits a bistable behaviour [Zhou et al., 2008]. Such an effect is potentially useful for designing novel optical devices such as optical switches or high resolution sensors [Yin and Hesselink, 2006].

At the same time, the propagation of nonlinear SPPs on an interface between a metal and a Kerr dielectric received attention by the scientific community [Agranovich et al., 1980; Boardman et al., 1987; Mihalache et al., 1987; Stegeman et al., 1985]. Maxwell equations accounting for the Kerr nonlinearity involve the coupling of the two components (transverse and longitudinal) of the TM plasmonic mode. A simplification of the generally coupled nonlinear problem is provided

by the uniaxial approximation, where nonlinearity is approximated as dependent only on the longitudinal [Agranovich et al., 1980] or transverse [Stegeman et al., 1985] components of the electric field. Such uniaxial assumptions are satisfactory only in specific cases, while the problem of determining the nonlinear SPP modes of a generic plasmonic structure requires a more general vectorial approach.

In 1987, Mihalache et al. published a seminal paper for the theoretical modelling of nonlinear SPPs [Mihalache et al., 1987]. They considered a single interface between a metal and a Kerr material neglecting loss, as schematically depicted in Fig. 3.1. Using the ansatz $\vec{\mathcal{E}}(\vec{r},t) = [iE_x(z)\hat{x} + E_z(z)\hat{z}]\, e^{i\omega t - i\beta x}$, Maxwell equations for TM modes are

$$\frac{dE_x}{dz} = \frac{1}{\beta}\left[\epsilon_{zz} - \beta^2\right] E_z, \tag{3.1}$$

$$\frac{d}{dz}(\epsilon_{zz}E_z) = -\beta\epsilon_{xx}E_x, \tag{3.2}$$

$$H_y = -\frac{\epsilon_0 c}{\beta}\epsilon_{zz}E_z, \tag{3.3}$$

where z is the dimensionless transverse variable (rescaled to $k^{-1} = c/\omega$) and $\epsilon_{xx}, \epsilon_{zz}$ are the nonlinear susceptibility components

$$\epsilon_{xx} = \epsilon_L(z) + (\alpha_1 E_x^2 + \alpha_2 E_z^2)\theta(z), \tag{3.4}$$

$$\epsilon_{zz} = \epsilon_L(z) + (\alpha_1 E_z^2 + \alpha_2 E_x^2)\theta(z). \tag{3.5}$$

Eqs. (3.1-3.3) are subject to the boundary conditions

$$\epsilon_{zz}(0^-)E_z(0^-) = \epsilon_{zz}(0^+)E_z(0^+), \tag{3.6}$$

$$E_x(0^-) = E_x(0^+), \tag{3.7}$$

$$H_y(0^-) = H_y(0^+). \tag{3.8}$$

The step-like function

$$\epsilon_L(z) = \epsilon_m\theta(-z) + \epsilon_d\theta(z) \tag{3.9}$$

is the linear susceptibility profile, where ϵ_m, ϵ_d are the dielectric constants of the metal and of the Kerr materials, respectively. $\theta(z)$ is the Heaviside step function and $\alpha_1 = 3\alpha_2 = 3\chi_3/4$, where χ_3 is the Kerr nonlinear susceptibility. In the manuscript by Mihalache et al., anisotropic linear effects were also considered

[Mihalache et al., 1987]. Such effects are not included here since they are not relevant for the purpose of this section. The basic assumption of the analysis made by Mihalache et al. is the neglecting of loss. Indeed, in the absence of loss, the Maxwell equations have a first integral [Berkhoer and Zakharov, 1970; Boardman et al., 1987; Ciattoni et al., 2005] that can be written as

$$I = (\beta^2 - \epsilon_L)E_z^2 - \epsilon_L E_x^2 - \left[\alpha_2 (E_x E_z)^2 + \frac{\alpha_1}{2}(E_x^4 + E_z^4)\right]\theta(z) - \left(\frac{dE_x}{dz}\right)^2 = 0. \quad (3.10)$$

The metallic optical response is assumed linear. Hence, the mode profile within the metal is shaped by the exponential function

$$E_x = E_{0x} e^{q_m z} \qquad (z < 0), \quad (3.11)$$

where $q_m^2 = \beta^2 - \epsilon_m$. From the boundary conditions for the continuity of E_x and $\epsilon_{zz} E_z$ one gets

$$E_{0x} = -\frac{q_m}{\beta \epsilon_m}(\epsilon_d + \alpha_1 E_{0z}^2 + \alpha_2 E_{0x}^2) E_{0z}, \quad (3.12)$$

where E_{0z} is the transverse field amplitude in the nonlinear medium at $z = 0^+$: $E_{0z} = E_z(0^+)$. On the other hand, the first integral yields another equation for E_{0x}, E_{0z}, β

$$\frac{1}{2}\alpha_1 E_{0x}^4 + \left[\epsilon_d + \frac{\epsilon_m^2}{q_m^2}\right] E_{0x}^2 + \frac{\beta \epsilon_m}{q_m} E_{0x} E_{0z} - \frac{1}{2}\alpha_1 E_{0z}^4 = 0. \quad (3.13)$$

The numerical solution of Eqs. (3.12,3.13) by the Newton-Raphson method, which is presented in appendix B, provides the nonlinear dispersion of the plasmonic modes for the geometry considered. The dimensionless propagation constant β (rescaled to $k = \omega/c$) depends on the SPP field intensity, which is a characteristic feature of nonlinear systems, as discussed in section 1.3. Such a semi-analytical approach allows calculating the constants E_{0x}, E_{0z} for the family of solutions parametrized by the propagation constant β. Once having determined such constants, the nonlinear mode profile can be numerically computed integrating Eqs. (3.1,3.2) by Runge-Kutta method, which is described in appendix D.

Results are plotted in Figs. 3.2a,b: (a) the nonlinear E_x mode profile and (b) the trajectory in the $E_x - E_z$ space for an interface between silver ($\epsilon_m = -15$)

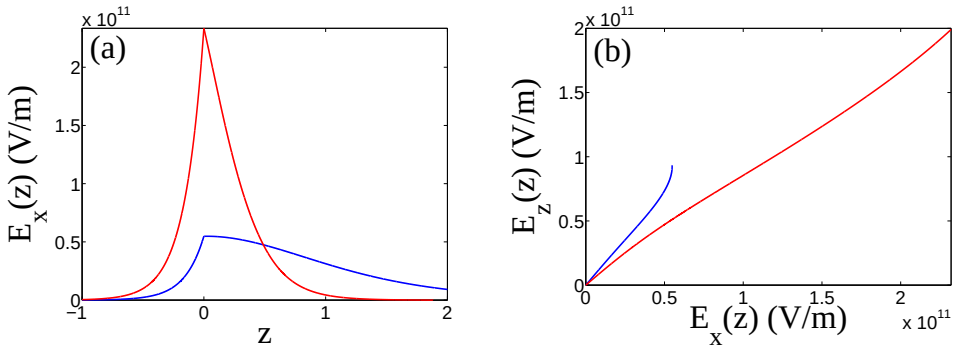

Figure 3.2: (a) Plasmonic mode E_x profile and (b) trajectory in the $E_x - E_z$ space for an interface between silver ($\epsilon_m = -15$) and silica glass ($\epsilon_d = 2.1$) at wavelength $\lambda = 650nm$. In both figures the nonlinear parameter of silica glass is assumed $\chi_3 = 2 \times 10^{-22} m^2/V^2$. Blue (red) curves correspond to $\beta = 2$ ($\beta = 5$).

and silica glass ($\epsilon_d = 2.1, \chi_3 = 2 \times 10^{-22}$) at the vacuum wavelength $\lambda = 650nm$. Blue and red curves correspond to $\beta = 2, 5$, respectively. For focusing nonlinearity ($\chi_3 > 0$), nonlinear modes exist if $\beta > \beta_L$, where β_L is the linear propagation constant $\beta_L = \sqrt{\epsilon_d \epsilon_m/(\epsilon_d + \epsilon_m)}$.

The time averaged Poynting vector is

$$\vec{S} = -(1/2) H_y E_z \hat{x}. \tag{3.14}$$

H_y, E_z are real quantities and the total power density carried in the x-direction is given by the flux

$$P = \frac{\epsilon_0 c}{2k\beta} \int_{-\infty}^{+\infty} dz \epsilon_{zz} E_z^2. \tag{3.15}$$

Since the metal loss is neglected, the total power density P is a conserved quantity in this approximation. For every fixed β, we numerically solved Eqs. (3.12,3.13) by the Newton Raphson algorithm, used the two solutions E_{x0}, E_{z0} as initial values for the Runge-Kutta integration of Eqs. (3.1,3.2) and determined the total power density P by numerically computing the integral of Eq. (3.15). Results of such a procedure are plotted in Figs. 3.3a,b, which represent the power vs β plots for a single interface between silver and (a) silica glass, (b) chalcogenite glass As_2Se_3. For the numerical computations we considered (a) $\epsilon_m = -15, \epsilon_d =$

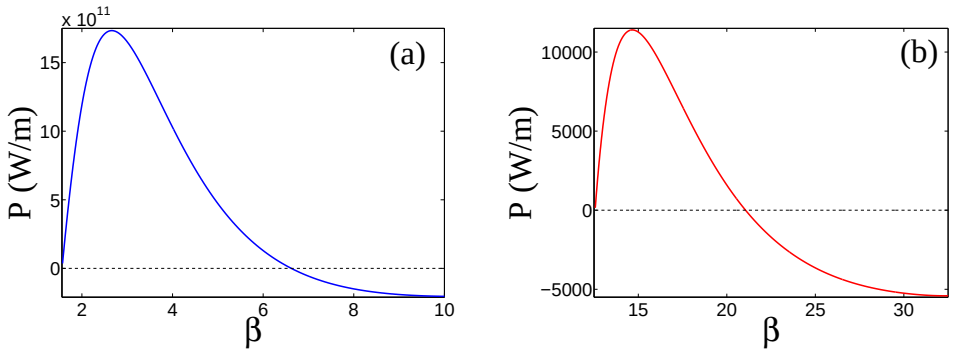

Figure 3.3: Nonlinear dispersion relation for a single interface between (a) silver ($\epsilon_m = -15$) and silica glass ($\epsilon_d = 2.1, \chi_3 = 2 \times 10^{-22} m^2/V^2$) at wavelength $\lambda = 650nm$, (b) silver ($\epsilon_m = -8.25$) and chalcogenite glass As_2Se_3 ($\epsilon_d = 7.84, \chi_3 = 1.4 \times 10^{-18} m^2/V^2$) at wavelength $\lambda = 480nm$.

$2.1, \chi_3 = 2 \times 10^{-22} m^2/V^2$ and (b) $\epsilon_m = -8.25, \epsilon_d = 7.84, \chi_3 = 1.4 \times 10^{-18} m^2/V^2$ [Asobe et al., 1993].

The role played by the focusing Kerr nonlinearity is to squeeze the SPP field profile, as can be understood from Fig. 3.2a. The P vs β curve, depicted in Fig. 3.3, exhibits a non monotonic behaviour. In particular, a maximum (P_{max}) and a point of zero power density appear $P = 0$. For the particular condition where $P = 0$, the onward power density carried within the Kerr medium is thoroughly balanced by the backward power density carried within the metal. For every fixed positive power density $P < P_{max}$ there exist two nonlinear modes with different propagation constants. Note that, in Fig. 3.3b, the peak power density $P_{max} \approx 10^4 W/m$ is much smaller than in Fig. 3.3a. This is mainly due to the large linear susceptibility of chalcogenite glass $\epsilon_d \approx -\epsilon_m$, which is responsible for the tight confinement of the SPP linear mode $\beta_L \approx 12$. For $P < 0$, the backward power carried within the metal overcomes the onward power carried in the Kerr dielectric and thus the phase velocity is opposite in sign with the velocity of energy. Such a derivation is valid only if the metal loss ϵ_m'' is neglected and the results are in line with the ones reported in Refs. [Huang et al., 2009; Mihalache et al., 1987]. Similar results have also been obtained for a nonlinear insulator-metal-insulator (IMI) geometry without considering the first integral,

but by resorting to the shooting method to derive the P vs β curve [Davoyan et al., 2008].

If one wants to include the effect of metal loss, the approach described in this section is not applicable. Indeed, the first integral does not exist in this case and it is impossible to achieve the dispersion relation. To consider simultaneously nonlinearity and loss one can rely on perturbative methods, treating loss and nonlinearity as small quantities and achieving a propagation equation for the SPP amplitude. Such methods have been used to describe plasmon-soliton formation [Davoyan et al., 2009b; Feigenbaum and Orenstein, 2007] and nonlinear nano-focusing in tapered waveguides [Davoyan et al., 2010b]. In the following sections we perturbatively derive the dispersion law for amplified SPPs and the propagation equation for dissipative plasmon-solitons.

3.2 Dispersion law for nonlinear and amplified SPPs

As discussed in chapter 2, the optical propagation in plasmonic structures is damped by the large intrinsic ohmic loss of the metal, which limits the use of SPPs for nonlinear applications. The SPP propagation on a single interface between a metal and an amplifying dielectric material has been described in section 2.6, reproducing the results of Ref. [Nezhad et al., 2004]. In section 2.6, we also modelled the amplification of SPPs in the linear regime [Bergman and Stockman, 2003; Nezhad et al., 2004; Noginov et al., 2006b; Winter et al., 2006], where the nonlinear saturation of gain is neglected. The gain threshold condition, where the metal loss is exactly balanced by the gain of the amplifying dielectric medium, is mathematically expressed by the requirement that the propagation constant is purely real.

The gain vs loss balance can also be achieved above the linear threshold, if the nonlinear saturation of gain is considered. Experimental demonstration of SPP amplification using optically pumped dyes [Noginov et al., 2006b; Seidel et al., 2005; Winter et al., 2006] and erbium doped glass [Ambati et al., 2008] has been reported. Signature of amplification is found in the gain threshold for the output

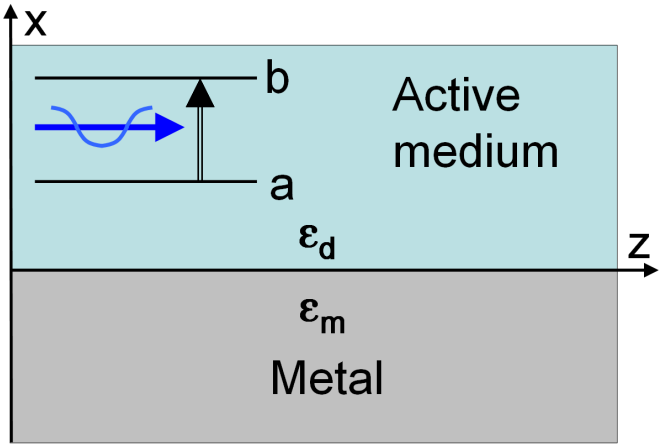

Figure 3.4: Schematic representation of the single interface between metal and an externally pumped amplifying medium.

SPP intensity and the correspondent narrowing of its spectrum [Gather et al., 2010; Noginov et al., 2006b].

In this section, we derive a perturbative theory accounting for the nonlinear saturation of gain, describing the formation of stationary nonlinear SPP modes above the linear gain threshold. In what follows, we consider a single interface between a metal and an amplifying dielectric medium, which is schematically depicted in Fig. 3.4. We start our analysis from the time independent Maxwell equations for TM waves

$$\partial_{zx}\mathcal{E}_z - \partial_{zz}\mathcal{E}_x = \mathcal{D}_x, \tag{3.16}$$

$$\partial_{zx}\mathcal{E}_x - \partial_{xx}\mathcal{E}_z = \mathcal{D}_z, \tag{3.17}$$

where x, z are the transverse and longitudinal coordinates, which are perpendicular and parallel to the propagation direction respectively, as represented in Fig. 3.4. Both coordinates are rescaled to dimensionless variables: scaling back to physical units can be achieved by multiplying x, z with $1/k = \lambda/2\pi$, where λ is the vacuum wavelength. Amplification in the dielectric medium is modelled through the two-level model [Boyd, 2003], which is reported in appendix A. In

the limit of relatively small SPP intensities, the saturated optical susceptibility

$$\chi(\delta) = \alpha \frac{\delta - i}{1 + \delta^2 + |\vec{\mathcal{E}}|^2/|E_S|^2} \tag{3.18}$$

can be approximated by the sum of a linear term and a cubic correction

$$\chi(\delta) \approx \alpha \frac{\delta - i}{1 + \delta^2} + \alpha \frac{i - \delta}{(1 + \delta^2)^2} \left| \frac{\vec{\mathcal{E}}}{E_S} \right|^2, \tag{3.19}$$

where δ is the detuning of the SPP angular frequency ω from the atomic resonance $\omega_{ba} = \omega_b - \omega_a$ normalized to the dephasing rate $1/T_2$, α is the dimensionless gain parameter and E_S is the saturation field.

Such an approximation is valid only in the limit $|\vec{\mathcal{E}}| << |E_S|$. The particular value of the saturation field E_S, dependent on the material used, is not crucial for the derivation below, where E_S plays the mere role of a scaling factor for the electric field $\vec{\mathcal{E}}$. For $\alpha > 0$, the two-level model provides a linear gain and a nonlinear absorption that are maximal at the resonance $\delta = 0$. Linear and nonlinear corrections due to the two-level active inclusions in the dielectric medium enter the constitutive relation

$$\vec{\mathcal{D}} = \epsilon_0(\epsilon + \gamma|\vec{\mathcal{E}}|^2)\vec{\mathcal{E}}, \tag{3.20}$$

where $\epsilon = \epsilon' + i\epsilon''$ is the linear dielectric profile and $\gamma = \gamma' + i\gamma''$ is the nonlinear susceptibility. With $\epsilon_{d,m}$ we indicate the susceptibility of dielectric ($x > 0$) and metallic ($x < 0$) media, respectively. The metal is assumed linear ($\gamma_m = 0$) and nonlinear effects are assumed to take place only in the dielectric medium:

$$\gamma_d = \alpha \frac{i - \delta}{(1 + \delta^2)^2}. \tag{3.21}$$

We seek solutions of Eqs. (3.16-3.17) in the form

$$\vec{\mathcal{E}}(x, z) = E_S \vec{E}(x) \exp(i\beta z), \tag{3.22}$$

where β is the dimensionless propagation constant rescaled to $k = \omega/c$. As explained above, the saturation field E_S plays the mere role of a scaling factor for the electric field $\vec{\mathcal{E}}$. The particular value of the saturation field E_S does not

affect the calculations below, which depend on the rescaled electric field $\vec{E}$. The linear susceptibility of the amplifying medium is

$$\epsilon_d = \epsilon_b + \alpha \frac{\delta - i}{1 + \delta^2}, \tag{3.23}$$

where ϵ_b is the dielectric constant of the background material hosting the two-level active inclusions. In the linear limit ($\gamma_d = 0$), the perturbative theory developed below provides us with a complex β, representing the dispersion law of amplified ($\beta'' = Im\beta < 0$) or damped ($\beta'' = Im\beta > 0$) SPPs. Conversely, nonlinear results derived below ($\gamma_d \neq 0$) require the SPP intensity to be stationary with respect to the propagation coordinate z. Such a condition is achieved when the amplification in the dielectric medium perfectly balances the metal loss, providing $\beta'' = Im\beta = 0$. For $x < 0$, the boundary value problem is linear and the solutions are exponential functions:

$$E_x = Be^{q_m x}, \tag{3.24}$$

$$E_z = \frac{iq_m}{\beta} Be^{q_m x}, \tag{3.25}$$

where $q_m^2 = \beta^2 - \epsilon_m$ ($q'_m = Req_m > 0$) and B is the E_x field component on the metal side of the interface $x = 0^-$. For $x > 0$, Maxwell equations provide us with the nonlinear system of differential equations

$$\beta^2 E_x + i\beta \partial_x E_z = \left[\epsilon_d + \gamma_d \left(|E_x|^2 + |E_z|^2\right)\right] E_x, \tag{3.26}$$

$$i\beta \partial_x E_x - \partial_{xx} E_z = \left[\epsilon_d + \gamma_d \left(|E_x|^2 + |E_z|^2\right)\right] E_z. \tag{3.27}$$

The boundary conditions for the continuity of E_z, D_x at $x = 0$ provide two equations for the constants B, E_{x0}, E_{z0}

$$\epsilon_m B = \left[\epsilon_d + \gamma_d \left(|E_{x0}|^2 + |E_{z0}|^2\right)\right] E_{x0}, \tag{3.28}$$

$$\frac{iq_m}{\beta} B = E_{z0}, \tag{3.29}$$

where E_{x0}, E_{z0} are the field amplitudes in the dielectric side of the interface $x = 0^+$. The two boundary conditions can be reduced to a single equation for the amplitudes E_{x0}, E_{z0}

$$\beta \epsilon_m E_{z0} = iq_m \left[\epsilon_d + \gamma_d \left(|E_{x0}|^2 + |E_{z0}|^2\right)\right] E_{x0}. \tag{3.30}$$

Eqs. (3.26,3.27) can be solved perturbatively under the assumption that nonlinear terms $\gamma_d|\vec{E}|^2$ are small. In the linear approximation ($\gamma_d = 0$) the plasmonic mode is given by

$$E_x^{(0)} = Ae^{-q_d x}, \tag{3.31}$$
$$E_z^{(0)} = \frac{q_d}{i\beta} Ae^{-q_d x}, \tag{3.32}$$

where $q_d^2 = \beta^2 - \epsilon_d$, $q_d' = Req_d > 0$ and A represents the linear amplitude of the SPP E_x field on the dielectric side of the interface $x = 0^+$, which remains arbitrary in the linear regime. At the next order, nonlinear terms are considered as small perturbations depending on the linear modes. Hence, nonlinear Maxwell equations are reduced to an inhomogeneous system of differential equations

$$(\beta^2 - \epsilon_d)E_x^{(1)} + i\beta\partial_x E_z^{(1)} = \gamma_d \left(|E_x^{(0)}|^2 + |E_z^{(0)}|^2\right) E_x^{(0)}, \tag{3.33}$$
$$i\beta\partial_x E_x^{(1)} - \epsilon_d E_z^{(1)} - \partial_{xx} E_z^{(1)} = \gamma_d \left(|E_x^{(0)}|^2 + |E_z^{(0)}|^2\right) E_z^{(0)}. \tag{3.34}$$

The electric field corrections of the order $o(|\gamma_d|)$ can be calculated straightforwardly

$$E_x^{(1)} = -\gamma_d |A|^2 A w_x e^{-q_d x - 2q_d' x}, \tag{3.35}$$
$$E_z^{(1)} = \frac{iq_d}{\beta} \gamma_d |A|^2 A w_z e^{-q_d x - 2q_d' x}, \tag{3.36}$$

where the constants w_x, w_z are given by

$$w_x = \left(1 + \frac{|q_d|^2}{\beta^2}\right) \frac{\epsilon_d + 2q_d'(2q_d' + q_d)}{4\epsilon_d q_d'(q_d' + q_d)}, \tag{3.37}$$
$$w_z = \left(1 + \frac{|q_d|^2}{\beta^2}\right) \frac{\epsilon_d + 2\beta^2 q_d'/q_d}{4\epsilon_d q_d'(q_d' + q_d)}. \tag{3.38}$$

The general solution is expressed as the sum of the linear modes with the nonlinear corrections

$$E_x = Ae^{-q_d x}\{1 - w_x \gamma_d |A|^2 e^{-2q_d' x} + o(|\gamma_d|^2)\}, \tag{3.39}$$
$$E_z = \frac{q_d}{i\beta} Ae^{-q_d x}\{1 - w_z \gamma_d |A|^2 e^{-2q_d' x} + o(|\gamma_d|^2)\}. \tag{3.40}$$

Substituting Eqs. (3.39,3.40) into Eq. (3.30), one finds the nonlinear dispersion law for the amplified SPPs

$$\epsilon_m q_d + \epsilon_d q_m = \gamma_d |A|^2 F + o(|\gamma_d|^2), \tag{3.41}$$

where the constant F is given by

$$F = \left(1 + \frac{|q_d|^2}{\beta^2}\right) \frac{q_d\epsilon_m + q_m\epsilon_d - 2q'_d(q_m q_d - \beta^2\epsilon_m/\epsilon_d)}{4q'_d(q'_d + q_d)}. \tag{3.42}$$

The dispersion of nonlinear SPPs in the absence of gain and loss has been derived in the previous section, following the procedure of Ref. [Mihalache et al., 1987]. For $A = 0$, Eq. (3.41) provides us with the well known linear dispersion law for SPPs at a single metal-dielectric interface $\beta = \beta_L = \sqrt{\epsilon_d\epsilon_m/(\epsilon_d + \epsilon_m)}$. For $\epsilon_b = 1.8$ and $\epsilon_m = -15{+}0.4i$ (silver at $\lambda = 530$ nm), the SPP attenuation length is $L_A = (2k\beta''_L)^{-1} \simeq 15\mu$m. Neglecting nonlinearity, the threshold condition $\beta''_L = 0$ allowing for stationary propagation of SPPs is achieved at $\alpha = \alpha_0$, where the threshold gain α_0 is

$$\alpha_0 = \frac{1}{2\epsilon''_m}\left[|\epsilon_m|^2 - 2\epsilon''_m\epsilon_b\delta - \sqrt{\left(|\epsilon_m|^2 - 2\epsilon''_m\epsilon_b\delta\right)^2 - 4(\epsilon''_m)^2(\epsilon_b)^2\left(1+\delta^2\right)}\right]. \tag{3.43}$$

The minimum gain $\alpha_0 = \alpha_{min}$ required for the stationary SPP propagation corresponds to the resonance $\delta = 0$: $\alpha_{min} \simeq 0.00575$. Above the gain threshold, for $\alpha = 1.5\alpha_{min}, 2\alpha_{min}$, the characteristic SPP gain lengths are $L_G = (2k\beta''_L)^{-1} \simeq 30\mu m, 15\mu m$, respectively.

Since nonlinearity is considered small $\gamma_d|A|^2 << 1$, the nonlinear SPP phase shift $|\Delta\beta| << |\beta_L|$ can be derived by setting $\beta = \beta_L + \Delta\beta$; Eq. (3.41) can be linearized retaining only the first order $\Delta\beta$ corrections and can be solved with respect to $\Delta\beta$:

$$\Delta\beta = \gamma_d|A|^2\frac{\beta_L q_d(|q_d|^2 + \beta_L^2)}{2\epsilon_d^2(q'_d + q_d)}, \tag{3.44}$$

where $q_{d,m}$ are calculated for $\beta = \beta_L$. Above the gain threshold ($\alpha > \alpha_{min}$), the metal loss and the nonlinear saturation are perfectly balanced by the linear gain, allowing for the stationary propagation of SPPs. The equation above is valid only if the condition $\beta'' = 0$ holds, providing the existence condition for stationary SPPs. In the linear approximation, the condition $\beta''_L = 0$ implies $\alpha = \alpha_0$, where α_0 is given by Eq. (3.43), and the corresponding real propagation constant is $\beta_L(\alpha_0) = \beta_0$. The Taylor series expansion of β in terms of $(\alpha - \alpha_0)$ yields

$$\beta = \beta_0 + \partial_\alpha\beta_L(\alpha - \alpha_0) + \beta_{NL}|A|^2, \tag{3.45}$$

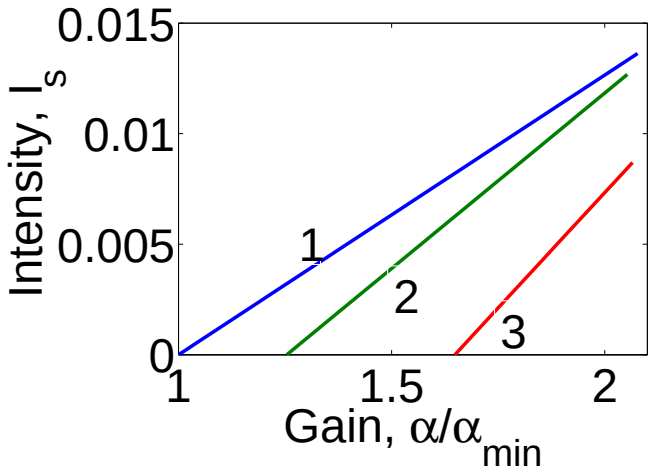

Figure 3.5: Stationary SPP intensity I_s vs the gain parameter α/α_{min}. Line 1 corresponds to $\delta = 0$, Line 2 to $\delta = 0.4$ and Line 3 to $\delta = 0.8$.

where

$$\beta_{NL} = \frac{\gamma_d \beta_L q_d (|q_d|^2 + \beta_L^2)}{2\epsilon_d^2 (q_d' + q_d)}, \tag{3.46}$$

and $q_{d,m}$ are calculated for $\beta = \beta_0$.

Hence, in the proximity of the gain threshold, the existence condition for the stationary propagation of SPPs ($\beta'' = 0$) is satisfied by the intensity

$$|A|^2 = I_s = (\alpha_0 - \alpha)\frac{\mathrm{Im}\partial_\alpha \beta_L}{\mathrm{Im}\beta_{NL}}, \tag{3.47}$$

where $\partial_\alpha \beta_L$ and β_{NL} are calculated for $\alpha = \alpha_0$. Fig. 3.5 depicts the stationary intensity I_s as a function of the rescaled gain α/α_{min} for $\delta = 0, 0.4, 0.8$ (lines 1,2,3, respectively). The purely real propagation constant of the stationary SPPs above the gain threshold is given by

$$\beta = \beta_s = \beta_0 + \mathrm{Re}\partial_\alpha \beta_L (\alpha - \alpha_0) + \mathrm{Re}\beta_{NL} I_s. \tag{3.48}$$

Fig. 3.6(a,b) plots the real β' and imaginary β'' parts of β_s, β_L. The stationary mode (β_s) arises at the threshold crossover ($\beta_L'' = 0$) where it bifurcates with the linear amplified and damped solutions. Note that, for $\alpha < \alpha_{min}$, the stationary

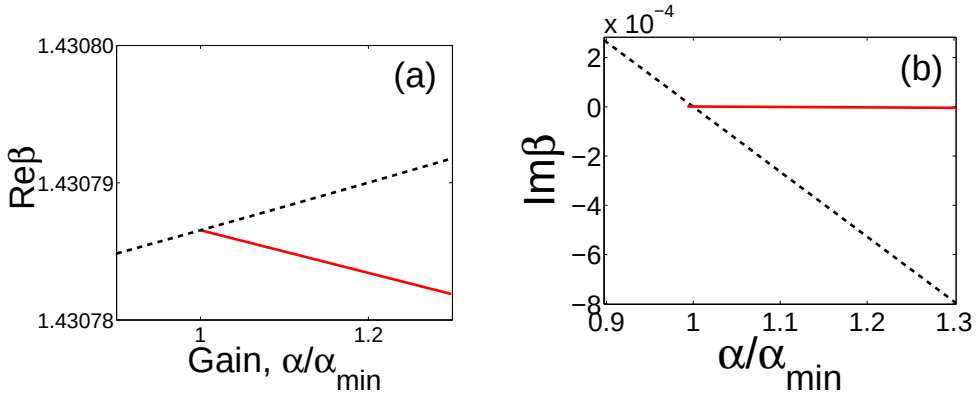

Figure 3.6: (a) Real (β') and (b) imaginary (β'') parts of the SPP propagation constant β vs the normalized gain parameter α/α_{min} for $\delta = 0$. The solid red lines represent the stationary nonlinear SPPs (β_s) and the dashed black lines the linear SPPs (β_L).

solution does not exist. For $\alpha > \alpha_{min}$, the nonlinear stationary SPP is characterised by the real propagation constant β_s ($\beta_s'' = 0$), which is reduced with respect to the propagation constant of the linear amplified SPP $\beta_s < \beta_L'$.

3.3 Propagation equation for amplified SPPs at a single interface

In the previous section, we have considered the nonlinear optical propagation in one-dimensional amplifying plasmonic structures, which enable tight confinement of the electromagnetic field only in the transverse direction perpendicular to the metal surface. In the absence of lateral boundaries, the SPPs diffract in the direction parallel to the metal-dielectric interface and perpendicular to the propagation direction. The application of SPPs for optical interconnection [Ebbesen et al., 2008; Ozbay, 2006] requires the tight spatial confinement in both of the transverse directions. In order to suppress diffraction one needs to resort to two-dimensionally structured plasmonic waveguides [Bozhevolnyi et al., 2006b]. Several geometries have been proposed and realised: metal films [Leosson et al.,

2006], triangular wedges [Yatsui et al., 2001] and grooves [Bozhevolnyi et al., 2005; Novikov and Maradudin, 2002; Pile and Gramotnev, 2004], cylindrical wires with rectangular [Jung et al., 2007] and circular [Schmidt and Russell, 2008; Schroter and Dereux, 2001; Takahara et al., 1997] cross-section, where the confinement is achieved in both of the transverse directions.

Alternatively, the nonlinear optical properties of the dielectric medium can be used to enable the propagation of spatial plasmon-solitons, which are localised self-sustaining nonlinear modes that do not diffract in the lateral direction [Davoyan et al., 2009b; Feigenbaum and Orenstein, 2007]. Other transverse nonlinear effects, such as self-focusing and filamentation of SPPs [Lin et al., 2009], are important in frequency conversion and switching experiments. Filamentation is a mechanism analogous to the modulational instability, which was briefly introduced in section 1.3, and has received significant attention in nonlinear optics [Abraham and Firth, 1990; Kivshar and Agrawal, 2003].

As described in the previous chapter, the use of SPP nonlinear functionalities [MacDonald et al., 2009; Wurtz et al., 2006] is considerably limited by the ohmic losses of the metallic components. The amplification of SPPs by doping and pumping the dielectric has been proposed and demonstrated [Ambati et al., 2008; Gather et al., 2010; Noginov et al., 2008b]. Nonlinear Schrödinger models have been recently proposed for SPPs propagating in a metal-insulator-metal (MIM) waveguide [Feigenbaum and Orenstein, 2007] and at a single interface [Davoyan et al., 2009b]. The perturbative theory adopted in such approaches, the *averaging method*, is a traditional theory extensively used in the context of dielectric waveguides [Agrawal, 2001b]. Such a perturbative approach develops in three steps. In the first step, the nonlinearity is neglected and the linear modes of Maxwell equations are derived: $\vec{E}_0 = A\vec{F}(x)e^{i\beta z}$, where β is the propagation constant, A is the arbitrary field amplitude and x, z are the transverse and longitudinal directions, perpendicular and parallel to the propagation direction, respectively. In the second step, the nonlinear terms are considered as small perturbations dependent only on the zero order mode $\vec{E}_0$ and the amplitude A is set as a slowly varying function of y, z: $A = A(y, z)$. In the ultimate step, the first order expansion of Maxwell equations is *averaged* in x by taking the scalar

product with the zero order mode $\vec{E}_0$, providing us with the propagation equation for the amplitude A [Davoyan et al., 2009b; Feigenbaum and Orenstein, 2007].

A problem of this approach is that the boundary condition for the continuity of the displacement component D_x is satisfied only in the linear approximation and the nonlinear corrections at the boundaries are neglected. In dielectric waveguides the above approach works well since the light intensity is peaked within the dielectric core and the nonlinear surface contributions are small. On the other hand, for plasmonic structures the SPP intensity is peaked at the metal surface and surface effects are crucial. Hence, the development of a rigorous perturbative theory accounting for surface effects through the explicit use of boundary conditions is important to describe the nonlinear propagation of SPPs with improved accuracy. A general perturbative approach accounting for surface effects is derived in chapter 4, where the averaging method and the importance of surface contributions are described with more detail.

In what follows, we develop a multiple scale asymptotic expansion of Maxwell equations to describe the propagation of amplified and nonlinear SPPs at a single interface between a metal and an active gain material. As in the previous section, the nonlinear effects result from the two-level active inclusions embedded in the dielectric medium [Boyd, 2003]. In the calculations below, the first order expansion of Maxwell equations around the gain threshold α_0 is solved analytically. The metal loss (ϵ_m''), the gain deviation from the stationary threshold ($\alpha - \alpha_0$) and the nonlinearity of the two-level active inclusions are treated as small perturbations. Boundary conditions (BCs) accounting for the first order corrections are imposed. The result of such a mathematical procedure is the complex Ginzburg-Landau propagation equation for the amplitude A, which takes account of the lateral diffraction in the interface plane, the metallic loss, the gain and the nonlinearity of the dielectric medium. The nonlinearity enhancement factor of the Ginzburg-Landau model derived below is intrinsically complex, while the averaging approach provides us with a real enhancement factor. The SPP nonlinearity enhancements predicted by the two theories are in good agreement in the long-wavelength range, where SPP localisation is weak; the difference between the two approaches increases in the short wavelength limit, where SPPs get tightly con-

fined at the interface and the nonlinear part of the boundary condition provides a significant contribution.

The geometry considered for the calculations below is the same of the previous section and is depicted in Fig. 3.4. The interface between the metal ($x < 0$) and the gain material ($x > 0$) is located at $x = 0$, while the SPP beam is assumed to propagate in the z direction and to diffract in the y direction. We start our analysis from the time independent Maxwell equations for the harmonic fields

$$\vec{\mathcal{E}}(x, y, z, t) = \vec{E}(x, y, z)e^{-i\omega t}, \tag{3.49}$$

$$\vec{\mathcal{H}}(x, y, z, t) = \vec{H}(x, y, z)e^{-i\omega t}. \tag{3.50}$$

Combining the curl equations for the electric $\vec{E}$ and magnetic $\vec{H}$ fields, one reaches a system of partial differential equations for the electric field components E_x, E_y, E_z

$$\partial^2_{xy}E_y - \partial^2_{yy}E_x - \partial^2_{zz}E_x + \partial^2_{zx}E_z = \epsilon E_x, \tag{3.51}$$

$$\partial^2_{yz}E_z - \partial^2_{zz}E_y - \partial^2_{xx}E_y + \partial^2_{xy}E_x = \epsilon E_y, \tag{3.52}$$

$$\partial^2_{xz}E_x - \partial^2_{xx}E_z - \partial^2_{yy}E_z + \partial^2_{zy}E_y = \epsilon E_z. \tag{3.53}$$

The partial derivatives $\partial_x, \partial_y, \partial_z$ are taken with respect to the dimensionless spatial coordinates x, y, z normalized to $k^{-1} = \lambda/2\pi$, where λ is the vacuum wavelength. The permittivity on the dielectric side of the interface ($x > 0$) is

$$\epsilon = \epsilon_d + \chi(|E_x|^2 + |E_y|^2 + |E_z|^2), \tag{3.54}$$

where $\epsilon_d = \epsilon'_d + i\epsilon''_d$ is the linear dielectric constant and $\chi = \chi' + i\chi''$ is the nonlinear susceptibility. As done in the previous section, the amplification in the gain material is modelled by the two-level susceptibility in the limit where the light intensity is much smaller than the transition saturation intensity I_S [Boyd, 2003]:

$$\epsilon_d = \epsilon_b - \alpha\frac{i - \delta}{1 + \delta^2}, \tag{3.55}$$

$$\chi = \alpha\frac{i - \delta}{(1 + \delta^2)^2}. \tag{3.56}$$

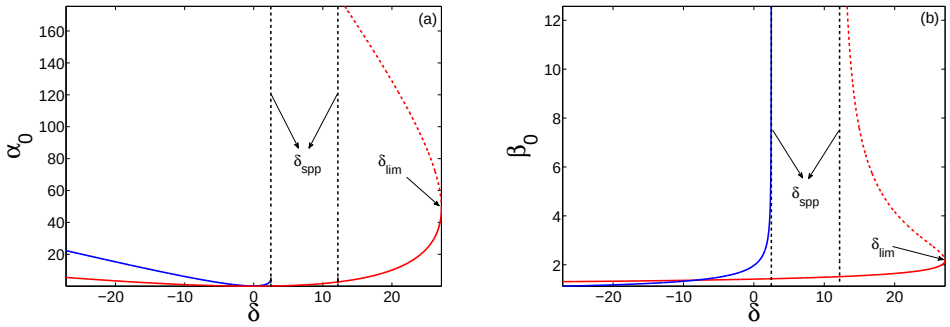

Figure 3.7: (a) Threshold gain α_0 as a function of the detuning δ for two different atomic resonances: $\lambda_{ba} = 400nm$ (blue line) and $\lambda_{ba} = 700nm$ (red line). (b) β_0 vs δ, the parameters are the same of (a). The full (dashed) line corresponds to the minus (plus) in Eq. (3.59).

ϵ_b is the dielectric constant of the background material hosting the two-level active inclusions, $\delta = (\omega - \omega_{ba})T_2$ is the dimensionless detuning from the atomic resonance $\omega_{ba} = \omega_b - \omega_a = 2\pi c/\lambda_{ba}$ normalized to the dephasing rate T_2^{-1} and α is the dimensionless gain at the line centre. The electric field is normalized to the saturation field $E_S = \sqrt{I_s}$, which plays the mere role of a scaling factor for the electric field in the calculations developed below.

On the other hand, the permittivity on the metal side ($x < 0$) is

$$\epsilon = \epsilon_m = \epsilon'_m + i\epsilon''_m. \tag{3.57}$$

The propagation constant β of the linear SPP is

$$\beta = \sqrt{\frac{\epsilon_d \epsilon_m}{\epsilon_d + \epsilon_m}}. \tag{3.58}$$

In the previous section, we derived the gain threshold condition $\alpha = \alpha_0$

$$\alpha_0(\omega) = \frac{1}{2\epsilon''_m}\left(|\epsilon_m|^2 - 2\epsilon''_m\epsilon_b\delta\right) \pm \frac{1}{2\epsilon''_m}\sqrt{|\epsilon_m|^4 - 4\epsilon''_m\epsilon_b\left(\epsilon''_m\epsilon_b + \delta\,|\epsilon_m|^2\right)}, \tag{3.59}$$

where β becomes real [Nezhad et al., 2004]:

$$\beta(\alpha_0) = \beta_0, \tag{3.60}$$

$$Im\beta_0 = \beta''_0 = 0. \tag{3.61}$$

The linear and nonlinear susceptibilities of the gain material for $\alpha = \alpha_0$ are $\epsilon_d(\alpha_0) = \epsilon_{d0}$ and $\chi(\alpha_0) = \chi_0$. The stationary propagation of SPPs is not enabled if the detuning δ is larger than the critical value $\delta = \delta_{lim}$, which is determined by the condition that the square root in Eq. (3.59) becomes zero. At this point, the two solutions for α_0 are degenerate, see Fig. 3.7. δ_{lim} does not coincide with the plasmon resonance frequency δ_{spp}, which corresponds to the zero of the denominator of β_0. The upper branch of the α_0 solution, corresponding to the dashed lines in Fig. 3.7, is characterised by an extremely high gain coefficient ($\alpha_0 \approx 100$) corresponding to a refractive index of the order $n \approx 10$. Such gain values are not very practical and in our subsequent numerical examples we focus our attention on the relatively small δ range, corresponding to the lower branch of α_0 represented by the solution with minus sign in front of the square root in Eq. (3.59). Note that $\epsilon_m(\omega) = \epsilon_m(\omega_{ba} + \delta/T_2)$ is frequency dependent. Hence, the threshold gain α_0 is a function of both δ and ω_{ba}.

3.3.1 Multiple-scale expansion of Maxwell equations

In the multiple scale expansion developed below, we assume small deviations of the gain coefficient from the stationary threshold value α_0:

$$\alpha - \alpha_0 = \alpha_0 g, \tag{3.62}$$

where $|g| \ll 1$. The ansatz for the field components is

$$E_{x,j} = \left[A^{(0)}_{x,j} + A^{(1)}_{x,j} + o(|g|^{5/2})\right] e^{i\beta_0 z}, \tag{3.63}$$

$$E_{y,j} = \left[A^{(0)}_{y,j} + o(|g|^{2})\right] e^{i\beta_0 z}, \tag{3.64}$$

$$E_{z,j} = \left[A^{(0)}_{z,j} + A^{(1)}_{z,j} + o(|g|^{5/2})\right] e^{i\beta_0 z}, \tag{3.65}$$

where $j = d, m$ labels dielectric and magnetic regions respectively and

$$A^{(0)}_{x,j}, A^{(0)}_{z,j} \sim |g|^{1/2}, \tag{3.66}$$

$$A^{(0)}_{y,j} \sim |g|, \tag{3.67}$$

$$A^{(1)}_{x,j}, A^{(1)}_{z,j} \sim |g|^{3/2}, \tag{3.68}$$

are functions of x, y, z. Their dependence on y, z is assumed slow relative to the fast oscillations of $e^{i\beta_0 z}$:

$$\partial_y \sim |g|^{1/2}, \tag{3.69}$$

$$\partial_z \sim |g|. \tag{3.70}$$

The order of of the x, z field components ($A^{(0)}_{x,j}, A^{(0)}_{z,j} \sim |g|^{1/2}$) is set in such a way that both the linear ($\alpha - \alpha_0$) and nonlinear ($\chi|\vec{E}|^2$) correction terms are of the same order ($|g|^{3/2}$).

The y field component $A^{(0)}_{y,j} \sim |g|$ is non-null when the field has finite size along y, but it is assumed to stay relatively small with respect to $A^{(0)}_{x,j}, A^{(0)}_{z,j}$. The dielectric susceptibility is expanded into the g-series

$$\epsilon_d = \epsilon_{d0} + \epsilon_{d1}, \tag{3.71}$$

where $\epsilon_{d1} = g\alpha_0 \partial_\alpha \epsilon_d$. Since nonlinearity is small, the dependence of the nonlinear coefficient χ on the linear gain α is a higher order term and in the calculations below χ is taken exactly at the gain threshold $\chi_0 = \chi(\alpha_0)$.

At $|g|^{1/2}$ order, substituting Eqs. (3.63) into Eqs. (3.51-3.53) one finds

$$\hat{\mathcal{M}}_j \begin{bmatrix} A^{(0)}_{x,j} \\ A^{(0)}_{z,j} \end{bmatrix} = 0, \tag{3.72}$$

where $j = d, m$ labels dielectric and metal regions, respectively. The linear $\hat{\mathcal{M}}_j$ operator is given by

$$\hat{\mathcal{M}}_j = \begin{pmatrix} q_j^2 & i\beta_0 \partial_x \\ 0 & \partial_{xx}^2 - q_j^2 \end{pmatrix}, \tag{3.73}$$

where

$$q_d^2 = \beta_0^2 - \epsilon_{d0}, \tag{3.74}$$

$$q_m^2 = \beta_0^2 - \epsilon_m. \tag{3.75}$$

Eq. (3.72) is a linear homogeneous system of differential equations for the SPP modes, where the nonlinear and transverse (y-dependent) effects are disregarded.

The SPP solution of Eqs. (3.72) is

$$A^{(0)}_{x,d} = \frac{i\beta_0}{q_d} A(y,z) e^{-q_d x}, \tag{3.76}$$

$$A^{(0)}_{z,d} = A(y,z) e^{-q_d x}, \tag{3.77}$$

$$A^{(0)}_{x,m} = -\frac{i\beta_0}{q_m} A(y,z) e^{q_m x}, \tag{3.78}$$

$$A^{(0)}_{z,m} = A(y,z) e^{q_m x}, \tag{3.79}$$

where $A(y,z)$ is the arbitrary linear SPP amplitude of the z field component at $x = 0$: $A(y,z) = A^{(0)}_{z,m}(0) = A^{(0)}_{z,d}(0)$. Eqs. (3.76-3.79) satisfy the continuity of the normal component of the displacement and of the tangential components of the electric field

$$\epsilon_{d0} A^{(0)}_{x,d}(0) = \epsilon_m A^{(0)}_{x,m}(0), \tag{3.80}$$

$$A^{(0)}_{z,m}(0) = A^{(0)}_{z,d}(0). \tag{3.81}$$

The BCs above imply $\epsilon_{d0} q_m = -\epsilon_m q_d$, giving (after some algebra) the expression for the linear propagation constant

$$\beta_0 = \sqrt{\frac{\epsilon_d \epsilon_m}{\epsilon_d + \epsilon_m}}. \tag{3.82}$$

At $|g|^1$ order, one finds the linear equations for the y component of the electric field

$$q_j^2 A^{(0)}_{y,j} - \partial^2_{xx} A^{(0)}_{y,j} = 0, \tag{3.83}$$

which are readily solved

$$A^{(0)}_{y,d} = B(y,z) e^{-q_d x} \tag{3.84}$$

$$A^{(0)}_{y,m} = B(y,z) e^{q_m x}. \tag{3.85}$$

To determine the unknown functions $A(y,z)$ ($|A| \sim |g|^{1/2}$) and $B(y,z)$ ($|B| \sim |g|$) one needs to proceed to the higher orders of the perturbation expansion.

At $|g|^{3/2}$ order, the Maxwell equations provide an inhomogeneous system of differential equations for the field corrections to the linear SPP solution. The correction equations on the metal side are

$$\hat{M}_m \begin{bmatrix} A^{(1)}_{x,m} \\ A^{(1)}_{z,m} \end{bmatrix} = \begin{bmatrix} K_x \\ K_z \end{bmatrix} e^{q_m x}, \tag{3.86}$$

where

$$K_x = \frac{\beta_0^2 + \epsilon_m}{q_m}\partial_z A - q_m \partial_y B - \frac{i\beta_0}{q_m}\partial_{yy}^2 A, \tag{3.87}$$

$$K_z = -2i\beta_0 \partial_z A - \partial_{yy}^2 A. \tag{3.88}$$

The general solution of Eqs. (3.86) is the sum of a particular solution of the inhomogeneous problem and the solution of the homogeneous system (achieved by setting $K_{x,z} = 0$)

$$A_{x,m}^{(1)} = \frac{1}{2q_m^3}\left[-i\beta_0 K_z(1 + q_m x) + 2q_m K_x\right] e^{q_m x} - C\frac{i\beta_0}{q_m}e^{q_m x}, \tag{3.89}$$

$$A_{z,m}^{(1)} = \frac{K_z}{2q_m} x e^{q_m x} + C e^{q_m x}, \tag{3.90}$$

where C is a constant that can be determined from the boundary conditions. The righthand side of the $|g|^{3/2}$ order correction equations in the dielectric include the nonlinear terms N_x, N_z and are more cumbersome

$$\hat{M}_d \begin{bmatrix} A_{x,d}^{(1)} \\ A_{z,d}^{(1)} \end{bmatrix} = \begin{bmatrix} L_x \\ L_z \end{bmatrix} e^{-q_d x} + \begin{bmatrix} N_x \\ N_z \end{bmatrix} e^{-(2q_d' + q_d)x}, \tag{3.91}$$

where $q_d' = \mathrm{Re} q_d$ and

$$L_x = -\frac{1}{q_d}(\beta_0^2 + \epsilon_{d0})\partial_z A + \frac{i\beta_0}{q_d}\epsilon_{d1} A + q_d \partial_y B + \frac{i\beta_0}{q_d}\partial_{yy}^2 A, \tag{3.92}$$

$$L_z = -2i\beta_0 \partial_z A - \epsilon_{d1} A - \partial_{yy}^2 A, \tag{3.93}$$

$$N_x = \frac{i\beta_0}{q_d}\left(\frac{\beta_0^2}{|q_d|^2} + 1\right)\chi_0 |A|^2 A, \tag{3.94}$$

$$N_z = -\frac{(\epsilon_{d0} q_d + 2\beta_0^2 q_d')\left(|q_d|^2 + \beta_0^2\right)}{\epsilon_{d0} q_d |q_d|^2}\chi_0 |A|^2 A. \tag{3.95}$$

The solutions of Eqs. (3.91) are

$$A_{x,d}^{(1)} = \frac{1}{2q_d^3}\left[i\beta_0 L_z(1 - q_d x) + 2q_d L_x\right] e^{-q_d x} + \\ + \frac{1}{q_d^2}\left[N_x + \frac{i\beta_0}{4q_d'}\frac{2q_d' + q_d}{q_d' + q_d} N_z\right] e^{-(2q_d' + q_d)x}, \tag{3.96}$$

$$A_{z,d}^{(1)} = -\frac{1}{2q_d} L_z x e^{-q_d x} + \frac{1}{4q_d'(q_d' + q_d)} N_z e^{-(2q_d' + q_d)x}. \tag{3.97}$$

Without any loss of generality, the solution of the homogeneous system has not been included in Eqs. (3.96,3.97). The BCs accounting for the linear (ϵ_{d1}) and nonlinear ($\chi_0|\vec{E}|^2$) corrections at $|g|^{3/2}$ order require that

$$\begin{aligned} A^{(1)}_{z,m}(0) &= A^{(1)}_{z,d}(0), && (3.98)\\ \epsilon_m A^{(1)}_{x,m}(0) &= \epsilon_{d0} A^{(1)}_{x,d}(0) + \epsilon_{d1} A^{(0)}_{x,d}(0) + \\ &\quad +\chi_0(|A^{(0)}_{x,d}(0)|^2 + |A^{(0)}_{z,d}(0)|^2) A^{(0)}_{x,d}(0), && (3.99) \end{aligned}$$

where $A^{(0)}_{x,d}, A^{(0)}_{z,d}, A^{(0)}_{x,m}, A^{(0)}_{z,m}$ are given by Eqs. (3.76-3.79) and $A^{(1)}_{x,m}, A^{(1)}_{z,m}, A^{(1)}_{x,d}, A^{(1)}_{z,d}$ are given by Eqs. (3.89,3.90,3.96,3.97). By solving Eqs. (3.98,3.99) one finds that the constant C is given by

$$C = \frac{1}{4(q'_d + q_d)q'_d} N_z, \tag{3.100}$$

and that the amplitude A satisfies the complex Ginzburg-Landau equation

$$2i\beta_0 \partial_z A + \partial^2_{yy} A + fA + \Upsilon |A|^2 A = 0, \tag{3.101}$$

where $\Upsilon = h\chi_0$ and

$$f = g \frac{\alpha_0 \epsilon_m^2 \partial_\alpha \epsilon_d}{(\epsilon_{d0} + \epsilon_m)^2}, \tag{3.102}$$

$$h = \frac{\beta_0^4}{\epsilon_{d0}^2} \frac{q_d(|q_d|^2 + \beta_0^2)}{(q'_d + q_d)|q_d|^2}. \tag{3.103}$$

All the terms containing $B(y,z)$ cancel out. The particular value of the amplitude $B(y,z)$ can be determined by considering the magnetic field

$$\vec{H} = \frac{1}{ic\mu_0} \nabla \times \vec{E}, \tag{3.104}$$

which was completely ignored up to now. At $|g|^{1/2}$ order, the magnetic field is polarised in the y direction: $\vec{H}_j = H^{(0)}_{y,j} \hat{y}$,

$$H^{(0)}_{y,j} = \frac{1}{ic\mu_0}(i\beta_0 A^{(0)}_{x,j} - \partial_x A^{(0)}_{z,j}) e^{i\beta_0 z}. \tag{3.105}$$

At this order, the BC for the continuity of $H^{(0)}_{y,j}$ at the interface $x = 0$ is ensured by the BCs for $A^{(0)}_{x,j}, A^{(0)}_{z,j}$. At the $|g|^1$ order, the magnetic field acquires a z-component and lies in the $y - z$ plane: $\vec{H}_j = H^{(0)}_{y,j} \hat{y} + H^{(1)}_{z,j} \hat{z}$,

$$H^{(1)}_{z,j} = \frac{1}{ic\mu_0}(\partial_x A^{(0)}_{y,j} - \partial_y A^{(0)}_{z,j}) e^{i\beta_0 z}. \tag{3.106}$$

At this order, the BC for the continuity of $H_{y,j}^{(1)}$ at the interface $x = 0$ fixes the amplitude $B(y, z)$ to

$$B(y, z) = \frac{1}{i\beta_0}\partial_y A(y, z). \tag{3.107}$$

It is worthwhile noting that, in such a derivation of the Ginzburg-Landau (GL) equation, the nonlinear boundary conditions are satisfied at the $|g|^{3/2}$ order.

$f' = \mathrm{Re}f$ is the linear phase shift term due to the gain deviation from the threshold and $f'' = \mathrm{Im}f$ is the SPP effective amplification ($\alpha > \alpha_0$) or damping ($\alpha < \alpha_0$) coefficient. The nonlinear term is complex, providing the nonlinear phase shift $\Upsilon'|A|^2$ ($\Upsilon' = \mathrm{Re}\Upsilon$) and the nonlinear loss $\Upsilon''|A|^2$ ($\Upsilon'' = \mathrm{Im}\Upsilon$).

The complex nature of the nonlinearity enhancement h introduces some unphysical effects. The effective complex nonlinear coefficient Υ is characterised by the real part $\Upsilon' = h'\chi_0' - h''\chi_0''$, which is responsible for self-focusing ($\Upsilon' > 0$) or self-defocusing ($\Upsilon' < 0$), and by the imaginary part $\Upsilon'' = h'\chi_0'' + h''\chi_0'$, which describes the nonlinear absorption $\Upsilon'' > 0$. However, in the particular case where $h''\chi_0' - h'\chi_0'' < 0$ the GL model predicts a nonlinear gain.

In this case, the perturbative expansion of the two-level susceptibility up to the second order

$$\chi \approx \epsilon_d + \chi_0|\vec{\mathcal{E}}|^2, \tag{3.108}$$

it is not sufficient to describe adequately the nonlinear saturation of gain, and the higher order terms (like $\chi \approx \Gamma|\vec{\mathcal{E}}|^4$) need to be included:

$$\chi \approx \epsilon_d + \chi_0|\vec{\mathcal{E}}|^2 + \Gamma|\vec{\mathcal{E}}|^4. \tag{3.109}$$

In the numerical computations below we consider the case $h''\chi_0' - h'\chi_0'' > 0$, where the perturbative expansion adopted is physically meaningful.

3.3.2 Comparison with the averaging approach

The nonlinearity enhancement factor h is a complex number that depends on the geometric and on the optical properties of the plasmonic structure. Such a parameter accounts for the modified optical nonlinear response experienced by the propagating SPPs with respect to plane waves in the nonlinear dielectric bulk. These findings are in contrast with the ones provided by the averaging

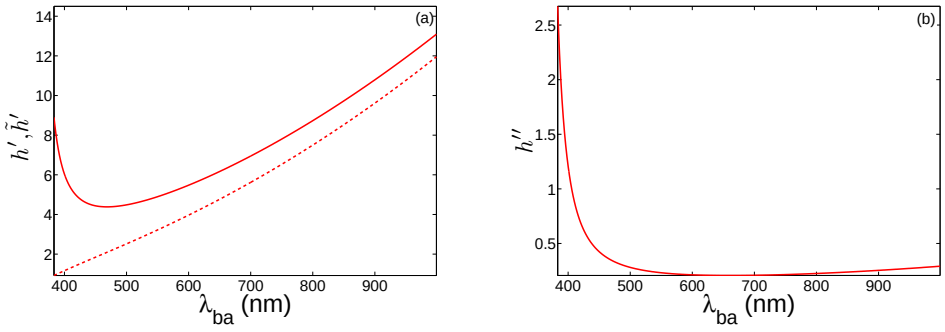

Figure 3.8: Nonlinearity enhancement coefficients: (a) h' (solid line) and $\tilde{h}'$ (dashed line) calculated using two different approaches vs λ_{ba}. (b) h'' vs λ_{ba}. Varying δ inside the transition linewidth leads only to small difference in h. The graphs shown correspond to $\delta = -0.5$. The short wavelength boundary of the both plots corresponds to the point where β_0 becomes imaginary.

approach [Agrawal, 2001b; Davoyan et al., 2009b; Feigenbaum and Orenstein, 2007], where the nonlinearity enhancement factor is purely real. The averaging approach gives a different expression for the effective nonlinearity experienced by SPPs. Following this method, the geometric nonlinearity enhancement $\tilde{h}$ is

$$\tilde{h} = \frac{\int_0^{+\infty} dx \left|\vec{F}\right|^4}{\int_{-\infty}^{+\infty} dx \left|\vec{F}\right|^2}. \tag{3.110}$$

In the above integral expression, the vector $\vec{F}$ is the $|g|^{1/2}$ plasmonic field:

$$\vec{F} = \begin{pmatrix} A_{x,d}^{(0)} \\ A_{z,d}^{(0)} \end{pmatrix} \theta(x) + \begin{pmatrix} A_{x,m}^{(0)} \\ A_{z,m}^{(0)} \end{pmatrix} \theta(-x). \tag{3.111}$$

In chapter 4, we derive an integral expression for the nonlinear parameter Υ, explaining with more detail the role played by the surface terms in the boundary conditions. In Fig. 3.8, h and $\tilde{h}$ are plotted as functions of the resonance wavelength λ_{ba} for the fixed detuning $\delta = -0.5$. The two approaches yield qualitatively similar results for the enhancement coefficients $h, \tilde{h}$ in the long wavelength limit, where h'' is negligible and h is almost real. However, for shorter wavelengths, our approach accounting for the nonlinear contributions in the BCs predicts a

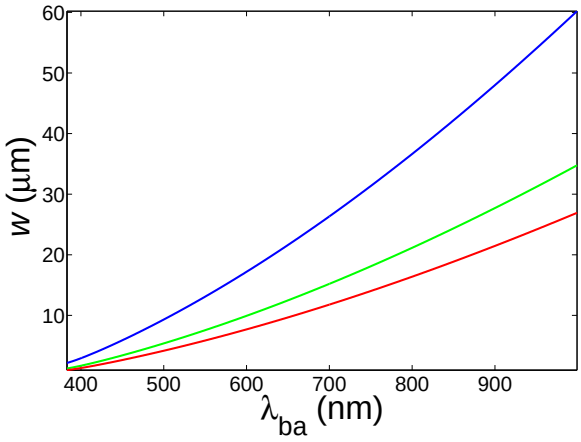

Figure 3.9: The characteristic filament size w (scaled back to physical units) as a function of λ_{ba} for $\delta = -0.5$. The gain parameters $g = 0.1, 0.3, 0.5$ correspond to the blue, green and red curves, respectively.

considerably increased nonlinearity enhancement h with respect to the averaging approach $\tilde{h}$. $h', \tilde{h}$ increase with the resonance wavelength λ_{ba} since the metal becomes highly reflective: $\epsilon_m \to -\infty$ as $\lambda_{ba} \to +\infty$ (electrostatic limit). Thus, the SPP intensity mainly resides in the nonlinear dielectric and the effective nonlinearity is enhanced (since the optical response of the metal is assumed linear in our model). On the other hand, for short wavelengths, the SPP profile gets squeezed at the interface and the nonlinear contribution in the BCs becomes relevant. In this limit, the nonlinear surface contribution provides an increased difference between h' and $\tilde{h}$.

3.3.3 Filamentation of SPPs

The plane wave solution of Eq. (3.101) is

$$A_0 = \rho e^{i\eta z}, \tag{3.112}$$

where

$$\eta = \frac{1}{2\beta_0}(f' - \rho^2 \Upsilon'), \tag{3.113}$$

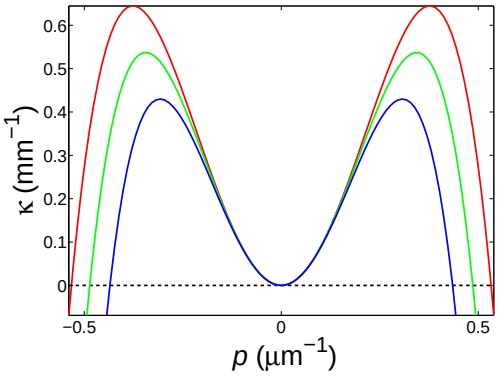

Figure 3.10: Instability growth rate κ (scaled back to physical units) as a function of the transverse momentum (p). The parameters used to plot the figure are $\lambda_{ba} = 594\ nm$, $\delta = -0.3$, $\alpha_0 = 0.0063$. Gain parameters $g = 0.4, 0.5, 0.6$ correspond to the red, green and blue curves, respectively.

$$\rho^2 = -\frac{f''}{\Upsilon''}. \tag{3.114}$$

The solution above exists only if the condition $\rho^2 > 0$ holds. Such a condition is satisfied for $-f'', \Upsilon'' > 0$ and implies that the linear gain provided by the amplifying dielectric overcomes the threshold ($\alpha > \alpha_0$), being saturated by the absorptive nonlinearity $\Upsilon''|A_0|^2$. The amplitude ρ diverges if the nonlinear absorption is null. In this case, the quintic nonlinearity needs to be taken into account in order to achieve stationary nonlinear plane waves. This case will not be discussed in this dissertation.

As discussed in section 1.3.1, plane waves constitute a family of solutions for the Nonlinear Schrödinger Equation (NLSE) and are parametrized either by the field amplitude or by the propagation constant. Conversely, in the dissipative case considered in this section, the plane wave solution of the Ginzburg-Landau equation is unique. The stationary plane waves propagating without distortion (amplification or damping) exist only for the particular amplitude $|A| = \rho$, where the amplification deviation from the stationary threshold is exactly compensated by the nonlinear absorption $\Upsilon''|A|^2$. Hence, the nonlinear plane waves can be unstable with respect to a specific perturbation pattern forming filamentation

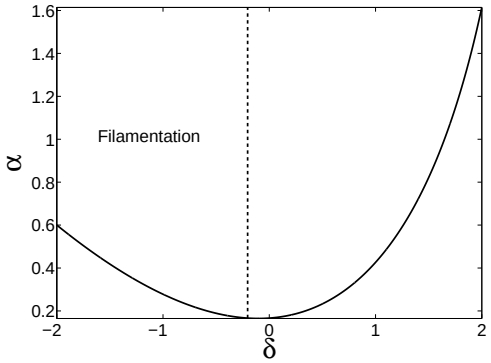

Figure 3.11: Lossless SPPs exist above the full line corresponding to $\alpha = \alpha_0$. SPPs are unstable on the left from the dashed vertical line, which corresponds to $\Upsilon' = 0$. The resonance wavelength was set to $\lambda_{ba} = 400\ nm$.

instability [Aranson and Kramer, 2002]. In order to study the stability of plane waves expressed by Eq. 3.112, one needs to perturb the solution $A = A_0$ with small amplitude waves modulated with transverse momentum p:

$$A = (1 + q_+ e^{\kappa z + ipy} + q_-^* e^{\kappa^* z - ipy}) A_0. \tag{3.115}$$

Inserting Eq.(3.115) into Eq.(3.101) and linearizing the resulting equations for small amplitude corrections $|q_\pm|$, one finds the following expression for the eigenvalue κ

$$2\beta_0 \kappa = f'' + \sqrt{(f'')^2 - p^2(p^2 - 2p_{max}^2)}. \tag{3.116}$$

The onset condition enabling filamentation instability is provided by $\kappa' > 0$. κ' is a function of the transverse momentum p and has a typical two peak dependence, see Fig. 3.10. The maximum instability growth rate is achieved for $p = \pm p_{max}$, where

$$p_{max}^2 = \rho \Upsilon'. \tag{3.117}$$

From the maximum transverse momentum (p_{max}) it is possible to evaluate the typical filament length

$$w \simeq \lambda / p_{max}. \tag{3.118}$$

The dependence of the filament width (w) on the resonance wavelength (λ_{ba}) is depicted in Fig. 3.9. The instability domain in the (δ, α)-plane is represented in

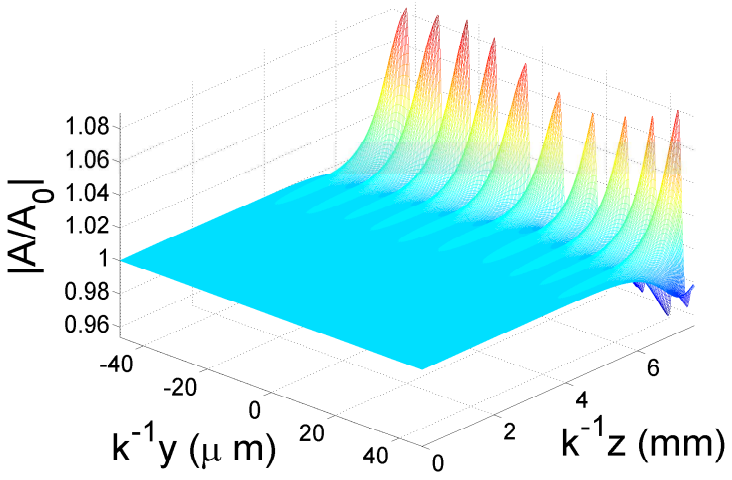

Figure 3.12: Filamentation of nonlinear SPPs: $\lambda_{ba} = 594nm$, $\delta = -0.3$, $\alpha = 0.0183$, $\alpha_0 = 0.0063$.

Fig. 3.11. Filamentation occurs only for self-focusing nonlinearity ($\Upsilon' > 0$). In the long wavelength limit, where the nonlinearity enhancement factor is almost real ($|h''| << |h'|$), the instability onset $\Upsilon' = 0$ is achieved at the line centre $\delta = 0$. For smaller wavelengths, the imaginary part of the nonlinearity enhancement factor $h'' \neq 0$ implies a shift of the instability onset from $\delta = 0$, as depicted in Fig. 3.11. In Fig. 3.12, the filamentation of plane waves in periodic patterns is depicted for $\lambda_{ba} = 594nm$, $\delta = -0.3$, $\alpha = 0.0183$, $\alpha_0 = 0.0063$. The typical lengthscale for filament formation is $L_F \approx 1mm$. To model the propagation of nonlinear SPP waves we used the split-step beam propagation method, which is described in appendix C.

3.3.4 Bright and dark plasmon-solitons

Analogously to the Nonlinear Schrödinger Equation (NLSE), introduced in section 1.3, also the Ginzburg-Landau (GL) equation admits solitary wave solutions [Akhmediev and Ankiewicz, 1997; Aranson and Kramer, 2002]. The existence of such solutions is suggested by the bistability of the trivial zero solution $A = 0$

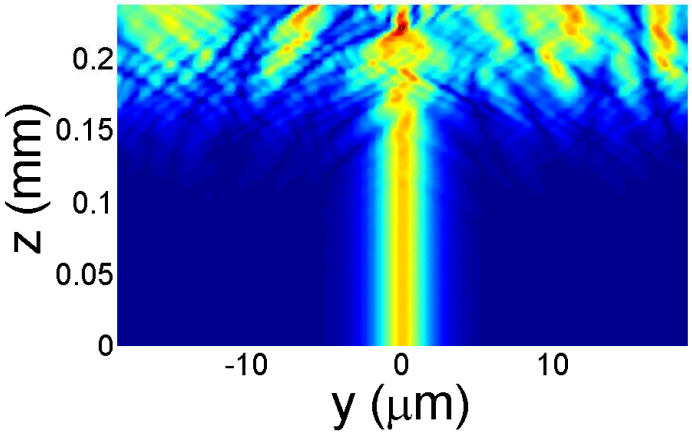

Figure 3.13: Propagation of a bright localised solution and instability of its background: $\lambda_a = 594\ nm$, $\delta = -0.3$, $\alpha = 0.0183$, $\alpha_0 = 0.0063$.

and the plane wave solution $A_0 = \rho e^{i\eta z}$.

There is a fundamental difference between solitary waves in conservative and dissipative systems. Indeed, the existence of the bright Pereira-Stenflo [Pereira and Stenflo, 1977] and of the dark Nozaki-Bekki [Nozaki and Bekki, 1984] solitons implies a dynamical transfer of energy. In this sense, the nonlinearity vs diffraction balance is completed with the nonlinear absorption vs gain equilibrium in dissipative systems described by the GL equation.

Both bright and dark localised solutions exist under the same conditions:

$$f'' < 0, \tag{3.119}$$

$$\Upsilon'' > 0, \tag{3.120}$$

$$\Upsilon' \neq 0. \tag{3.121}$$

The expression for the bright plasmon-soliton is

$$A(y,z) = \rho\sqrt{\frac{3}{2}}\,[sech(Ky)]^{1+ia}\,exp(iuz), \tag{3.122}$$

while for the the dark plasmon-soliton:

$$A(y,z) = \rho\frac{tanh(sy)}{[cosh(sy)]^{ib}}exp(ivz), \tag{3.123}$$

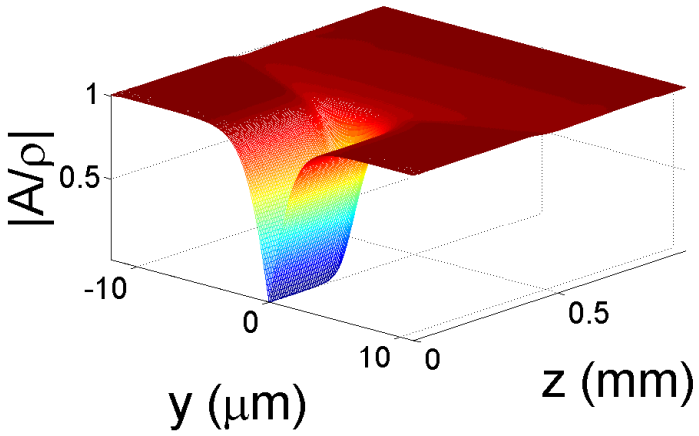

Figure 3.14: Destabilisation of the dark soliton due to the core instability: $\lambda_a = 594\ nm$, $\delta = -0.3$, $\alpha = 0.0183$, $\alpha_0 = 0.0063$.

where

$$a = -\frac{3\Upsilon'}{2\Upsilon''} + \sqrt{2 + \left(\frac{3\Upsilon'}{2\Upsilon''}\right)^2}, \tag{3.124}$$

$$b = -\frac{3\Upsilon'}{2\Upsilon''} - \sqrt{2 + \left(\frac{3\Upsilon'}{2\Upsilon''}\right)^2}, \tag{3.125}$$

$$K^2 = -\frac{1}{2a} f'', \tag{3.126}$$

$$s^2 = \frac{1}{3b} f'', \tag{3.127}$$

$$u = \frac{1}{2\beta_0} f' + \frac{a^2 - 1}{4\beta_0 a} f'', \tag{3.128}$$

$$v = \frac{1}{2\beta_0} f' - \frac{1}{3b\beta_0} f''. \tag{3.129}$$

In the limit $|y| \to \infty$ the dark soliton tends to the plane wave solution, expressed by Eq. (3.112). The bright soliton is unstable because the zero background $A = 0$ is unstable above the threshold. This instability is relatively slow and bright SPP solitons can propagate for distances of approximately $\approx 100\mu m$, as depicted in Fig. 3.13. On the other hand, the dark soliton is unstable with respect to the core instability and the filamentation of the background [Chate

and Manneville, 1992], as shown in Fig. 3.14. Such instabilities prevent plasmon-solitons to propagate over long distances, disabling their striking application as miniaturised optical channels. Nevertheless, it is possible to stabilise SPP solitons by using the coupling with a purely passive interface [Malomed and Winful, 1996]. The stabilisation of plasmon-solitons is explained in detail in chapter 6.

3.4 Concluding remarks

The tight electromagnetic field enhancement provided by SPPs can be used in nonlinear active devices, which have been reviewed in the beginning of this chapter. We have described the effect of Kerr nonlinearity on the optical propagation of SPPs along a single interface, reproducing the results reported in Ref. [Mihalache et al., 1987]. The nonlinear modes in such a configuration can be determined by a semi-analytical approach if the metal loss is neglected. Such an approach relies on the use of the first integral of the nonlinear dynamical system for TM modes [Berkhoer and Zakharov, 1970; Boardman et al., 1987; Ciattoni et al., 2005]. However, if the metal loss is not neglected, such an approach is not applicable since the first integral does not exist.

In turn, we have developed a novel perturbative theory accounting for the metal loss, the amplification and the nonlinearity of a gain material embedded in the plasmonic structure. Such an analytical approach allowed us to derive the nonlinear dispersion law for the homogeneous stationary SPPs and the Ginzburg-Landau (GL) propagation equation for the SPP beams with a finite width on the transverse direction. The study of the GL propagation equation predicted the filamentation of the homogeneous nonlinear waves and the formation of bright and dark plasmon-solitons. However, the stability analysis revealed the presence of substantial instabilities preventing the solitons to propagate over long distances. The original results reported in this chapter have been published in Refs. [Marini et al., 2009; Marini and Skryabin, 2010].

Chapter 4

Nonlinear TM waves in 1D subwavelength structures

The delivery of electromagnetic energy at the subwavelength scale has been achieved both by using silicon on insulator (SOI) slot waveguides [Almeida et al., 2004a,b], which have been briefly introduced in section 1.2.4, and surface plasmon polaritons (SPPs) [Ozbay, 2006]. Promising practical applications of nonlinear SOI slot waveguides include frequency conversion and ultrafast all-optical signal processing [DiFalco et al., 2008; Koos et al., 2009]. Other more fundamental applications of metal and dielectric slot waveguides involve self-focusing and optical solitons [Davoyan et al., 2008, 2009b; Feigenbaum and Orenstein, 2007; Gorbach and Skryabin, 2009]. Optical fibres with subwavelength core diameter [Tong et al., 2003; Wiederhecker et al., 2007] and plasmonic cylindrical waveguides [Schmidt and Russell, 2008; Schroter and Dereux, 2001; Takahara et al., 1997] have also been developed to guide electromagnetic energy on the subwavelength scale and are described in detail in chapter 7.

In a recent work, Afshar et al. derived the propagation equation for subwavelength optical fibres by using the *Lorentz Reciprocity Theorem* (LRT) [Afshar and Monro, 2009; Afshar et al., 2009]. They demonstrated that the nonlinear parameter achieved by such a procedure fits the experimental measurements in the subwavelength regime with an improved accuracy with respect to the *averaging approach*. The traditional averaging approach dates back to the scalar wave

equation [Agrawal, 2001b] and it has been extended to the vectorial case recently [Daniel and Agrawal, 2010].

The tight confinement of light in one dimensional photonic and plasmonic structures intrinsically implies non-paraxiality, i.e. that TM modes have significant non-zero longitudinal component of the electric field, as discussed in section 1.2.3. Existing theories deriving the nonlinear parameter of photonic and plasmonic waveguides use either the averaging approach [Davoyan et al., 2009b; Feigenbaum and Orenstein, 2007] or the reciprocity theorem [Afshar and Monro, 2009; Koos et al., 2007; Osgood et al., 2009].

In the previous chapter, we have derived from the first principles the complex Ginzburg-Landau (GL) equation by a multiple scale expansion of Maxwell Equations. The GL propagation equation is obtained by calculating the field corrections and by imposing boundary conditions accounting for nonlinearity, dielectric gain and metal loss. This derivation is rigorous but does not provide an insightful understanding of the underpinning physical mechanisms inducing the modified nonlinear response. In addition, the calculations are cumbersome and strongly depend on the photonic structure under examination. Similarly, also the reciprocity theorem approach does not shed much light on the physical origin of the enhanced nonlinear response in subwavelength photonic structures [Afshar et al., 2009; Koos et al., 2009].

In this chapter we develop a more transparent asymptotic theory, demonstrating that the enhancement of the nonlinear response of TM-modes in planar subwavelength waveguides ensues from *surface effects*. The surface enhancement factor depends on the product of the transverse field component discontinuity at the boundary of the waveguide with the surface value of the longitudinal field component and can be summed up over the boundaries of the photonic structure. In the multiple scale expansion presented below, the propagation equation is achieved without calculating explicitly the field corrections, but is derived as a scalar product equation that represents the solvability condition in the respective order. For this reason, such a theory is more flexible and suitable to obtain the propagation equation in complex one-dimensional geometries.

We emphasise that, conversely to the previous chapter where the perturbative theory was developed around the stationary threshold (where the amplification

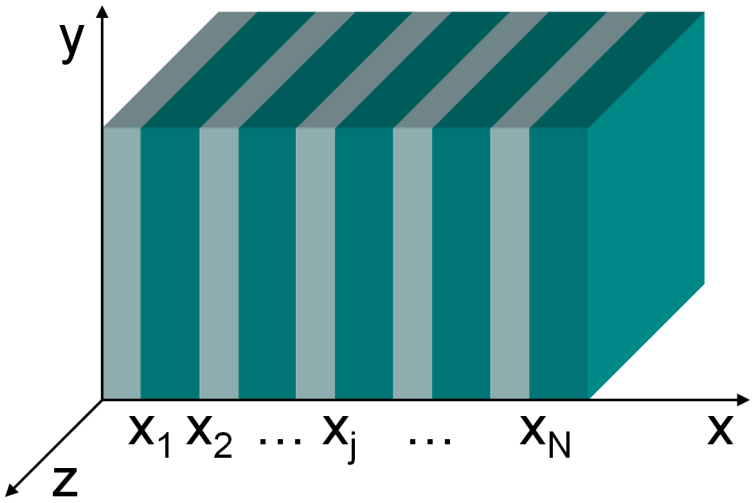

Figure 4.1: Schematic representation of a planar subwavelength photonic structure.

perfectly compensates for the metal loss), here the imaginary part of the dielectric susceptibility profile (accounting for gain/loss) is considered as a small perturbation. A generalised version of this one-dimensional (1D) theory to the two-dimensional (2D) case of subwavelength cylindrical waveguides is presented in chapter 7.

4.1 Multiple scale expansion of Maxwell equations

In what follows, we consider a generic planar subwavelength photonic structure, which is schematically depicted in Fig. 4.1. x is the direction perpendicular to the interfaces, z is the propagation direction and y is the unbound transverse direction, where light can diffract along. For monochromatic fields $\vec{\mathcal{E}}e^{-i\omega t}, \vec{\mathcal{H}}e^{-i\omega t}$, the macroscopic Maxwell equations in the absence of free charges and currents can be combined to achieve the equation for the electric field

$$\vec{\nabla} \times \vec{\nabla} \times \vec{\mathcal{E}} = \frac{1}{\epsilon_0}\vec{\mathcal{D}}, \tag{4.1}$$

subject to the boundary conditions (BCs) at the interfaces $x_1, x_2, ..., x_j, ..., x_N$ (see below). In the complex formalism, the physical electric field and displacement vectors are represented by the real parts $Re\vec{\mathcal{E}}e^{-i\omega t}, Re\vec{\mathcal{D}}e^{-i\omega t}$. ϵ_0 is the vacuum susceptibility and the coordinates x, y, z are normalized to the inverse wavenumber $k^{-1} = \lambda/2\pi$, where λ is the vacuum wavelength. $\epsilon(x)$ is the dielectric susceptibility profile, which varies sharply at the interfaces $x_1, x_2, ..., x_j, ..., x_N$ between different materials. The constitutive relation is given by

$$\vec{\mathcal{D}} = \epsilon_0\epsilon\vec{\mathcal{E}} + \epsilon_0\vec{\mathcal{N}}, \tag{4.2}$$

where $\vec{\mathcal{N}}$ is the nonlinear part of the displacement. The solution of Eq. (4.1) is sought in the form

$$\vec{\mathcal{E}} = \vec{E}(x, y, z)e^{i\beta z}, \tag{4.3}$$

$$\vec{\mathcal{H}} = \vec{H}(x, y, z)e^{i\beta z}, \tag{4.4}$$

$$\vec{\mathcal{N}} = \vec{N}e^{i\beta z}, \tag{4.5}$$

where β is the normalized propagation constant, rescaled to $k = \omega/c$. In the perturbative expansion derived below, we assume that the dielectric susceptibility profile can be expressed as the sum $\epsilon = \epsilon_a + \epsilon_b$, where $\epsilon_a(x)$ is the leading term and $\epsilon_b(x)$ is the susceptibility correction, accounting for linear absorbtion or amplification (for gain materials). In what follows, we derive a multiple scale expansion for the TM modes of the photonic structure depicted in Fig. 4.1, which are characterised by the two field components E_x (perpendicular to the interfaces) and E_z (parallel to the propagation direction). The linear TM modes are unbound in the y direction. Hence, as an optical beam with a finite width impinges on the photonic structure, it diffracts along the transverse direction y, implying that H_z, E_y are nonzero. However, if the beam width w is much larger than the wavelength $w >> \lambda$, the field components H_z, E_y stay relatively small

$$|H_z| << |H_y|, \tag{4.6}$$

$$|E_y| << |E_x|, |E_z|. \tag{4.7}$$

Basically, the diffraction introduces new directions of propagation in the $y - z$ plane and it is impossible to talk strictly about TM polarised optical beams, i.e.

that the magnetic field is perpendicular to the direction of propagation. Instead, the optical beam is quasi TM-polarised since it is given by a superposition of TM modes with respect to every propagation direction lying in the y-z plane. Since diffraction is assumed weak, the optical field practically propagates along the z-direction.

The magnetic field $\vec{H}$ is related to the electric field components E_x, E_y, E_z through the curl equation

$$\vec{H} = \frac{1}{i\mu_0 c} e^{-i\beta z} \nabla \times [\vec{E} e^{i\beta z}]. \tag{4.8}$$

Generic boundary conditions at the interfaces $x_1, x_2, ..., x_j, ...x_N$ can be derived directly from Maxwell equations [Jackson, 1999], providing that the tangential component of $\vec{E}$, the normal component of the displacement $\epsilon\vec{E} + \vec{N}$ and all components of the magnetic field $\vec{H}$ are continuous:

$$E_x : \ \Delta_j[\epsilon E_x + N_x] = 0, \tag{4.9}$$

$$E_y : \ \Delta_j[E_y] = 0, \tag{4.10}$$

$$E_z : \ \Delta_j[E_z] = 0, \tag{4.11}$$

$$H_y : \ \Delta_j[\partial_x E_z - e^{-i\beta z}\partial_z(E_x e^{i\beta z})] = 0, \tag{4.12}$$

$$H_z : \ \Delta_j[\partial_x E_y - \partial_y E_x] = 0. \tag{4.13}$$

The operator $\Delta_j[f]$ acting on the generic function $f(x)$ is defined as

$$\Delta_j[f] = \lim_{\delta \to 0} \left[f(x_j - \delta) - f(x_j + \delta) \right], \tag{4.14}$$

where x_j are the interface coordinates. BCs on H_y, H_z are redundant and in principle can be eliminated for the exact linear modes of Maxwell equations [Jackson, 1999]. However, for the approximate solution of nonlinear Maxwell equations by the asymptotic expansion, it is convenient to retain the boundary condition for H_z.

For Kerr materials the nonlinear part of the displacement is given by

$$\vec{N}(E_x, E_y, E_z) = \frac{1}{2}\chi_3(|\vec{E}|^2\vec{E} + \frac{1}{2}(\vec{E}\cdot\vec{E})\vec{E}^*), \tag{4.15}$$

where $\chi_3(x)$ is the nonlinear susceptibility. The x-dependence is kept in order to describe a photonic structure composed by layers of different materials. We assume that the exponential factor $e^{i\beta z}$ varies in z much faster than $\vec{E}(z)$:

$$|\partial_z \vec{E}| \ll \beta |\vec{E}|. \tag{4.16}$$

Further, it is assumed that

$$|\sqrt{\chi_3} E_{x,z}| \sim o(s^{1/2}), \tag{4.17}$$

$$|\epsilon_b|, |\sqrt{\chi_3} E_y| \sim o(s), \tag{4.18}$$

$$|\sqrt{\chi_3}\partial_z E_{x,z}|, \left|\sqrt{\chi_3}\partial_y^2 E_{x,z}\right|, |\epsilon_b\sqrt{\chi_3} E_{x,z}|, |\sqrt{\chi_3} N_{x,z}| \sim o(s^{3/2}), \tag{4.19}$$

where $s \ll 1$ is a small dummy parameter. For the electric field $\vec{E}$ we use the following ansatz

$$E_x = A_x(\psi, x) + B_x(\psi, x) + o(s^{5/2}), \tag{4.20}$$

$$E_y = C(\psi, x) + o(s^2), \tag{4.21}$$

$$E_z = A_z(\psi, x) + B_z(\psi, x) + o(s^{5/2}), \tag{4.22}$$

where

$$A_{x,z} \sim o(s^{1/2}), \tag{4.23}$$

$$C \sim o(s), \tag{4.24}$$

$$B_{x,z} \sim o(s^{3/2}). \tag{4.25}$$

The fields $A_{x,z}, B_{x,z}, C$ do not depend on y, z explicitly, but only by means of the slowly varying function $\psi(z, y)$.

At the $o(s^{1/2})$ order, Maxwell equations provide the linear system of differential equations

$$\hat{\mathfrak{L}}\vec{A} = 0, \tag{4.26}$$

subject to the BCs

$$E_x: \ \Delta_j[\epsilon_a A_x] = 0, \tag{4.27}$$

$$E_z: \ \Delta_j[A_z] = 0, \tag{4.28}$$

where

$$\hat{\mathfrak{L}} = \begin{pmatrix} \beta^2 - \epsilon_a & i\beta\partial_x \\ i\beta\partial_x & -\partial_{xx}^2 - \epsilon_a \end{pmatrix}, \tag{4.29}$$

and

$$\vec{A} = \begin{pmatrix} A_x \\ A_z \end{pmatrix}. \tag{4.30}$$

For $\mathrm{Im}\epsilon_a = 0$, the linear Boundary Value Problem (BVP) above is self-adjoint [Boyce and DiPrima, 1997]. We assume that the solution of such a BVP is a non-degenerate bound mode $\vec{A} = I^{1/2}\psi(z,y)\vec{e}$, where

$$\lim_{x\to\pm\infty} |\vec{e}| = 0, \tag{4.31}$$

$$\hat{\mathfrak{L}}\vec{e} = 0, \tag{4.32}$$

$\vec{e}(x) = (e_x, e_z)^T$ and ψ is the arbitrary amplitude of the linear mode ($|\psi| \sim o(s^{1/2})$). Without any loss of generality the linear mode profile $\vec{e}$ can be assumed dimensionless if the physical units are carried by the free amplitude $I^{1/2}\psi$. The magnetic field component H_y can be expressed in terms of the linear mode $\vec{A} = I^{1/2}\psi(z,y)\vec{e}$ through Eq. (4.8), which gives

$$H_y = \frac{\epsilon_a}{\beta}\epsilon_0 c I^{1/2}\psi e_x. \tag{4.33}$$

The power density (measured in W/m) bridged in the z-direction can be calculated as the flux of the z-component of the Poynting vector

$$P_z = \frac{1}{4k}\int_{-\infty}^{+\infty}(A_x H_y^* + A_x^* H_y)dx = I|\psi|^2\frac{\epsilon_0 c}{2\beta k}Q, \tag{4.34}$$

where

$$Q = \int_{-\infty}^{+\infty}\epsilon_a|e_x|^2 dx. \tag{4.35}$$

The normalization factor I is fixed in such a way that $|\psi|^2$ represents the power density carried in z direction $P_z = |\psi|^2$:

$$I = \frac{2\beta k}{\epsilon_0 c Q}. \tag{4.36}$$

Hence, the squared amplitude $|\psi|^2$ is measured in the units of the power density (W/m).

In the following $o(s)$ order of the multiple scale expansion, one finds the BVP for the transvere field component $E_y = C(\psi, x)$:

$$\partial^2_{xx} C - (\beta^2 - \epsilon_a) C = 0, \tag{4.37}$$

with the BC

$$E_y : \ \Delta_j[C] = 0. \tag{4.38}$$

The z-component of the magnetic field H_z ($H_z \sim o(s)$) can be calculated from Eq. (4.8):

$$H_z = \frac{1}{i\mu_0 c} \left(\partial_x C - I^{1/2} \partial_y \psi e_x \right). \tag{4.39}$$

The continuity of H_z requires that $\Delta_j[\partial_x C] = I^{1/2} \partial_y \psi \Delta_j[e_x]$. In general the solution of the BVP is

$$C = I^{1/2} \partial_y \psi e_y, \tag{4.40}$$

where $e_y(x)$ is bound ($|e_y| \to 0$ as $x \to \pm\infty$), continuous and solves the above BVP with the BCs

$$\Delta_j[e_y] = 0, \tag{4.41}$$

$$\Delta_j[\partial_x e_y] = \Delta_j[e_x]. \tag{4.42}$$

The requirement for the mode to be quasi TM polarised at the $o(s)$ order is expressed through the condition

$$H_x = \frac{1}{i\mu_0 c} I^{1/2} \partial_y \psi (e_z - i\beta e_y) = 0, \tag{4.43}$$

which is satisfied by $e_y = e_z / i\beta$. Indeed, manipulating Eq. (4.26) it is straightforward to demonstrate that e_z satisfies the same BVP of e_y. In addition, by setting $e_y = e_z / i\beta$ Eq. (4.42) is automatically satisfied. The identity $e_y = e_z / i\beta$ couples the diffraction induced transverse field e_y with the longitudinal field e_z and enables the possibility to eliminate e_y from the following calculations.

At the $o(s^{3/2})$ order, Maxwell equations provide an inhomogeneous system of differential equations

$$\hat{\mathcal{L}} \vec{B} = I^{1/2} \vec{J}, \tag{4.44}$$

with the BCs

$$E_x: \ \Delta_j[\epsilon_a B_x] = -\Delta_j[\epsilon_b A_x] - I^{1/2}\psi|\psi|^2\Delta_j[n_x], \tag{4.45}$$

$$E_z: \ \Delta[B_z] = 0. \tag{4.46}$$

$\vec{B} = (B_x, B_z)^T$ and $\vec{J} = (J_x, J_z)^T$ is the displacement induced by the perturbations

$$\begin{aligned} J_x &= \partial_z\psi(2i\beta e_x - \partial_x e_z) + \partial_{yy}^2\psi(e_x - \partial_x e_y) + \psi\epsilon_b e_x + \\ &\quad +\psi|\psi|^2 I N_x(e_x, 0, e_z), \end{aligned} \tag{4.47}$$

$$J_z = -\partial_z\psi\partial_x e_x + \psi\epsilon_b e_z + \psi|\psi|^2 I N_z(e_x, 0, e_z), \tag{4.48}$$

where the functions $N_{x,z}(e_x, 0, e_z)$ are provided by Eq. (4.15).

4.2 Nonlinear Schrödinger equation (NLSE)

Unlike done in the the previous chapter, where we directly calculated the field corrections ($\vec{B}$) and imposed the BCs, here the propagation equation is determined by projecting Eq. (4.44) onto the linear TM-mode $\vec{e} = (e_x \ e_x)^T$:

$$\int_{-\infty}^{\infty}(\vec{e}^* \cdot \hat{\mathfrak{L}}\vec{B})dx = I^{1/2}\int_{-\infty}^{\infty}(\vec{e}^* \cdot \vec{J})dx. \tag{4.49}$$

The scalar product condition above constitutes the solvability condition for the multiple scale expansion and guarantees the absence of secular terms in the solution for the field correction $\vec{B}$. We emphasise an important aspect of the projection procedure, which is the application of integration by parts

$$\int_{-\infty}^{\infty} f'g dx = \sum_{j=1}^{N}\Delta_j\left[fg\right] - \int_{-\infty}^{+\infty} fg' dx. \tag{4.50}$$

Such an aspect is important since it allows using boundary conditions accounting for both the linear and nonlinear corrections to evaluate the off-integral terms. Importantly, both right and left hand sides of Eq. (4.49) yield non-zero contributions:

$$\int_{-\infty}^{\infty}(\vec{e}^* \cdot \hat{\mathfrak{L}}\vec{B})dx = -i\beta\eta P I^{1/2}\partial_z\psi, \tag{4.51}$$

$$\int_{-\infty}^{\infty}(\vec{e}^{*}\cdot\vec{J})dx = i\beta(2+\eta)P\partial_z\psi + (1+\eta)P\partial^2_{yy}\psi + \psi\int_{-\infty}^{\infty}\epsilon_b|\vec{e}|^2dx +$$
$$+\psi|\psi|^2 I\int_{-\infty}^{\infty}\left[e_x^* N_x(e_x,0,e_z) + e_z^* N_z(e_x,0,e_z)\right]dx, \tag{4.52}$$

where

$$\eta = \frac{1}{\beta P}\sum_j (ie_z(x_j))^*\Delta_j[e_x] \tag{4.53}$$

and

$$P = \int_{-\infty}^{\infty}|\vec{e}|^2dx. \tag{4.54}$$

The resulting nonlinear Schrödinger equation (NLSE) for the field amplitude ψ is

$$i\frac{\partial\psi}{\partial(z/k)} + \frac{1}{2\beta k}\frac{\partial^2\psi}{\partial(y/k)^2} + \alpha\psi + \Upsilon|\psi|^2\psi = 0, \tag{4.55}$$

where the linear parameter α is

$$\alpha = \sqrt{g}l, \tag{4.56}$$
$$l = \frac{k\sqrt{g}}{2P\beta}\int_{-\infty}^{\infty}\epsilon_b|\vec{e}|^2dx, \tag{4.57}$$

and the nonlinear parameter Υ can be expressed as

$$\Upsilon = g\gamma, \tag{4.58}$$
$$\gamma = \frac{2k^2}{3\beta^2P^2}\int_{-\infty}^{\infty}\epsilon_a n_2\left[|\vec{e}|^4 + \frac{1}{2}|\vec{e}^2|^2\right]dx. \tag{4.59}$$

In the equation above we expressed the nonlinear susceptibility $\chi_3 = (4/3)n_2\epsilon_0\epsilon_a c$ in terms of the Kerr coefficient n_2.

We emphasise that BCs enter Eqs. (4.51,4.52) through the surface term η, given by Eq. (4.53), affecting both the linear and nonlinear terms in the resulting NLSE. Importantly, the nonlinear coefficient Υ differs from γ by the factor g

$$g = \frac{1}{(1+\eta)^2}, \tag{4.60}$$

which we call the *surface induced nonlinearity enhancement factor*. The units of n_2 are m^2/W, while the units of γ and Υ in the one dimensional geometry are

1/W since $|\psi|^2$ represents the power density carried in the z-direction (measured in W/m).

The effective nonlinear parameter $\Upsilon = g\gamma$ is significantly enhanced ($g > 1$) if η deviates from $\eta = 0$. The surface term η is given by Eq. (4.53) and depends on the product of the longitudinal field component at the boundaries $e_z(x_j)$ with the discontinuities of the transverse field component $\Delta_j[e_x]$ summed over all the interfaces x_j ($j = 1, 2, ...N$). Note that the divergence condition for linear TM modes

$$\nabla \cdot \left[\epsilon_a \vec{\mathcal{E}}\right] = 0 \tag{4.61}$$

links the field components e_x, e_z through the equation

$$\partial_x \epsilon_a e_x = -i\beta \epsilon_a e_z. \tag{4.62}$$

Hence, the transverse (e_x) and longitudinal (e_z) field components are characterised by a $\pi/2$ phase shift and as a consequence the surface term is purely real:

$$\eta = (1/\beta P) \sum_j (ie_z(x_j))^* \Delta_j[e_x] \in \Re. \tag{4.63}$$

We calculated η for different metallic and dielectric waveguides, finding that $-1 < \eta < 0$. This implies that $g > 1$ and as a consequence the surface term η, depending on the transverse field discontinuities and on the longitudinal fields at the boundaries $x_1, x_2, ...x_N$, leads to the enhancement of the nonlinear response of the TM guided modes. Note that, together with the effective nonlinear response, also the effective linear coefficient α (accounting for loss/gain) is enhanced: $\alpha = \sqrt{g}l$.

4.3 Comparison with other approaches

If the surface term is neglected ($\eta = 0$, $g = 1$), the left hand side contribution to the NLSE is null

$$\int_{-\infty}^{\infty} (\vec{e}^* \cdot \hat{\mathcal{L}} \vec{B}) dx = 0, \tag{4.64}$$

since the linear mode ($\vec{e}$) is eigenvector of the linear operator ($\hat{\mathcal{L}}$) with zero eigenvalue: $\hat{\mathcal{L}}\vec{e} = 0$.

The resulting nonlinear parameter γ coincides with the averaging approach dating back to the use of the scalar wave equation [Agrawal, 2001b] later extended to the vectorial case in order to model propagation of SPPs [Davoyan et al., 2009b, 2010b; Feigenbaum and Orenstein, 2007]. Further, in the weakly guiding limit of quasi-transverse modes

$$e_z \to 0, \tag{4.65}$$

$$\beta^2 \to \epsilon_a, \tag{4.66}$$

the nonlinear parameter γ reduces to

$$\gamma \simeq \frac{n_2 k}{L_x}, \tag{4.67}$$

where

$$L_x = k^{-1} \frac{\left(\int |e_x|^2 dx\right)^2}{\int |e_x|^4 dx} \tag{4.68}$$

is the characteristic modal length along the x-direction. Such an expression perfectly coincides with the one dimensional analogue of the nonlinear parameter γ calculated in the scalar approximation [Agrawal, 2001b].

In addition, by substituting the linear Maxwell equations in Eq. (4.34) and by applying the integration by parts, it is straightforward to demonstrate that

$$Q = (1+\eta)\beta^2 P = \beta \int_{-\infty}^{+\infty} Re\left[\vec{e} \times \vec{h}^*\right] \cdot \hat{z} dx, \tag{4.69}$$

where Q, P are given by Eqs. (4.35,4.54) and

$$\vec{h} = h_y \hat{y}, \tag{4.70}$$

$$h_y(x) = \frac{\epsilon_a}{\beta} e_x(x), \tag{4.71}$$

$$H_y = \epsilon_0 c I^{1/2} \psi h_y(x). \tag{4.72}$$

In turn, the nonlinear parameter Υ accounting for the surface term η can be reduced to

$$\Upsilon = \frac{k^2}{3} \frac{\int_{-\infty}^{\infty} \epsilon_a n_2 \left[2|\vec{e}|^4 + |\vec{e}^2|^2\right] dx}{\left(\int_{-\infty}^{+\infty} Re\left[\vec{e} \times \vec{h}^*\right] \cdot \hat{z} dx\right)^2}. \tag{4.73}$$

Note that the expression above does not contain explicitly the surface term η, which has been used in the integration by parts to get $Re\left[\vec{e}\times\vec{h}^{*}\right]$ from P. Such an expression for Υ thoroughly coincides with the one-dimensional analogue of the nonlinear coefficient provided by the approach based on the *Lorentz Reciprocity Theorem* (LRT) for two dimensional subwavelength waveguides [Afshar and Monro, 2009; Koos et al., 2007; Osgood et al., 2009]. To the best of our knowledge, the application of the LRT approach to one-dimensional photonic structures, where diffraction in the transverse direction y is considered as a perturbation, has not been developed. Hence, a complete comparison between our method and the LRT approach is not possible at this stage. A thorough equivalence is demonstrated in chapter 7, where the multiple scale expansion is applied to subwavelength cylindrical waveguides.

In view of the above observations, the nonlinearity enhancement observed in Ref. [Koos et al., 2007] is completely explained in terms of *surface effects* originating from the boundaries, which are relevant in the subwavelength regime. Such effects are automatically taken into account in the LRT approach, while they are neglected in the averaging perturbative methods [Agrawal, 2001b; Davoyan et al., 2009b, 2010b; Feigenbaum and Orenstein, 2007].

The propagation operator in the NLSE derived by us is given by

$$i\partial_z + \frac{1}{2\beta}\partial_{yy}^2 \tag{4.74}$$

and is characterised by the diffraction coefficient $1/2\beta$, finding confirmation in Ref. [DellaValle and Longhi, 2010]. Conversely, in other studies focused on the diffraction and self-focusing of SPPs [Davoyan et al., 2009b], the diffraction coefficient is affected by a geometry-dependent correction.

4.4 Nonlinearity enhancement in basic waveguide geometries

In this section, we calculate explicitly the surface term η given by Eq. (4.53) for several one-dimensional photonic structures. Figs. 4.2(d-f) depict the surface-induced nonlinearity enhancement factor $g = (1+\eta)^{-2}$ for the three geometries

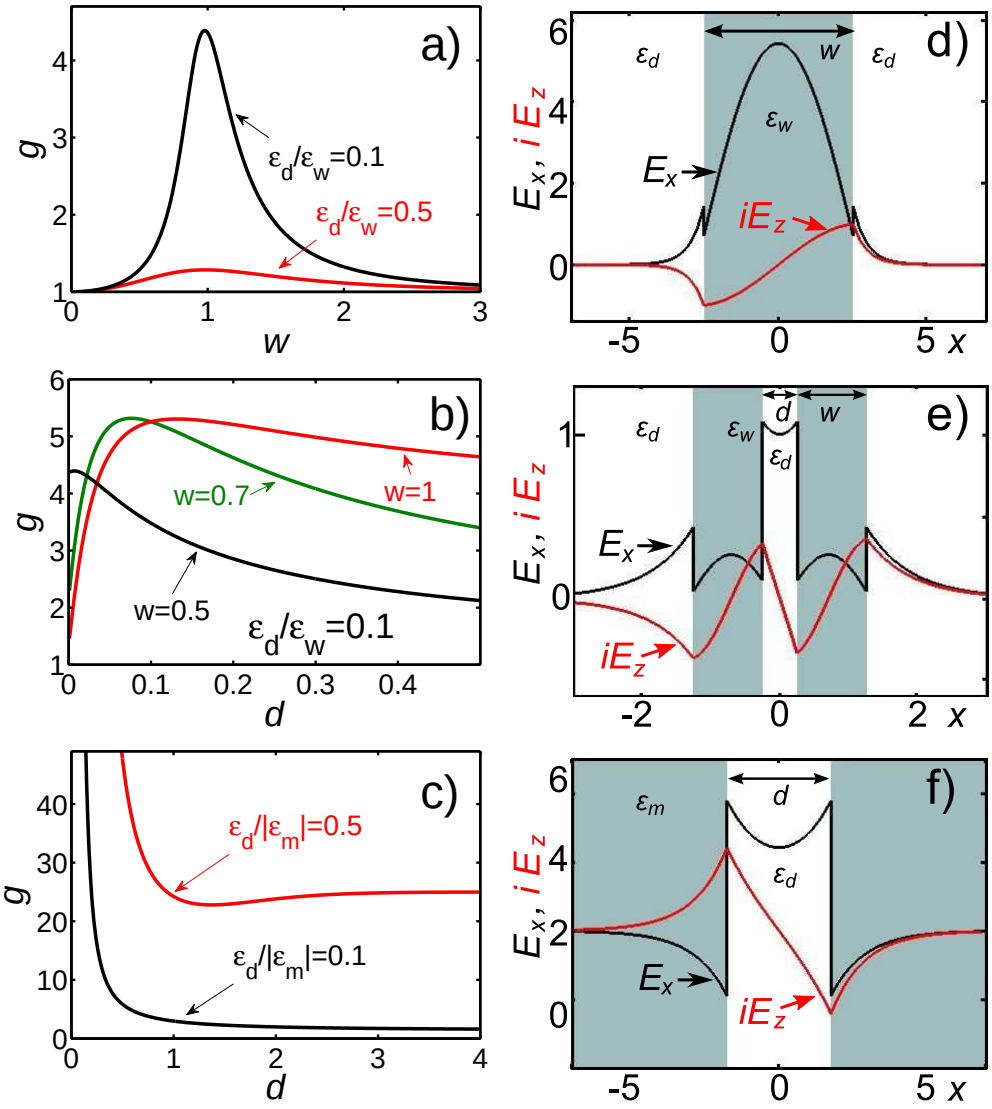

Figure 4.2: (a-c) Surface induced nonlinearity enhancement factor g for three different waveguide geometries. The corresponding waveguides and the electric field profiles are depicted in (d-f). (a,d) Single dielectric waveguide of width w. (b,e) Dielectric slot waveguide: two dielectric waveguides separated by the distance d. (c,f) Metal slot waveguide: two metal interfaces separated by distance d. This figure is a courtesy of A. Gorbach.

shown in Figs. 4.2(a-c). The surface term η is determined directly from the analytical expressions of the linear modes and of the corresponding dispersion relations. In what follows, we focus our attention only on the TM modes with *symmetric* transverse field (e_x) component (and antisymmetric longitudinal e_z field component), which exhibit the extreme field enhancement observed in slot dielectric waveguides [Almeida et al., 2004b].

4.4.1 Slab dielectric waveguide

In the first place, we consider an optical waveguide composed of a high-index dielectric slab ($n_w^2 = \epsilon_w$) of width w (rescaled to k^{-1} where $k = \omega/c$) embedded in a low-index cladding material ($n_d^2 = \epsilon_d < \epsilon_w$). The TM mode of this waveguide is solution of Eq. (4.32):

$$e_x = \begin{cases} \dfrac{i\beta}{\kappa}\cos(\kappa x) & |x| < w/2\ , \\ \dfrac{i\beta}{q}\sin(\kappa w/2)e^{-q(|x|-w/2)} & |x| > w/2\ , \end{cases} \tag{4.75}$$

$$e_z = \begin{cases} \sin(\kappa x) & |x| < w/2\ , \\ \dfrac{x}{|x|}\sin(\kappa w/2)e^{-q(|x|-w/2)} & |x| > w/2\ , \end{cases} \tag{4.76}$$

where $\kappa^2 = \epsilon_w - \beta^2$, $q^2 = \beta^2 - \epsilon_d$. The modal field components above automatically solve the BCs given by Eqs. (4.27,4.28), providing that the propagation constant β satisfies the dispersion relation

$$q\epsilon_w = \kappa\epsilon_d \tan(\kappa w/2). \tag{4.77}$$

Inserting Eqs. (4.75,4.76) into Eq. (4.53) one achieves the following analytical expression for the surface term η

$$\eta = \frac{2(1-\epsilon_w/\epsilon_d)}{(\epsilon_w/\epsilon_d)(1+\beta^2/q^2) - (1-\beta^2/\kappa^2) + w\kappa(1+\beta^2/\kappa^2)/\sin(\kappa w)}.$$

Such a surface term is always negative and becomes negligible $|\eta| << 1$ in both limits $w >> 1$ and $w << 1$. As a consequence, the nonlinearity enhancement $g = (1+\eta)^{-2}$ deviates significantly from $g = 1$ only for the optimal width $w \approx 1$, where the nonlinear response of the slab waveguide is resonant. Fig.

4.2a depicts the nonlinearity enhancement g for a silicon slab surrounded by air ($\epsilon_w = 10, \epsilon_d = 1$, black curve), where the resonant peak reaches $g \simeq 4$, and for a silica slab surrounded by air ($\epsilon_w = 2, \epsilon_d = 1$, red curve), where the resonant peak reaches $g \simeq 0.2$. In turn, surface effects are considerably relevant for slab waveguides with high index-step, where the field discontinuities at the boundaries are significant.

The equations of this section are courtesy of A. Gorbach.

4.4.2 Dielectric slot waveguide

A dielectric slot waveguide is composed of two identical high-index $n_w^2 = \epsilon_w$ dielectric slabs of width w separated by a small gap d (both rescaled to k^{-1}) and surrounded by a low-index dielectric medium $n_d^2 = \epsilon_d < \epsilon_w$ (see Fig. 4.2e) [Almeida et al., 2004b]. The TM mode with symmetric transverse field ($e_x(x) = e_x(-x)$) gets tightly confined within the low-index slot, as shown in Fig. 4.2e. The e_x, e_z field profiles are:

$$e_x = \begin{cases} -\dfrac{i\beta}{q_d}\Pi e^{-q_d(|x|-s)} & |x| > s\ , \\ \dfrac{i\beta}{q_w}\Pi \sin[q_w(|x|-s)] + \dfrac{i\beta}{q_w}\Lambda\cos[q_w(|x|-s)] & d/2 < |x| < s\ , \\ -\dfrac{i\beta}{q_d}\cosh(q_d x) & |x| < d/2\ , \end{cases}$$

$$e_z = \begin{cases} -\dfrac{x}{|x|}\Pi e^{-q_d(|x|-s)} & |x| > s\ , \\ -\dfrac{x}{|x|}\Pi \cos[q_w(|x|-s)] + \dfrac{x}{|x|}\Lambda\sin[q_w(|x|-s)] & d/2 < |x| < s\ , \\ \sinh(q_d x) & |x| < d/2\ , \end{cases}$$

where $q_{d,w}^2 = \beta^2 - \epsilon_{d,w}$, $s = w + d/2$, the constants Π, Λ are given by

$$\Pi = \frac{q_w\epsilon_d\cosh(q_d d/2)}{q_d\epsilon_w\sin(q_w w) + q_w\epsilon_d cos(q_w w)}, \tag{4.78}$$

$$\Lambda = -\frac{q_w\epsilon_d}{q_d\epsilon_w}\Pi, \tag{4.79}$$

and the propagation constant satisfies the dispersion relation

$$\tanh(q_d d/2) = \frac{q_w\epsilon_d}{q_d\epsilon_w}\frac{q_w\epsilon_d\tan(q_w w) - q_d\epsilon_w}{q_d\epsilon_w\tan(q_w w) + q_w\epsilon_d}. \tag{4.80}$$

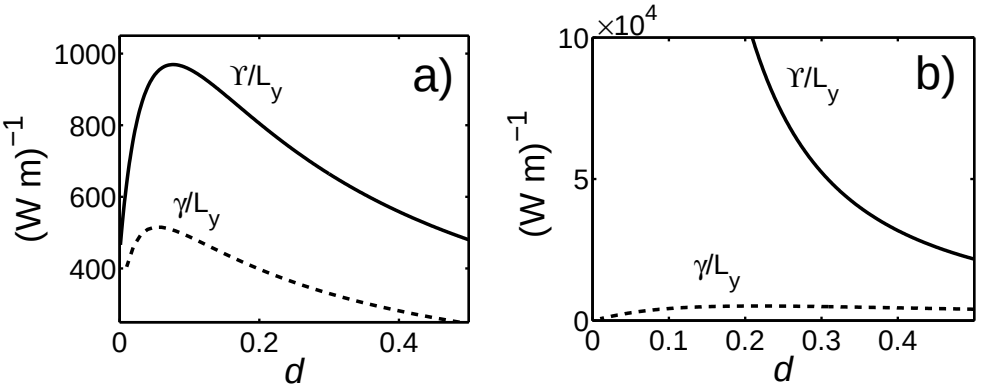

Figure 4.3: Comparison between γ/L_y (dashed lines) and the surface enhanced Υ/L_y (solid lines) nonlinear parameters for the silicon (a) and metal (b) slot waveguides with the polymer filled slot. n_2 for silicon and polymer are assumed to be the same $4 \cdot 10^{-18}\mathrm{m}^2/\mathrm{W}$, while the dielectric constants are $\epsilon_w = 12$ and $\epsilon_d = 3.2$, respectively. $w = 0.7$, $\lambda = 1.5\mu$m and $L_y = 100$nm. In (b), the metal is assumed linear and $\epsilon_m = -25$, $\epsilon_d = 4$, $\lambda = 0.8\mu$m. This figure is a courtesy of A. Gorbach.

Note that the mode dispersion converges to the dispersion of dielectric slab waveguides of width w and $2w$ in the limits $d >> 1$ and $d << 1$, respectively. An explicit analytic expression for the surface term η can be calculated straightforwardly by substituting the mode profiles e_x, e_z into Eq. (4.53). However, such an expression is cumbersome and is not included here. The dependence of the nonlinearity enhancement $g = (1+\eta)^{-2}$ on the slot width for a silicon slot waveguide ($\epsilon_w = 10, \epsilon_d = 1$) is depicted in Fig. 4.2b for several slab widths: $w = 0.5, 0.7, 1$. The position of the maximum of the nonlinearity enhancement g varies with the slab width w, but it remains around $d \approx 0.1$.

The nonlinear parameters $\gamma/L_y, \Upsilon/L_y$ (in $W^{-1}m^{-1}$ physical units) are plotted as functions of the slot spacing d in Fig. 4.3a, where $L_y = 100nm$ is the typical length scale of silicon slot waveguides in the y-direction [Koos et al., 2007]. For the numerical computations we considered a hybrid silicon-organic polymer slot waveguide [Koos et al., 2009]. The nonlinear parameters of the silicon and of the polymer are assumed to be the same $n_2 = 4 \cdot 10^{-18}\mathrm{m}^2/\mathrm{W}$, while the dielec-

tric susceptibilities are $\epsilon_w = 12$ (silicon) and $\epsilon_d = 3.2$ (organic polymer). The two nonlinear parameters $\gamma/L_y, \Upsilon/L_y$ differ considerably at $d \approx 0.1$, where the effective nonlinear response of the slot waveguide is resonant.

4.4.3 Metal-Insulator-Metal (MIM) slot waveguide

In this section we consider the Metal-Insulator-Metal (MIM) slot waveguide depicted in Fig. 4.2f. Such a plasmonic structure is composed of two metals ($\epsilon_m < 0$) with planar interfaces that sandwich a dielectric slot of width d ($\epsilon_d > 0$). The plasmonic mode with symmetric transverse field component $e_x(x) = e_x(-x)$ and antisymmetric longitudinal field component $e_z(x) = -e_z(-x)$ is

$$e_x = \begin{cases} -\dfrac{i\beta}{q_d}\cosh(q_d x) & |x| < d/2\,, \\ \dfrac{i\beta}{q_m}\sinh(q_d d/2)e^{-q_m(|x|-d/2)} & |x| > d/2\,, \end{cases} \tag{4.81}$$

$$e_z = \begin{cases} \sinh(q_d x) & |x| < d/2\,, \\ \dfrac{x}{|x|}\sinh(q_d d/2)e^{-q_m(|x|-d/2)} & |x| > d/2\,, \end{cases} \tag{4.82}$$

where $q_{d,m}^2 = \beta^2 - \epsilon_{d,m}$ and the propagation constant β solves the dispersion law

$$\tanh(q_d d/2) = -\frac{q_m \epsilon_d}{q_d \epsilon_m}. \tag{4.83}$$

The surface term η in this case is given by

$$\eta = \frac{2(1-\epsilon_d/\epsilon_m)}{(\epsilon_d/\epsilon_m)(1+\beta^2/q_m^2) - (1+\beta^2/q_d^2) + q_d d(1-\beta^2/q_d^2)/\sinh(q_d d)}. \tag{4.84}$$

The equations above are courtesy of A. Gorbach.

The nonlinearity enhancement $g = (1+\eta)^{-2}$ is plotted as a function of the slot width d in Fig. 4.2c for $\epsilon_d = 1, \epsilon_m = -2$ (red line) and $\epsilon_d = 1, \epsilon_m = -10$ (black line). The metal loss ϵ_m'' is considered as a small perturbation, which is taken into account by the damping parameter α. Note that for this geometry the nonlinear enhancement is considerably high $g \simeq 20 - 50$ and diverges as it approaches the plasmon resonance. As the slot width d tends to zero, the surface term η converges to

$$\lim_{d\to 0}\eta = -1, \tag{4.85}$$

and the nonlinearity enhancement $g = (1+\eta)^{-1}$ diverges sharply with the typical power law $g \sim 1/d^2$. Thus, conversely to dielectric slot waveguide where g, γ, Υ tend to zero in the limit $d << 1$, here the nonlinear parameters Υ, γ behave in a completely different manner. Indeed, in the limit $d \to 0$, the nonlinear parameter γ resulting from the averaging approach tends to zero

$$\lim_{d\to 0} \gamma = 0, \tag{4.86}$$

while the nonlinear parameter Υ accounting for surface effects diverges

$$\lim_{d\to 0} \Upsilon = \infty. \tag{4.87}$$

Hence, for narrow metallic slot waveguides, the surface-induced nonlinearity enhancement originating from the boundaries affects dramatically the effective nonlinear response. In turn, approaches neglecting the surface contribution [Davoyan et al., 2009b, 2010b; Feigenbaum and Orenstein, 2007] are not appropriate to model optical propagation in this regime.

In the opposite limiting case $d >> 1$, the SPPs at the single planar interfaces $x = \pm d/2$ are weakly coupled and the dispersion of the metallic slot waveguide tends to the single interface one

$$\lim_{d\to +\infty} \beta = \frac{\epsilon_d \epsilon_m}{\epsilon_d + \epsilon_m}. \tag{4.88}$$

The plasmonic mode profiles are well approximated by

$$\begin{aligned} e_x &= \frac{i\beta}{q_d} e^{-q_d(x+d/2)}\theta(x+d/2) - \frac{i\beta}{q_m} e^{q_m(x+d/2)}\theta(-d/2-x) + \\ &\quad -\frac{i\beta}{q_m} e^{-q_m(x-d/2)}\theta(x-d/2) + \frac{i\beta}{q_d} e^{q_d(x-d/2)}\theta(d/2-x), \qquad (4.89) \\ e_z &= e^{-q_d(x+d/2)}\theta(x+d/2) + e^{q_m(x+d/2)}\theta(-d/2-x) + \\ &\quad -e^{-q_m(x-d/2)}\theta(x-d/2) - e^{q_d(x-d/2)}\theta(d/2-x), \qquad (4.90) \end{aligned}$$

where $\theta(x)$ is the Heaviside function. The surface term η is

$$\eta = \frac{2\epsilon_d \epsilon_m}{\epsilon_d^2 + \epsilon_m^2}, \tag{4.91}$$

and the nonlinearity enhancement factor $g = (1+\eta)^{-2}$ assumes the simple form

$$g_{SPP} = \frac{(\epsilon_d^2 + \epsilon_m^2)^2}{(\epsilon_d + \epsilon_m)^4}. \tag{4.92}$$

The nonlinearity enhancement g_{SPP} diverges at the surface plasmon resonance wavelength λ_{SPP}, characterised by the condition $\epsilon_m(\lambda_{SPP}) = -\epsilon_d$. An explicit form of the nonlinear parameter γ resulting from the averaging approach for SPPs at a single interface is

$$\gamma = \frac{2}{3} k^2 n_2 \epsilon_d \epsilon_m^2 \frac{(\epsilon_d + \epsilon_m)^2}{(\epsilon_m^2 + \epsilon_d^2)^2} \left[1 + \frac{1}{2} \left(\frac{\epsilon_d + \epsilon_m}{\epsilon_d - \epsilon_m} \right)^2 \right]. \tag{4.93}$$

Note that γ tends to zero at the surface plasmon resonance: $\lim_{\epsilon_d \to \epsilon_m} \gamma = 0$. Conversely, the nonlinear parameter Υ including surface effects originating from the boundaries

$$\Upsilon_{spp} = \frac{2}{3} k^2 n_2 \frac{\epsilon_d \epsilon_m^2}{(\epsilon_d + \epsilon_m)^2} \left[1 + \frac{1}{2} \left(\frac{\epsilon_d + \epsilon_m}{\epsilon_d - \epsilon_m} \right)^2 \right] \tag{4.94}$$

diverges to infinity in the surface plasmon resonance limit

$$\lim_{\epsilon_d \to \epsilon_m} \Upsilon = \infty, \tag{4.95}$$

since the enhancement factor $g_{spp} \simeq (\epsilon_d + \epsilon_m)^{-4}$ grows at a rate faster than $(1/\gamma) \simeq (\epsilon_d + \epsilon_m)^{-2}$.

4.5 Concluding remarks

In this chapter we have developed a novel perturbative approach to model the nonlinear propagation of TM waves in generic one-dimensional plasmonic structures. In such an approach the propagation equation is achieved as the solvability condition of the multiple scale expansion. Indeed, it is not necessary to calculate the residual field corrections due to loss, gain and nonlinearity in order to achieve the equation of propagation for the field amplitude. For this reason such a perturbative theory is more flexible and suitable to model optical propagation in complex plasmonic geometries. Besides, such a perturbative approach is more

transparent since it allows to identify the physical origin of the modified effective loss and nonlinear response: *surface-effects*. Such contributions in the boundary conditions are neglected in the traditional perturbative theory used to model the propagation in optical fibres [Agrawal, 2001a]. As a consequence, the nonlinear Schrödinger equation (NLSE) for the field amplitude is modified by the surface term η. We observe a nonlinearity enhancement $g = (1+\eta)^{-2}$ and a loss enhancement $\sqrt{g}$ with respect to the traditional approach [Davoyan et al., 2009b; Feigenbaum and Orenstein, 2007]. The original results reported in this chapter have been published in Ref. [Skryabin et al., 2011].

Chapter 5

Coupled mode theory for SPP arrays

Research in optics in the last two decades has been revolutionised by the advent of photonic crystals [John, 1987; Yablonovitch, 1987], which have been briefly introduced in section 1.2.5. Optical propagation in layered structures has been studied extensively since the end of the nineteenth century [Rayleigh, 1888], discovering that the reflective properties of such systems are strongly dependent on the optical wavelength and can be described in terms of photonic bands and gaps [Joannopoulos et al., 2008]. Two-dimensional photonic crystals with complete photonic bandgaps have been exploited for guiding light in Hollow Core Photonic Crystal Fibres (HCPCFs), which find enormous applications in optical communications, nonlinear devices, fibre-based lasers and gas sensing [Cregan et al., 1999; Knight et al., 1996; Russell, 2003].

In general, if two optical waveguides lie in close proximity, the optical power is transferred from one waveguide to the other (and viceversa) owing to the evanescent overlap of the electromagnetic field tails. Such a passive device is commonly named *directional coupler* and has found useful applications in trasmission lines [Bergh et al., 1980; Trinh et al., 1995]. In principle, a directional coupler can be thought of as a waveguide on its own possessing two principal modes with different propagation constants, named *supermodes*; if the coupled waveguides are identical, supermodes are either symmetric or antisymmetric. Hence, if a generic superposition of the two modes is excited, the beating between symmetric and

antisymmetric supermodes occurs owing to propagation-dependent cycles of constructive and destructive interference [Agrawal, 2001a]. If the two waveguides are nonlinear, it is possible to use the nonlinear coupler for all-optical switching [Jensen, 1982], which has been demonstrated both theoretically and experimentally [Friberg et al., 1988; LiKamWa et al., 1985; Stegeman and Seaton, 1985].

In waveguide arrays, the optical field can be expressed in terms of a generic superposition of Floquet-Bloch modes of the entire structure. In the tight binding approximation, the electromagnetic coupling between the single modes of neighbouring waveguides is responsible for *discrete diffraction*, which was first considered by Allan Jones in the study of optical coupling mechanisms [Jones, 1965] and later observed in GaAs waveguide arrays [Somekh et al., 1973]. Unlike isotropic materials, where diffraction is a constant, for waveguide arrays it has been demonstrated that it is possible to manipulate discrete refraction [Locatelli et al., 2006; Rosberg et al., 2005] and diffraction [Eisenberg et al., 2000; Pertsch et al., 2002], which can be reduced, canceled or reversed in the proximity of the edge of the Brillouin zone. Further, in inhomogeneous arrays where the propagation constants of every waveguide change linearly with respect to the transverse position in the array, Bloch oscillations [Morandotti et al., 1999b; Pertsch et al., 1999; Peschel et al., 1998] and Landau-Zener tunnelling [Longhi, 2008; Trompeter et al., 2006a,b] have been observed.

For arrays of nonlinear waveguides, it is possible to suppress the discrete diffraction by exciting particular electromagnetic field patterns: *optical discrete solitons* [Christodoulides and Joseph, 1988; Eisenberg et al., 1998]. Basically, an array of coupled nonlinear waveguides can be modelled by a coupled system of nonlinear oscillators and the discrete solitons represent the localised collective oscillations of the nonlinear chain.

Analogously to the Kerr solitons in homogeneous media, discrete solitons result from the perfect balance between nonlinearity and discrete diffraction. Hence, the power flow remains confined only in few waveguides, and the discrete soliton pattern propagates without distorting and diffracting.

Another interpretation of discrete soliton formation borrows ideas from photonic crystal theory. On-site nonlinearity can be interpreted as a defect that breaks the perfect periodicity, since it is responsible for the local propagation

constant shifts at every site of the waveguide array. From this perspective, a discrete soliton can be thought of as a confined defect state induced by the nonlinearity [Lederer et al., 2008]. Discrete self-focusing can be achieved in arrays of nonlinearly coupled defocusing waveguides within the momentum space bandgap [Kivshar, 1993], analogously to spatio-temporal gap solitons that arise within the frequency bandgap [Aceves and Wabnitz, 1989; Chen and Mills, 1987; Christodoulides and Joseph, 1989]. Conversely to solitons in continuous and isotropic media that are invariant under rotation and translation symmetries, for discrete solitons the rotational symmetry is broken and the translational symmetry becomes discrete. Nevertheless, discrete solitons can propagate with a tilted angle φ under certain conditions depending on the optical power and on the φ-dependent Peierls-Nabarro barrier [Kivshar and Campbell, 1993].

Linear and nonlinear effects in waveguide arrays are still receiving attention by the scientific community, but a complete description of such effects goes beyond the extent of this thesis. In this chapter, we derive a coupled mode theory in order to describe SPP propagation in arrays of plasmonic waveguides and discrete/gap plasmon soliton formation. We will demonstrate that the inclusion of metallic components introduces a new quantitative and qualitative phenomenology both in the linear and nonlinear regimes.

The intrinsic subwavelength nature of SPPs attracts interest for potential applications, since the tight confinement of SPPs enhances nonlinear effects that can be exploited for frequency conversion, nonlinear switching and soliton formation. In chapter 3, we demonstrated that the embedding of gain and nonlinearity can balance the diffraction and loss of SPPs, allowing for plasmon-soliton formation [Davoyan et al., 2009b; Feigenbaum and Orenstein, 2007]. On the other hand, as mentioned above, diffraction can be controlled also by using periodic structures [Eisenberg et al., 2000; Pertsch et al., 2002], which are responsible for the formation of bands and gaps [Lederer et al., 2008].

Optical propagation in coupled plasmonic waveguides is receiving a considerable interest by the scientific community. Indeed, the interplay between the subwavelength nature of SPP waves with the periodic modulation of the plasmonic structure can lead to relevant results. One of these results concerns the possibility to achieve negative coupling in plasmonic arrays [Guasoni et al., 2010;

Xu and Aitchison, 2009], which can lead to Tamm-like and Shockley-like surface mode formation [Nam et al., 2010b], conical-like diffraction [Nam et al., 2010a] and negative refraction [Fan et al., 2006], which has been also observed in two-dimensional arrays of metallic nanowires [Liu et al., 2008]. Negative refraction has been investigated since the 1960s [Veselago, 1968] and has recently found an experimental implementation in *metamaterials* [Dolling et al., 2006, 2007; Shelby et al., 2001; Zhang et al., 2005]. Applications of negative refraction include superlensing [Pendry, 2000] and cloaking devices [Leonhardt, 2006; Schurig et al., 2006; Valentine et al., 2009].

Theoretical modelling of optical propagation in nonlinear metamaterials has been investigated recently; steplike optical transmission [Husakou and Herrmann, 2007] and giant nonlinear response in epsilon-near-zero (ENZ) metamaterials [Ciattoni et al., 2010a,b,c, 2011] have been reported. The effective optical response ϵ_{eff} of metamaterials is determined through the long-wavelength limit of the exact dispersion of Bloch modes [Elser et al., 2007; Yang et al., 2010, 2011; Yannopapas and Vanakaras, 2011]. Nonlinear propagation of SPPs in plasmonic couplers [Davoyan et al., 2011; Salgueiro and Kivshar, 2010] and arrays [Davoyan et al., 2008; Liu et al., 2007; Wang et al., 2008; Ye et al., 2010, 2011] has been studied by first principle numerical solution of nonlinear Maxwell equations. Such an approach for solving nonlinear Maxwell equations in subwavelength plasmonic structures yields accurate results but provides a limited understanding of the underpinning physical mechanisms leading to the modified phenomenology. Thus, the development of reliable analytical models for the description of SPP propagation in plasmonic waveguide arrays is an important task to address.

In what follows, we develop a coupled mode theory for nonlinear SPPs propagating along the interfaces of a metal-dielectric stack, predicting the existence of a plasmonic band-gap structure and reporting families of discrete and gap solitons.

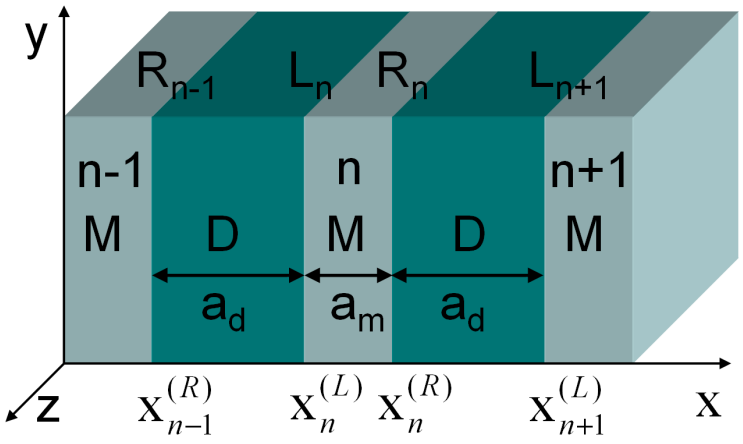

Figure 5.1: Schematic representation of an array of plasmonic waveguides, composed of a dielectric-metal stack. Dielectric and metallic slabs of width a_d, a_m (normalized to k^{-1}) and dielectric susceptibilities ϵ_d, ϵ_m are labelled by D,M, respectively. The integer n labels the nth metallic stripe.

5.1 Discrete nonlinear Schrödinger equation for SPP arrays

In this section, we derive the discrete nonlinear Schrödinger equation (DNLSE) for SPPs propagating in a metal-dielectric stack, which is schematically depicted in Fig. 5.1. Such a one-dimensional structure is homogeneous in the y, z directions, periodic in the x-direction and consists of alternating metal and dielectric slabs of widths $a_{d,m}$, respectively. Without any loss of generality, we assume that SPP waves propagate in the z-direction along every metal-dielectric interface and are infinitely extended in the y-direction. As done in chapter 4, we start our analysis from the Maxwell equations for the monochromatic fields $\vec{\mathcal{E}}e^{-i\omega t}, \vec{\mathcal{H}}e^{-i\omega t}$:

$$\nabla \times \nabla \times \vec{\mathcal{E}} = \frac{1}{\epsilon_0}\vec{\mathcal{D}}, \tag{5.1}$$

subject to boundary conditions at the interfaces $x = x_n^{(L)}, x_n^{(R)}$ $(-\infty < n < +\infty,$ $|n| \in N)$. x, y, z coordinates are dimensionless and normalized to the inverse wave vector $k^{-1} = \lambda/2\pi$, where λ is the vacuum wavelength. Like in the previous

chapter, the physical electric and magnetic fields are provided by the real parts $Re[\vec{\mathcal{E}}e^{-i\omega t}], Re[\vec{\mathcal{H}}e^{-i\omega t}]$ and the vector $\vec{\mathcal{D}}$ is the electric displacement

$$\vec{\mathcal{D}} = \epsilon_0(\epsilon\vec{\mathcal{E}} + \vec{\mathcal{N}}), \tag{5.2}$$

where the nonlinear part $\vec{\mathcal{N}}$ is assumed Kerr-like

$$\vec{\mathcal{N}} = \frac{1}{2}\chi_3\left[|\vec{\mathcal{E}}|^2\vec{\mathcal{E}} + \frac{1}{2}(\vec{\mathcal{E}}\cdot\vec{\mathcal{E}})\vec{\mathcal{E}}^*\right]. \tag{5.3}$$

The linear dielectric susceptibility profile $\epsilon(x)$ is periodic, corresponding to $\epsilon = \epsilon'_m + i\epsilon''_m$ and $\epsilon = \epsilon_d$ in metal (M) and dielectric (D) regions, respectively. The nonlinear parameter $\chi_3 = (4/3)\epsilon_0 c\epsilon_d n_2$ represents the Kerr susceptibility and is measured in m^2V^{-2}. In what follows, we assume that the nonlinear processes occur only in the dielectric medium and we neglect the metal nonlinearity. Hence, the nonlinear susceptibility profile $\chi_3(x)$ is null within the metallic slabs and a non-zero constant in the dielectric regions. Since the electric and magnetic fields are assumed infinitely extended along the y-direction, ∂_y derivatives in Eq. (5.2) are null and it is possible to achieve a system of differential equations for the $\mathcal{E}_x, \mathcal{E}_z$ field components of plasmonic TM waves ($\mathcal{E}_y = 0$)

$$\partial^2_{xz}\mathcal{E}_z - \partial^2_{zz}\mathcal{E}_x = \frac{1}{\epsilon_0}\mathcal{D}_x, \tag{5.4}$$

$$\partial^2_{xz}\mathcal{E}_x - \partial^2_{xx}\mathcal{E}_z = \frac{1}{\epsilon_0}\mathcal{D}_z. \tag{5.5}$$

The magnetic field $\vec{\mathcal{H}} = \mathcal{H}_y\hat{y}$ is determined by

$$\vec{\mathcal{H}} = \frac{1}{i\mu_0 c}\nabla\times\vec{\mathcal{E}}. \tag{5.6}$$

The geometrical parameters $a_{d,m}$ of the metal-dielectric stack are assumed such that the SPPs propagating along the single interfaces $x = x^{(R)}_{n-1}, x^{(L)}_n, x^{(R)}_n, x^{(L)}_{n+1}$ are weakly interacting and are not affected by the presence of the neighbouring SPPs at the lowest order of the multiple scale expansion. For example, if $\lambda = 550nm$, $\epsilon_d = 1.8$ and $\epsilon'_m = -15$ (silver), the SPP amplitude is reduced by a factor e for the typical distances $l_d \simeq 170nm$ on the dielectric side and $l_m \simeq 20nm$ on the metal side, corresponding to $kl_d \simeq 2$ and $kl_m \simeq 0.24$ in dimensionless units. Hence, if

we set the interface spacings to $a_d = 5$ (dielectric width) and $a_m = 0.5$ (metal width), the effective coupling between SPPs propagating along different planar interfaces is considerably small and a coupled mode approach is justified.

Before proceeding with the perturbative expansion, we note that SPPs propagating in the metal-dielectric stack can be separated in two classes with opposite chirality. The first class is composed by Dielectric-Metal (DM) SPPs propagating along the left interface of the nth metallic stripe (represented by the amplitude L_n, see Fig. 5.1). On the other hand, the second class is constituted by Metal-Dielectric (MD) SPPs propagating along the right interface of the nth metallic stripe (represented by the amplitude R_n, see Fig. 5.1).

Following the same mathematical procedure described in chapter 4, we make the assumption

$$\epsilon = \epsilon_a + \epsilon_b, \tag{5.7}$$

where ϵ_a is ϵ'_m, ϵ_d in metal and dielectric regions, respectively (see Fig. 5.2), while ϵ_b is non-zero only in the metallic regions and accounts for the metallic loss $i\epsilon''_m$. Introducing the small dummy variable s, we make the following ansatz

$$\begin{aligned}
\mathcal{E}_x(x,z) &= \mathfrak{I}^{1/2} \sum_{n=-\infty}^{+\infty} \left[L_n(z) e_x^{(L)}(x - x_n^{(L)}) + R_n(z) e_x^{(R)}(x - x_n^{(R)}) \right] e^{i\beta_0 z} + \\
&\quad + \delta E_x e^{i\beta_0 z} + o(s^{5/2}), \qquad (5.8) \\
\mathcal{E}_z(x,z) &= \mathfrak{I}^{1/2} \sum_{n=-\infty}^{+\infty} \left[L_n(z) e_z^{(L)}(x - x_n^{(L)}) + R_n(z) e_z^{(R)}(x - x_n^{(R)}) \right] e^{i\beta_0 z} + \\
&\quad + \delta E_z e^{i\beta_0 z} + o(s^{5/2}), \qquad (5.9)
\end{aligned}$$

and assume that

$$\left| \sqrt{\chi_3}\mathfrak{I} L_n e_{x,z}^{(L,R)} \right|, \ \left| \sqrt{\chi_3}\mathfrak{I} R_n e_{x,z}^{(L,R)} \right| \sim o(s^{1/2}), \tag{5.10}$$

$$|\epsilon_b|, \ e^{-q_d a_d}, \ e^{-q_m a_m} \sim o(s), \tag{5.11}$$

$$\left| \sqrt{\chi_3}\mathfrak{I} \partial_z L_n e_{x,z}^{(L,R)} \right|, \ \left| \sqrt{\chi_3}\mathfrak{I} \partial_z R_n e_{x,z}^{(L,R)} \right|, \ |\sqrt{\chi_3}\mathcal{N}_{x,z}| \sim o(s^{3/2}), \tag{5.12}$$

where $q_d^2 = \beta_0^2 - \epsilon_d$, $q_m^2 = \beta_0^2 - \epsilon'_m$ and $x_n^{(L)}, x_n^{(R)}$ are the positions of the left and right interfaces of the nth metallic stripe, respectively. The SPP amplitudes

$L_n(z), R_n(z)$ and the mode profiles $\vec{e}_{L,R}$ are dimensionless. The physical dimensions are carried by the constant $\mathfrak{I}^{1/2}$ (measured in V/m) that will be determined later. At the $o(s^{1/2})$ order, for every nth metal stripe, Maxwell equations provide

$$\hat{\mathfrak{L}}_k \vec{e}_k = 0, \tag{5.13}$$

where $\vec{e}_k$ are the uncoupled linear mode profiles $\vec{e}_k = (e_x^{(k)} \; e_z^{(k)})^T$, the labels $k = L, R$ represent the left (DM) and right (MD) SPPs, respectively, and

$$\hat{\mathfrak{L}}_k = \begin{pmatrix} \beta_0^2 - \epsilon_k & i\beta_0 \partial_x \\ i\beta_0 \partial_x & -\epsilon_k - \partial_{xx}^2 \end{pmatrix}. \tag{5.14}$$

The dielectric susceptibility profiles $\epsilon_k = \epsilon_{L,R}$, schematically depicted in Fig. 5.2, are explicitly given by

$$\epsilon_L = \epsilon'_m \theta\left(x - x_n^{(L)}\right) + \epsilon_d \theta\left(x_n^{(L)} - x\right), \tag{5.15}$$

$$\epsilon_R = \epsilon'_m \theta\left(x_n^{(R)} - x\right) + \epsilon_d \theta\left(x - x_n^{(R)}\right), \tag{5.16}$$

where $\theta(x)$ is the Heaviside step function. BCs at $o(s^{1/2})$ order require the continuity of $e_z^{(k)}(x - x_n^{(k)})$ and $\epsilon_k e_x^{(k)}(x - x_n^{(k)})$ at $x = x_n^{(k)}$ $(k = L, R)$:

$$\epsilon_d e_x^{(L)}(0^-) = \epsilon'_m e_x^{(L)}(0^+), \tag{5.17}$$

$$e_z^{(L)}(0^-) = e_z^{(L)}(0^+), \tag{5.18}$$

$$\epsilon'_m e_x^{(R)}(0^-) = \epsilon_d e_x^{(R)}(0^+), \tag{5.19}$$

$$e_z^{(R)}(0^-) = e_z^{(R)}(0^+). \tag{5.20}$$

Note that $\vec{e}_L, \vec{e}_R$ are defined as functions of $\tilde{x} = x - x_n^{(L)}$ and $\tilde{x} = x - x_n^{(R)}$, respectively. Thus, BCs for the continuity of $\epsilon_a \mathcal{E}_x, \mathcal{E}_z$ at the interfaces $x = x_n^{(L)}, x = x_n^{(R)}$ correspond to the continuity of the mode components $\epsilon_L e_x^{(L)}(\tilde{x})$, $\epsilon_R e_x^{(R)}(\tilde{x})$, $e_z^{(L)}(\tilde{x})$, $e_z^{(R)}(\tilde{x})$ at $\tilde{x} = 0$. Eq. (5.13) can be solved straightforwardly, yielding the mode profiles $\vec{e}_{L,R}$:

$$\begin{aligned} \vec{e}_L(x - x_n^{(L)}) \;\; = \;\; & \begin{pmatrix} -\dfrac{i\beta_0}{q_d} \\ 1 \end{pmatrix} e^{q_d(x - x_n^{(L)})} \theta\left(x_n^{(L)} - x\right) + \\ & + \begin{pmatrix} \dfrac{i\beta_0}{q_m} \\ 1 \end{pmatrix} e^{-q_m(x - x_n^{(L)})} \theta\left(x - x_n^{(L)}\right), \end{aligned} \tag{5.21}$$

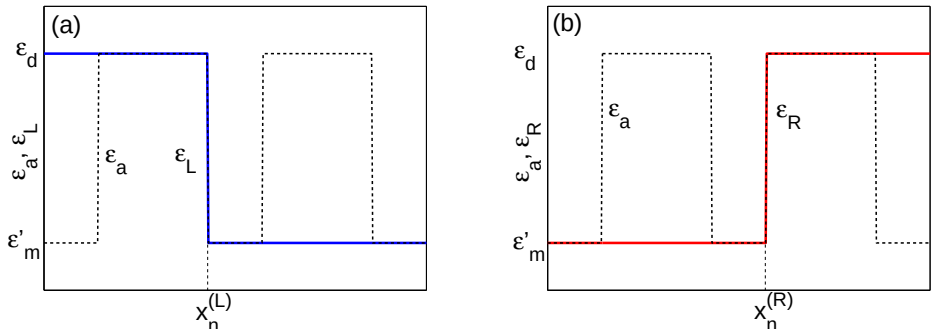

Figure 5.2: Schematic representation of the single interface dielectric susceptibility profiles: (a) ϵ_L (DM: $x = x_n^{(L)}$ interface, blue step profile) and (b) ϵ_R (MD: $x = x_n^{(R)}$ interface, red step profile). In both figures, the dashed black line corresponds to the periodic dielectric susceptibility profile ϵ_a.

$$\vec{e}_R(x - x_n^{(R)}) = \begin{pmatrix} -\dfrac{i\beta_0}{q_m} \\ 1 \end{pmatrix} e^{q_m(x-x_n^{(R)})}\theta\left(x_n^{(R)} - x\right) + \\ + \begin{pmatrix} \dfrac{i\beta_0}{q_d} \\ 1 \end{pmatrix} e^{-q_d(x-x_n^{(R)})}\theta\left(x - x_n^{(R)}\right). \tag{5.22}$$

Further, inserting Eqs. (5.21,5.22) into Eqs. (5.17-5.20), one achieves the linear dispersion law for SPPs at a generic single interface (DM/MD)

$$\beta_0 = \sqrt{\frac{\epsilon_d \epsilon'_m}{\epsilon_d + \epsilon'_m}}. \tag{5.23}$$

At the $o(s^{3/2})$ order, the linearized Maxwell equations for the residual field $\delta\vec{E} = (\delta E_x \ \delta E_z)^T$ of the nth metallic stripe yield

$$\hat{\mathcal{L}}_a \delta\vec{E} + \mathfrak{I}^{1/2}\hat{\mathcal{L}}_a \left[R_{n-1}\vec{e}_R(x - x_{n-1}^{(R)}) + L_n\vec{e}_L(x - x_n^{(L)}) + R_n\vec{e}_R(x - x_n^{(R)}) + \right. \\ \left. + L_{n+1}\vec{e}_L(x - x_{n+1}^{(L)})\right] + \mathfrak{I}^{1/2}\hat{F}\left[L_n\vec{e}_L(x - x_n^{(L)}) + R_n\vec{e}_R(x - x_n^{(R)})\right] + \\ -\mathfrak{I}^{3/2}|L_n|^2 L_n\vec{N}[\vec{e}_L(x - x_n^{(L)})] - \mathfrak{I}^{3/2}|R_n|^2 R_n\vec{N}[\vec{e}_R(x - x_n^{(R)})] = 0, \tag{5.24}$$

where

$$\hat{F} = \begin{pmatrix} -\epsilon_b - 2i\beta_0\partial_z & \partial_{xz}^2 \\ \partial_{xz}^2 & -\epsilon_b \end{pmatrix}, \tag{5.25}$$

$$\vec{N}[\vec{e}\,] \;=\; \frac{1}{2}\chi_3\left[|\vec{e}\,|^2\vec{e}+\frac{1}{2}(\vec{e}\cdot\vec{e}\,)\vec{e}^{\,*}\right]. \tag{5.26}$$

In the derivation of this equation for the residual field $\delta\vec{E}$ of the nth metal stripe, only the contributions from nearest SPP neighbours were considered. Note also that the linear operator

$$\hat{\mathfrak{L}}_a = \begin{pmatrix} \beta_0^2-\epsilon_a & i\beta_0\partial_x \\ i\beta_0\partial_x & -\epsilon_a-\partial_{xx}^2 \end{pmatrix} \tag{5.27}$$

is different from $\hat{\mathfrak{L}}_{L,R}$. Indeed, $\hat{\mathfrak{L}}_a$ depends on the complete dielectric susceptibility profile ϵ_a instead of the single interface profiles $\epsilon_{L,R}$, see Fig. 5.2. As a result, the linear $o(s^{1/2})$ order modes $\vec{e}_L, \vec{e}_R$ are not eigenvectors of the operator $\hat{\mathfrak{L}}_a$, which accounts for the coupling terms.

Following the same procedure described in chapter 4, we take the scalar product of Eq. (5.24) with the single interface linear modes $\vec{e}_L, \vec{e}_R$. The nonlinear BCs accounting for the nearest neighbours coupling, loss and nonlinearity are explicitly given by

$$\epsilon_d\delta E_x(x_n^{(L)^-}) + \mathfrak{I}^{1/2}R_{n-1}e_x^{(R)}(a_d) + \mathfrak{I}^{3/2}|L_n|^2L_nN_x[\vec{e}_L(0^-)] = \epsilon_m'\delta E_x(x_n^{(L)^+}) + \\ +\mathfrak{I}^{1/2}R_ne_x^{(R)}(-a_m) + i\epsilon_m''\mathfrak{I}^{1/2}L_ne_x^{(L)}(0^+), \tag{5.28}$$

$$\epsilon_m'\delta E_x(x_n^{(R)^-}) + \mathfrak{I}^{1/2}L_ne_x^{(R)}(a_m) + i\epsilon_m''\mathfrak{I}^{1/2}R_ne_x^{(R)}(0^-) = \epsilon_d\delta E_x(x_n^{(R)^+}) + \\ +\mathfrak{I}^{1/2}L_{n+1}e_x^{(R)}(-a_d) + \mathfrak{I}^{3/2}|R_n|^2R_nN_x[\vec{e}_L(0^+)], \tag{5.29}$$

$$\delta E_z(x_n^{(L)^-}) + \mathfrak{I}^{1/2}R_{n-1}e_z^{(R)}(a_d) = \delta E_z(x_n^{(L)^+}) + \mathfrak{I}^{1/2}R_ne_z^{(R)}(-a_m), \tag{5.30}$$

$$\delta E_z(x_n^{(R)^-}) + \mathfrak{I}^{1/2}L_ne_z^{(L)}(a_m) = \delta E_z(x_n^{(R)^+}) + \mathfrak{I}^{1/2}L_{n+1}e_z^{(L)}(-a_d). \tag{5.31}$$

Eqs. (5.28-5.31) enter the off-integral terms arising from integration by parts, which is applied to calculate the scalar products, as explained in detail in chapter 4. Note that while the residual field $\delta\vec{E}(x)$ is defined as a function of x, the left and right linear modes $\vec{e}_L(x-x_n^{(L)}), \vec{e}_R(x-x_n^{(R)})$ are defined as functions of $x-x_n^{(L)}$ and $x-x_n^{(R)}$, respectively. The coupling coefficients through dielectric κ_d and metallic κ_m media ensue from the overlap integrals

$$\mathcal{O}_d \;=\; \int_{-\infty}^{+\infty} dx\vec{e}_R^{\,*}(x-x_{n-1}^{(R)})\cdot\hat{\mathfrak{L}}_a\vec{e}_L(x-x_n^{(L)}) =$$

$$= \int_{-\infty}^{+\infty} dx \Delta\epsilon_L \vec{e}_R^*(x - x_{n-1}^{(R)}) \cdot \vec{e}_L(x - x_n^{(L)}), \tag{5.32}$$

$$\mathcal{O}_m = \int_{-\infty}^{+\infty} dx \vec{e}_L^*(x - x_n^{(L)}) \cdot \hat{\mathcal{L}}_a \vec{e}_R(x - x_n^{(R)}) =$$

$$= \int_{-\infty}^{+\infty} dx \Delta\epsilon_R \vec{e}_L^*(x - x_n^{(L)}) \cdot \vec{e}_R(x - x_n^{(R)}), \tag{5.33}$$

where $\Delta\epsilon_{L,R} = \epsilon_a - \epsilon_{L,R}$. The integral expression for the coupling coefficients κ_d, κ_m is given by

$$\kappa_d = \frac{1}{2}\mathcal{O}_d \times \left\{ \int_{-\infty}^{+\infty} dx Re[\vec{e}_L \times \vec{h}_L^*] \right\}^{-1}, \tag{5.34}$$

$$-\kappa_m = \frac{1}{2}\mathcal{O}_m \times \left\{ \int_{-\infty}^{+\infty} dx Re[\vec{e}_R \times \vec{h}_R^*] \right\}^{-1}. \tag{5.35}$$

After taking the scalar products one achieves the propagation equations for left L_n and right R_n amplitudes of the nth metallic stripe

$$i\partial_z L_n + i\alpha L_n = \kappa_d R_{n-1} - \kappa_m R_n - f\Upsilon |L_n|^2 L_n, \tag{5.36}$$

$$i\partial_z R_n + i\alpha R_n = \kappa_d L_{n+1} - \kappa_m L_n - f\Upsilon |R_n|^2 R_n, \tag{5.37}$$

where f is the scaling factor $f = P/kh_y$, so that $|L_n|^2 = 1, |R_n|^2 = 1$ correspond to the peak power P and the constant $\mathcal{I}$ is set to $\mathcal{I} = P/(\epsilon_0 ckh_y)$. h_y is the characteristic length of the layered structure along the y-direction and has been introduced only for the scaling purposes. For the derivation to be valid, h_y is assumed much longer than the characteristic mode width in the x-direction. Other parameters of Eqs. (5.36,5.37) are given by

$$\alpha = \frac{\beta_0^3 \epsilon_m''}{2(\epsilon_m')^2}, \tag{5.38}$$

$$\kappa_d = \frac{2\beta_0^3}{\epsilon_d - \epsilon_m'} e^{-q_d a_d}, \tag{5.39}$$

$$\kappa_m = \frac{2\beta_0^3}{\epsilon_d - \epsilon_m'} e^{-q_m a_m}, \tag{5.40}$$

$$\Upsilon = \frac{2}{3} k^2 n_2 \epsilon_d \left[\frac{(\epsilon_m')^2}{(\epsilon_d + \epsilon_m')^2} + \frac{(\epsilon_m')^2}{2(\epsilon_d - \epsilon_m')^2} \right]. \tag{5.41}$$

For the parameters chosen, the attenuation coefficient is $\alpha \simeq 0.0026$ and corresponds to the damping length $l_a \simeq 33\mu m$. The coupling coefficients through

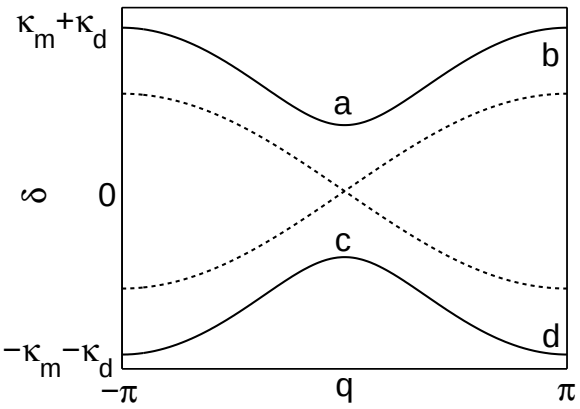

Figure 5.3: Band structure of the periodic metal-dielectric stack. Dashed lines correspond to $\kappa_d = \kappa_m$.

the metallic and dielectric media are $\kappa_d \simeq 0.029$ and $\kappa_m \simeq 0.044$ and the corresponding coupling lengths are $l_c^d \simeq 9.4\mu m$ and $l_c^m \simeq 6.2\mu m$, respectively. Υ is the effective nonlinear coefficient of SPPs propagating along a single interface, which coincides with the one derived in section 4.4.3. Continuity of the displacement transverse component $\mathcal{D}_x$ at the metal-dielectric interfaces implies a π phase jump for the transverse electric field $\mathcal{E}_x$, which is discontinuous. Hence, the couplings through metallic and dielectric media are characterised by opposite signs in front of $\kappa_{m,d}$ in Eqs. (5.36,5.37) [Guasoni et al., 2010; Nam et al., 2010a,b].

5.2 Floquet-Bloch modes and band structure

Eqs. (5.36,5.37) constitute the propagation equations resulting from the perturbative coupled mode approach for the optical field in a metal-dielectric stack. Such a set of equations, named *Discrete Nonlinear Schrödinger Equations* (DNLSEs), belongs to a class of models for diatomic lattices that are known to have a linear spectrum composed of two bands separated by the gap [Efremidis et al., 2010; Nam et al., 2010a; Vicencio and Johansson, 2009]. Linear Floquet-Bloch modes and the corresponding two-band structure are determined by setting $\Upsilon = 0$ and

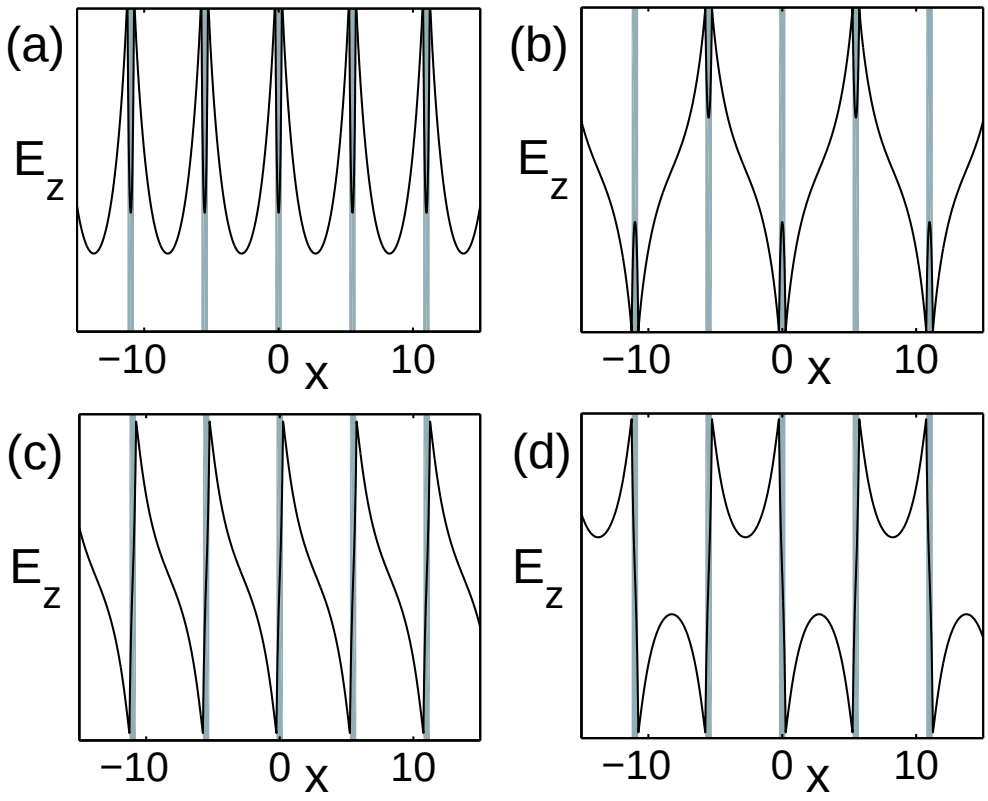

Figure 5.4: Linear Bloch modes. Letters on the panels correspond to the respectively marked points in the band structure diagram in Fig. 5.3.

making the ansatz

$$L_n = le^{iqn+i\delta z-\alpha z}, \tag{5.42}$$

$$R_n = re^{iqn+i\delta z-\alpha z}, \tag{5.43}$$

where q is the quasi-momentum in the x-direction. The secular equation of Floquet-Bloch modes is found by inserting Eqs. (5.42,5.43) into Eqs. (5.36,5.37) and requiring that the 2×2 coefficient matrix $\hat{\mathfrak{M}}$ of the system of algebraic equations for the constants l, r is singular ($det\hat{\mathfrak{M}} = 0$):

$$\delta(q) = \pm\sqrt{\kappa_m^2 + \kappa_d^2 - 2\kappa_m\kappa_d cosq}. \tag{5.44}$$

The shift of the propagation constant $\delta(q)$ constitutes the diffraction law for plasmons and is depicted in Fig. 5.3. The signs $+/-$ correspond to the upper and

lower bands, respectively, separated by the gap around $\delta = 0$. The Floquet-Bloch modes are explicitly given by Eqs. (5.42,5.43), where the constant r is

$$r = l(\kappa_m - \kappa_d e^{iq})/\delta(q), \tag{5.45}$$

and the constant l is arbitrary. The inherent structure of such linear modes can be understood by considering the two limiting cases $\kappa_m >> \kappa_d$, $\kappa_m << \kappa_d$.

In the first case ($\kappa_m >> \kappa_d$), the metal-dielectric stack is composed of thin metallic stripes of width a_m embedded in a dielectric medium and separated by the distance $a_d >> a_m$. The averaged susceptibility is positive, since the amount of metal inclusion is limited. Hence, the plasmonic structure is dielectric-like and can be thought of as a system of weakly coupled insulator-metal-insulator (IMI) (or dielectric-metal-dielectric DMD) waveguides. Every IMI waveguide supports symmetric S_n and antisymmetric A_n modes, which can be expressed as superpositions of left and right single interface SPPs in the coupled mode approach:

$$S_n = \frac{1}{2}(L_n + R_n), \tag{5.46}$$

$$A_n = \frac{1}{2}(L_n - R_n). \tag{5.47}$$

In Fig. 5.3, the coupling through the metal is assumed larger than the coupling through the dielectric, like in the case we are considering. The $q = 0$ points in the band structure correspond to the minimum $\delta = \kappa_m - \kappa_d$ for the upper band and the maximum $\delta = \kappa_d - \kappa_m$ for the lower band. Note that in the limiting case $\kappa_d \to 0$ the two bands become flat: the upper $\delta \simeq \kappa_m$ and the lower $\delta \simeq -\kappa_m$ branches represent the symmetric S_n and the antisymmetric A_n modes, respectively. If $\kappa_d \neq 0$, but still $\kappa_m >> \kappa_d$, the modes of the upper and of the lower bands resemble the symmetric and antisymmetric modes

$$S_n \simeq \frac{1}{2}(l + r)e^{iqn + i\delta_s z - \alpha z}, \tag{5.48}$$

$$A_n \simeq \frac{1}{2}(l - r)e^{iqn + i\delta_a z - \alpha z}, \tag{5.49}$$

with dispersions

$$\delta_s \simeq \kappa_m - \kappa_d \cos q, \tag{5.50}$$

$$\delta_a \simeq -\kappa_m + \kappa_d \cos q. \tag{5.51}$$

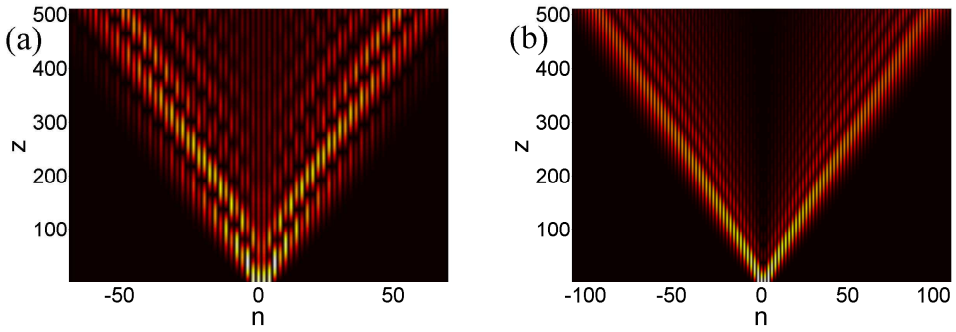

Figure 5.5: Discrete diffraction of the SPP array for (a) $\kappa_m = 0.044, \kappa_d = 0.029$ and (b) $\kappa_m = \kappa_d = 0.05$.

For the upper branch, the symmetric modes are in phase at $q = 0$ and are π out of phase at $q = \pi$, see Figs. 5.4a,b. As for the upper branch, also for the lower branch the antisymmetric modes are in phase at $q = 0$ and are π out of phase at $q = \pi$, see Figs. 5.4c,d.

The above considerations remain practical for $\kappa_m > \kappa_d$ upto $\kappa_m = \kappa_d$, where they lose validity. Indeed, as can be understood from Fig. 5.3, if $\kappa_m = \kappa_d$ the maximum of the lower band ($\delta_{max} = \kappa_d - \kappa_m$) and the minimum of the upper band ($\delta_{min} = \kappa_m - \kappa_d$) fold up at $q = 0$ and the gap closes ($\delta_{max} = \delta_{min} = 0$). Such a case corresponds to the condition where the averaged susceptibility in the x direction is null [Ciattoni et al., 2010a,b,c, 2011] and discrete diffraction is conical-like [Efremidis et al., 2010; Nam et al., 2010a]. In Fig. 5.5a,b, discrete diffraction of SPPs propagating in the metal-dielectric stack is depicted for (a) $\kappa_m = 0.044, \kappa_d = 0.029$ and (b) $\kappa_m = \kappa_d = 0.05$. Such figures represent the dynamical propagation of the intensities $|L_n(z)|^2, |R_n(z)|^2$ corresponding to the four-channel excitation at $z = 0$: $L_{-1}(0) = R_{-1}(0) = L_1(0) = R_1(0) = 1$ and $L_n(0), R_n(0) = 0$ for $n \neq \pm 1$. As reported in Ref. [Nam et al., 2010a], we also observe conical-like discrete diffraction in the degenerate regime $\kappa_m = \kappa_d$, see Fig. 5.5b.

In the opposite case $\kappa_m << \kappa_d$, the metal-dielectric stack is represented by narrow dielectric slots of width a_d embedded in a metallic medium and separated by the distance $a_m >> a_d$. The averaged susceptibility is negative, since the

amount of dielectric inclusion is limited. Thus, the plasmonic structure is metal-like and can be thought of as a system of weakly coupled metal-insulator-metal (MIM) (or dielectric-metal-dielectric DMD) waveguides. Every MIM waveguide supports symmetric S_n and antisymmetric A_n modes, which can be expressed as superpositions of left and right single interface SPPs in the coupled mode approach:

$$S_n = \frac{1}{2}(R_n + L_{n+1}), \tag{5.52}$$

$$A_n = \frac{1}{2}(R_n - L_{n+1}). \tag{5.53}$$

Note that in the limiting case $\kappa_m \to 0$ the two bands become flat and the upper $\delta \simeq \kappa_d$ and lower $\delta \simeq -\kappa_d$ bands characterise symmetric S_n and antisymmetric A_n modes, respectively. If $\kappa_m \neq 0$, but still $\kappa_m << \kappa_d$, the modes of the upper and of the lower bands resemble the symmetric and antisymmetric modes

$$S_n \simeq \frac{1}{2}(r + l)e^{iqn + i\delta_s z - \alpha z}, \tag{5.54}$$

$$A_n \simeq \frac{1}{2}(r - l)e^{iqn + i\delta_a z - \alpha z}, \tag{5.55}$$

with dispersions

$$\delta_s \simeq \kappa_d - \kappa_m \cos q, \tag{5.56}$$

$$\delta_a \simeq -\kappa_d + \kappa_m \cos q. \tag{5.57}$$

Note that, in the case $\kappa_m < \kappa_d$, the symmetric and antisymmetric modes are defined in terms of a different unit cell (dielectric slot R_n, L_{n+1}) with respect to the case $\kappa_m > \kappa_d$ (metal stripe L_n, R_n). Note also that the modes with $\kappa_d > \kappa_m$ can be straightforwarldy achieved by making the substitution $\kappa_m \longleftrightarrow \kappa_d$, which satisfies Eqs. (5.36,5.37) for the staggered mode $(L_n, R_n) \to (-R_{n-1}, L_n)$. In what follows, we consider only the case $\kappa_m > \kappa_d$, where the amount of metal is limited and the effective optical response is dielectric-like.

5.3 Discrete and gap soliton families

In this section, we study the localised solutions of Eqs. (5.36,5.37) for $\Upsilon > 0$ ($n_2 > 0$). Since the self-focusing nonlinearity increases the propagation constant

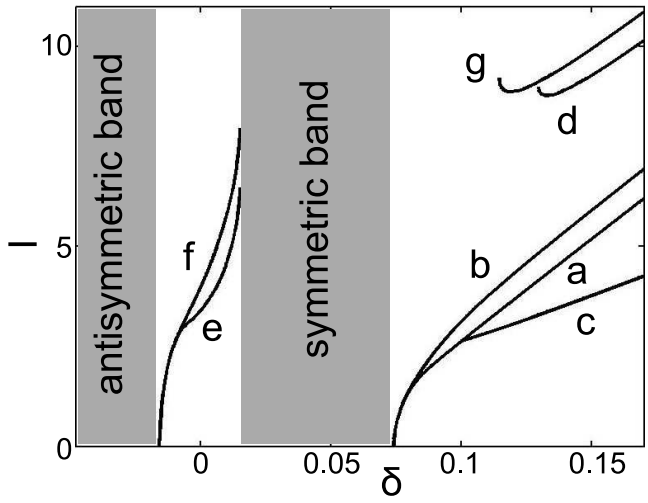

Figure 5.6: Normalized intensity $I = \sum_n (|R_n|^2 + |L_n|^2)$ vs δ for the families of discrete and gap solitons. (a), (e) and (g) families are symmetric with respect to the centre of a metal stripe and can be considered as the on-site solitons in the case $\kappa_m > \kappa_d$. Conversely, the (b), (d) and (f) soliton branches represent the off-site families centred on a dielectric stripe. The (c) branch represents the asymmetric solitons without any centre of symmetry.

of SPP waves, the formation of *discrete soliton* and *gap soliton* families is expected above the upper band and inside the bandgap, respectively.

In the analysis of discrete and gap soliton modes, we disregard the effect of the metal loss by setting $\alpha = 0$. In order to find soliton solutions of Eqs. (5.36,5.37), we substitute the ansatz

$$L_n = l_n e^{i\delta z}, \tag{5.58}$$

$$R_n = r_n e^{i\delta z}, \tag{5.59}$$

reaching a system of algebraic equations for the constants l_n, r_n

$$\delta l_n - \kappa_m r_n + \kappa_d r_{n-1} - f\Upsilon |l_n|^2 l_n = 0, \tag{5.60}$$

$$\delta r_n - \kappa_m l_n + \kappa_d l_{n+1} - f\Upsilon |r_n|^2 r_n = 0. \tag{5.61}$$

Such an algebraic system can be numerically solved by using the Newton-Raphson method, which is described in appendix B. In Fig. 5.6, the normalized

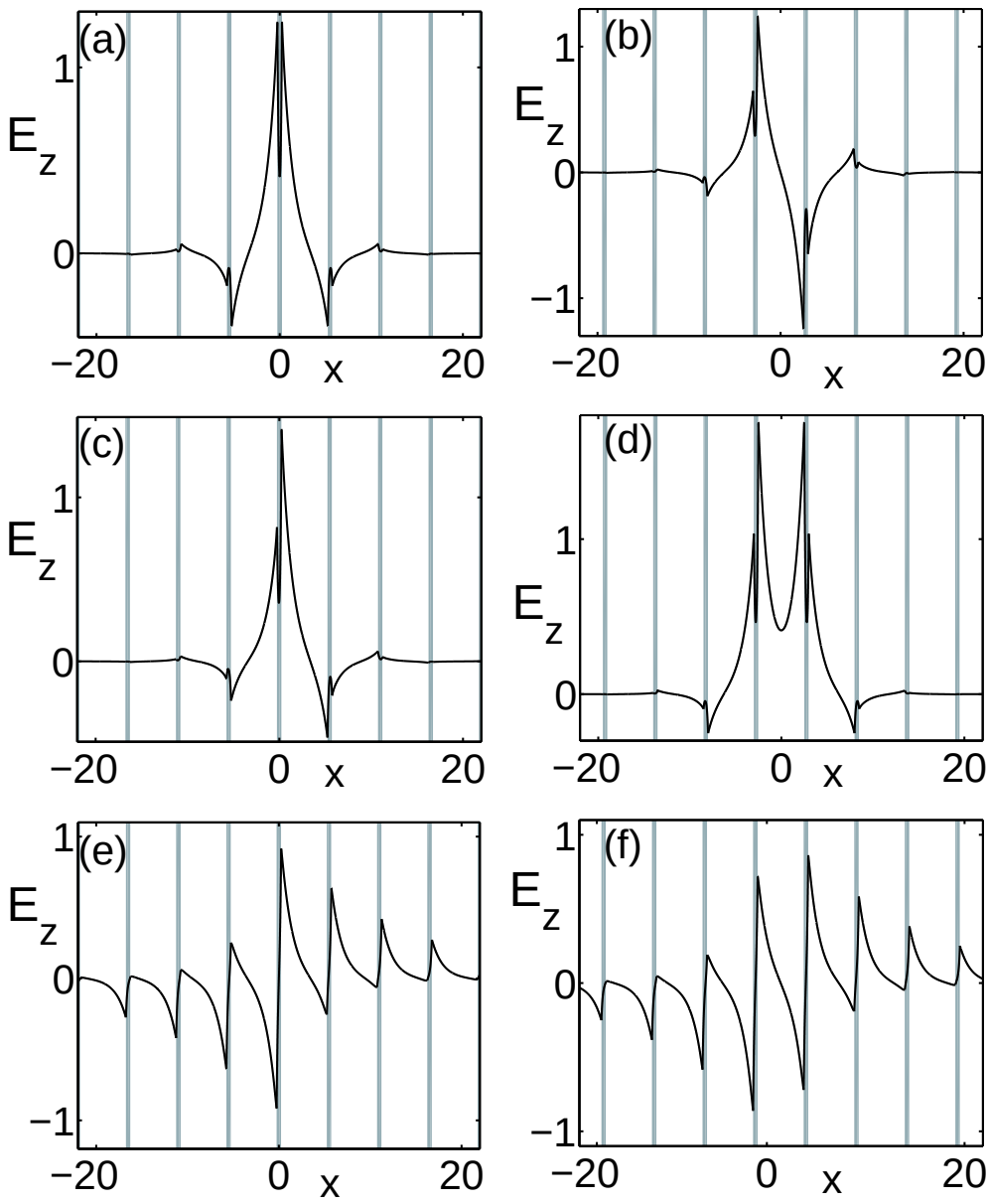

Figure 5.7: Spatial profiles of the discrete and gap solitons. Letters on the panels correspond to the respectively marked soliton branches in Fig. 5.6. $\delta = 0.114$ for solitons in (a)-(d), and $\delta = 0$ in (e) and (f).

intensity $I = \sum_n (|R_n|^2 + |L_n|^2)$ is plotted as a function of the phase shift δ in the regime $\kappa_m > \kappa_d$ for different families of discrete and gap solitons, which profiles are depicted in Fig. 5.7.

Two primary branches of discrete solitons (a, b) bifurcate from the edge of the top band at $q = \pi$ and $\delta = \kappa_m + \kappa_d$, inheriting the structure of the corresponding Floquet-Bloch modes. The a-branch soliton envelopes are symmetric with respect to the centre of a fixed metal stripe, while the b-branch envelopes are antisymmetric with respect to the centre of a dielectric slot, see Figs. 5.7a,b. Hence, since for $\kappa_m > \kappa_d$ the unit cell is the metal stripe, the a-branch represents the on-site soliton family, while the b-branch represents the off-site soliton family. Indeed, the a-branch is immediately stable after it ensues from the top of the upper linear band, while the b-branch is always unstable, as will be demonstrated in section 5.3.1. For the critical value of the total power corresponding to the point of symmetry breaking, the a-branch loses its stability in favour of the stable asymmetric soliton family (represented by the c-branch), which bifurcates from the on-site soliton family (a-branch).

The d, g soliton families have large threshold powers and their spatial structure resemble the linear Floquet-Bloch modes of the lower band. Stability properties of these families are more involved and they can be either stable or oscillatory unstable. In the unstable case, discrete solitons of the d, g families collapse to the stable asymmetric discrete soliton of the c-branch in the dynamical propagation.

Gap solitons ensue from the top of the lower band, inheriting the symmetry of the corresponding Floquet-Bloch modes. The e-branch solitons depicted in Fig. 5.7e are stable for $\delta \lesssim 0$, becoming unstable in the phase shift range $0 \lesssim \delta < \delta_{min}$, where $\delta_{min} = \kappa_m - \kappa_d$ is the bottom phase shift of the linear upper band. Gap solitons from the f-family, shown in Fig. 5.7f, are always unstable in their existence domain $\kappa_d - \kappa_m < \delta < \kappa_m - \kappa_d$. The maximum confinement of both the gap soliton e, f-branches is achieved at the gap centre $\delta = 0$.

The bifurcation picture explained above changes if the condition $\kappa_m > \kappa_d$ ceases to be valid. Indeed, discrete and gap soliton families corresponding to the case $\kappa_m < \kappa_d$ can be obtained by substituting

$$\kappa_m \longrightarrow \kappa_d, \tag{5.62}$$

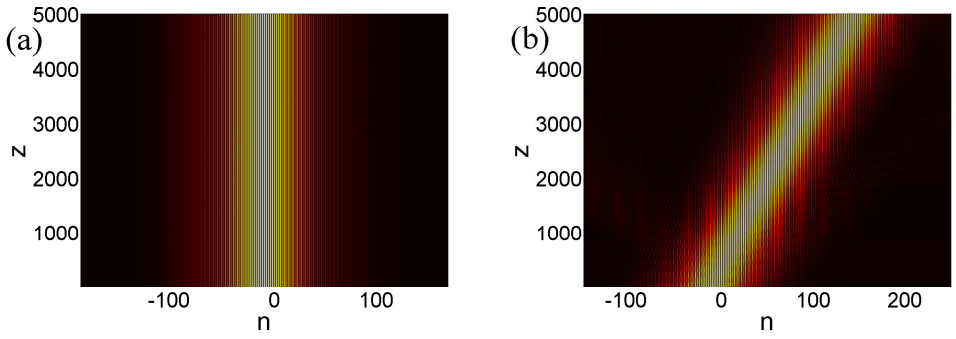

Figure 5.8: Propagation of a gap soliton for $\delta = -0.014$ and transverse momentum (a) $q = 0$ and (b) $q = 0.1$.

$$\kappa_d \rightarrow \kappa_m, \tag{5.63}$$

$$L_n \rightarrow -R_{n-1}, \tag{5.64}$$

$$R_n \rightarrow L_n. \tag{5.65}$$

In this case the bifurcation diagram coincides with the one depicted in Fig. 5.6, with the difference that the linear modes of the upper band correspond to the ones of the lower band in the $\kappa_m > \kappa_d$ case, i.e. the staggered mode.

In Fig. 5.8a, the propagation of the gap soliton $L_n, R_n = \xi_n, \zeta_n$ is depicted for $\delta = -0.014$. Note that, for such a δ-value, the on-site and off-site e, f-soliton branches merge together, so that for a fixed power $I = \sum_n (|R_n|^2 + |L_n|^2)$ they are characterised by a practically identical propagation constant δ (see Fig. 5.6). Hence, the Peierls-Nabarro barrier [Kivshar, 1993; Krolikowski and Kivshar, 1996; Morandotti et al., 1999a] is relatively small and the gap soliton can propagate in a tilted direction. Fig. 5.8b plots tilted propagation of the gap soliton $L_n, R_n = \xi_n e^{iqn}, \zeta_n e^{iqn}$ for $\delta = -0.014$ and $q = 0.1$. Note that tilted propagation can be achieved also for discrete solitons in the range where a, b families merge together.

5.3.1 Stability

The stability properties of discrete and gap soliton families, which have been discussed qualitatively in the previous section, can be quantitatively determined by perturbing every soliton solution $L_n, R_n = \xi_n, \zeta_n$ with small amplitude waves

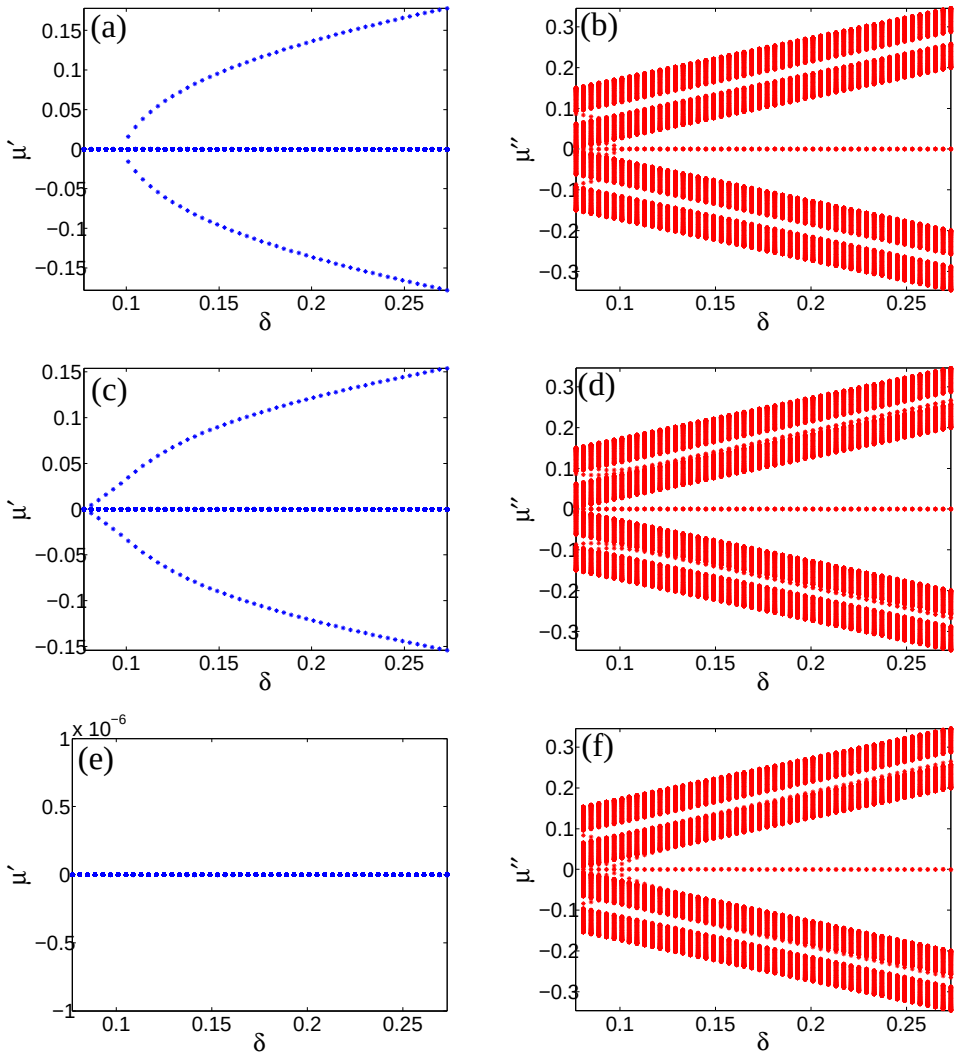

Figure 5.9: Instability eigenvalues μ for the discrete soliton branches: (a,b) a-branch, (c,d) b-branch and (e,f) c-branch. Figures on the left (a,c,e) represent the growth rates μ', while figures on the right (b,d,f) show the imaginary parts μ''.

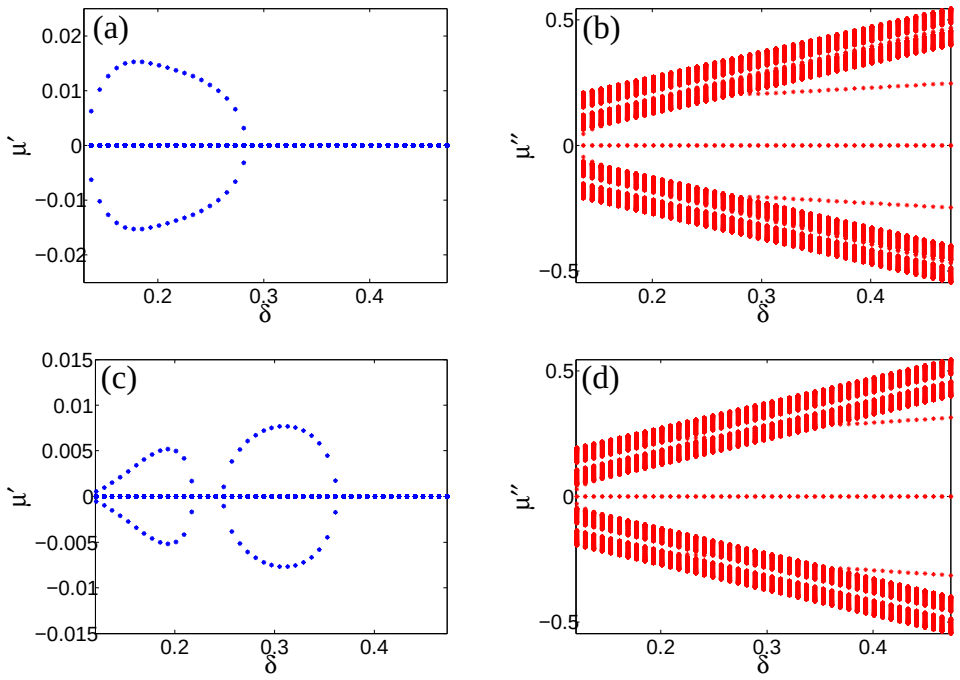

Figure 5.10: Real (a,c) (μ') and imaginary (b,d) (μ'') parts of the unstable eigenvalue μ for (a,b) d-branch and (c,d) g-branch of discrete solitons.

a_n, b_n, c_n, d_n:

$$L_n = \left[\xi_n + a_n e^{\mu z} + b_n^* e^{\mu^* z}\right] e^{i\delta z}, \tag{5.66}$$

$$R_n = \left[\zeta_n + c_n e^{\mu z} + d_n^* e^{\mu^* z}\right] e^{i\delta z}, \tag{5.67}$$

where

$$|a_n|, |b_n| << |\xi_n|, \tag{5.68}$$

$$|c_n|, |d_n| << |\zeta_n|, \tag{5.69}$$

and the real part of the μ parameter ($\mu' = Re\mu$) determines the growth rate of small perturbations.

Inserting Eqs.(5.66,5.67) into Eqs.(5.36,5.37) ($\alpha = 0$) one gets a homogeneous system of linearized algebraic equations for the small amplitudes a_n, b_n, c_n, d_n. Non-trivial solutions exist only if the determinant of the coefficient matrix $\hat{\mathcal{C}}$ is null:

$$det\hat{\mathcal{C}} = 0. \tag{5.70}$$

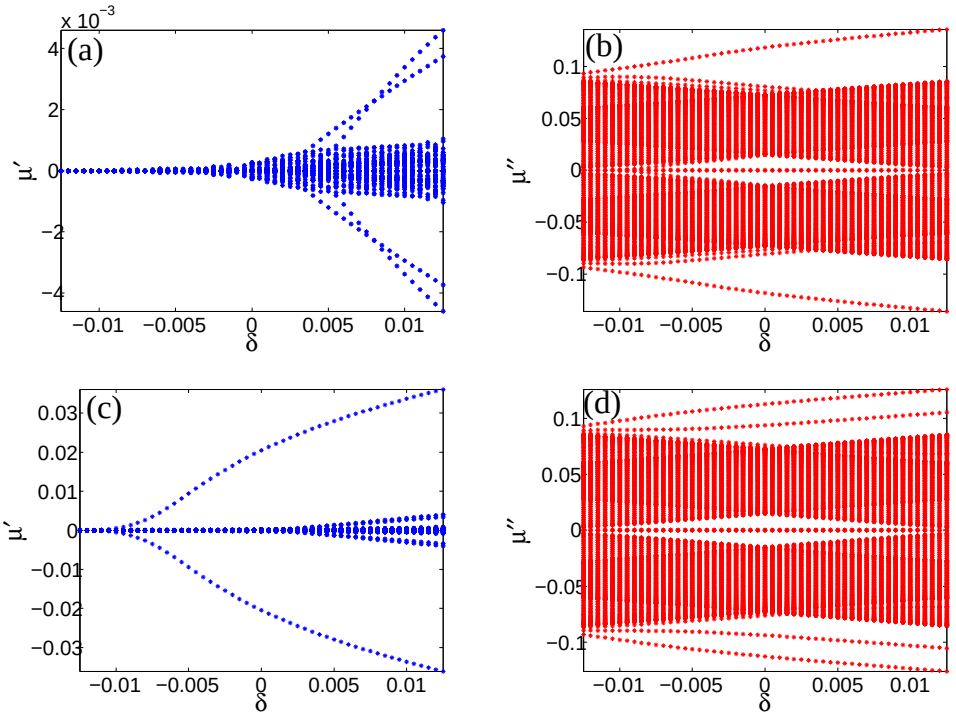

Figure 5.11: Real (a,c) (μ') and imaginary (b,d) (μ'') parts of the unstable eigenvalue μ for (a,b) e-branch and (c,d) f-branch of gap solitons.

Solving the above secular equation by the Newton-Raphson method allows for the determination of the instability eigenvalues μ. If such eigenvalues are purely imaginary, then the gap/discrete soliton is stable, otherwise it is unstable.

Results of the stability analysis in the $\kappa_m > \kappa_d$ regime are plotted in Figs. 5.9, 5.10, 5.11.

Figs. 5.9a,b depict the real μ' and imaginary μ'' parts of the instability eigenvalues for the discrete solitons belonging to the a-branch. Note that for $\delta \lesssim 0.1$ the growth rate is null $max[\mu'] = 0$, while for $\delta \gtrsim 0.1$ a distinct eigenvalue is characterised by the positive real part $\mu' > 0$.

As a result, the a-branch is stable for $\delta \lesssim 0.1$ and loses its stability for $\delta \gtrsim 0.1$ in favour of the c-branch family, which bifurcates from the a-branch at $\delta \simeq 0.1$ (see Fig. 5.6). The real μ' and imaginary μ'' parts of the instability eigenvalues for the c-branch are plotted in Figs. 5.9e,f. Note that for this branch the growth

rate is null $max[\mu'] = 0$ and, as a consequence, the discrete solitons of the c-family are always stable.

The stability picture of the b-family is represented in Figs. 5.9c,d. This family is always unstable in its existence domain, since for every δ there exists an eigenvalue μ with non-zero real part: $max[\mu'] = g > 0$. Indeed, the b-branch discrete solitons represent off-site soliton solutions, which are centred on the dielectric slot (the unit cell is the metal stripe in the case considered $\kappa_m > \kappa_d$).

Figs. 5.10 depict the stability analysis of discrete solitons from the d, g-families, respectively. Discrete solitons from such branches inherit the spatial structure of the lower linear band and arise after a certain threshold δ_{th} (see Fig. 5.6). In turn, their stability properties are more involved and depend on the particular value of the coupling coefficients κ_m, κ_d. For the values chosen ($\kappa_d = 0.029, \kappa_m = 0.044$) one can observe the presence of the stability and instability regions in both of the d, g-branches.

The instability picture for the gap solitons of e, f-branches is represented in Fig. 5.11. Gap solitons from the e-family retain the structure of the lower linear band (see Fig. 5.7e) and are centred on a metal stripe. Thus, they constitute the on-site soliton solutions and are stable in the lower half of the gap $\delta \lesssim 0$, becoming unstable for $0 \lesssim \delta < \kappa_m - \kappa_d$. Conversely, the f-branch corresponds to the off-site soliton solutions and is always unstable.

5.4 Concluding remarks

In this chapter we have used the perturbative theory derived in chapter 4 to model the optical propagation of SPPs in a metal-dielectric stack in the tight binding approximation. The coupled mode theory allows predicting a characteristic two-band structure ensuing from the different couplings through metallic and dielectric regions. Importantly, the coupling coefficients through the metal and the dielectric layers are not only different in modulus but also in sign, confirming the results reported in Refs. [Guasoni et al., 2010; Xu and Aitchison, 2009]. Using the coupled mode theory, we have been able to demonstrate conical-like diffraction, which finds confirmation in Ref. [Nam et al., 2010a]. The various families of discrete and gap plasmon-solitons have been numerically calculated

and their stability properties have been analysed. We have been able to identify two main regimes: the dielectric-like regime (where the coupling through the dielectric layer is much stronger than the coupling through the metallic layer) and the metallic-like regime (where the coupling through the dielectric layer is much weaker than the coupling through the metallic layer). In the metallic-like regime, the asymmetric discrete soliton bifurcates from the antisymmetric branch, finding confirmation in Ref. [Salgueiro and Kivshar, 2010]. The original results reported in this chapter have been published in Ref. [Marini et al., 2010].

Chapter 6

Stable plasmon-solitons in metallic stripes

As discussed in the previous chapters, the diffraction of light constitutes a fundamental barrier for the realisation of nano-scaled all-optical devices in the subwavelength regime. In the second chapter, we described the optical propagation in basic plasmonic structures, highlighting the importance of the metal loss [Gramotnev and Bozhevolnyi, 2010; Maier, 2007] and reviewing the literature on amplified SPPs [Gather et al., 2010; Nezhad et al., 2004; Noginov et al., 2008a]. Further, in chapter 3, we have considered the nonlinear propagation of amplified SPPs, deriving the nonlinear dispersion law for the SPP plane waves unbound in the transverse direction and the Ginzburg-Landau (GL) equation for the dynamical propagation of SPPs.

Although the SPPs are inherently confined in the transverse x-direction perpendicular to the $y-z$ metal-dielectric interface, they can diffract in the in-plane y-direction perpendicular to the z propagation axis [Gramotnev and Bozhevolnyi, 2010]. In order to achieve localised light beams in both of the transverse x, y directions, several two-dimensional geometries have been proposed and realised [Bozhevolnyi, 2008; Bozhevolnyi et al., 2005, 2006a; Pile and Gramotnev, 2004; Pile et al., 2005; Yatsui et al., 2001].

An interesting alternative to such two-dimensional approaches is to use plasmon-solitons in one-dimensional geometries, where the in-plane diffraction is suppressed by the nonlinear self-focusing [Davoyan et al., 2009b; Feigenbaum and

Orenstein, 2007]. However, ohmic losses from metallic components are responsible for the soliton attenuation, which occurs over a very short lengthscale ($L_A \approx 20\mu m$ at optical wavelengths). Nevertheless, by embedding amplifying inclusions in the dielectric medium, it is possible to achieve plasmon-solitons where the diffraction vs nonlinearity balance is complemented with the gain vs loss compensation [Akhmediev and Ankiewicz, 1997]. Such *dissipative plasmon solitons* inherently stem from the bistability of two spatially homogeneous solutions: the zero backround and the nonlinear plane wave solutions. The explicit expressions for the plasmon-solitons have been derived in chapter 3, demonstrating that substantial instabilities develop both in the core and in the background. These instabilities are common in the third order GL systems, which are characterised by a *super-critical* transition from the trivial zero-solution to the nonlinear plane wave solution [Akhmediev and Ankiewicz, 1997].

Accounting for the higher order nonlinearities in generalized GL models can lead to different behaviours. For example, the transition can become *sub-critical* if the complex quintic nonlinearity is included [Akhmediev and Ankiewicz, 1997; Fauve and Thual, 1990; Malomed, 1987]. In this case, the subcritical bifurcation ensues from the competition of the third-order nonlinear gain with the quintic nonlinear loss, which ensures the stability of the system [Fauve and Thual, 1990]. However, the two-level atom nonlinearity for amplifying dielectrics [Boyd, 2003] (see appendix A) provides always a third-order nonlinear loss and the approach above is not viable.

Alternatively, the core and background instabilities can be drained by coupling the active system with a purely passive waveguide [Atai and Malomed, 1996; Firth and Paulau, 2010; Malomed and Winful, 1996]. In this case, the coupling with the passive waveguide shifts the instability threshold and the bifurcation point with respect to the uncoupled case. As a consequence, it is possible to achieve the sub-critical bifurcation also for the third-order coupled GL system, characterised by the linear gain and the nonlinear loss.

In what follows, we model the optical propagation in an active dielectric-metal-dielectric structure, which is schematically depicted in Fig. 6.1. SPPs at the two active dielectric-metal (DM) and passive metal-dielectric (MD) single interfaces are assumed weakly interacting; as a consequence, the coupled mode

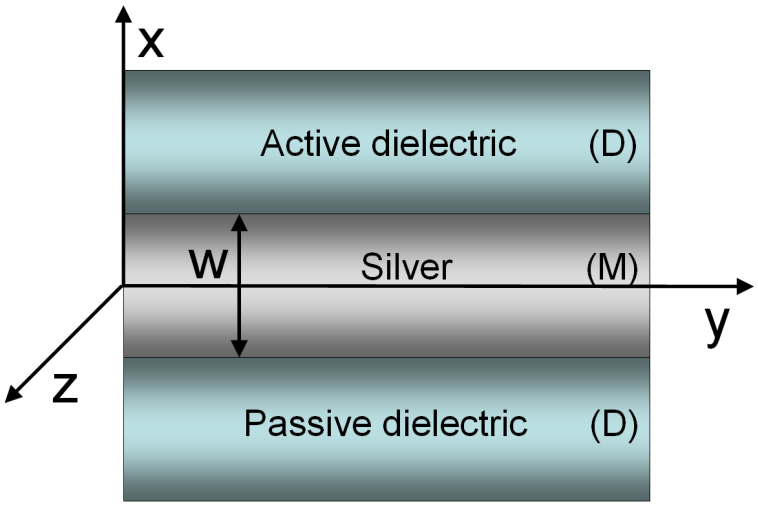

Figure 6.1: Schematic representation of a dielectric-metal-dielectric structure composed of a metal stripe and two active and passive dielectric media.

approach described in chapter 5 can be adopted. In such an active geometry, the system of *discrete nonlinear Schrödinger equations* (DNLSEs) derived in the previous chapter transforms into two coupled Ginzburg-Landau (GL) equations for the weakly coupled SPPs propagating at the interfaces $x = \pm w/2$. The analysis of the transition from the zero background to the spatially homogeneous solution reveals the existence of a sub-critical region where *stable* propagation of SPP solitons is achievable.

6.1 Coupled mode derivation of the Ginzburg-Landau system

As done in the previous chapters, we start our analysis from the time independent Maxwell equations for the monochromatic fields $\vec{\mathcal{E}}e^{-i\omega t}, \vec{\mathcal{H}}e^{-i\omega t}$. In the complex formalism, the physical electric and magnetic fields are provided by the real parts $Re[\vec{\mathcal{E}}e^{-i\omega t}], Re[\vec{\mathcal{H}}e^{-i\omega t}]$. Combining the curl equations one gets

$$\nabla \times \nabla \times \vec{\mathcal{E}} = \epsilon(x)\vec{\mathcal{E}}, \tag{6.1}$$

where the spatial coordinates are rescaled to $k^{-1} = \lambda/2\pi$ and λ is the vacuum wavelength. We assume that the SPPs at every metal-dielectric interface $x = \pm w/2$ propagate in the z-direction and diffract in the transverse in-plane y-direction (see Fig. 6.1). The dielectric susceptibility profile is

$$\epsilon(x) = \epsilon_P \theta(-x - w/2) + \epsilon_m \left[\theta(x + w/2) - \theta(x - w/2)\right] + \epsilon_A \theta(x - w/2), \quad (6.2)$$

where $\theta(x)$ is the Heaviside step function and $\epsilon_m = \epsilon'_m + i\epsilon''_m$ is the dielectric constant inside the metal ($\epsilon'_m < 0$, $\epsilon''_m > 0$). The optical response of the gain material lying on the top of the metal stripe is modelled through the two-level system in the small-saturation limit

$$\epsilon_A = (\epsilon_d + \alpha/2) + i\epsilon''_a + \chi_3 |\vec{\mathcal{E}}|^2, \quad (6.3)$$

which was introduced in chapter 1 and is described with more detail in appendix A. In the expression above, $\epsilon''_a < 0$ represents the linear gain of the amplifying medium and $\chi_3 = \chi'_3 + i\chi''_3$ is the complex nonlinear susceptibility, characterised by the nonlinear absorption $\chi''_3 > 0$ and the self-focusing/self-defocusing term χ'_3 that can be either positive or negative, depending on the sign of the detuning δ. On the other hand, ϵ_P is the real dielectric susceptibility of the passive medium

$$\epsilon_P = \epsilon_d - \alpha/2. \quad (6.4)$$

The asymmetric parameter α is assumed small and the IMI structure depicted in Fig. 6.1 is symmetric in the leading order of our perturbation theory. Corrections due to asymmetry $|\alpha| << \epsilon_d$ are accounted for in the first order. Such an assumption is not essential for the derivation below, but simplifies considerably the analytical calculations.

Introducing the small dummy parameter s, we assume that

$$\epsilon''_m, |\alpha|, |\epsilon''_a|, |\chi_3 \vec{\mathcal{E}}|^2 \sim o(s). \quad (6.5)$$

In addition, we also assume that the width w of the metal stripe is much longer than the electromagnetic field penetration, so that we can apply the coupled mode theory developed in the previous chapter. Neglecting the dielectric asymmetry

(α), gain (ϵ_a''), nonlinearity ($\chi_3|\vec{\mathcal{E}}|^2$) and metal loss ($\epsilon_m''$), one obtains straightforwardly the uncoupled mode profiles for the linear SPPs propagating at the two interfaces $x = \pm w/2$:

$$\begin{aligned}
\vec{e}_a = \begin{pmatrix} e_x^a \\ e_z^a \end{pmatrix} &= \begin{pmatrix} i\dfrac{\beta}{q_m} \\ 1 \end{pmatrix} e^{-q_m(x+w/2)}\theta(x+w/2) + \\
&- \begin{pmatrix} i\dfrac{\beta}{q_d} \\ -1 \end{pmatrix} e^{q_d(x+w/2)}\theta(-x-w/2), \qquad (6.6) \\
\vec{e}_p = \begin{pmatrix} e_x^p \\ e_z^p \end{pmatrix} &= \begin{pmatrix} i\dfrac{\beta}{q_d} \\ 1 \end{pmatrix} e^{-q_d(x-w/2)}\theta(x-w/2) + \\
&- \begin{pmatrix} i\dfrac{\beta_0}{q_m} \\ -1 \end{pmatrix} e^{q_m(x-w/2)}\theta(-x+w/2), \qquad (6.7)
\end{aligned}$$

where $q_d^2 = \beta^2 - \epsilon_d$, $q_m^2 = \beta^2 - \epsilon_m'$ and a, p label the metal surfaces adjacent to active and passive media, respectively. Such linear modes are characterised by the single-interface SPP dispersion

$$\beta = \sqrt{\frac{\epsilon_d \epsilon_m'}{\epsilon_d + \epsilon_m'}}. \qquad (6.8)$$

In the coupled mode approach, in order to solve Eq. (6.1), one takes the ansatz

$$\begin{aligned}
\mathcal{E}_x &= \left[\psi_p(y,z)e_x^p(x) + \psi_a(y,z)e_x^a(x) + \delta E_x + o(s^{5/2})\right] e^{i\beta z}, \qquad (6.9) \\
\mathcal{E}_y &= \left[\phi_p(y,z)e_y^p(x) + \phi_a(y,z)e_y^a(x) + o(s^2)\right] e^{i\beta z}, \qquad (6.10) \\
\mathcal{E}_z &= \left[\psi_p(y,z)e_z^p(x) + \psi_a(y,z)e_z^a(x) + \delta E_z + o(s^{5/2})\right] e^{i\beta z}, \qquad (6.11)
\end{aligned}$$

where the amplitudes $\psi_{p,a} \sim o(s^{1/2})$ and $\phi_{p,a} \sim o(s)$ are slow functions of y, z, such that $\partial_z \sim o(s)$, $\partial_y \sim o(s^{1/2})$. In addition to the coupled mode approach derived in chapter 5, we here include also diffraction as done in chapters 3,4. Hence, the transverse $\mathcal{E}_y \sim o(s)$ amplitude due to the finite beam size is non-zero, but it is assumed much smaller than the $\mathcal{E}_{x,z} \sim o(s^{1/2})$ amplitudes. We do not provide here all the details of the derivation, which can be found in chapters

4,5. Equations for the $o(s^{3/2})$ order residual field $\delta\vec{E} = (\delta E_x \ \delta E_z)^T$ accounting for gain, loss and nonlinearity are given by

$$\hat{\mathcal{L}}\delta\vec{E} = (\hat{\mathcal{F}} - \hat{\mathcal{L}})(\psi_p\vec{e}_p + \psi_a\vec{e}_a) - \vec{b}, \tag{6.12}$$

where $\vec{e}_{p,a} = (e_x^{p,a} \ e_x^{p,a})^T$ and

$$\hat{\mathcal{L}} = \begin{pmatrix} \beta^2 - \epsilon^{(0)} & i\beta\partial_x \\ i\beta\partial_x & -\epsilon^{(0)} - \partial_{xx}^2 \end{pmatrix}, \tag{6.13}$$

$$\hat{\mathcal{F}} = \begin{pmatrix} 2i\beta\partial_z + \partial_{yy}^2 + \delta\epsilon & -\partial_{xz}^2 \\ -\partial_{xz}^2 & \partial_{yy}^2 + \delta\epsilon \end{pmatrix}, \tag{6.14}$$

$$\vec{b} = \begin{pmatrix} \partial_y\phi_p\partial_x e_y^p + \partial_y\phi_a\partial_x e_y^a \\ i\beta\partial_y\phi_p e_y^p + i\beta\partial_y\phi_a e_y^a \end{pmatrix}. \tag{6.15}$$

In the expressions above, the dielectric susceptibility profile was set to $\epsilon = \epsilon^{(0)} + \delta\epsilon$, where

$$\begin{aligned} \epsilon^{(0)} &= \epsilon'_m\left[\theta(x + w/2) - \theta(x - w/2)\right] + \\ &\quad + \epsilon_d\left[\theta(-x - w/2) + \theta(x - w/2)\right], \end{aligned} \tag{6.16}$$

$$\begin{aligned} \delta\epsilon &= i\epsilon''_m\left[\theta(x + w/2) - \theta(x - w/2)\right] + \left[i\epsilon''_a + \chi_3|\psi_a|^2|\vec{e}_a|^2\right]\theta(x - w/2) + \\ &\quad + \frac{\alpha}{2}\left[\theta(x - w/2) - \theta(-x - w/2)\right]. \end{aligned} \tag{6.17}$$

Note that the linear operator $\hat{\mathcal{L}}$ depends on the complete dielectric profile $\epsilon^{(0)}$. The linear modes $\vec{e}_p, \vec{e}_a$ are eigenvectors of the single-interface operators $\hat{\mathcal{L}}_p, \hat{\mathcal{L}}_a$, which dielectric susceptibility profiles $\epsilon^{(p)}$, $\epsilon^{(a)}$ do not coincide with $\epsilon^{(0)}$, as described in chapter 5. Hence, $\vec{e}_p, \vec{e}_a$ are not the exact, but the approximate eigenvectors of $\hat{\mathcal{L}}$. This fact gives rise to the coupling terms in Eqs. (6.18,6.19).

The propagation equations for the field amplitudes ψ_p, ψ_a are derived by taking the scalar product of Eq. (6.12) with the linear modes $\vec{e}_p, \vec{e}_a$. Coupling terms arise via the overlap integral $\mathcal{O}_m$, which is written explicitly in section 5.1. In the calculation of the scalar products we use the boundary conditions (BCs) accounting for linear $\epsilon''_m, \epsilon''_a$ and nonlinear $\chi_3|\psi_a|^2$ corrections, which are responsible for the surface enhancement η of effective gain, loss and nonlinearity, as discussed in chapter 4. As a result of the scalar product operation, one finds that the complex

amplitudes ψ_p, ψ_a satisfy the two coupled complex GL equations

$$i\partial_z\psi_p + \frac{1}{2\beta}\partial_{yy}^2\psi_p + (il - \Delta\beta)\psi_p + \kappa\psi_a = 0, \tag{6.18}$$

$$i\partial_z\psi_a + \frac{1}{2\beta}\partial_{yy}^2\psi_a + [i(l-g) + \Delta\beta]\,\psi_a + f\Upsilon|\psi_a|^2\psi_a + \kappa\psi_p = 0, \tag{6.19}$$

where

$$\Delta\beta = \frac{\beta^3}{2\epsilon_d^2}\alpha, \tag{6.20}$$

$$l = \frac{\beta^3}{2(\epsilon_m')^2}\epsilon_m'', \tag{6.21}$$

$$g = -\frac{\beta^3}{2\epsilon_d^2}\epsilon_a'', \tag{6.22}$$

$$\kappa = \frac{2\beta^3}{\epsilon_d - \epsilon_m'}e^{-q_m w}. \tag{6.23}$$

The parameters l, g, κ are the dimensionless loss, gain and coupling coefficients, respectively. Transition to physical quantities like attenuation, amplification and coupling rates is achieved by multiplying l, g, κ with $k = 2\pi/\lambda$. $\Delta\beta$ is the shift between the propagation constants of the single-interface SPPs $(\vec{e}_p, \vec{e}_a)$ and depends on the asymmetry constant α. The scaling factor f is set to $f = P/k$, so that the field amplitudes $\psi_{p,a}$ are dimensionless and $|\psi_{p,a}|^2 = 1$ represents the linear power density P (measured in Watts/m). The nonlinear parameter $\Upsilon = \Upsilon' + i\Upsilon''$ entering Eqs. (6.18,6.19) is given by

$$\Upsilon = k^2 n_2 \frac{\beta^3}{2\epsilon_d^2}(\epsilon_d - \epsilon_m'), \tag{6.24}$$

and is measured in W^{-1}. In order to achieve such a relation, we expressed the complex nonlinear susceptibility $\chi_3 = \chi_3' + i\chi_3'' = 2cn_2\epsilon_0\epsilon_d$ in terms of the complex Kerr coefficient n_2, which is measured in m^2W^{-1}.

6.2 Bistability and subcritical bifurcation of SPPs

If the coupling between the SPPs propagating along the $x = \pm w/2$ interfaces is neglected ($w >> 1, \kappa = 0$), then Eqs. (6.18,6.19) reduce to the uncoupled

equations

$$i\partial_z\psi_p + \frac{1}{2\beta}\partial^2_{yy}\psi_p + (il - \Delta\beta)\psi_p = 0, \tag{6.25}$$

$$i\partial_z\psi_a + \frac{1}{2\beta}\partial^2_{yy}\psi_a + [i(l-g) + \Delta\beta]\,\psi_a + f\Upsilon|\psi_a|^2\psi_a = 0. \tag{6.26}$$

Eq. (6.25) describes the optical propagation in a linear absorbing medium and the solutions are exponentially decaying functions $\psi_p \sim e^{-(l+i\Delta\beta)z}$. On the other hand, Eq. (6.26) provides the trivial solution $\psi_a = 0$ and the spatially homogeneous plane wave $|\psi_a| = \mathcal{A}$:

$$\mathcal{A} = \sqrt{\frac{g-l}{f\Upsilon''}}, \tag{6.27}$$

which exists only for $g \geq l$. Note that, conversely to the conservative case where the plane waves constitute a family of solutions parametrized either by the propagation constant or the amplitude, in the dissipative case the spatially homogeneous plane wave solution is unique [Akhmediev and Ankiewicz, 1997; Aranson and Kramer, 2002]. The stability analysis of the trivial zero solution reveals that it is stable for $g < l$, becoming unstable at $g = l$, where it bifurcates with the plane wave solution provided by Eq. (6.27). A schematic representation of such a *supercritical* bifurcation is shown in Fig. 6.2.

For $g > l$, the bistability is responsible for the formation of the Pereira-Stenflo plasmon-solitons of Eq. (6.26) [Pereira and Stenflo, 1977], which are explicitly given by

$$\psi_a = \sqrt{\frac{3}{2}}\mathcal{A}\,[sech(\nu y)]^{1+ia}\,e^{i\mu z}, \tag{6.28}$$

where

$$a = -\frac{3\Upsilon'}{2\Upsilon''} + \sqrt{2 + \left(\frac{3\Upsilon'}{2\Upsilon''}\right)^2}, \tag{6.29}$$

$$\nu^2 = \frac{g-l}{2a}, \tag{6.30}$$

$$\mu = \Delta\beta + (1-a^2)\nu^2. \tag{6.31}$$

Plasmon-solitons exist on the zero background $\psi_a = 0$, which is unstable in the soliton existence domain $g > l$, as demonstrated in chapter 3.

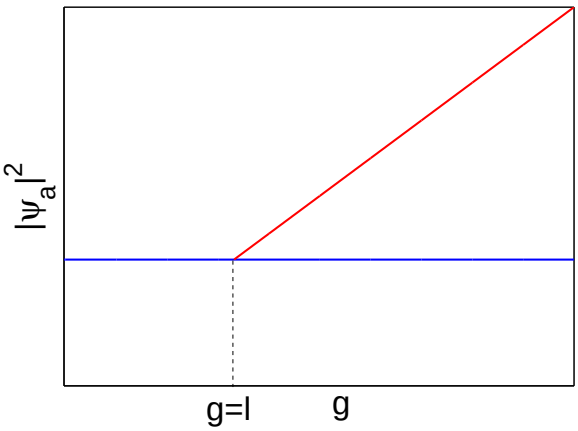

Figure 6.2: Schematic representation of the *supercritical* bifurcation between the trivial solution $\psi_a = 0$ and the plane wave $\psi_a = \mathcal{A}$ in the uncoupled case $\kappa = 0$.

In the coupled case $\kappa \neq 0$, the bifurcation behaviour is more involved. In this case, the stability of the trivial solution $\psi_a = \psi_p = 0$ can be analysed by studying the effect of the small perturbations ξ_p, ξ_a ($\xi_p, \xi_a << 1$):

$$\psi_p = \xi_p e^{\sigma z}, \tag{6.32}$$

$$\psi_a = \xi_a e^{\sigma z}. \tag{6.33}$$

Inserting Eqs. (6.32,6.33) into Eqs. (6.18,6.19) and linearizing the following system one gets

$$\hat{\mathcal{Z}}\vec{\xi} = 0, \tag{6.34}$$

where $\vec{\xi} = (\xi_p \ \xi_a)^T$ and

$$\hat{\mathcal{Z}} = \begin{pmatrix} i(l+\sigma) - \Delta\beta & \kappa \\ \kappa & i(l-g+\sigma) + \Delta\beta \end{pmatrix}. \tag{6.35}$$

The homogeneous system (6.34) provides non-zero solutions if the determinant of the coefficient matrix $\hat{\mathcal{Z}}$ is null:

$$\sigma^2 + (2l-g)\sigma + [l(l-g) + \kappa^2 - ig\Delta\beta + \Delta\beta^2] = 0. \tag{6.36}$$

For every fixed gain and loss coefficients g, l, the solution of the equation above provides us with the instability growth rate σ. The instability threshold is found

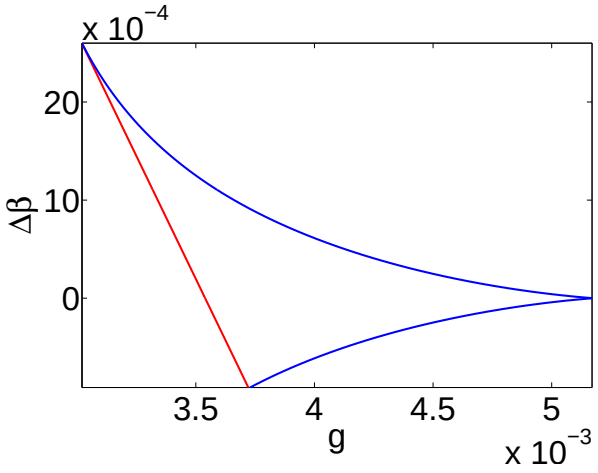

Figure 6.3: The coexistence domain of the stable zero and nonzero spatially homogeneous SPPs in the $(g, \Delta\beta)$-plane. g_{th} is indicated with the blue lines and g_0 with the red one. Other parameters are $\beta = 1.43$, $l = 0.0026$, $f\Upsilon = 3.5 \times 10^{-3}(1 + 0.1i)$, $\kappa = 0.0028$ (dimensional stripe width: $k^{-1}w = 98nm$).

by setting $\sigma' = Re\sigma = 0$, achieving the third order algebraic equation for the gain threshold g_{th}:

$$\left(g_{\text{th}} - l - \frac{\kappa^2}{l}\right)(g_{\text{th}} - 2l)^2 = 4\Delta\beta^2(l - g_{\text{th}}). \tag{6.37}$$

The non-zero spatially homogeneous plane wave solution is obtained by taking the ansatz

$$\psi_p = Se^{i\mu z}, \tag{6.38}$$

$$\psi_a = Re^{i\mu z}. \tag{6.39}$$

Inserting the equations above into Eqs. (6.18,6.19) one gets the solution

$$S = \frac{\kappa R}{\mu + \Delta\beta - il}, \tag{6.40}$$

$$|R|^2 = \frac{1}{f\Upsilon''}\left[g - l - \frac{\kappa^2 l}{(\mu + \Delta\beta)^2 + l^2}\right], \tag{6.41}$$

where the propagation constant μ is determined by the solution of the nonlinear algebraic equation

$$\mu - \Delta\beta - \frac{\kappa^2(\mu + \Delta\beta)}{(\mu + \Delta\beta)^2 + l^2} - f\Upsilon'|R|^2 = 0. \tag{6.42}$$

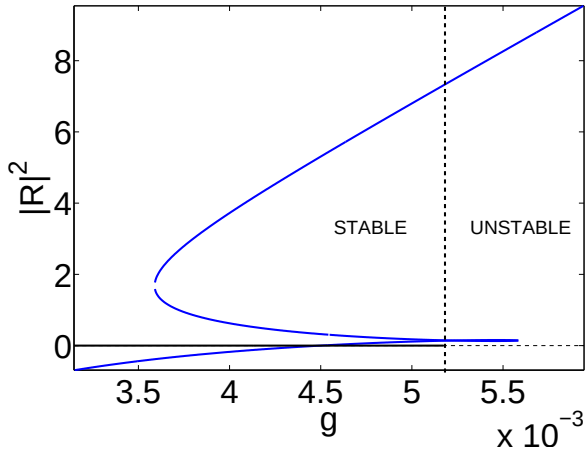

Figure 6.4: Squared amplitude $|R|^2$ of the spatially homogeneous SPP vs gain g showing subcritical transitions between the zero to nonzero states for $\Delta\beta = -2.5\times10^{-4}$. Other parameters are $\beta = 1.43$, $l = 0.0026$, $f\Upsilon = 3.5\times10^{-3}(1+0.1i)$, $\kappa = 0.0028$ (dimensional stripe width: $k^{-1}w = 98nm$).

Conversely to the uncoupled case $\kappa = 0$, the plane wave solution exists not only for $g > g_{th}$, but also in the *subcritical* region $g_0 < g < g_{th}$. The analytical calculation of the subcritical edge g_0 is cumbersome and is not included here. Fig. 6.3 depicts the range of g and $\Delta\beta$ values allowing for the existence of the subcritical bifurcation. Blue curves correspond to the instability threshold g_{th}, while the red curve represent the lower edge g_0. Note that the subcritical range $\Delta g = g_{\text{th}} - g_0$ is maximum for symmetric IMI structures: $\Delta\beta = 0$. For non-zero phase shift $\Delta\beta$, the subcritical range Δg shrinks, becoming null for a critical phase shift threshold $\Delta\beta_{\text{th}}$.

An example of the subcritical dependence of $|R|^2$ vs g is shown in Fig. 6.4. The bistability of the stable zero background and the plane wave solution suggests the possibility of achieving stable propagation of plasmon-solitons [Atai and Malomed, 1996; Malomed and Winful, 1996].

In our numerical computations we assumed that both the active and passive dielectric media are characterised by the dielectric susceptibility $\epsilon_d = 1.8$. The metal is assumed silver at wavelength $\lambda = 530$nm, so that $\epsilon'_m = -15$, $\epsilon''_m =$

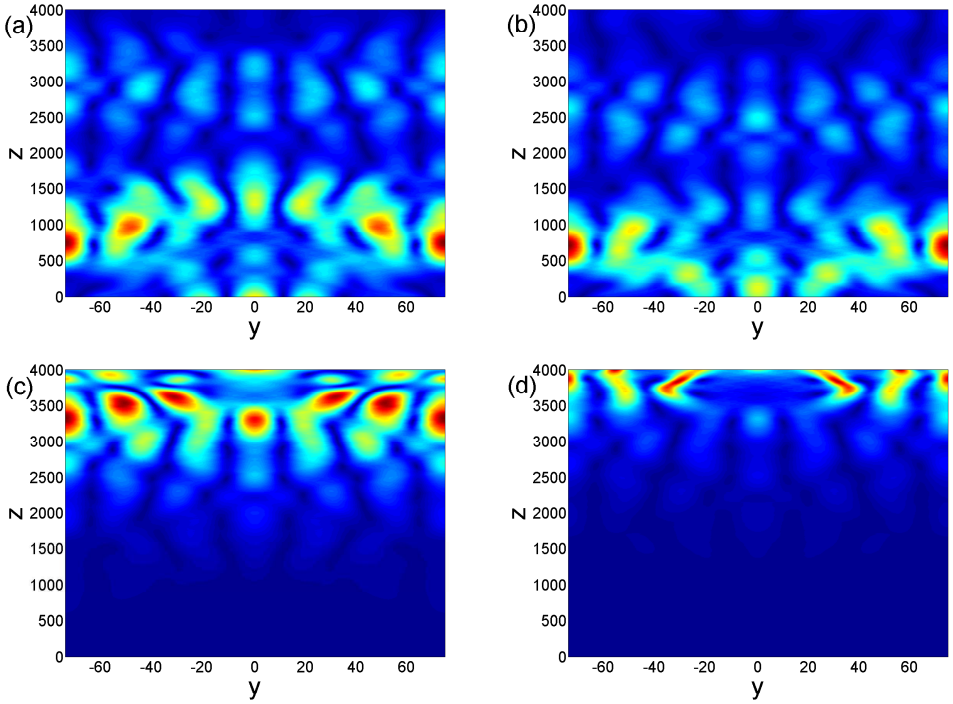

Figure 6.5: Propagation plot for the amplitudes (a,c) $|\psi_p|$ and (b,d) $|\psi_a|$. Input was set to the slightly perturbed trivial solution $|\psi_p| = |\psi_a| = 0$. Gain values correspond to (a,b) subcritical $g = 0.0045$ and (c,d) supercritical $g = 0.006$ values. Other parameters used for the simulation are: $\beta = 1.43$, $\Delta\beta = 0$, $l = 0.0026$, $f\Upsilon = 3.5 \times 10^{-3}(1 + 0.1i)$, $\kappa = 0.0028$ (dimensional stripe width: $k^{-1}w = 98nm$).

0.4. The dimensionless gain values used can be scaled back to physical units by multiplying them with the constant factor $\mathcal{F} \sim 12\mu m^{-1}$.

Hence, the physical amplification length at the threshold gain is $L_A \sim 20\mu m$. The amplification length achieved in experiments with dye organic molecules [Noginov et al., 2008a] is of the order $L_A \sim 20\ \mu m$ (corresponding to the gain coefficient $\mathcal{F}g_{\text{th}} \sim 420\ cm^{-1}$) while for quantum dots [Bolger et al., 2010] it is $L_A \sim 500\ \mu m$ (corresponding to the gain coefficient $\mathcal{F}g_{\text{th}} \sim 17cm^{-1}$). The intensity plot shown in Fig. 6.4 is achieved for $f\Upsilon = 3.5 \times 10^{-3}(1 + 0.1i)$.

In Figs. 6.5, the propagation of the slightly perturbed trivial solution $|\psi_p| = |\psi_a| = 0$ is depicted. Figs. 6.5a,b show *subcritical* ($g < g_{\text{th}}$) optical propagation

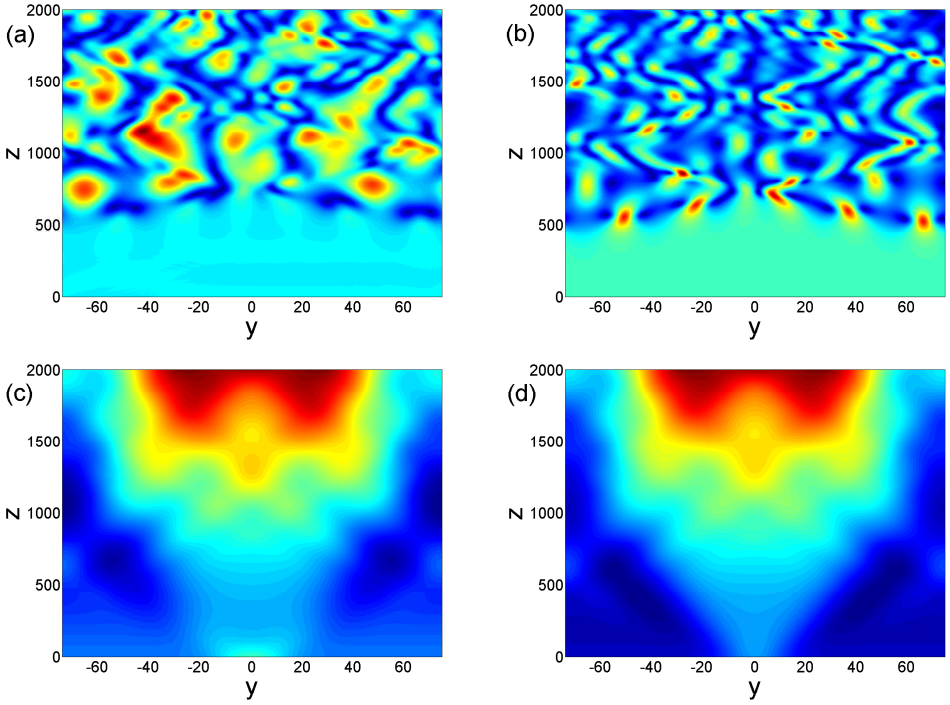

Figure 6.6: Propagation plot for the amplitudes (a,c) $|\psi_p|$ and (b,d) $|\psi_a|$. Input was set to the slightly perturbed spatially homogeneous solution $\psi_p = S$, $\psi_a = R$ for (a,b) the upper and (c,d) the lower branches, respectively. Parameters used for the simulation are: $\beta = 1.43$, $\Delta\beta = 0$, $l = 0.0026$, $f\Upsilon = 3.5 \times 10^{-3}(1 + 0.1i)$, $\kappa = 0.0028$ (dimensional stripe width: $k^{-1}w = 98nm$).

for (a) ψ_p and (b) ψ_a, respectively. As predicted by the stability analysis, the zero background is stable for $g < g_{\text{th}}$ and small perturbations are exponentially absorbed. SPP propagation dynamics has been computed by using the split-step Fast Fourier Transform (FFT) described in appendix C. Figs. 6.5c,d show the *supercritical* ($g > g_{\text{th}}$) optical propagation for (c) ψ_p and (d) ψ_a, respectively. In this case, the zero background becomes unstable and the arbitrarily small perturbations grow exponentially $\sim e^{\sigma z}$. The parameters used for the computations are provided in the figure captions.

Figs. 6.6a,b show the subcritical propagation of the slightly perturbed spatially homogeneous solutions (a) $|\psi_p| = |S|$ and (b) $|\psi_a| = |R|$ correponding to

the upper branch of Fig. 6.4. Such a propagation plot suggests that the SPP plane waves from the upper branch are unstable and are destroyed by arbitrarily small perturbations. SPPs are gradually absorbed and converge to the stable trivial solution $\psi_p = \psi_a = 0$ for long propagation distances. Figs. 6.6c,d depict the subcritical propagation of the slightly perturbed spatially homogeneous solutions (c) $|\psi_p| = |S|$ and (d) $|\psi_a| = |R|$ correponding to the lower branch of Fig. 6.4. The propagation dynamics of this SPP plane wave is more involved. Indeed, it appears to converge to a stable confined solution, suggesting the existence of stable SPP solitons.

6.3 Stable plasmon-solitons

In this section, we analyse the existence of the subcritical solitons by using an approximate semi-analytical theory and a numerical approach based on the Newton-Raphson iterations. The stability is studied by the numerical propagation of the plasmon-solitons.

The semi-analytical approach is borrowed from Refs. [Atai and Malomed, 1996; Malomed and Winful, 1996]. The total power N carried by the coupled SPPs is given by

$$N(z) = \int_{-\infty}^{+\infty} dy \left[|\psi_a(y,z)|^2 + |\psi_p(y,z)|^2 \right]. \tag{6.43}$$

For the plasmon-soliton solutions

$$\psi_a(y,z) = u_a(y) e^{i\phi z}, \tag{6.44}$$

$$\psi_p(y,z) = u_p(y) e^{i\phi z}, \tag{6.45}$$

where $\phi \in \Re$, the total power N is a conserved quantity.

In general, for the arbitrary input amplitude profiles $\psi_a(y,0)$, $\psi_p(y,0)$, the dynamical propagation of the total power N is governed by the differential equation

$$\frac{dN}{dz} + \int_{-\infty}^{+\infty} dy \left[2l|\psi_p|^2 - 2(g-l)|\psi_a|^2 + 2f\Upsilon''|\psi_a|^4 \right] = 0, \tag{6.46}$$

which represents the energy balance for the optical field. Such a balance equation is achieved by differentiating Eq. (6.43) with respect to z and by using Eqs. (6.18,6.19). In the limiting case $g = l = \Upsilon'' = 0$, the above balance equation reduces to $dN/dz = 0$, describing the conservation of power in the absence of gain and loss.

Assuming that $\Delta\beta = 0$ and neglecting all the dissipative ($g = l = \Upsilon'' = 0$) and coupling ($\kappa = 0$) terms, Eq. (6.19) reduces to the NLSE, which provides the exact analytical soliton solution

$$\psi_a = \eta\mathcal{B}\mathrm{sech}(\eta y)e^{i\phi z}, \tag{6.47}$$

where

$$\phi = \frac{\eta^2}{2\beta}, \tag{6.48}$$

$$\mathcal{B} = \sqrt{\frac{1}{\beta f\Upsilon'}}. \tag{6.49}$$

In this uncoupled conservative case, at the passive interface $x = -w/2$ the amplitude ψ_p is null, while at the active interface $x = w/2$ the amplitude ψ_a is a Kerr plasmon-soliton. In the limit where $g \sim l \sim \kappa \sim f\Upsilon''|\psi_a|^2$, the soliton in the second core $\psi_p \sim \kappa$ is assumed of the form

$$\psi_p(y, z) = u(y)e^{i\phi z}. \tag{6.50}$$

Inserting the expression above and Eq. (6.47) into Eq. (6.18) and neglecting the loss term, one gets a differential equation for the u amplitude

$$\frac{d^2u}{dy^2} - \eta^2 u = -\kappa\eta\sqrt{\frac{4\beta}{f\Upsilon'}}\mathrm{sech}(\eta y), \tag{6.51}$$

which can be solved by the Fourier transform method [Boyce and DiPrima, 1997]:

$$\psi_p = \frac{2\kappa}{\eta}\sqrt{\frac{\beta}{f\Upsilon'}}\left\{\cosh(\eta y)\ln\left[2\cosh(\eta y)\right] - \eta y\sinh(\eta y)\right\}e^{i\phi z}, \tag{6.52}$$

where $\phi = \eta^2/2\beta$ and $\eta > 0$ parameterizes the soliton family. Inserting Eqs.(6.47,6.52) into Eq. (6.46), one finds the evolution equation for the soliton family η parameter:

$$\frac{d\eta}{dz} + \beta^2\kappa^2 lC\eta^{-3} - 2(g - l)\eta + \frac{4\Upsilon''}{3\beta\Upsilon'}\eta^3 = 0, \tag{6.53}$$

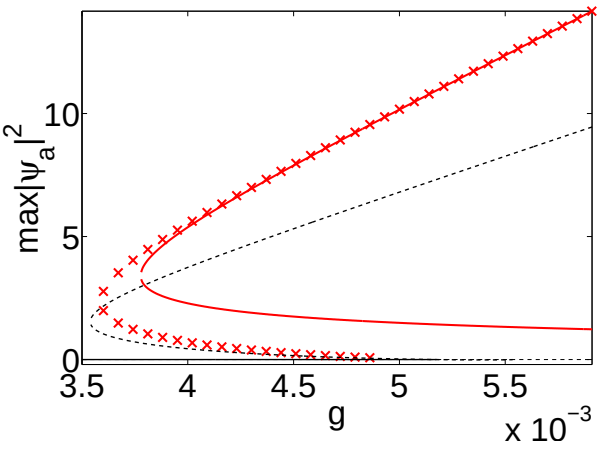

Figure 6.7: Maximum of the soliton intensity, $\max|\psi_a|^2$ vs gain g. The crosses correspond to the Newton-Raphson method, while the full line corresponds to the analytical results. The dotted line correspond to the spatially homogeneous SPPs. The other parameters are as in Fig. 6.4.

where

$$C = \int_{-\infty}^{+\infty} d\xi \left\{ e^{-\xi} ln\left[1 + e^{2\xi}\right] + e^{\xi} ln\left[1 + e^{-2\xi}\right] \right\}^2 \simeq 5.694. \tag{6.54}$$

The stationary η-solutions ($d\eta/dz = 0$) satisfy the cubic equation for η^2

$$\beta^2\kappa^2 lC - 2(g-l)\eta^4 + \frac{4\Upsilon''}{3\beta\Upsilon'}\eta^6 = 0, \tag{6.55}$$

which roots provide the family parameter η for the approximate dissipative plasmon-soliton, given by Eqs. (6.47,6.52). Within the subcritical range $\Delta g = g_{\rm th} - g_0$ we have found two positive roots η^2 of Eq. (6.55), which provide the approximate profiles for two separate plasmon-soliton solutions. In Fig. 6.7, the maximum of $|\psi_a|^2$ corresponding to the two η-roots is plotted as a function of the gain parameter g with the full red lines. The soliton profiles ψ_p, ψ_a corresponding to the upper amplitude-branch are plotted with the full lines in Figs. 6.8a,b, respectively.

The soliton perturbative theory provides accurate predictions in the limit $\Upsilon'' << \Upsilon'$ and $\Delta\beta = 0$. However, it is not able to provide approximate soliton

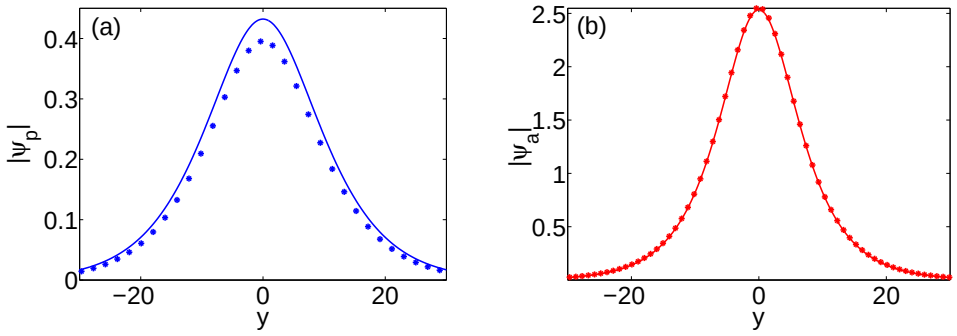

Figure 6.8: Star markers mark the numerically computed soliton profiles (a) $|\psi_p|$ and (b) $|\psi_a|$. Full lines represent the soliton profiles predicted by the perturbation theory. The solitons shown correspond to the large amplitude branch: $g = 0.0042$ and the other parameters as in Fig. 6.4 $|\psi_p|$ and $|\psi_a|$ are shown in Figs. 6.8a,b, respectively.

profiles for the case $\Delta\beta \neq 0$, which needs the use of numerical methods. Solitons are sought in the form

$$\psi_a = v_a(y_n)e^{i\phi z}, \tag{6.56}$$

$$\psi_p = v_p(y_n)e^{i\phi z}, \tag{6.57}$$

where $y_n = n\Delta y$ $(n = 0, \pm 1, \pm 2, ...)$ and Δy is the numerical grid spacing. Inserting the equations above into Eqs. (6.18,6.19) and approximating ∂^2_{yy} derivatives with the second order finite differences one achieves a nonlinear system of algebraic equations for the variables $v_a(y_n), v_p(y_n), \phi$, which can be solved by the Newton-Raphson method described in appendix B. The soliton propagation constant ϕ is treated as one of the unknowns and the perturbation theory provides an initial guess for the iterative procedure. Note that, since ϕ is an unknown, the system formally contains N equations and $N + 1$ unknowns. However, the number of variables can be reduced by one fixing $\mathrm{Im}\psi_a(0) = 0$. Such an operation is possible since Eqs. (6.18,6.19) are left invariant by an arbitrary phase shift $\psi_p, \psi_a \rightarrow \psi_p e^{i\varphi}, \psi_a e^{i\varphi}$. Hence φ can be chosen in such a way that $\mathrm{Im}\psi_a e^{i\varphi} = 0$.

The numerical soliton branches are plotted in Fig. 6.7 and are represented by the red cross markers. The corresponding numerical soliton profiles $|\psi_p|$ and $|\psi_a|$

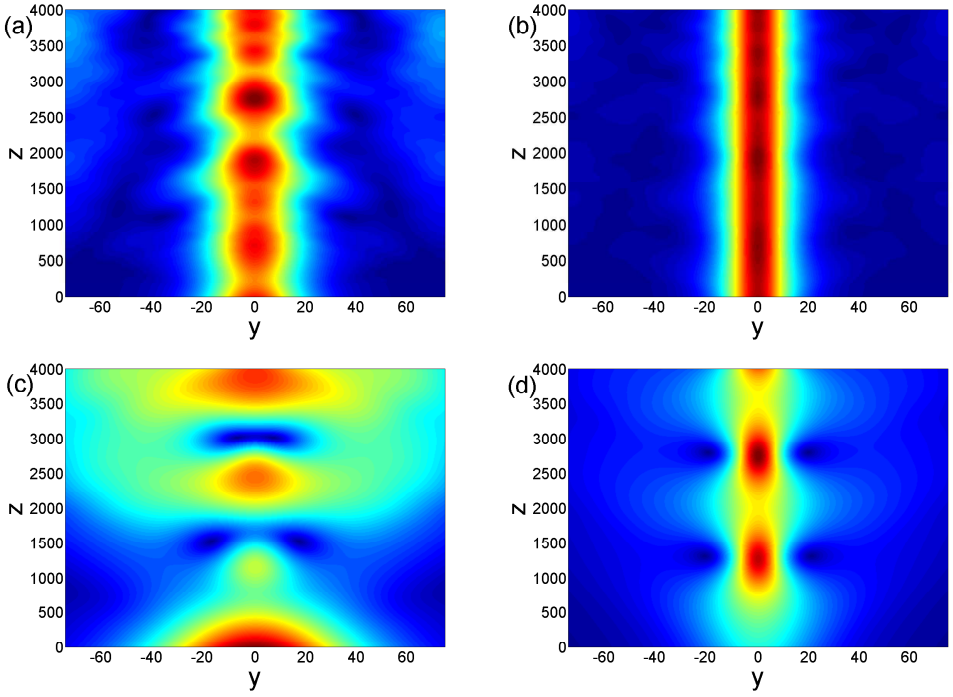

Figure 6.9: Split-step FFT propagation of the optical amplitudes (a,c) $|\psi_p|$ and (b,d) $|\psi_a|$. The initial condition $\psi_p(y,0), \psi_a(y,0)$ was set to the perturbative prediction of the (a,b) upper and (c,d) lower soliton branches, respectively. Parameters used: $\beta = 1.43$, $\Delta\beta = 0$, $g = 0.0042$, $l = 0.0026$, $\kappa = 0.0028$, $f\Upsilon = 3.5 \times 10^{-3}(1 + 0.1i)$.

are shown in Figs. 6.8a,b, respectively. We find excellent quantitative agreement between numerical and analytical approaches. The perturbative theory predicts the existence of the smaller amplitude soliton branch solitons both in the subcritical ($g < g_{\rm th}$) and supercritical ($g > g_{\rm th}$) ranges. Conversely, numerical results show that the smaller plasmon-soliton amplitude goes to zero as $g \to g_{\rm th}$ and for $g > g_{\rm th}$ only one solution exists. The large amplitude solitons exist on both sides $g_0 < g < g_{th}$, $g > g_{th}$ but their tails are stable only for $g < g_{th}$.

Eqs. (6.18,6.19) can also be solved directly by using the split step FFT method. We set the inital input $\psi_p(y,0), \psi_a(y,0)$ to the perturbative approximation of the large and small amplitude soliton branches in the subcritical region $g = 0.0042 < g_{th}$ and used the split step FFT to propagate it. Figs. 6.9a,b

show the optical propagation of initial field profiles $\psi_p(y,0), \psi_a(y,0)$ corresponding to the large amplitude soliton branch. Note that, although the perturbative plasmon-soliton solution is not exact, it converges rapidly to the exact solution oscillating around it. Such propagation plots confirm the possibility to achieve stable soliton propagation for the large amplitude branch in the subcritical region.

Figs. 6.9c,d depict the optical propagation of the initial field profiles $\psi_p(y,0)$, $\psi_a(y,0)$ corresponding to the small amplitude soliton branch. The instability of such solitons is not unexpected, since the small amplitude solitons separate the attraction basins of the stable zero solution and of the stable large-amplitude soliton.

6.4 Concluding remarks

In this chapter we have proposed and described a method to stabilise plasmon-solitons in an Insulator-Metal-Insulator (IMI) structure. The IMI geometry is composed of a metal slab sandwiched between a passive dielectric and a nonlinear amplifying material. In the limit where the metal slab is infinitely thick, the SPPs propagating at the active and the passive interfaces are completely uncoupled and the propagation dynamics is determined by the Ginzburg-Landau (GL) equation derived in chapter 3. In this limit, the dark and bright plasmon-solitons ensue from an *overcritical* bifurcation from the zero-background and suffer from the intrinsic instability of the background itself, as discussed in chapter 3. However, if the thickness of the metal slab lies in a particular range, the coupling of the active nonlinear interface with the passive one modifies the bifurcation picture, which becomes *subcritical*. In this regime, it is possible to achieve the bistability of the nonlinear homogeneous wave with a stable zero-background, opening the possibility for the formation of stable bright plasmon-solitons. Basically, the role played by the passive interface is to absorb the perturbations that would otherwise destabilise the zero-background. We developed a semi-analytical perturbative approach to approximate the plasmon-soliton profiles and compared the results with the fully numerical Newton-Raphson approach. The stability has been verified in propagation by using the split-step beam propagation method.

The original results reported in this chapter have been published in Ref. [Marini et al., 2011b].

Chapter 7

Optical propagation in nonlinear subwavelength nanowires

In order to achieve two-dimensional (2D) confinement, several plasmonic geometries have been proposed and realised: metal films [Leosson et al., 2006], triangular wedges [Eguiluz and Maradudin, 1976; Yatsui et al., 2001] and grooves [Bozhevolnyi et al., 2005; Novikov and Maradudin, 2002; Pile and Gramotnev, 2004], cylindrical wires with rectangular [Jung et al., 2007] and circular cross-section [Prade and Vinet, 1994; Schmidt and Russell, 2008; Schroter and Dereux, 2001; Takahara et al., 1997; Ung and Skorobogatiy, 2011; Zhang et al., 2011].

In what follows, we extend the multiple scale approach derived in chapter 4 to the two-dimensional case of cylindrical waveguides and calculate nonlinearity enhancement in different metallic, and dielectric/semiconductor setups. Results are thoroughly coincident with previously reported experimental and theoretical findings based on the reciprocity theorem approach [Afshar and Monro, 2009; Afshar et al., 2009].

7.1 Multiple scale expansion of Maxwell equations

The optical propagation of a monochromatic electromagnetic field $\vec{\mathcal{E}}e^{-i\omega t}, \vec{\mathcal{H}}e^{-i\omega t}$ in a photonic nanowire, which is schematically depicted in Fig. 7.1, is determined

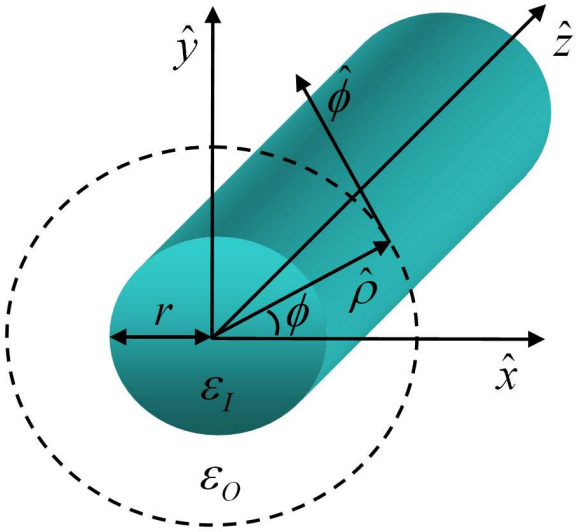

Figure 7.1: Schematic representation of cylindrical nanowire.

by the time-independent Maxwell equations

$$\nabla \times \vec{\mathcal{E}} = ic\mu_0 \vec{\mathcal{H}}, \tag{7.1}$$

$$\nabla \times \vec{\mathcal{H}} = -ic\epsilon_0(\epsilon_a + i\epsilon_b)\vec{\mathcal{E}} - ic\vec{\mathcal{D}}_{NL}. \tag{7.2}$$

$\partial_x, \partial_y, \partial_z$ derivatives are taken with respect to the dimensionless spatial coordinates x, y, z rescaled to $k^{-1} = \omega/c$, where ω is the angular frequency and c is the speed of light.

For the geometry considered, it is natural to work in cylindrical coordinates (ρ, ϕ, z), where

$$\rho = \sqrt{x^2 + y^2}, \tag{7.3}$$

$$\phi = \tan^{-1}(y/x). \tag{7.4}$$

In terms of cylindrical coordinates, the optical response of the nanowire is given by the real-valued dielectric susceptibility function

$$\epsilon_a(\rho) = \epsilon_I \theta(r - \rho) + \epsilon_O \theta(\rho - r), \tag{7.5}$$

where $\theta(x)$ is the Heaviside step function, r is the dimensionless core radius rescaled to $k^{-1} = \lambda/2\pi$ ($r = kR$) and ϵ_I, ϵ_O are the dielectric constants of the core and cladding materials, respectively. $\epsilon_b(\rho)$ accounts for losses, while $\vec{\mathcal{D}}_{NL}$ is the nonlinear contribution to the displacement vector. For isotropic Kerr nonlinearity:

$$\vec{\mathcal{D}}_{NL}(\vec{\mathcal{E}}) = \frac{1}{2}\epsilon_0\chi_3(\rho)\left[|\vec{\mathcal{E}}|^2\vec{\mathcal{E}} + \frac{1}{2}\vec{\mathcal{E}}^2\vec{\mathcal{E}}^*\right]. \tag{7.6}$$

Combining Eqs. (7.1,7.2) it is possible to achieve the single equation for the electric field $\vec{\mathcal{E}}$

$$\nabla\times\nabla\times\vec{\mathcal{E}} = (\epsilon_a + i\epsilon_b)\vec{\mathcal{E}} + \frac{1}{\epsilon_0}\vec{\mathcal{D}}_{NL}. \tag{7.7}$$

The $\hat{\mathcal{M}} = \nabla\times\nabla\times$ differential operator can be expressed in cylindrical coordinates in the $\hat{\rho}, \hat{\phi}, \hat{z}$ basis:

$$\hat{\mathcal{M}} = \frac{1}{\rho^2}\begin{pmatrix} -\rho^2\partial_z^2 - \partial_\phi^2 & \rho\partial^2_{\rho\phi} + \partial_\phi & \rho^2\partial^2_{\rho z} \\ \rho\partial^2_{\rho\phi} - \partial_\phi & 1 - \rho^2\partial_z^2 - \rho^2\partial_\rho^2 - \rho\partial_\rho & \rho\partial^2_{\phi z} \\ \rho^2\partial^2_{\rho z} + \rho\partial_z & \rho\partial^2_{\phi z} & -\rho^2\partial_\rho^2 - \rho\partial_\rho - \partial_\phi^2 \end{pmatrix}. \tag{7.8}$$

Introducing a small dummy variable $s \ll 1$, in what follows we assume that losses and nonlinearity are small quantities of the order $o(s^{3/2})$: $|\epsilon_b\vec{\mathcal{E}}|, |\vec{\mathcal{D}}_{NL}| \sim o(s^{3/2})$. In order to solve Eqs. (7.1,7.2) we use the ansatz:

$$\vec{\mathcal{E}} = \left[I^{1/2}\psi(z)\vec{e}(\rho) + \vec{j}(\rho,\phi,z) + o(s^{5/2})\right]e^{i\beta z + im\phi}, \tag{7.9}$$

$$\vec{\mathcal{H}} = \epsilon_0 c\left[I^{1/2}\psi(z)\vec{h}(\rho) + \vec{l}(\rho,\phi,z) + o(s^{5/2})\right]e^{i\beta z + im\phi}, \tag{7.10}$$

where

$$|\psi| \sim o(s^{1/2}), \tag{7.11}$$

$$|\vec{j}|, |\vec{l}|, |\partial_z\psi| \sim o(s^{3/2}). \tag{7.12}$$

$\vec{e} = (e_\rho, e_\phi, e_z)^T, \vec{h} = (h_\rho, h_\phi, h_z)^T$ are the linear guided mode profiles, β is the mode propagation constant and $m \in \mathbb{Z}$ is the winding number.

Boundary Conditions (BCs) at the interface $\rho = r$ can be derived directly from Maxwell equations [Jackson, 1999], providing that the tangential component of $\vec{\mathcal{E}}$,

the normal component of the displacement $\vec{\mathcal{D}}$ and all components of the magnetic field $\vec{\mathcal{H}}$ are continuous:

$$e_\rho : \ [(\epsilon_a + i\epsilon_b)e_\rho + (1/\epsilon_0)\mathcal{D}_\rho^{NL}(\vec{e})]_{r^-}^{r^+} = 0, \tag{7.13}$$

$$e_\phi : \ [e_y]_{r^-}^{r^+} = 0, \tag{7.14}$$

$$e_z : \ [e_z]_{r^-}^{r^+} = 0, \tag{7.15}$$

$$h_\rho : \ [h_\rho]_{r^-}^{r^+} = 0, \tag{7.16}$$

$$h_\phi : \ [h_\phi]_{r^-}^{r^+} = 0, \tag{7.17}$$

$$h_z : \ [h_z]_{r^-}^{r^+} = 0, \tag{7.18}$$

where we have used the notation

$$[f(\rho)]_{r^-}^{r^+} = \lim_{\delta \to 0}[f(r+\delta) - f(r-\delta)]. \tag{7.19}$$

Without any loss of generality, the linear mode profiles $\vec{e}, \vec{h}$ can be assumed dimensionless, so that the field units are carried by $I^{1/2}\psi$. The normalization factor I is chosen below in such a way that $|\psi|^2$ is the power (measured in Watts) carried in the z-direction, see Eq. (7.37).

Substituting the ansatz (7.9,7.10) into Maxwell equations (7.1,7.2) and collecting terms of the order $o(s^{1/2})$, one obtains a homogeneous system of differential equations for the linear mode components e_ρ, e_ϕ, e_z. By solving this system and applying the $o(s^{1/2})$ order BCs one gets the linear mode profile $\vec{e}, \vec{h}$. $o(s^{3/2})$ order terms provide an inhomogeneous system of differential equations for the residual field components j_ρ, j_ϕ, j_z. Analogously to the one-dimensional case, the propagation equation for the field amplitude $\psi(z)$ is found as a solvability condition for the multiple scale expansion.

7.1.1 Linear guided modes

Solving the linear system of differential equations

$$\hat{\mathfrak{M}}[e^{i\beta z + im\phi}\vec{e}] = \epsilon_a e^{i\beta z + im\phi}\vec{e} \tag{7.20}$$

is not a task that can be accomplished straightforwardly. Indeed, the differential equations for the transverse field components $e_\rho, e_\phi, h_\rho, h_\phi$ are coupled and finding

the recurrence relation in the solution by power series is troublesome [Arfken and Weber, 2001]. Such a calculation is greatly simplified by expressing the transverse field components $e_\rho, e_\phi, h_\rho, h_\phi$ in terms of the longitudinal ones e_z, h_z. Combining the curl equations [Marcuse, 1982]:

$$e_\rho = -\frac{i}{q^2}\left[im(1/\rho)h_z + \beta\partial_\rho e_z\right], \tag{7.21}$$

$$e_\phi = \frac{i}{q^2}\left[\partial_\rho h_z - im\beta(1/\rho)e_z\right], \tag{7.22}$$

$$h_\rho = \frac{i}{q^2}\left[im\epsilon_a(1/\rho)e_z - \beta\partial_\rho h_z\right], \tag{7.23}$$

$$h_\phi = -\frac{i}{q^2}\left[\epsilon_a\partial_\rho e_z + im\beta(1/\rho)h_z\right], \tag{7.24}$$

where $q^2 = \beta^2 - \epsilon_a$. The longitudinal field components e_z, h_z satisfy two uncoupled Bessel equations:

$$\partial_\rho^2 e_z + (1/\rho)\partial_\rho e_z - \left[q^2 + m^2/\rho^2\right] e_z = 0, \tag{7.25}$$

$$\partial_\rho^2 h_z + (1/\rho)\partial_\rho h_z - \left[q^2 + m^2/\rho^2\right] h_z = 0. \tag{7.26}$$

Generally, each of the above second order linear differential equations admits two independent solutions, namely Bessel functions of first J_m and second Y_m kind, which can be calculated by power series [Arfken and Weber, 2001]. The Bessel functions of first kind J_m remain finite at $\rho = 0$ and characterise the mode profile inside the core.

On the other hand, the Bessel functions of second kind Y_m tend to infinity as $\rho \to 0$. Another pair of solutions, which constitutes a different basis, is provided by the Hankel functions of first $H_m = J_m + iY_m$ and second kind $H_m^{(2)} = J_m - iY_m$. The Hankel function of first kind H_m tends to zero as $\rho \to \infty$ (when its argument is imaginary) and represents the mode profile in the cladding medium.

Thus, the longitudinal mode components e_z, h_z are expressed in terms of Bessel and Hankel functions:

$$e_z = A\frac{J_m(iq_I\rho)}{J_m(iq_I r)}\theta(r-\rho) + C\frac{H_m(iq_O\rho)}{H_m(iq_O r)}\theta(\rho - r), \tag{7.27}$$

$$h_z = B\frac{J_m(iq_I\rho)}{J_m(iq_I r)}\theta(r-\rho) + D\frac{H_m(iq_O\rho)}{H_m(iq_O r)}\theta(\rho - r), \tag{7.28}$$

where $q_{I,O} = \sqrt{\beta^2 - \epsilon_{I,O}}$. Boundary conditions provide a homogeneous system of four algebraic equations for the constants A, B, C, D:

$$e_\rho : \ \frac{q_O^2}{q_I^2}\left[\frac{im}{r}B + iq_I\beta\frac{J'_m(iq_Ir)}{J_m(iq_Ir)}A\right] = \left[\frac{im}{r}D + iq_O\beta\frac{H'_m(iq_Or)}{H_m(iq_Or)}C\right], \quad (7.29)$$

$$e_\phi : \ \frac{q_O^2}{q_I^2}\left[iq_IB\frac{J'_m(iq_Ir)}{J_m(iq_Ir)} - \frac{im\beta}{r}A\right] = \left[iq_OD\frac{H'_m(iq_Or)}{H_m(iq_Or)} - \frac{im\beta}{r}C\right], \quad (7.30)$$

$$e_z : \ A = C, \quad (7.31)$$

$$h_z : \ B = D. \quad (7.32)$$

The BCs for h_ρ, h_ϕ are automatically satisfied if the conditions above are set. The solution of the homogeneous system above is non-trivial only if the determinant of the coefficient matrix is null [Stratton, 1941]:

$$\left[q_I\epsilon_O\frac{H'_m(iq_Or)}{H_m(iq_Or)} - q_O\epsilon_I\frac{J'_m(iq_Ir)}{J_m(iq_Ir)}\right] \times \quad (7.33)$$
$$\times \left[q_O\frac{J'_m(iq_Ir)}{J_m(iq_Ir)} - q_I\frac{H'_m(iq_Or)}{H_m(iq_Or)}\right] = \left[\frac{m\beta(\epsilon_O - \epsilon_I)}{q_Oq_Ir}\right]^2.$$

The prime superscript of functions J'_m, H'_m denotes the derivative with respect to the argument of functions J_m, H_m. The solution of the above transcendental equation for every fixed m gives the mode propagation constant β, which is then used to calculate the coefficients $A - D$ and thus the corresponding mode profile. Note that the localised modes are cut-off when q_O^2 becomes negative and that modes with the same $|m|$ have equal propagation constants β. For $m = 0$, the dispersion relation can be factorised as the product of two β-functions. The roots of these functions provide Transverse Electric (TE, $e_z = e_\rho = 0, e_\phi \neq 0$) and Transverse Magnetic (TM, $h_z = h_\rho = 0, h_\phi \neq 0$) modes. For every $m > 0$ there are, generally, two types of modes (HE and EH modes) where all of the electric field components are non-zero [Marcuse, 1982]. However, for metallic nanowires ($\epsilon_I < 0$), only one mode exists for every fixed $|m|$ [Takahara et al., 1997]. At $o(s^{1/2})$ order, the z-component of the Poynting vector is given by

$$\begin{aligned} P_z &= (\pi/k^2)\int_0^{+\infty} \rho \mathrm{Re}\left[E_\rho H_\phi^* - E_\phi H_\rho^*\right] d\rho = \\ &= \frac{\epsilon_0 c}{2k^2}\beta I|\psi|^2(1+\eta)P, \end{aligned} \quad (7.34)$$

where

$$P = 2\pi \int_0^{+\infty} \rho |\vec{e}|^2 d\rho, \tag{7.35}$$

$$\eta = \frac{2\pi r}{\beta P} \mathrm{Im}[e_\rho^* e_z]_{r^-}^{r^+}. \tag{7.36}$$

The scaling constant I can be fixed in such a way that $|\psi|^2 = P_z$:

$$I = 2k^2/(\beta \epsilon_0 c(1+\eta)P). \tag{7.37}$$

Note that η is generally non-zero since e_ρ is discontinuous across the boundary.

7.1.2 Propagation equation

At $o(s^{3/2})$ order, Eq. (7.7) provides an inhomogeneous system of equations for the residual field correction $\vec{j}$:

$$\hat{\mathcal{L}}_m \vec{j} = I^{1/2}(i\epsilon_b \psi - \partial_z \psi \hat{\mathcal{D}}_z^{(m)})\vec{e} + \frac{1}{\epsilon_0}\vec{\mathcal{D}}_{nl}(I^{1/2}\psi \vec{e}), \tag{7.38}$$

where

$$\hat{\mathcal{L}}_m = \frac{1}{\rho^2}\begin{pmatrix} q^2\rho^2 + m^2 & im\partial_\rho \rho & i\beta\rho^2\partial_\rho \\ im\rho^2\partial_\rho \frac{1}{\rho} & q^2\rho^2 - \rho^2\partial_\rho \frac{1}{\rho}\partial_\rho \rho & -m\beta\rho \\ i\beta\rho\partial_\rho\rho & -m\beta\rho & p^2\rho^2 - \rho^2\partial_\rho\frac{1}{\rho}\partial_\rho\rho \end{pmatrix} \tag{7.39}$$

is the linear Maxwell operator in cylindrical coordinates, $p^2 = (m^2-1)/\rho^2 - \epsilon_a$, and

$$\hat{\mathcal{D}}_z^{(m)} = \frac{1}{\rho}\begin{pmatrix} -2i\beta\rho & 0 & \rho\partial_\rho \\ 0 & -2i\beta\rho & im \\ \partial_\rho\rho & im & 0 \end{pmatrix}. \tag{7.40}$$

The propagation equation can be determined by taking the scalar product of both sides of Eq. (7.38) with the linear mode $\vec{e}$:

$$\langle \vec{e}|\hat{\mathcal{L}}_m|\vec{j}\rangle = -I^{1/2}\partial_z\psi\langle\vec{e}|\hat{\mathcal{D}}_z^{(m)}|\vec{e}\rangle + iI^{1/2}\psi\langle\vec{e}|\epsilon_b|\vec{e}\rangle + \frac{1}{\epsilon_0}\langle\vec{e}|\vec{\mathcal{D}}_{NL}\rangle. \tag{7.41}$$

If one neglects corrections due to loss and nonlinearity in the BCs [Agrawal, 2001b; Davoyan et al., 2009b; Feigenbaum and Orenstein, 2007], then

$$\langle \vec{e}|\hat{\mathcal{L}}_m|\vec{j}\rangle = 0, \tag{7.42}$$

since $\vec{e}$ is an eigenvector of the self-adjoint operator $\hat{\mathcal{L}}_m$ with zero eigenvalue. However, the account of linear and nonlinear corrections in the BCs removes the self-adjoint property in the $o(s^{3/2})$ order:

$$\langle\vec{e}|\hat{\mathcal{L}}_m|\vec{j}\rangle \neq \langle\vec{j}|\hat{\mathcal{L}}_m|\vec{e}\rangle^* \neq 0. \tag{7.43}$$

The full set of BCs for the electric field $\vec{\mathcal{E}}$ is:

$$[\mathcal{E}_z]_{R^-}^{R^+} = 0, \tag{7.44}$$

$$[\mathcal{E}_\phi]_{R^-}^{R^+} = 0, \tag{7.45}$$

$$\left[(\epsilon_a + i\epsilon_b)\mathcal{E}_\rho + \frac{1}{\epsilon_0}\mathcal{D}_{NL,\rho}\right]_{R^-}^{R^+} = 0\ . \tag{7.46}$$

In the calculations below we also use the boundary condition for $\mathcal{H}_z$:

$$[\mathcal{H}_z]_{R^-}^{R^+} = 0. \tag{7.47}$$

Calculating the integral $\langle\vec{e}|\hat{L}_m|\vec{j}\rangle$ by parts and applying the above BCs, at $o(s^{3/2})$ order one gets

$$\langle\vec{e}|\hat{\mathcal{L}}_m|\vec{j}\rangle = 2\pi R I^{1/2}\partial_z\psi\,[e_z^* e_\rho]_{R^-}^{R^+}\ . \tag{7.48}$$

Note that $\vec{e}$ satisfies the BCs (7.44-7.46) at $o(s^{1/2})$ order, hence e_ϕ, e_z are continuous, while e_ρ is discontinuous at the waveguide interface $\rho = r = kR$. As a result, the right hand side of Eq. (7.48) is generally non-zero. The approximation $\langle\vec{e}|\hat{\mathcal{L}}_m|\vec{j}\rangle \simeq 0$ is well satisfied for optical fibres with a small index step and a large core radius $R >> k\lambda$. Indeed, in this regime the longitudinal component of the electric field (e_z) is generally small, while the discountinuity of the normal component e_ρ is proportional to $|\epsilon_I - \epsilon_O|$ and is also small. However, for sub-wavelength waveguides with large refractive index contrast and small core sizes this approximation is no longer valid, and the surface term in Eq. (7.48) becomes essential.

Direct calculation of $\langle\vec{e}|\hat{\mathcal{D}}_z^{(m)}|\vec{e}\rangle$ reveals another contribution from the surface:

$$\langle\vec{e}|\hat{\mathcal{D}}_z^{(m)}|\vec{e}\rangle = -2i\beta P - 2\pi R\left[e_z e_\rho^*\right]_{R^-}^{R^+}. \tag{7.49}$$

where the quantity P is given by Eq. (7.35). Substituting Eqs. (7.48,7.49) into Eq. (7.41) and calculating the other scalar product integrals, one finally achieves

the propagation equation for the slowly varying amplitude $\psi(z)$:

$$i\partial_z\psi + i\alpha\psi + \Upsilon|\psi|^2\psi = 0, \tag{7.50}$$

where $\Upsilon = g\gamma, \alpha = \sqrt{g}a$ and

$$a = \frac{\pi}{\beta P}\int_0^{+\infty} \rho\epsilon_b|\vec{e}|^2 d\rho, \tag{7.51}$$

$$\gamma = \frac{4\pi k^2}{3\beta^2 P^2}\int_0^{+\infty} \rho\epsilon_a n_2 \left[|\vec{e}|^4 + \frac{1}{2}|\vec{e}^2|^2\right] d\rho. \tag{7.52}$$

Here, we used $\chi_3 = (4/3)n_2\epsilon_0 c\epsilon_a$, where n_2 is the Kerr coefficient. The parameter γ is defined to be similar to the one derived in the approaches dating back to the use of the scalar wave equation [Agrawal, 2001b]. Analogously to planar geometries described in chapter 4, the nonlinear coefficient Υ differs from γ by the *surface-induced enhancement factor* g:

$$g = \frac{1}{(1+\eta)^2}, \tag{7.53}$$

where η is given by Eq. (7.36). On the other hand, also the effective loss coefficient α is enhanced by the square root of g: $\alpha = \sqrt{g}a$. Note that the rigorous account of surface terms in *both sides* of Eq. (7.38) eventually leads to the correct *real-valued* nonlinearity enhancement factor g. Conversely, neglecting the surface contribution in the left hand side of Eq. (7.35)

$$\langle\vec{e}|\hat{L}_m|\vec{j}\rangle \simeq 0, \tag{7.54}$$

one gets an unphysical complex enhancement factor g for $m \neq 0$ modes. The surface term η, provided by Eq. (7.36), is determined by the product of the longitudinal field component e_z and the radial component e_ρ discontinuity jump at the waveguide interface. For linear modes $\vec{e}$, the amplitude is left arbitrary; for convenience, we can fix the linear mode amplitude in such a way that $e_z(r) = 1$.

The units of n_2 are m^2W^{-1} and the units of γ, Υ are W^{-1}. If one considers the physical longitudinal coordinate $Z = z/k$ instead of the dimensionless z, the resulting nonlinear coefficient is $k\Upsilon$, which is measured in $m^{-1}W^{-1}$. Neglecting the surface contribution η, the expression for the nonlinear parameter coincides

to the one achieved with traditional methods [Agrawal, 2001b; Davoyan et al., 2009b; Feigenbaum and Orenstein, 2007].

It is worthwhile noting that our results thoroughly coincide with the theoretical modelling of nonlinear optical propagation based on the reciprocal theorem [Afshar and Monro, 2009; Afshar et al., 2009; Ye et al., 2010]. Indeed, from Eq. (7.34), it is straightforward to obtain the analytical expression

$$P = (1+\eta)^{-1} \int\int \rho Re\left[\vec{e}\times\vec{h}^{*}\right]\cdot\hat{z}d\rho d\phi, \tag{7.55}$$

where $\hat{z}$ is the z-direction unit vector and the integration is performed across the entire waveguide cross-section. Thus, the nonlinear parameter Υ can be expressed as

$$\Upsilon = \frac{k^2}{3\beta^2}\frac{\int\int \rho\epsilon_a n_2\left[2|\vec{e}|^4+|\vec{e}^2|^2\right]d\rho d\phi}{\left(\int\int \rho \mathrm{Re}\left[\vec{e}\times\vec{h}^{*}\right]\cdot\hat{z}d\rho d\phi\right)^2}. \tag{7.56}$$

Hence, the nonlinearity enhancement observed in Refs. [Afshar and Monro, 2009; Afshar et al., 2009] is entirely due to the surface contribution η, which is neglected in other approaches but becomes significant in the subwavelength regime.

7.1.3 Lorentz Reciprocity Theorem

The Lorentz Reciprocity Theorem (LRT) is a relevant theorem of electromagnetic theory [Snyder and Love, 1983], stating that

$$\partial_z \int_{\mathbb{S}} \vec{\mathcal{F}}_C\cdot\hat{z}d\mathbb{S} = \int_{\mathbb{S}} \nabla\cdot\vec{\mathcal{F}}_C d\mathbb{S}, \tag{7.57}$$

where the integral is taken over the entire transverse plane $\mathbb{S} = x-y$ of a generic two dimensional waveguide and $\hat{z}$ is the longitudinal unit vector. The vector field $\vec{\mathcal{F}}_C$ is constructed with two arbitrary guided electromagnetic fields $\vec{\mathcal{E}}_0, \vec{\mathcal{H}}_0$ and $\vec{\mathcal{E}}_1, \vec{\mathcal{H}}_1$:

$$\vec{\mathcal{F}}_C = \vec{\mathcal{E}}_0^{*}\times\vec{\mathcal{H}}_1 + \vec{\mathcal{E}}_1\times\vec{\mathcal{H}}_0^{*}. \tag{7.58}$$

The electric and magnetic fields

$$\vec{\mathcal{E}}_0 = I^{1/2}\psi\vec{e}(\vec{r}_\perp)e^{i\beta z-i\omega t}, \tag{7.59}$$

$$\vec{\mathcal{H}}_0 = \epsilon_0 c I^{1/2}\psi\vec{h}(\vec{r}_\perp)e^{i\beta z-i\omega t}, \tag{7.60}$$

constitute the linear mode of the unperturbed waveguide with dielectric susceptibility profile ϵ_a where $\vec{r}_\perp = (x, y)$. The scaling factor I can be fixed in such a way that the squared amplitude $|\psi|^2$ represents the power carried by the two dimensional waveguide

$$P_z = \frac{1}{2k^2}\int_{\mathcal{S}} Re\left[\vec{\mathcal{E}}_0 \times \vec{\mathcal{H}}_0^*\right]\cdot \hat{z} d\mathcal{S} = |\psi|^2. \tag{7.61}$$

On the other hand, the electric and magnetic fields $\vec{\mathcal{E}}_1, \vec{\mathcal{H}}_1$ correspond to the perturbed electromagnetic field accounting for linear $\epsilon_b\vec{\mathcal{E}}_0$ and nonlinear $\vec{\mathcal{D}}_{NL}$ corrections. Taking the divergence of the vector field $\vec{\mathcal{F}}_C$

$$\begin{aligned}\nabla\cdot\vec{\mathcal{F}}_C &= \nabla\cdot\left(\vec{\mathcal{E}}_0^*\times\vec{\mathcal{H}}_1\right)+\nabla\cdot\left(\vec{\mathcal{E}}_1\times\vec{\mathcal{H}}_0^*\right) = \\ &= \left(\nabla\times\vec{\mathcal{E}}_0^*\right)\cdot\vec{\mathcal{H}}_1 - \vec{\mathcal{E}}_0^*\cdot\left(\nabla\times\vec{\mathcal{H}}_1\right)+ \\ &\quad +\left(\nabla\times\vec{\mathcal{E}}_1\right)\cdot\vec{\mathcal{H}}_0^* - \vec{\mathcal{E}}_1\cdot\left(\nabla\times\vec{\mathcal{H}}_0^*\right),\end{aligned} \tag{7.62}$$

and using the curl Maxwell equations one obtains

$$\partial_z\int_{\mathcal{S}}(\vec{\mathcal{E}}_0^*\times\vec{\mathcal{H}}_1+\vec{\mathcal{E}}_1\times\vec{\mathcal{H}}_0^*)\cdot\hat{z}d\mathcal{S} = ic\int_{\mathcal{S}}\delta\vec{\mathcal{P}}\cdot\vec{\mathcal{E}}_0 d\mathcal{S}, \tag{7.63}$$

where

$$\delta\vec{\mathcal{P}} = \epsilon_0\epsilon_b\vec{\mathcal{E}}_0 + \vec{\mathcal{D}}_{NL}. \tag{7.64}$$

It is assumed that linear and nonlinear polarisation corrections are small and therefore the perturbed modes are approximated by the unperturbed ones in the right hand side of Eq. (7.63). Conversely, in the left hand side, the perturbed electric and magnetic fields are expressed as

$$\vec{\mathcal{E}}_1 = I^{1/2}\psi(z)\vec{e}(\vec{r}_\perp)e^{i\beta z - i\omega t}, \tag{7.65}$$

$$\vec{\mathcal{H}}_1 = \epsilon_0 c I^{1/2}\psi(z)\vec{h}(\vec{r}_\perp)e^{i\beta z - i\omega t}, \tag{7.66}$$

where the mode amplitude ψ becomes z-dependent: $\psi(z)$.

Inserting Eqs. (7.59,7.60,7.65,7.66) into Eq. (7.63) one gets

$$\partial_z\psi + \alpha\psi + \Upsilon|\psi|^2\psi = 0, \tag{7.67}$$

where the parameters α, Υ thoroughly coincide with the expressions derived by us and the equivalence between our results and the LRT approach is demonstrated. In the following sections, we evaluate the surface-induced contributions to the effective loss and nonlinearity parameters α and Υ in different setups.

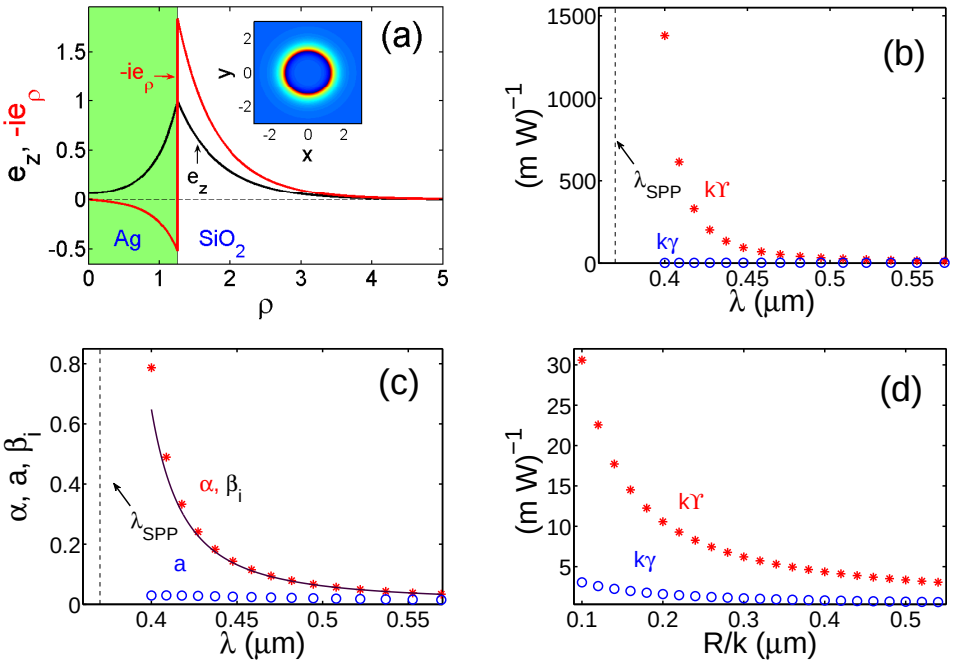

Figure 7.2: (a) TM mode of a metallic wire ($r/k = 100nm$, $\lambda = 500nm$) made of silver and surrounded by silica glass. (b,c) Nonlinear and loss coefficients as function of λ ($r/k = 100nm$). (d) $k\Upsilon, k\gamma$ vs r/k for $\lambda = 500nm$.

7.2 Plasmonic waveguide

In this section we report the results for the loss and nonlinearity enhancements of a silver rod waveguide surrounded by silica glass.

We modelled the metal susceptibility $\epsilon_I(\omega)$ by the Drude-Lorentz fit of the experimental data [Ung and Sheng, 2007], and the silica glass susceptibility $\epsilon_O(\omega)$ by the Sellmeier expansion [Agrawal, 2001b]. The nonlinear Kerr coefficient of silica glass was fixed to $n_2 = 3 \times 10^{-20} m^2/W$. In Fig. 7.2, the results are presented for the $m = 0$ TM guided mode. Modes with higher winding number $|m| > 0$ exhibit a similar behaviour. The inset in Fig. 7.2 shows the cross-section of the z-component of the Poynting vector. For the case of metallic nanowires, only the TM guided modes with non-zero e_z and e_ρ components exist. Both electric field components have peak amplitudes at the waveguide interface, and

the discontinuity in e_ρ is significant due to the opposite signs of ϵ_I and ϵ_O. e_z and e_ρ are characterised by a $\pi/2$ phase shift, so that the surface coefficient η provided by Eq. (7.36) is always negative:

$$-1 < \eta < 0. \tag{7.68}$$

As a result, the surface term enhances both nonlinearity and loss:

$$g = (1+\eta)^{-2} > 1. \tag{7.69}$$

In Figs. 7.2b,c, we compare the nonlinear $k\Upsilon$ (red star markers in Fig. 7.2b), $k\gamma$ (blue circle markers in Fig. 7.2b) and loss α (red star markers in Fig. 7.2c), a (blue circle markers in Fig. 7.2c), β_i (black curve in Fig. 7.2c) coefficients as functions of the wavelength λ for a fixed waveguide radius $R = r/k = 100nm$. The discrepancy between the two theories becomes significant as wavelength decreases. As the wavelength approaches the surface plasmon resonance $\lambda = \lambda_{SPP} \approx 370nm$ ($|\epsilon_I(\lambda_{SPP})| = \epsilon_O(\lambda_{SPP})$ [Boardman, 1982]), the mode gets tightly localised at the interface and the enhancement factor g diverges ($\eta \to -1$). In order to validate our theory, we calculated the loss parameter β_i directly through the dispersion relation, see Eq. (7.33. Indeed, by substituting the complex-valued dielectric susceptibility ϵ_I of metal in Eq. (7.33), one gets the corresponding complex-valued propagation constant $\beta = \beta_r + i\beta_i$. The imaginary part of the propagation constant β_i provides us with the decay rate of the corresponding quasi-guided mode and is plotted in Fig. 7.2c with the black solid curve. Note that the perturbative loss coefficients accounting for the surface contribution α perfectly match the exact loss parameter β_i calculated through the dispersion relation.

Fig. 7.2d depicts the nonlinear parameters $k\Upsilon$ (red star markers), $k\gamma$ (blue cricle markers) as functions of the rod radius $R = r/k$ for the fixed wavelength $\lambda = 500nm$. The surface-induced enhancement factor grows as the waveguide radius is reduced, analogously to the results reported in chapter 4 for the metal slot planar geometry. Note that there is no cut-off radius for the plasmonic nanowire modes, which opens the opportunity to tune the effective nonlinear parameter to any high value at the expense of an increasing loss.

7.3 Dielectric waveguide

In this section, we consider a dielectric rod waveguide surrounded by air cladding ($\epsilon_O = 1$). Fig. 7.3 summarises the analysis of TM modes of waveguides composed of silica glass and silicon cores, which dielectric susceptibilities $\epsilon_I(\omega) = \epsilon_{SiO_2}(\omega), \epsilon_{Si}(\omega)$ were modelled through Sellmeier [Agrawal, 2001b] and Herzberger expansions [Edwards and Ochoa, 1980], while Kerr coefficients were fixed to $n_2 = 3 \times 10^{-20} m^2/W$ (silica glass SiO_2), $n_2 = 4.5 \times 10^{-18} m^2/W$ (silicon Si).

Similar to the previous case of plasmonic waveguides, the TM modes of dielectric waveguides have non-zero transverse field component e_ρ with discontinuity at the waveguide interface, see Figs. 7.3a,b, ensuring non-zero surface contribution $g = (1+\eta)^{-2}$ to the effective nonlinearity coefficient. For the case of silica glass waveguide, the dielectric susceptibility step is relatively weak $\epsilon_I - \epsilon_O \sim 1$ ($\epsilon_I \sim 2$, $\epsilon_O = 1$). As a result, the surface contribution η stays small for a wide range of wavelengths, see Fig. 7.3c. Hence, the use of traditional perturbative theories is justified, as expected.

For silicon nanowires, the dielectric susceptibility jump increases $\epsilon_I - \epsilon_O \sim 10$ ($\epsilon_I \sim 12$, $\epsilon_O = 1$), the mode becomes more localised and the surface-induced enhancement factor $g = (1+\eta)^{-2}$ increases. Remarkably, the nonlinearity enhancement exhibits a resonant behaviour. The difference between $k\gamma$ and $k\Upsilon$ is negligible for long $\lambda \to \infty$ and short wavelengths $\lambda \to \lambda_{CO}$, where λ_{CO} is the cut-off wavelength. The difference between the two perturbation theories becomes significant around a certain critical wavelength $\lambda \approx 3\mu m$ (see Fig. 7.3d), where the enhancement factor reaches its maximum ($g \sim 3$). This resonant-like nonlinearity enhancement is confirmed in Figs. 7.3e,f, where the nonlinear coefficients for silica glass and silicon waveguides are plotted as functions of the waveguide radius at a fixed wavelength. In both cases, g reaches its maximum when the waveguide diameter becomes comparable with the wavelength inside the dielectric core: $r_0/k \sim \lambda/(2\sqrt{\epsilon_I})$ ($r_0/k \sim 300nm$ for silica glass SiO_2 waveguide at wavelength $\lambda = 540nm$ and $r_0/k \sim 600nm$ for silicon Si waveguide at wavelength $\lambda = 3\mu$m).

Similar resonant behaviour of the nonlinearity enhancement is observed for modes with $m \neq 0$. Fig. 7.4 summarises the results for $m = 1$ modes of a silicon

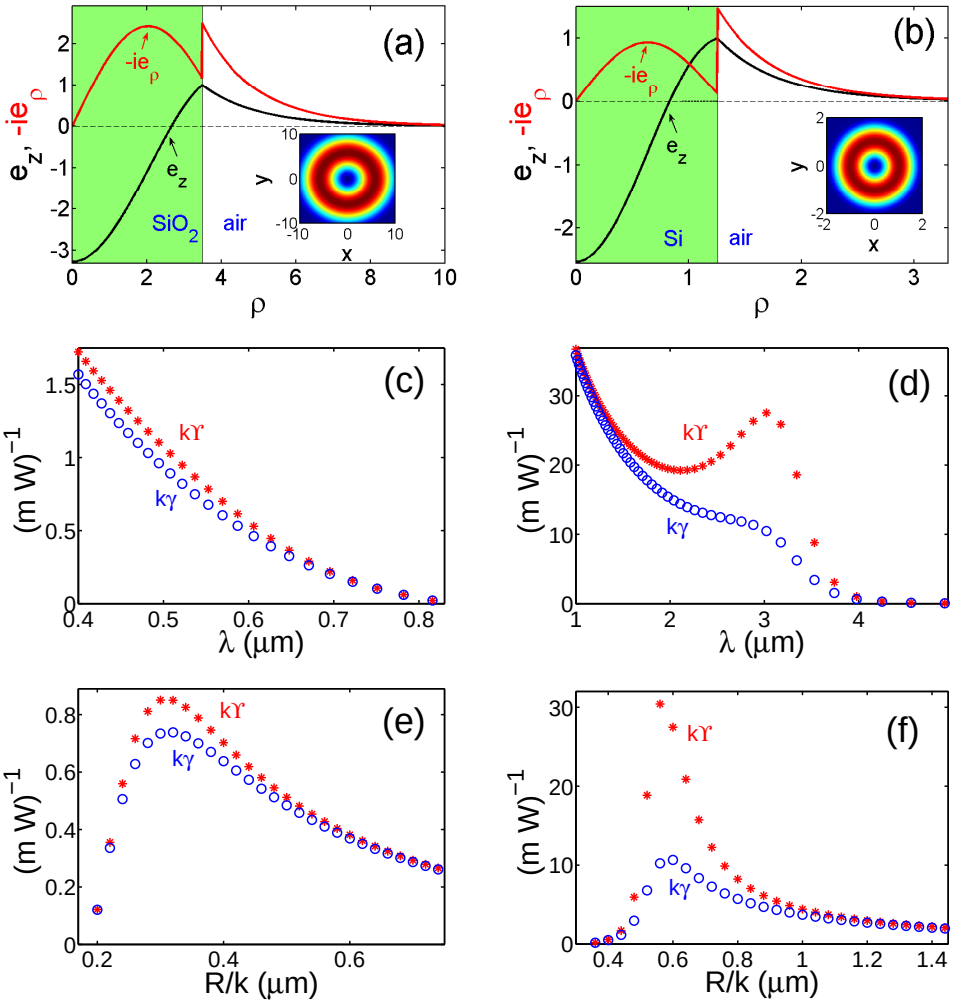

Figure 7.3: TM guided modes of (a,c,e) silica glass (SiO_2) and (b,d,f) silicon (Si) rod waveguides with air cladding. (a,b) Mode profiles with insets showing cross-section of the z-component of the Poynting vector for (a) $R = r/k = 300nm$, $\lambda = 540nm$ and (b) $R = r/k = 600nm$, $\lambda = 3\mu m$. (c,d) Nonlinear coefficients vs wavelength λ corresponding to (a) and (b) modes, respectively. (e,f) Nonlinear coefficients vs waveguide radius $R = r/k$ corresponding to the modes (a,b), respectively, and for fixed wavelengths (e) $\lambda = 540nm$ and (f) $\lambda = 3\mu m$.

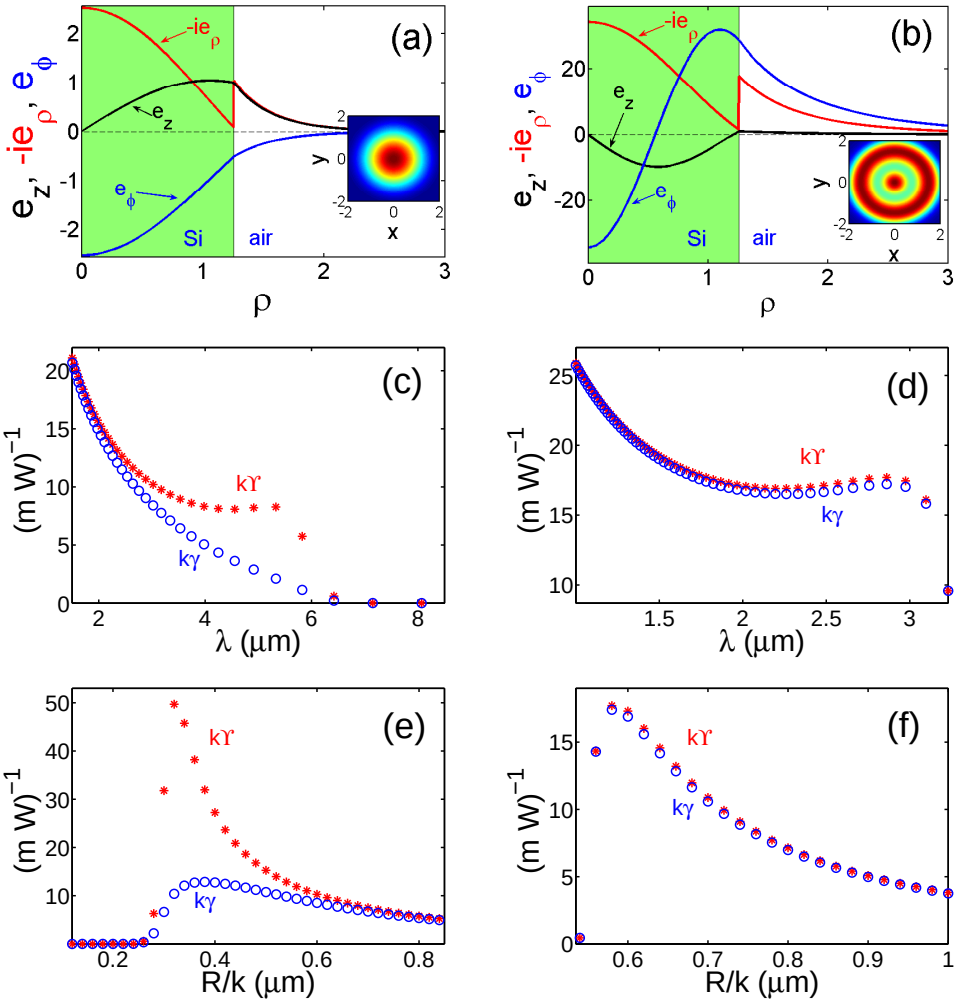

Figure 7.4: Figure equivalent to Fig. 7.3, but corresponding to $m = 1$ modes of the silicon (Si) waveguide: (a,c,e) HE_{11} and (b,d,f) EH_{11} modes.

nanowire: HE_{11} (which is the fundamental mode with no cut-off) and EH_{11}. The surface effect is much stronger for the HE_{11} mode, since this mode has stronger e_ρ and e_z components and is more localised than the EH_{11} mode. The resonant enhancement of nonlinearity for $m = 1$ modes occurs at a larger wavelength (for fixed waveguide radius) and a smaller radius (for fixed wavelength) than for $m = 0$ modes, see. Figs. 7.4c,f.

7.4 Concluding remarks

In this chapter we have extended the one-dimensional perturbative theory developed in chapter 4 to the case of dielectric and metallic cylindrical nanowires. The propagation equation is determined as the scalar product solvability condition for the multiple scale expansion. Our approach accounts for the loss and the nonlinearity corrections in the boundary conditions, which affect the propagation equation with a surface term η. Such a contribution from the surface is neglected in the traditional approach developed in the theory of optical fibres [Agrawal, 2001b], which has been used also to model the optical propagation of nonlinear SPPs [Davoyan et al., 2009b; Feigenbaum and Orenstein, 2007]. We demonstrated the complete equivalence of our perturbative approach with the Lorentz Reciprocity Theorem (LRT) approach, which has been used to model the optical propagation in both dielectric and metallic subwavelength nanowires [Afshar and Monro, 2009; Afshar et al., 2009; Ye et al., 2010]. We also demonstrated that the surface-induced contribution to the effective loss and nonlinearity becomes the leading term in the subwavelength regime both for metallic and silicon nanowires. Thus, we uncovered the physical origin of the modified prediction provided by the LRT approach [Afshar and Monro, 2009; Afshar et al., 2009; Ye et al., 2010] with respect to the traditional theory [Agrawal, 2001b; Davoyan et al., 2009b; Feigenbaum and Orenstein, 2007]. The original results reported in this chapter have been published in Ref. [Marini et al., 2011a].

Chapter 8

Conclusions

This thesis is focused on the theoretical modelling of the optical propagation in photonic nanostructures. The delivery of electromagnetic energy on the subwavelength scale is one of the primary tasks for the research in nano-optics. The embedding of metallic components in photonic structures can provide a tight confinement of light, owing to the excitation of surface plasmon polaritons (SPPs). SPPs constitute one of the most promising candidates for the realisation of miniaturised optical interconnection in optoelectronic circuitry. The inherent subwavelength nature of SPPs provides a tight localisation that enhances the nonlinear optical processes. Such an enhanced nonlinear response is important for the realisation of active plasmonic components. The tight localisation of light in the subwavelength scale is paid in terms of an enhanced dissipation due to the ohmic loss of the metal components. Although several geometries have been proposed for the reduction of the dissipation, the inherent trade-off between loss and localisation can be overcome only by embedding gain materials in the plasmonic structure.

In summary, we have developed some analytical and numerical tools to model the propagation of light in subwavelength photonic structures. The analytical technique is a novel perturbative theory for the Maxwell equations, accounting for the surface contribution in the boundary conditions due to the loss and the nonlinearity. Such a contribution affects the propagation equation of the SPPs with the surface term η, which enhances both the effective loss and nonlinear coefficients.

The numerical techniques involved the use of the Newton-Raphson routine, the split-step beam propagation method and the Runge-Kutta algorithm to solve the nonlinear equations derived by the analytical methods and to study the stability of the solutions.

The original results achieved can be summarised as follows:

- *Nonlinear dispersion law for amplified SPPs.* By using a perturbative theory accounting for the gain deviation from the amplification threshold and the complex two-level atom nonlinearity, we have been able to derive the dispersion law of the homogeneous nonlinear SPPs at a single interface between a metal and an active dielectric. In such a perturbative approach, we explicitly calculated the residual field corrections due to the nonlinearity and the gain deviation from the amplification threshold. Then, we imposed the boundary conditions that accounted for the linear and nonlinear corrections, achieving the dispersion law of the nonlinear eigenvalue problem. The physical origin of the formation of the homogeneous nonlinear SPPs resides in the exact balance between the metal loss, the linear amplification and the nonlinear saturation of gain. Such a result is reported in section 3.2 and has been published in Ref. [Marini et al., 2009].

- *Ginzburg-Landau propagation equation for amplified SPPs.* By using the same perturbative approach, we have been able to derive the Ginzburg-Landau (GL) propagation equation for the SPP beams at a single interface between a metal and an active dielectric. If the diffraction is included in the derivation, the GL equation naturally arises from the imposition of the boundary conditions. The dispersion law of the homogeneous nonlinear SPPs is recovered in the limit where the SPP beam width tends to infinity. On the other hand, if the SPP beam width is finite, the propagation dynamics involves the interplay of metal loss, dielectric amplification, diffraction and complex nonlinearity. It is well known for the GL systems that there exist some dissipative soliton solutions that ensue from the bistability of the zero-background and the homogeneous nonlinear wave. For such special SPP beams, the diffraction vs self-focusing equilibrium is complemented with the effective amplification vs nonlinear gain saturation balance. The

stability analysis of the dark and bright plasmon-solitons revealed an intrinsic instability that limits the propagation of plasmon-solitons. Such results are described in section 3.3 and have been published in Ref. [Marini and Skryabin, 2010].

- *Physical origin of the enhanced nonlinearity.* The explicit calculation of the residual field corrections due to diffraction, loss and nonlinearity does not allow an insightful understanding of the underpinning physical mechanisms providing the modified effective nonlinearity. For this reason, we have developed a general perturbative theory that is suitable for every TM wave propagating in a generic nonlinear subwavelength photonic structure. Such a theory does not involve the explicit calculation of the field corrections. In this case the propagation equation is achieved as the scalar product solvability condition for the multiple scale expansion. The surface contributions to the effective loss and nonlinearity enter the propagation equation through the term η, which results from the off-integral terms after the projection on the linear mode is carried out. Such a term is generally disregarded in the traditional approach used to model the propagation of light in optical fibres. Indeed, for the case of optical fibres, the intensity profile is peaked within the fibre core and the contribution to the effective nonlinearity coming from the boundary is relatively small. However, in the case of subwavelength photonic structures like silicon on insulator (SOI) or plasmonic waveguides the surface contribution is relevant. For SPPs around the plasma frequency, we demonstrated that the surface-induced nonlinearity is the leading term. Indeed, in the extreme subwavelength plasmonic regime, the surface nonlinearity becomes crucial since the light gets tightly confined at the interface between the metal and the dielectric. Such findings are described in chapter 4 and have been published in Ref. [Skryabin et al., 2011].

- *Two-band dispersion and discrete/gap plasmon-soliton formation in metal-dielectric stacks.* The effective refraction and diffraction properties of materials can be managed by using concepts of photonic crystal theory. We have developed a coupled-mode perturbative theory for the propagation of SPPs

in metal-dielectric stacks. Our perturbative approach allowed us to derive a system of coupled discrete nonlinear Schrödinger equations (NLSEs) for the SPPs propagating at every metal-dielectric interface. The different couplings through the metal and dielectric layers are responsible for the formation of a characteristic two-band dispersion, which allows the formation of various gap and discrete plasmon-soliton families. Such results are reported in chapter 5 and have been published in Ref. [Marini et al., 2010].

- *Stabilisation of amplified plasmon-solitons.* The bright and dark dissipative plasmon-solitons propagating along an interface between a metal and an active dielectric are unstable. Hence, they can not be used to deliver optical energy at the nanoscale. Such solitary waves ensue from the overcritical bifurcation of the homogeneous nonlinear SPPs from the zero-background and suffer from the inherent instability of the background. In turn, we proposed and developed a method to stabilise such localised self-sustaining optical beams by exploiting the coupling with a passive interface in an Insulator-Metal-Insulator (IMI) plasmonic structure. For such a geometry, we demonstrated the existence of a subcritical bifurcation of the homogeneous nonlinear SPP waves from the zero background, which allows the propagation of stable bright plasmon-solitons. Basically, the role played by the passive interface is to absorb the perturbations that would otherwise destabilise the plasmon-soliton. We calculated the approximated soliton profiles by a semi-analytical perturbative approach and compared the results with the fully numerical Newton-Raphson approach. The stability has been verified by perturbing the soliton field and propagating it by the split-step beam propagation method. Such a result is reported in chapter 6 and has been published in Ref. [Marini et al., 2011b].

- *Explanation of the nonlinearity enhancement in subwavelength nanowires predicted by the Lorentz reciprocity approach.* We extended the one dimensional perturbative theory to the case of cylindrical nanowires. Calculating explicitly the effective loss and nonlinear parameters, we found complete agreement with the results achieved by the Lorentz reciprocity approach.

Our perturbative theory predicted the nonlinearity enhancement in subwavelength nanowires reported in Refs. [Afshar and Monro, 2009; Afshar et al., 2009], which can then be identified as the surface nonlinearity that is not accounted for in the traditional approach [Agrawal, 2001a]. Such a result is described in chapter 7 and has been published un Ref. [Marini et al., 2011a].

8.1 List of publications

Most of the results reported have been published in international journals

- A. Marini, R. Hartley, A. V. Gorbach and D. V. Skryabin, *"Surface-induced nonlinearity enhancement in subwavelength rod waveguides"*, Physical Review A 84, 063839 (2011).
- A. Marini, D.V. Skryabin and B. Malomed, *"Stable spatial plasmon solitons in a dielectric-metal-dielectric geometry with gain and loss"*, Optics Express 19, 6616 (2011).
- D.V. Skryabin, A.V. Gorbach and A. Marini, *"Surface induced nonlinearity enhancement of TM-modes in planar subwavelength waveguides"*, JOSA B 28, 109 (2011).
- A. Marini, A.V. Gorbach and D.V. Skryabin, *"Coupled mode approach to surface plasmon polaritons in nonlinear periodic structures"*, Optics Letters 35, 3532 (2010).
- A. Marini and D.V. Skryabin, *"Ginzburg-Landau equation bound to the metal-dielectric interface and transverse nonlinear optics with amplified plasmon polaritons"*, Physical Review A 81, 033850 (2010).
- A. Marini, A.V. Gorbach, D.V. Skryabin and A. Zayats, *"Amplification of surface plasmon polaritons in the presence of nonlinearity and spectral signatures of threshold crossover"*, Optics Letters 34, 2864 (2009).

Appendix A

The two-level atom model

For the nonresonant electronic nonlinearity, which was introduced in section 1.3, it is possible to expand the nonlinear polarisation in terms of powers of the electric field $\vec{E}$; the Kerr nonlinearity includes the third order terms of such an expansion. However, in some circumstances, the Taylor expansion of $\vec{P}_{NL}$ does not converge. In particular, when the electronic transitions are resonantly excited by the optical field, the expansion of the polarization in terms of the Taylor series is not appropriate to describe the dielectric response. In such cases, it is a good approximation to treat the material as a *two-level system*, accounting for absorption/emission and saturation effects [Boyd, 2003].

If an electronic transition is resonant with the external field, it is usually adequate to consider the system as composed only by the two resonant states, as depicted in Fig. 1.7. Even though this simplified two-level model ignores other effects occurring in real systems, it is very advantageous for the description of the physical process of saturable absorption/emission.

The Hamiltonian of a two-level system can be expressed as the sum $\hat{H} = \hat{H}_0 + \hat{V}(t)$, where $\hat{H}_0$ is the unperturbed atomic Hamiltonian and $\hat{V}(t)$ is the Hamiltonian of interaction between the atom and the external electromagnetic field. The unperturbed Hamiltonian can be expressed in the diadic representation

$$\hat{H}_0 = \hbar\omega_a|a\rangle\langle a| + \hbar\omega_b|b\rangle\langle b|, \tag{A.1}$$

where $\hbar\omega_a, \hbar\omega_b$ ($\omega_b > \omega_a$) are the energy levels of states a, b corresponding to the Hamiltonian eigenvectors $|a\rangle, |b\rangle$ [Cohen-Tannoudji et al., 1977].

In the electric dipole approximation, the interaction Hamiltonian is provided by

$$\hat{V}(t) = -\left[\mu_{ba}|b\rangle\langle a| + \mu_{ba}^{*}|a\rangle\langle b|\right] E(t), \tag{A.2}$$

where μ_{ba} is the atomic dipole moment and $E(t)$ is the external electric field. The state of the system is described by means of the density matrix $\hat{\rho}$, which representation in the orthonormal basis $|a\rangle, |b\rangle$ is provided by

$$\hat{\rho} = \begin{pmatrix} \rho_{aa} & \rho_{ba}^{*} \\ \rho_{ba} & \rho_{bb} \end{pmatrix}. \tag{A.3}$$

In the Heisenberg picture [Cohen-Tannoudji et al., 1977], the temporal evolution of $\hat{\rho}$ is governed by

$$\frac{d}{dt}\hat{\rho} = \frac{i}{\hbar}[\hat{H}, \hat{\rho}]. \tag{A.4}$$

If the decay rate of the upper level b due to spontaneous emission ($\Gamma_{ba} = 1/T_1$) and the dephasing rate of the atomic dipole moment ($\gamma_{ba} = 1/T_2$) are taken into account, the time evolution of the density matrix elements is determined by

$$\dot{\rho}_{ba} = -(i\omega_{ba} + 1/T_2)\rho_{ba} - (i/\hbar)\mu_{ba}(\rho_{bb} - \rho_{aa})E(t), \tag{A.5}$$

$$\dot{\rho}_{bb} = -\rho_{bb}/T_1 + (i/\hbar)(\mu_{ba}\rho_{ba}^{*} - \mu_{ba}^{*}\rho_{ba})E(t), \tag{A.6}$$

$$\dot{\rho}_{aa} = \rho_{bb}/T_1 + (i/\hbar)(\mu_{ba}^{*}\rho_{ba} - \mu_{ba}\rho_{ba}^{*})E(t), \tag{A.7}$$

where $\omega_{ba} = \omega_b - \omega_a$ [Boyd, 2003]. Note that the condition

$$\dot{\rho}_{aa} + \dot{\rho}_{bb} = 0, \tag{A.8}$$

is implicitly satisfied, representing the conservation of total number of electrons $\rho_{aa} + \rho_{bb} = 1$. Since the equation for the off-diagonal element ρ_{ba} depends only on the difference $\rho_{bb} - \rho_{aa}$, it is convenient to introduce the evolution equation for the difference of population $(\rho_{bb} - \rho_{aa})$:

$$\dot{\rho}_{bb} - \dot{\rho}_{aa} = -\left[1 + (\rho_{bb} - \rho_{aa})\right]/T_1 - (2i/\hbar)(\mu_{ba}^{*}\rho_{ba} - \mu_{ba}\rho_{ba}^{*})E(t). \tag{A.9}$$

Such an equation, in the absence of the external electromagnetic field ($E(t) = 0$), yields the steady state solution $(\rho_{bb} - \rho_{aa})_{eq} = -1$. Hence, combining the unperturbed steady-state solution with the conservation of the total number of electrons, one gets the equilibrium population densities

$$(\rho_{bb})_{eq} = 0, \tag{A.10}$$

$$(\rho_{aa})_{eq} = 1. \tag{A.11}$$

At the equilibrium, the electrons reside only in the state with lower energy (a).

For externally pumped active media, the inversion of population is achievable and Eq. (A.9) is generalized to

$$\dot{\rho}_{bb} - \dot{\rho}_{aa} = \frac{1}{T_1}\left[(\rho_{bb} - \rho_{aa})_{eq} - (\rho_{bb} - \rho_{aa})\right] - \frac{2i}{\hbar}(\mu^*_{ba}\rho_{ba} - \mu_{ba}\rho^*_{ba})E(t), \tag{A.12}$$

where $(\rho_{bb} - \rho_{aa})_{eq} \neq -1$. For a harmonic optical field

$$E(t) = Ee^{-i\omega t} + E^* e^{i\omega t}, \tag{A.13}$$

Eqs. (A.5,A.12) can not be solved analytically. However, an exact analytical solution can be determined in the *rotating wave approximation*. In the absence of the driving field $E(t)$, ρ_{ba} evolves in time as $e^{-i\omega_{ba}t}$. Thus, in the near-resonance regime $\omega \simeq \omega_{ba}$, the part of the electric field oscillating as $e^{-i\omega t}$ constitutes a driving term much more effecient with respect to the part oscillating as $e^{i\omega t}$. By substituting $\rho_{ba} = r_{ba}e^{-i\omega t}$ into Eqs. (A.5,A.12), one gets the system of equations

$$\dot{r}_{ba} = i(\omega - \omega_{ba})r_{ba} - \frac{1}{T_2}r_{ba} - \frac{i}{\hbar}\mu_{ba}E(\rho_{bb} - \rho_{aa}), \tag{A.14}$$

$$\dot{\rho}_{bb} - \dot{\rho}_{aa} = \frac{1}{T_1}\left[(\rho_{bb} - \rho_{aa})_{eq} - (\rho_{bb} - \rho_{aa})\right] + \frac{2i}{\hbar}(\mu_{ba}Er^*_{ba} - \mu^*_{ba}E^*r_{ba}) \tag{A.15}$$

Stationary solutions are found by setting

$$\dot{r}_{ba} = \dot{\rho}_{bb} - \dot{\rho}_{aa} = 0. \tag{A.16}$$

Thus, in this steady-state model, for ρ_{ba} it is assumed the harmonic temporal dependence $e^{-i\omega t}$, while the population difference $\rho_{bb} - \rho_{aa}$ is assumed time independent. The resulting analytical expressions for $\rho_{bb} - \rho_{aa}, \rho_{ba}$ are provided

by

$$\rho_{ba} = \frac{\mu_{ba}E(\rho_{bb}-\rho_{aa})}{\hbar(\omega-\omega_{ba}+i/T_2)}e^{-i\omega t}, \tag{A.17}$$

$$\rho_{bb}-\rho_{aa} = \frac{(\rho_{bb}-\rho_{aa})_{eq}\left[1+(\omega-\omega_{ba})^2T_2^2\right]}{1+(\omega-\omega_{ba})^2T_2^2+(4/\hbar^2)|\mu_{ba}|^2|E|^2T_1T_2}. \tag{A.18}$$

The average two-level induced polarisation, in the density matrix formalism, is provided by the trace

$$P(t) = NTr(\hat{\rho}\hat{\mu}) = N(\mu_{ba}^*\rho_{ba}+\mu_{ba}\rho_{ba}^*), \tag{A.19}$$

where N is the two-level atom density. Hence, the two-level susceptibility can be readily calculated:

$$\chi = \frac{N|\mu_{ba}|^2T_2^2}{\epsilon_0\hbar}(\rho_{bb}-\rho_{aa})_{eq}\frac{\omega-\omega_{ba}-i/T_2}{1+(\omega-\omega_{ba})^2T_2^2+(4/\hbar^2)|\mu_{ba}|^2T_1T_2|E|^2}. \tag{A.20}$$

Introducing the renormalized detuning frequency $\delta = (\omega-\omega_{ba})T_2$, the two-level susceptibility is expressed as

$$\chi = \alpha\frac{\delta-i}{1+\delta^2+|E/E_S|^2}, \tag{A.21}$$

where

$$|E_S|^2 = (\hbar^2/4)|\mu_{ba}|^{-2}(T_1T_2)^{-1}, \tag{A.22}$$

$$\alpha = \frac{N|\mu_{ba}|^2T_2}{\epsilon_0\hbar}(\rho_{bb}-\rho_{aa})_{eq}. \tag{A.23}$$

α is a dimensionless parameter, which sign depends on the equilibrium population difference $(\rho_{bb}-\rho_{aa})_{eq}$, while E_S is the resonant saturation field [Boyd, 2003]. If $(\rho_{bb}-\rho_{aa})_{eq} > 0$, such a model describes the dielectric response of a *gaining* material. In conclusion, in the two-level atom approximation, a saturated nonlinearity naturally arises from near-resonance stimulated absorption or emission, and the Taylor series expansion in terms of $|E/E_S|^2$ can be performed only in the limit $|E| << E_S$:

$$\chi \simeq \alpha\frac{\delta-i}{1+\delta^2}+\alpha\frac{i-\delta}{(1+\delta^2)^2}|E/E_S|^2+o(|E/E_S|^5). \tag{A.24}$$

Appendix B

The Newton-Raphson method

In numerical analysis, the Newton-Raphson method is a procedure to find approximate solutions of a generic $(N \times N)$ nonlinear real-valued system of continuously differentiable equations

$$\bar{f}(\bar{x}) = 0, \tag{B.1}$$

where $\bar{f} : \Re^N \to \Re^N$,

$$\bar{f} = \begin{pmatrix} f_1 \\ f_2 \\ ... \\ f_N \end{pmatrix}, \quad \bar{x} = \begin{pmatrix} x_1 \\ x_2 \\ ... \\ x_N \end{pmatrix}. \tag{B.2}$$

We assume that such a system admits the real solution $\bar{x} = \bar{x}_0$. For $\bar{x}_* \neq \bar{x}_0$, Eq. (B.1) is not satisfied:

$$\bar{f}(\bar{x}_*) = f_* \neq 0. \tag{B.3}$$

Assuming also that $|\bar{x}_* - \bar{x}_0| << |\bar{x}_0|$, under the hypothesis that $\bar{f}$ is a continuously differentiable function, Eq. (B.1) can be approximated by

$$\bar{f} \simeq \bar{f}_* + \hat{J}(\bar{x}_*)(\bar{x} - \bar{x}_*) = 0, \tag{B.4}$$

where $\hat{J}(\bar{x}_*)$ is the Jacobian matrix evaluated in $\bar{x} = \bar{x}_*$:

$$\hat{J}(\bar{x}_*) = \begin{pmatrix} \partial_{x_1} f_1(\bar{x}_*) & \partial_{x_1} f_2(\bar{x}_*) & \cdots & \partial_{x_1} f_N(\bar{x}_*) \\ \partial_{x_2} f_1(\bar{x}_*) & \partial_{x_2} f_2(\bar{x}_*) & \cdots & \partial_{x_2} f_N(\bar{x}_*) \\ \vdots & \cdots & \ddots & \vdots \\ \partial_{x_N} f_1(\bar{x}_*) & \partial_{x_N} f_2(\bar{x}_*) & \cdots & \partial_{x_N} f_N(\bar{x}_*) \end{pmatrix}. \tag{B.5}$$

By solving Eq. (B.4) one gets

$$\bar{x}_{**} = \bar{x}_* - \hat{J}^{-1}(\bar{x}_*)\bar{f}_*. \tag{B.6}$$

Note that such an operation is possible only if the Jacobian matrix $\hat{J}^{-1}(\bar{x}_*)$ is not singular, depending on the behaviour of the function $\bar{f}$ around the initial guess $\bar{x}_*$. If $\bar{x}_*$ is close enough to the exact solution $\bar{x}_0$, then $\bar{x}_{**}$ constitutes a better approximation of Eq. (B.1) and the iterative procedure [Hamming, 1986]

$$\bar{x}_n = \bar{x}_{n-1} - \hat{J}^{-1}(\bar{x}_{n-1})\bar{f}(\bar{x}_{n-1}), \tag{B.7}$$

where

$$\hat{J}(\bar{x}_n) = \begin{pmatrix} \partial_{x_1} f_1(\bar{x}_n) & \partial_{x_1} f_2(\bar{x}_n) & \cdots & \partial_{x_1} f_N(\bar{x}_n) \\ \partial_{x_2} f_1(\bar{x}_n) & \partial_{x_2} f_2(\bar{x}_n) & \cdots & \partial_{x_2} f_N(\bar{x}_n) \\ \vdots & \cdots & \ddots & \vdots \\ \partial_{x_N} f_1(\bar{x}_n) & \partial_{x_N} f_2(\bar{x}_n) & \cdots & \partial_{x_N} f_N(\bar{x}_n) \end{pmatrix}, \tag{B.8}$$

converges to the true solution $\bar{x}_0$ within the desired accuracy for an according number of iterations.

Appendix C

The split-step beam propagation method

The split-step beam propagation method (BPM) is a numerical procedure for the solution of a generic nonlinear differential equation

$$i\partial_\zeta \psi + \hat{\mathcal{D}}_\xi \psi + \hat{\mathcal{N}}(\psi)\psi = 0, \tag{C.1}$$

with the initial condition

$$\psi(\xi, \zeta_0) = \psi_0(\xi). \tag{C.2}$$

$\hat{\mathcal{D}}_\xi$ is a linear differential operator acting on the two-variable function $\psi(\zeta, \xi)$ and $\hat{\mathcal{N}}(\psi)$ is a nonlinear operator dependent on the function ψ.

In the numerical simulations of this thesis, ζ, ξ represent the propagation distance (z) and the transverse direction of diffraction (y), respectively. The differential operator $\hat{\mathcal{D}}_\xi = (1/2\beta)\partial^2_{\xi\xi}$ accounts for the linear diffraction and we considered only the case of third-order isotropic nonlinearity $\hat{\mathcal{N}}(\psi)\psi = \gamma|\psi|^2\psi$.

Neglecting the nonlinear terms, Eq. (C.1) can be solved in the Fourier k-domain of the ξ variable, as the linear differential operator $\hat{\mathcal{D}}_\xi$ becomes a simple multiplication factor. On the other hand, the nonlinear terms are more easy to handle in the real domain ξ.

The numerical solution to this problem is the split-step method, where a Fourier transform and an inverse Fourier transform are taken at every step in ζ. The split-step method provides approximate solutions by assuming that, within the small step h, the linear and nonlinear parts of Eq. (C.1) act independently ($\zeta = \zeta_0 + nh,\ n \in N$). The propagation from ζ to $\zeta + h$ is carried out in three steps: in the first and third steps $\mathcal{N} = 0$ and $\hat{\mathcal{D}}$ acts alone, while in the middle step $\hat{\mathcal{D}} = 0$ and the nonlinearity is assumed as a constant [Agrawal, 2001b]

$$\psi(\zeta + h, \xi) \approx e^{i\frac{h}{2}\hat{\mathcal{D}}} e^{ih\hat{\mathcal{N}}[\psi(\zeta,\xi)]} e^{i\frac{h}{2}\hat{\mathcal{D}}} \psi(\zeta, \xi). \tag{C.3}$$

The operator $e^{i\frac{h}{2}\hat{\mathcal{D}}}$ is evaluated in the Fourier k-domain of the ξ variable, acting as the multiplying k-function $e^{i\frac{h}{2}\tilde{D}(k)}$, where $\tilde{D}(k) = -k^2/2\beta$ in the case considered by us. Denoting the Fourier transform operator by $\mathcal{F}$ and the inverse Fourier transform by $\mathcal{F}^{-1}$, the BPM provides us with

$$\psi(\zeta + h, \xi) \approx \mathcal{F}^{-1}\{e^{i\frac{h}{2}\tilde{D}(k)} \mathcal{F}[e^{ih\hat{\mathcal{N}}[\psi(\zeta,\xi)]} \Phi(\xi)]\}, \tag{C.4}$$

where

$$\Phi(\xi) = \mathcal{F}^{-1}[e^{i\frac{h}{2}\tilde{D}(k)} \mathcal{F}\psi(\zeta, \xi)]. \tag{C.5}$$

The linear propagation $e^{ih\hat{\mathcal{N}}(\psi)}\Phi(\xi)$ from ζ to $\zeta + h$, where the nonlinear contribution is approximated by the constant $\hat{\mathcal{N}}[\psi(\zeta, \xi)]$ at the beginning of the step, can be performed by several methods, e.g. by the fourth-order Runge-Kutta method, which is described in appendix D. The Fourier transformations used in the BPM were implemented by the Fast Fourier Transform (FFT) routine in MATLAB.

Appendix D

The explicit Runge-Kutta method

In numerical analysis, the Runge-Kutta method is an iterative procedure for the approximate solution of an ordinary differential equation

$$\frac{d\bar{y}}{dt} = \bar{f}(t, \bar{y}), \tag{D.1}$$

with the inital value

$$\bar{y}(t_0) = \bar{y}_0. \tag{D.2}$$

The dynamical system $\bar{f}(t, \bar{y}) : \Re^N \rightarrow \Re^N$ is a linear and continuously differentiable function of $\bar{y}, t$.

An approximate solution of Eq. (D.1) can be calculated by introducing the discrete time ($n \in N$)

$$t \rightarrow t_0 + n\Delta t, \tag{D.3}$$

$$\bar{y}(t) \rightarrow \bar{y}_n = \bar{y}(t_n). \tag{D.4}$$

The explicit fourth-order Runge Kutta method [Hamming, 1986] provides the approximate solution

$$\bar{y}_{n+1} = \bar{y}_n + \frac{1}{6}(\bar{k}_1 + 2\bar{k}_2 + 2\bar{k}_3 + \bar{k}_4), \tag{D.5}$$

where

$$\bar{k}_1 = \Delta t \bar{f}(t_n, \bar{y}_n), \tag{D.6}$$

$$\bar{k}_2 = \Delta t \bar{f}(t_n + \frac{1}{2}\Delta t, \bar{y}_n + \frac{1}{2}\bar{k}_1), \tag{D.7}$$

$$\bar{k}_3 = \Delta t \bar{f}(t_n + \frac{1}{2}\Delta t, \bar{y}_n + \frac{1}{2}\bar{k}_2), \tag{D.8}$$

$$\bar{k}_4 = \Delta t \bar{f}(t_n + \Delta t, \bar{y}_n + \bar{k}_3). \tag{D.9}$$

References

Abraham, N. B. and Firth, W. J. (1990). Overview of transverse effects in nonlinear-optical systems. *Journal Of The Optical Society Of America B-Optical Physics*, 7(6):951–962. 82

Aceves, A. and Wabnitz, S. (1989). Self-induced transparency solitons in nonlinear refractive periodic media. *Physics Letters A*, 141:37. 123

Afshar, S. V. and Monro, T. M. (2009). A full vectorial model for pulse propagation in emerging waveguides with subwavelength structures part i: Kerr nonlinearity. *Optics Express*, 17:2298–2318. 5, 7, 100, 101, 112, 166, 175, 182, 187

Afshar, S. V., Zhang, W. Q., Ebendorff-Heidepriem, H., and Monro, T. M. (2009). Small core optical waveguides are more nonlinear than expected: experimental confirmation. *Optics Letters*, 34:3577–3579. 5, 7, 100, 101, 166, 175, 182, 187

Agranovich, V. and Mills, D. (1982). *Surface Polaritons*. North-Holland. 29

Agranovich, V. M., Babichenko, V., and Chernyak, Y. (1980). Nonlinear surface polaritons. *Soviet Physics JETP Letters*, 32:512–515. 68, 69, 70

Agrawal, G. P. (2001a). *Applications of Nonlinear Fiber Optics*. Academic Press. 120, 122, 187

Agrawal, G. P. (2001b). *Nonlinear Fiber Optics*. Academic press. 5, 15, 24, 82, 92, 101, 111, 112, 172, 174, 175, 177, 179, 182, 195

Akhmediev, N. N. and Ankiewicz, A. (1997). *Solitons: Nonlinear Pulses and Beams*. Chapman & Hall. 96, 147, 153

Akram, M. N., Silfvenius, C., Kjebon, O., and Schatz, R. (2004). Design optimization of ingaasp-ingaalas 1.55μm strain-compensated mqw lasers for direct modulation applications. *Semiconductor Science and Technology*, 19:615–625. 64

Alam, M. Z., Meier, J., Aitchison, J. S., and Mojahedi, M. (2007). Gain assisted surface plasmon polariton in quantum wells structures. *Optics Express*, 14:1611–1625. 64

Almeida, V., Barrios, C., Panepucci, R., and Lipson, M. (2004a). All-optical control of light on a silicon chip. *Nature*, 431:1081. 15, 100

Almeida, V., Xu, Q., Barrios, C., and Lipson, M. (2004b). Guiding and confining light in void nanostructure. *Optics Letters*, 29:1209. 15, 16, 100, 114, 115

Ambati, A., Nam, S. H., Ulin-Avila, E., Genov, A., Bartal, G., and Zhang, X. (2008). Observation of stimulated emission of surface plasmon polaritons. *Nano Letters*, 8:3998. 2, 30, 64, 67, 74, 82

Andrew, P. and Barnes, W. L. (2004). Energy transfer across a metal film mediated by surface plasmon polaritons. *Science*, 306:1002. 59

Anker, J. N., Hall, W. P., Lyandres, O., Shah, N. C., Zhao, J., and VanDuyne, R. P. (2008). Biosensing with plasmonic nanosensors. *Nature Materials*, 7:442. 29

Antoine, R., Pellarin, M., Palpant, B., Broyer, M., Prevel, B., Galletto, P., Brevet, P. F., and Girault, H. H. (1998). Surface plasmon enhanced second harmonic response from gold clusters embedded in an alumina matrix. *Journal of Applied Physics*, 84:4532–4536. 68

Aranson, I. S. and Kramer, L. (2002). The world of the complex ginzburg-landau equation. *Reviews Of Modern Physics*, 74(1):99–143. 95, 96, 153

Arfken, G. and Weber, H. (2001). *Mathematical methods for physicists*. Academic Press. 9, 14, 36, 170

Ashcroft, N. and Mermin, N. (1976). *Solid State Physics*. Harcourt College Publishers. 17, 31

Asobe, M., Kanamori, T., and Kubodera, K. (1993). Applications of highly nonlinear chalcogenite glass fibers in ultrafast all optical switches. *IEEE Journal of Quantum Electronics*, 29:2325–2333. 73

Atai, J. and Malomed, B. A. (1996). Stability and interactions of solitons in two-component active systems. *Physical Review E*, 54:4371. 147, 156, 159

Baehr-Jones, T., Hochberg, M., Walker, C., and Scherer, A. (2005). High-q optical resonators in silicon-on-insulator-based slot waveguides. *Applied Physics Letters*, 86:081101. 15

Barnes, W. L. (1998). Fluorescence near interfaces: The role of photonic mode density. *Journal of Modern Optics*, 45:661–699. 63

Barnes, W. L., Dereux, A., and Ebbesen, T. (2003). Surface plasmon subwavelength optics. *Nature*, 424:824. 2, 30

Bergh, R. A., Kotler, G., and Shaw, H. J. (1980). Single-mode fibre optic directional coupler. *Electronics Letters*, 16:260–261. 121

Bergman, D. J. and Stockman, M. I. (2003). Surface plasmon amplification by stimulated emission of radiation: Quantum generation of coherent surface plasmons in nanosystems. *Physical Review Letters*, 90:027402. 30, 58, 74

Berini, P. (1999). Plasmonpolariton modes guided by a metal film of finite width. *Optics Letters*, 24:1011. 50

Berini, P. (2000). Plasmon-polariton waves guided by thin lossy metal films of finite width: Bound modes of symmetric structures. *Physical Review B*, 61:10484. 50

Berini, P. (2001). Plasmon-polariton waves guided by thin lossy metal films of finite width: Bound modes of asymmetric structures. *Physical Review B*, 63:125417. 30, 50

Berini, P. (2009). Long-range surface plasmon polaritons. *Advances in Optics and Photonics*, 1:484588. 30, 49

Berkhoer, A. L. and Zakharov, V. E. (1970). *Zh. Eksp. Teor. Fiz.*, 58:903. 71, 99

Boardman, A. (1982). *Electromagnetic Surface Modes*. JohnWiley & Sons. 29, 42, 50, 178

Boardman, A. D., Maradudin, A. A., Stegeman, G. I., Twardowski, T., and Wright, E. M. (1987). Exact theory of nonlinear p-polarized optical waves. *Physical Review A*, 35:1159–1164. 69, 71, 99

Bolger, P. M., Dickson, W., Krasavin, A. V., Liebscher, L., Hickey, S. G., Skryabin, D. V., and Zayats, A. V. (2010). Amplified spontaneous emission of surface plasmon polaritons and limitations on the increase of their propagation length. *Optics Letters*, 8:1197–1199. 64, 67, 157

Boyce, W. and DiPrima, R. (1997). *Elementary differential equations and boundary value problems*. John Wiley & Sons. 10, 26, 36, 106, 160

Boyd, R., Lukishova, S., and Shen, Y. (2009). *Self-focusing: Past and Present*. Springer. 24

Boyd, R. W. (2003). *Nonlinear Optics*. Academic Press. 3, 15, 20, 21, 68, 75, 83, 84, 147, 188, 189, 191

Bozhevolnyi, S. (2008). *Plasmonic Nanowaveguides and Circuits*. Pan Stanford. 1, 146

Bozhevolnyi, S., Volkov, V., Devaux, E., and Ebbesen, T. (2005). Channel plasmon-polariton guiding by subwavelength metal grooves. *Physical Review Letters*, 95:046802. 56, 57, 82, 146, 166

Bozhevolnyi, S. I., Volkov, V. S., Devaux, E., Laluet, J., and Ebbesen, T. W. (2006a). Channel plasmon subwavelength waveguide components including interferometers and ring resonators. *Nature*, 440:508. 29, 146

Bozhevolnyi, S. I., Volkov, V. S., Devaux, E., Laluet, J. Y., and Ebbesen, T. W. (2006b). Channel plasmon subwavelength waveguide components including interferometers and ring resonators. *Nature*, 440(7083):508–511. 2, 81

Brongersma, M., Hartman, J., and Atwater, H. (2000). Electromagnetic energy transfer and switching in nanoparticle chain arrays below the diffraction limit. *Physical Review B*, 62:R16356. 56

Burke, J., Stegeman, G., and Tamlr, T. (1986). Surface-polariton-like waves guided by thin, lossy metal films. *Physical Review B*, 33:5186. 30, 49

Charbonneau, R., Berini, P., Berolo, E., and LisickaShrzek, E. (2000). Experimental observation of plasmon-polariton waves supported by a thin metal film of finite width. *Optics Letters*, 25:844. 49

Charbonneau, R., Lahoud, N., Mattiussi, G., and Berini, P. (2005a). Demonstration of integrated optics elements based on long-ranging surface plasmon polaritons. *Optics Express*, 13:977. 49

Charbonneau, R., Lahoud, N., Mattiussi, G., and Berini, P. (2005b). Demonstration of integrated optics elements based on long-ranging surface plasmon polaritons. *Optics Express*, 13:977. 56

Chate, H. and Manneville, P. (1992). Stability of the bekki-nozaki hole solutions to the one-dimensional complex ginzburg-landau equation. *Physics Letters A*, 171:183. 98

Chen, W. and Mills, D. (1987). Gap solitons and the nonlinear optical-response of superlattices. *Physical Review Letters*, 58:160. 123

Chiao, R., Garmire, E., and Townes, C. (1964). Self-trapping of optical beams. *Physical Review Letters*, 13:479. 25

Christodoulides, D. and Joseph, R. (1988). Discrete self-focusing in nonlinear arrays of coupled waveguides. *Optics Letters*, 12:794. 24, 122

Christodoulides, D. and Joseph, R. (1989). Slow bragg solitons in nonlinear periodic structures. *Physical Review Letters*, 62:1746. 123

Ciattoni, A., Crosignani, B., Porto, P. D., and Yariv, A. (2005). Perfect optical solitons: spatial kerr solitons as exact solutions of maxwells equations. *Journal Of The Optical Society Of America B*, 22:1384. 71, 99

Ciattoni, A., Rizza, C., and Palange, E. (2010a). Extreme nonlinear electrodynamics in metamaterials with very small linear dielectric permittivity. *Physical Review A*, 81:043839. 124, 135

Ciattoni, A., Rizza, C., and Palange, E. (2010b). Transmissivity directional hysteresis of a nonlinear metamaterial slab with very small linear permittivity. *Optics Letters*, 35:2130–2132. 124, 135

Ciattoni, A., Rizza, C., and Palange, E. (2010c). Transverse power flow reversing of guided waves in extreme nonlinear metamaterials. *Optics Express*, 18:11911–11916. 124, 135

Ciattoni, A., Rizza, C., and Palange, E. (2011). All-optical active plasmonic devices with memory and power-switching functionalities based on epsilon-near-zero nonlinear metamaterials. *Physical Review A*, 83:043813. 124, 135

Citrin, D. S. (2004). Coherent excitation transport in metal-nanoparticle chains. *Nano Letters*, 4:1561. 30, 56

Cohen-Tannoudji, C., Diu, B., and Laloe, F. (1977). *Quantum mechanics*. Wiley-Interscience. 13, 189

Cregan, R. F., Mangan, B. J., Knight, J. C., Birks, T. A., Russell, P. S. J., Roberts, P. J., and Allan, D. C. (1999). Single-mode photonic band gap guidance of light in air. *Science*, 285:1537–1539. 121

Daniel, B. A. and Agrawal, G. P. (2010). Vectorial nonlinear propagation in silicon nanowire waveguides: polarization effects. *Journal of the Optical Society of America B*, 27:956–965. 7, 101

Davoyan, A. R., Shadrivov, I. V., Bozhevolnyi, S. I., and Kivshar, Y. S. (2010a). Backward and forward modes guided by metal-dielectric-metal plasmonic waveguides. *Journal of Nanophotonics*, 4:043509. 45

Davoyan, A. R., Shadrivov, I. V., and Kivshar, Y. S. (2008). Nonlinear plasmonic slot waveguides. *Optics Express*, 16:21209–21214. 45, 74, 100, 124

Davoyan, A. R., Shadrivov, I. V., and Kivshar, Y. S. (2009a). Quadratic phase matching in nonlinear plasmonic nanoscale waveguides. *Optics Express*, 17:20063. 68

Davoyan, A. R., Shadrivov, I. V., and Kivshar, Y. S. (2009b). Self-focusing and spatial plasmon-polariton solitons. *Optics Express*, 17(24):21732–21737. 74, 82, 83, 92, 100, 101, 111, 112, 118, 120, 123, 146, 172, 175, 182

Davoyan, A. R., Shadrivov, I. V., and Kivshar, Y. S. (2011). Symmetry breaking in plasmonic waveguides with metal nonlinearities. *Optics Letters*, 36:930. 124

Davoyan, A. R., Shadrivov, I. V., Zharov, A. A., Gramotnev, D. K., and Kivshar, Y. S. (2010b). Nonlinear nanofocusing in tapered plasmonic waveguides. *Physical Review Letters*, 105:116804. 5, 74, 111, 112, 118

DeLaRue, R., Chong, H., Gnan, M., Johnson, N., Ntakis, I., Pottier, P., Sorel, M., Zain, A., Zhang, H., Camargo, E., Jin, C., Armenise, M., and Ciminelli, C. (2006). Photonic crystal and photonic wire nano-photonics based on silicon-on-insulator. *New Journal of Physics*, 8:256. 15

DeLeon, I. and Berini, P. (2008). Theory of surface plasmon-polariton amplification in planar structures incorporating dipolar gain media. *Physical Review B*, 78:161401. 62

DeLeon, I. and Berini, P. (2009). Modeling surface plasmon-polariton gain in planar metallic structures. *Optics Express*, 17:20191. 62

DellaValle, G. and Longhi, S. (2010). Geometric potential for plasmon polaritons on curved surfaces. *Journal Of Physics B: Atomic, Molecular and Optical Physics*, 43:051002. 112

Devaux, E., Ebbesen, T., Thomas, W., Weeber, J. C., and Dereux, A. (2003). Launching and decoupling surface plasmons viamicro-gratings. *Applied Physics Letters*, 83:49364938. 54

DiFalco, A., OFaolain, L., and Krauss, T. F. (2008). Dispersion control and slow light in slotted photonic crystal waveguides. *Applied Physics Letters*, 92:083501. 100

Dintinger, J., Klein, S., and Ebbesen, T. W. (2006). Molecule-surface plasmon interactions in hole arrays: Enhanced absorption, refractive index changes, and all-optical switching. *Advanced Materials*, 18:1267–1270. 60

Dionne, J. A., Verhagen, E., Polman, A., and Atwater, H. A. (2008). Are negative index materials achievable with surface plasmon waveguides? a case study of three plasmonic geometries. *Optics Express*, 16:19001. 3, 45

Ditlbacher, H., Hohenau, A., Wagner, D., Kreibig, U., Rogers, M., Hofer, F., Aussenegg, F. R., and Krenn, J. R. (2005). Silver nanowires as surface plasmon resonators. *Physical Review Letters*, 95:257403. 56

Ditlbacher, H., Krenn, J. R., Felidj, N., Lamprecht, B., Schider, G., Salerno, M., Leitner, A., and Aussenegg, F. R. (2002). Fluorescence imaging of surface plasmon fields. *Applied Physics Letters*, 80:404406. 54

Dolling, G., Enkrich, C., Wegener, M., Soukoulis, C. M., and Linden, S. (2006). Low-loss negative-index metamaterial at telecommunication wavelengths. *Optics Letters*, 31:1800–1802. 124

Dolling, G., Wegener, M., Soukoulis, C. M., and Linden, S. (2007). Negative-index metamaterial at 780 nm wavelength. *Optics Letters*, 32:53–55. 124

Drude, P. (1900). Zur elektronentheorie der metalle. *Annalen der Physik*, 306:566. 31

Ebbesen, T. W., Genet, C., and Bozhevolnyi, S. I. (2008). Surface-plasmon circuitry. *Physics Today*, 61:44. 29, 55, 81

Eckhardt, G., Hellwarth, R., McClung, F., Schwarz, S., D.Weiner, and Woodbury, E. (1962). Stimulated raman scattering from organic liquids. *Physical Review Letters*, 9:455. 20

Economou, E. N. (1969). Surface plasmons in thin films. *Physical Review Letters*, 182:539. 42

Edwards, D. (1985). *Handbook of Optical Constants of Solids*. Academic Press. 15

Edwards, D. F. and Ochoa, E. (1980). Infrared refractive index of silicon. *Applied Optics*, 19:4130. 179

Efremidis, N. K., Zhang, P., Chen, Z., Christodoulides, D. N., Ruter, C. E., and Kip, D. (2010). Wave propagation in waveguide arrays with alternating positive and negative couplings. *Physical Review A*, 81:053817. 132, 135

Eguiluz, A. and Maradudin, A. A. (1976). Electrostatic edge modes along a parabolic wedge. *Physical Review B*, 14:5526. 56, 166

Eisenberg, H. S., Silberberg, Y., Morandotti, R., and Aitchison, J. S. (2000). Diffraction management. *Physical Review Letters*, 85:1863–1866. 122, 123

Eisenberg, H. S., Silberberg, Y., Morandotti, R., Boyd, A., and Aitchison, J. S. (1998). Discrete spatial optical solitons in waveguide arrays. *Physical Review Letters*, 81:3383. 122

Elser, J., Podolskiy, V. A., Salakhutdinov, I., and Avrutsky, I. (2007). Nonlocal effects in effective-medium response of nanolayered metamaterials. *Applied Physics Letters*, 90:191109. 124

Engheta, N. and Ziolkowski, R. (2006). *METAMATERIALS: Physics and Engineering Explorations*. Wiley. 3

Fan, X., Wang, G. P., Lee, J. C. W., and Chan, C. T. (2006). All-angle broadband negative refraction of metal waveguide arrays in the visible range: Theoretical analysis and numerical demonstration. *Physical Review Letters*, 97:073901. 124

Fano, U. (1941). The theory of anomalous diffraction gratings and of quasi-stationary waves on metallic surfaces (sommerfelds waves). *Journal Of The Optical Society Of America*, 31:213222. 2

Fauve, S. and Thual, O. (1990). Solitary waves generated by subcritical instabilities in dissipative systems. *Physical Review Letters*, 64:282–284. 147

Fedyanin, D. Y., Arsenin, A. V., Leiman, V. G., and Gladun, A. D. (2010). Backward waves in planar insulatormetalinsulator waveguide structures. *Jornal of Optics*, 12:015002. 45

Feigenbaum, E. and Orenstein, M. (2007). Plasmonsoliton. *Optics Letters*, 32:674–676. 3, 5, 7, 74, 82, 83, 92, 100, 101, 111, 112, 118, 120, 123, 146, 172, 175, 182

Firth, W. J. and Paulau, P. V. (2010). Soliton lasers stabilized by coupling to a resonant linear system. *European Physical Journal D*, 59:13–21. 147

Folland, G. (1992). *Fourier analysis and its applications*. Wadsworth&Brooks. 9

Ford, G. and Weber, W. (1984). Electromagnetic interactions of molecules with metal surfaces. *Physics Reports*, 113:195–287. 63

Fox, M. (2001). *Optical properties of Solids*. Oxford University Press. 31

Franken, P., Hill, A., Peters, C., and Weinreich, G. (1961). Generation of optical harmonics. *Physical Review Letters*, 7:118. 20

Friberg, S., Weiner, A., Silberberg, Y., Sfez, B., and Smith, P. (1988). Femtosecond switching in a dual-core-fiber nonlinear coupler. *Optics Letters*, 13:904. 122

Gather, M., Danzc, N., Meerholzd, K., and Leosson, K. (2011). Lasers and electro optics / quantum electronics and laser science conference (cleo/qels). In *QFE5*. 64, 67

Gather, M. C., Meerholz, K., Danz, N., and Leosson, K. (2010). Net optical gain in a plasmonic waveguide embedded in a fluorescent polymer. *Nature Photonics*, 4:457. 64, 67, 75, 82, 146

Ginzburg, P., Hayat, A., Berkovitch, N., and Orenstein, M. (2010). Nonlocal ponderomotive nonlinearity in plasmonics. *Optics Letters*, 35:1551. 2

Gorbach, A. V. and Skryabin, D. V. (2009). Spatial solitons in periodic nanostructures. *Physical Review A*, 79:053812. 100

Gordon, J. (1983). Interaction forces among solitons in optical fibers. *Optics Letters*, 8:596. 25

Goubau, G. (1950). Surface waves and their application to transmission lines. *Journal of Applied Physics*, 21:11191128. 38

Gramotnev, D. K. and Bozhevolnyi, S. I. (2010). Plasmonics beyond the diffraction limit. *Nature Photonics*, 4:83–91. 146

Grandidier, J., ColasDesFrancs, G., Massenot, S., Bouhelier, A., Markey, L., Weeber, J. C., Finot, C., and Dereux, A. (2009). Gain-assisted propagation in a plasmonic waveguide at telecom wavelength. *Nano Letters*, 9:2935–2939. 64, 67

Grillot, F., Vivien, L., Laval, S., and Cassan, E. (2006). Propagation loss in single-mode ultrasmall square silicon-on-insulator optical waveguides. *Journal of Lightwave Technology*, 24:891. 15

Guasoni, M., Conforti, M., and Angelis, C. D. (2010). Light propagation in non-uinform plasmonic subwavelength waveguide arrays. *Optics Communications*, 283:1161–1168. 123, 132, 144

Hamming, R. W. (1986). *Numerical Methods for Scientists and Engineers*. 193, 196

Hansch, T. W., Varsanyi, F., and Schawlow, A. L. (1971). Image amplification by dye lasers. *Applied Physics Letters*, 18:108–110. 58

Hasegawa, A. (1984). Generation of a train of soliton pulses by induced modulational instability in optical fibers. *Optics Letters*, 9:288. 26

Hasegawa, A. and Tappert, F. (1973). Transmission of stationary nonlinear optical pulses in dispersive dielectric fibers. i. anomalous dispersion. *Applied Physics Letters*, 23:142. 25

Haurylau, M., Chen, G., Chen, H., Zhang, J., Nelson, N. A., Albonesi, D. H., Friedman, E. G., and Fauchet, P. M. (2006). On-chip optical interconnect roadmap: Challenges and critical directions. *IEEE Journal of Selected Topics in Quantum Electronics*, 12:1699. 55

Hendry, E., GarciaVidal, F. J., MartinMoreno, L., GomezRivas, J., Bonn, M., Hibbins, A. P., and Lockyear, M. J. (2008). Optical control over surface-plasmon-polariton-assisted thz transmission through a slit aperture. *Physical Review Letters*, 100:123901. 60

Hill, M. T., Marell, M., Leong, E. S. P., Smalbrugge, B., Y, Z., Sun, M., VanVeldhoven, P. J., Geluk, E. J., Karouta, F., Oei, Y. S., Notzel, R., Ning, C. Z., and Smit, M. K. (2009). Lasing in metal-insulator-metal sub-wavelength plasmonic waveguides. *Optics Express*, 17:11107. 59

Homola, J. (2006). *Surface Plasmon Resonance Based Sensors*. Springer. 1, 29

Hooper, I. R. and Sambles, J. R. (2004). Coupled surface plasmon polaritons on thin metal slabs corrugated on both surfaces. *Physical Review B*, 70:045421. 54

Huang, J. H., Chang, R., Leung, P. T., and Tsai, D. P. (2009). Nonlinear dispersion relation for surface plasmon at a metalkerr medium interface. *Optics Communications*, 282:1412–1415. 73

Husakou, A. and Herrmann, J. (2007). Steplike transmission of light through a metal-dielectric multilayer structure due to an intensity-dependent sign of the effective dielectric constant. *Physical Review Letters*, 99:127402. 124

Inoue, K. (1992). Four-wave mixing in an optical fiber in the zero-dispersion wavelength region. *Journal of Lightwave Technology*, 10:1553. 20

Jackson, J. (1999). *Classical Elctrodynamics*. Wiley. 8, 9, 10, 14, 32, 36, 37, 52, 62, 104, 168

Jensen, S. (1982). The nonlinear coherent coupler. *IEEE Journal of Quantum Electronics*, 18:1580. 122

Jeon, T. I. and Grischkowsky, D. (2006). Thz zenneck surface wave (thz surface plasmon) propagation on a metal sheet. *Applied Physics Letters*, 88:061113. 30

Joannopoulos, J., Meade, R., and Winn, J. (2008). *Photonic crystals*. Princeton University Press. 17, 18, 121

John, S. (1987). Strong localization of photons in certain disordered dielectric superlattices. *Physical Review Letters*, 58:2486–2489. 121

Johnson, P. B. and Christy, R. W. (1972). Optical constants of the noble metals. *Physical Review B*, 6:4370. 31

Jones, A. L. (1965). Coupling of optical fibers scattering in fibers. *Journal of the Optical Society of America*, 55:261. 122

Ju, J. J., Park, S., Kim, M., Kim, J. T., Park, S. K., Park, Y. J., and Lee, M. H. (2007). 40 gbit/s light signal transmission in long-range surface plasmon waveguides. *Applied Physics Letters*, 91:171117. 56

Jung, J., Sondergaard, T., and Bozhevolnyi, S. I. (2007). Theoretical analysis of square surface plasmon-polariton waveguides for long-range polarization-independent waveguiding. *Physical Review B*, 76:035434. 82, 166

Kittel, C. (1996). *Introduction to Solid State Physics*. Wiley. 17, 18, 31, 33

Kivshar, Y. (1993). Self-localization in arrays of defocusing waveguides. *Optics Letters*, 18:1147. 123, 140

Kivshar, Y. and Agrawal, G. P. (2003). *Optical Solitons: From Fibers to Photonic Crystals*. Academic Press. 3, 24, 27, 82

Kivshar, Y. and Campbell, D. (1993). Peierlsnabarro potential barrier for highly localized nonlinear modes. *Physical Review E*, 48:3077. 123

Klimov, V. I., Mikhailovsky, A. A., Xu, S., Malko, A., Hollingsworth, J. A., Leatherdale, C. A., Eisler, H. J., and Bawendi, M. G. (2000). Optical gain and stimulated emission in nanocrystal quantum dots. *Science*, 290:314–317. 64

Kneipp, K., Wang, Y., Kneipp, H., Perelman, L. T., Itzkan, I., Dasari, R. R., and Feld, M. S. (1997). Single molecule detection using surface-enhanced raman scattering (sers). *Physical Review Letters*, 78:1667. 29

Knight, J. C., Russell, T. A. B. P. S. J., and Atkin, D. M. (1996). All-silica single-mode optical fiber with photonic crystal cladding. *Optics Letters*, 21:1547–1549. 121

Koos, C., Jacome, L., Poulton, C., Leuthold, J., and Freude, W. (2007). Nonlinear silicon-on-insulator waveguides for all-optical signal processing. *Optics Express*, 15:5976–5990. 101, 112, 116

Koos, C., Vorreau, P., Vallaitis, T., Dumon, P., Bogaerts, W., Baets, R., Esembeson, B., Biaggio, I., Michinobu, T., Diederich, F., Freude, W., and Leuthold, J. (2009). All-optical high-speed signal processing with siliconorganic hybrid slot waveguides. *Nature Photonics*, 3:216. 16, 100, 101, 116

Krasavin, A. V., MacDonald, K. F., Zheludev, N. I., and Zayats, A. V. (2004). High-contrast modulation of light with light by control of surface plasmon polariton wave coupling. *Applied Physics Letters*, 85:3369. 57

Krasavin, A. V., Zayats, A. V., and Zheludev, N. I. (2005). Active control of surface plasmon-polariton waves. *Journal of Optics A*, 7:S85S89. 57, 59

Krasavin, A. V. and Zheludev, N. I. (2004). Active plasmonics: Controlling signals in au/ga waveguide using nanoscale structural transformations. *Applied Physics Letters*, 84:1416–1418. 59

Krenn, J. R. (2003). Watching energy transfer. *Nature Materials*, 2:210. 56

Krenn, J. R., Lamprecht, B., Ditlbacher, H., Schider, G., Salerno, M., Leitner, A., and Aussenegg, F. R. (2002). Nondiffraction-limited light transport by gold nanowires. *Europhysics Letters*, 60:663. 56

Kretschmann, E. and Raether, H. (1968). Radiative decay of non-radiative surface plasmons excited by light. *Z. Naturforsch. A*, 23:2135. 50, 51

Krolikowski, W. and Kivshar, Y. S. (1996). Soliton-based optical switching in waveguide arrays. *Journal of the Optical Society of America B*, 13:876. 140

Kroo, N., Varro, S., Farkas, G., Dombi, P., Oszetzky, D., Nagy, A., and Czitrovszky, A. (2008). Nonlinear plasmonics. *Journal of Modern Optics*, 55:3203–3210. 68

Kumar, A., Yu, S. F., and Li, X. F. (2009). Random laser action in dielectric-metal-dielectric surface plasmon waveguides. *Applied Physics Letters*, 95:231114. 64

Kumar, A., Yu, S. F., Li, X. F., and Lau, S. P. (2008). Surface plasmonic lasing via the amplification of coupled surface plasmon waves inside dielectric-metal-dielectric waveguides. *Optics Express*, 16:16113–16123. 64

Lal, S., Link, S., and Halas, N. J. (2007). Nano-optics from sensing to waveguiding. *Nature Photonics*, 1:641. 29

Lamprecht, B., Krenn, J. R., Leitner, A., and Aussenegg, F. R. (1999). Resonant and off-resonant light-driven plasmons in metal nanoparticles studied by femtosecond-resolution third-harmonic generation. *Physical Review Letters*, 83:4421–4424. 68

Lamprecht, B., Krenn, J. R., Schider, G., Ditlbacher, H., Salerno, M., Felidj, N., Leitner, A., and Aussenegg, F. R. (2001). Surface plasmon propagation in microscale metal stripes. *Applied Physics Letters*, 79:51–53. 49

Landau, L. and Lifshitz, E. (1984). *Electrodynamics of continuous media*. Pergamon Press. 9

Lawandy, N. M. (2004). Localized surface plasmon singularities in amplifying media. *Applied Physics Letters*, 85:5040–5042. 59

Lederer, F., Stegeman, G. I., Christodoulides, D. N., Assanto, G., Segev, M., and Silberberge, Y. (2008). Discrete solitons in optics. *Physics Reports*, 463:1–126. 123

Lee, K., Lim, D., Kimerling, L., Shin, J., and F, C. (2001). Fabrication of ultralow-loss si/sio2 waveguides by roughness reduction. *Optics Letters*, 26:1888. 15

Leonhardt, U. (2006). Optical conformal mapping. *Science*, 312:5781. 124

Leosson, K., Nikolajsen, T., Boltasseva, A., and Bozhevolnyi, S. I. (2006). Long-range surface plasmon polariton nanowire waveguides for device applications. *Optics Express*, 14:314. 50, 81, 166

Lereu, A. L., Passian, A., Goudonnet, J. P., Thundat, T., and Ferrell, T. L. (2005). Optical modulation processes in thin films based on thermal effects of surface plasmons. *Applied Physics Letters*, 86:154101. 60

LeRu, E. and Etchegoin, P. (2009). *Principles of Surface Enhanced Raman Spectroscopy and related plasmonic effects*. Elsevier. 2, 68

LiKamWa, P., Sitch, J., Mason, N., Roberts, J., and Robson, P. (1985). All-optical multiple-quantum-well waveguide switch. *Electronics Letters*, 21:26. 122

Lin, Y. Y., Lee, R. K., and Kivshar, Y. S. (2009). Transverse instability of transverse-magnetic solitons and nonlinear surface plasmons. *Optics Letters*, 34(19):2982–2984. 82

Liu, Y., Bartal, G., Genov, D. A., , and Zhang, X. (2007). Subwavelength discrete solitons in nonlinear metamaterials. *Physical Review Letters*, 99:153901. 124

Liu, Y., Bartal, G., and Zhang, X. (2008). All-angle negative refraction and imaging in a bulk medium made of metallic nanowires in the visible region. *Optics Express*, 16:15439. 124

Locatelli, A., Conforti, M., Modotto, D., and Angelis, C. D. (2006). Discrete negative refraction in photonic crystal waveguide arrays. *Optics Letters*, 31:1343. 122

Longhi, S. (2008). Optical bloch oscillations and zener tunneling with nonclassical light. *Physical Review Letters*, 101:193902. 122

Loudon, R. (1970). The propagation of electromagnetic energy through an absorbing dielectric. *Journal of Physics A*, 3:233. 47

Luther-Davies, B. and Kivshar, Y. (1998). Dark optical solitons: physics and applications. *Physics Reports*, 298:81. 26

MacDonald, K. F., Samson, Z. L., Stockman, M. I., and Zheludev, N. I. (2009). Ultrafast active plasmonics. *Nature Photonics*, 3:55. 2, 60, 82

Maier, S. A. (2007). *Plasmonics: Fundamentals and Applications*. Springer. 1, 38, 45, 58, 146

Maier, S. A. and Atwater, H. A. (2005). Plasmonics: Localization and guiding of electromagnetic energy in metal/dielectric structures. *Journal of Applied Physics*, 98:011101. 55

Maier, S. A., Barclay, P. E., Johnson, T. J., Friedman, M. D., and Painter, O. (2004). Low-loss fiber accessible plasmon waveguide for planar energy guiding and sensing. *Applied Physics Letters*, 20:3990. 56

Maier, S. A., Brongersma, M. L., Kik, P. G., Meltzer, S., Requicha, A. A. G., and Atwater, H. A. (2001). Plasmonics - a route to nanoscale optical devices. *Advanced Materials*, 13:1501. 29

Maier, S. A., Kik, P. G., and Atwater, H. A. (2002). Observation of coupled plasmon-polariton modes in au nanoparticle chain waveguides of different lengths: Estimation of waveguide loss. *Applied Physics Letters*, 81:1714–1716. 56

Maier, S. A., Kik, P. G., Atwater, H. A., Meltzer, S., Harel, E., Koel, B. E., and Requicha, A. A. G. (2003). Local detection of electromagnetic energy transport below the diffraction limit in metal nanoparticle plasmon waveguides. *Nature Materials*, 2:229–232. 30, 56

Malomed, B. and Winful, H. (1996). Stable solitons in two-component active systems. *Physical Review E*, 53:5365. 99, 147, 156, 159

Malomed, B. A. (1987). Evolution of nonsoliton and quasiclassical wavetrains in nonlinear schrdinger and korteweg de vries equations with dissipative perturbations. *Physica D*, 29:155–172. 147

Mamyshev, P. and Chernikov, S. (1990). Ultrashort-pulse propagation in optical fibers. *Optics Letters*, 15:1076. 25

Manton, N. (2008). Solitons as elementary particles: a paradigm scrutinized. *Nonlinearity*, 21:T221. 25

Marcuse, D. (1982). *Light transmission optics*. Van Nostrand Reinhold Company. 13, 170, 171

Marini, A., Gorbach, A. V., and Skryabin, D. V. (2010). Coupled-mode approach to surface plasmon polaritons in nonlinear periodic structures. *Optics Letters*, 35:3532–3534. 145, 186

Marini, A., Gorbach, A. V., Skryabin, D. V., and Zayats, A. V. (2009). Amplification of surface plasmon polaritons in the presence of nonlinearity and spectral signatures of threshold crossover. *Optics Letters*, 34:2864. 99, 184

Marini, A., Hartley, R., Gorbach, A. V., and Skryabin, D. V. (2011a). Surface-induced nonlinearity enhancement in subwavelength rod waveguides. *Physical Review A*, 84:063839. 182, 187

Marini, A. and Skryabin, D. V. (2010). Ginzburg-landau equation bound to the metal-dielectric interface and transverse nonlinear optics with amplified plasmon polaritons. *Physical Review A*, 81:033850. 99, 185

Marini, A., Skryabin, D. V., and Malomed, B. (2011b). Stable spatial plasmon solitons in a dielectric-metal-dielectric geometry with gain and loss. *Optics Express*, 19:6616. 165, 186

Michinobu, T., May, J., Lim, J., Boudon, C., Gisselbrecht, J., Seiler, P., Gross, M., Biaggio, I., and Diederich, F. (2005). A new class of organic donoracceptor molecules with large third-order optical nonlinearities. *Chemical Communications*, page 737. 22

Mihalache, D., Stegeman, G. I., Seaton, C. T., Wright, E. M., Zanoni, R., Boardman, A. D., and Twardowski, T. (1987). Exact dispersion relations for transverse magnetic polarized guided waves at a nonlinear interface. *Optics Letters*, 12:187–189. 69, 70, 71, 73, 79, 99

Morandotti, R., Peschel, U., Aitchison, J., Eisenberg, H., and Silberberg, Y. (1999a). Dynamics of discrete solitons in optical waveguide arrays. *Physical Review Letters*, 83:2726–2729. 140

Morandotti, R., Peschel, U., Aitchison, J. S., Eisenberg, H. S., and Silberberg, Y. (1999b). Experimental observation of linear and nonlinear optical bloch oscillations. *Physical Review Letters*, 83:4756–4759. 122

Nam, S. H., Taylor, A., and Efimov, A. (2010a). Diabolical point and conical-like diffraction in periodic plasmonic nanostructures. *Optics Express*, 18:10120. 124, 132, 135, 144

Nam, S. H., UlinAvila, E., Bartal, G., and Zhang, X. (2010b). Deep subwavelength surface modes in metal-dielectric metamaterials. *Optics Letters*, 35:1847. 124, 132

Nezhad, M. P., Tetz, K., and Fainman, Y. (2004). Gain assisted propagation of surface plasmon polaritons on planar metallic waveguides. *Optics Express*, 12:4072–4079. 60, 74, 85, 146

Nie, S. and Emory, S. R. (1997). Probing single molecules and single nanoparticles by surface-enhanced raman scattering. *Science*, 275:1102. 2, 29

Nikolajsen, T., Leosson, K., and Bozhevolnyi, S. I. (2004). Surface plasmon polariton based modulators and switches operating at telecom wavelengths. *Applied Physics Letters*, 85:5833. 60

Noginov, M. A., Podolskiy, V. A., Zhu, G., Mayy, M., Bahoura, M., Adegoke, J. A., Ritzo, B. A., and Reynolds, K. (2008a). Compensation of loss in propagating surface plasmon polariton by gain in adjacent dielectric medium. *Optics Express*, 16:1385. 2, 30, 64, 146, 157

Noginov, M. A., Zhu, G., Bahoura, M., Adegoke, J., Small, C. E., Drachev, B. A. R. V. P., and Shalaev, V. M. (2006a). Enhancement of surface plasmons in an ag aggregate by optical gain in a dielectric medium. *Optics Letters*, 31:30022. 64

Noginov, M. A., Zhu, G., Bahoura, M., Small, C. E., Davison, C., and Adegoke, J. (2006b). Enhancement of spontaneous and stimulated emission of a rhodamine 6g dye by an ag aggregate. *Physical Review B*, 74:184203. 64, 74, 75

Noginov, M. A., Zhu, G., Belgrave, A. M., Bakker, R., Shalaev, V. M., Narimanov, E. E., Stout, S., Herz, E., Suteewong, T., and Wiesner, U. (2009). Demonstration of a spaser-based nanolaser. *Nature Letters*, 460:1110–1113. 59

Noginov, M. A., Zhu, G., Mayy, M., Ritzo, B. A., Noginova, N., and Podolskiy, V. A. (2008b). Stimulated emission of surface plasmon polaritons. *Physical Review Letters*, 101:226806. 64, 82

Novikov, I. V. and Maradudin, A. A. (2002). Channel polaritons. *Physical Review B*, 66:035403. 56, 82, 166

Novotny, L. and Hect, B. (2006). *Principles of Nano-Optics*. Cambridge University Press. 1, 52, 53

Nozaki, K. and Bekki, N. (1984). Exact solutions of the generalized ginzburg-landau equation. *Journal of the Physical Society of Japan*, 53:1581. 97

Offerhaus, H. L., VanDenBergen, B., Escalante, M., Segerink, F. B., Korterik, J. P., and VanHulst, N. F. (2005). Creating focused plasmons by noncollinear phase-matching on functional gratings. *Nano Letters*, 5:21442148. 54

Osgood, R. M. J., Panoiu, N. C., Dadap, J. I., Liu, X., Chen, X., Hsieh, I., Dulkeith, E., Green, W. M., and Vlasov, Y. A. (2009). Engineering nonlinearities in nanoscale optical systems: physics and applications in dispersion-engineered silicon nanophotonic wires. *Advances in Optics and Photonics*, 1:162–235. 101, 112

Otto, A. (1968). Excitation of nonradiative surface plasma waves in silver by the method of frustrated total reflection. *Z. Physik A*, 216:398. 50, 51

Oulton, R. F., Sorger, V. J., Zentgraf, T., Ma, R. M., Gladden, C., Dai, L., Bartal, G., and Zhang, X. (2009). Plasmon lasers at deep subwavelength scale. *Nature Letters*, 461:629–632. 59

Ozbay, E. (2006). Plasmonics: Merging photonics and electronics at nanoscale dimensions. *Science*, 311:189–193. 2, 29, 55, 81, 100

Pacifici, D., Lezec, H. J., and Atwater, H. A. (2007). All-optical modulation by plasmonic excitation of cdse quantum dots. *Nature Photonics*, 1(7):402–406. 2, 60

Pala, R. A., Shimizu, K. T., Melosh, N. A., and Brongersma, M. L. (2008). A nonvolatile plasmonic switch employing photochromic molecules. *Nano Letters*, 8:1506–1510. 60

Palik, E. (1998). *Handbook of optical constants of solids*. Academic Press. 31

Palomba, S. and Novotny, L. (2008). Nonlinear excitation of surface plasmon polaritons by four-wave mixing. *Physical Review Letters*, 101:056802. 68

Park, S., Lee, G., Song, S. H., Oh, C. H., and Kim, P. S. (2003). Resonant coupling of surface plasmons to radiation modes by use of dielectric gratings. *Optics Letters*, 28:18701872. 54

Pelinovsky, D., Afanasjev, V., and Kivshar, Y. (1996). Nonlinear theory of oscillating, decaying, and collapsing solitons in the generalized nonlinear schrodinger equation. *Physical Review E*, 53:1940. 27

Pendry, J. B. (2000). Negative refraction makes a perfect lens. *Physical Review Letters*, 85:3966–3969. 3, 124

Pereira, N. R. and Stenflo, L. (1977). Nonlinear schroedinger equation including growth and damping. *The Physics of Fluids*, 20:1733. 97, 153

Pertsch, T., Dannberg, P., Elflein, W., Brauer, A., and Lederer, F. (1999). Optical bloch oscillations in temperature tuned waveguide arrays. *Physical Review Letters*, 83:4752–4755. 122

Pertsch, T., Zentgraf, T., Peschel, U., Brauer, A., and Lederer, F. (2002). Anomalous refraction and diffraction in discrete optical systems. *Physical Review Letters*, 88:093901. 122, 123

Peschel, U., Pertsch, T., and Lederer, F. (1998). Optical bloch oscillations in waveguide arrays. *Optics Letters*, 23:1701–1703. 122

Pettit, R. B., Silcox, J., and Vincent, R. (1975). Measurement of surface-plasmon dispersion in oxidized aluminum films. *Physical Review B*, 11:31163123. 50

Pile, D. F. P. and Gramotnev, D. K. (2004). Channel plasmonpolariton in a triangular groove on a metal surface. *Optics Letters*, 29:1069. 56, 82, 146, 166

Pile, D. F. P., Ogawa, T., Gramotnev, D. K., Matsuzaki, Y., Vernon, K. C., Yamaguchi, K., Okamoto, T., Haraguchi, M., and Fukui, M. (2005). Two-dimensionally localized modes of a nanoscale gap plasmon waveguide. *Applied Physics Letters*, 87:261114. 56, 146

Plotz, G. A., Simon, H. J., and Tucciarone, J. M. (1979). Enhanced total reflection with surface plasmons. *Journal of the Optical Society of America*, 69:419. 58

Ponath, H. E. and Stegeman, G. (1991). *Nonlinear Surface Electromagnetic Phenomena*. North-Holland. 68

Popov, O., Zilbershtein, A., and Davidov, D. (2006). Random lasing from dye-gold nanoparticles in polymer films: Enhanced gain at the surface-plasmon-resonance wavelength. *Applied Physics Letters*, 89:191116. 59

Prade, B., Vinet, J., and Mysyrowicz, A. (1991). Guided optical waves in planar heterostructures with negative dielectric constant. *Physical Review B*, 44:556. 42

Prade, B. and Vinet, J. Y. (1994). Guided optical waves in fibers with negative dielectric constant. *Journal of Lightwave Technology*, 12:6. 166

Protsenko, I. E., Uskov, A. V., Zaimidoroga, O. A., Samoilov, V. N., and OReilly, E. P. (2005). Dipole nanolaser. *Physical Review A*, 71:063812. 59

Quail, J. C., Rako, J. G., and Simon, H. J. (1983). Long-range surface-plasmon modes in silver and aluminum films. *Optics Letters*, 8:377. 30, 49

Quinten, M., Leitner, A., Krenn, J. R., and Aussenegg, F. R. (1998). Electromagnetic energy transport via linear chains of silver nanoparticles. *Optics Letters*, 23:1331 – 1333. 30, 56

Raether, H. (1988). *Surface Plasmons*. Springer-Verlag. 29, 50

Rakic, A. D., Djurisic, A. B., Elazar, J. M., and Majewski, M. L. (1998). Optical properties of metallic films for vertical-cavity optoelectronic devices. *Applied Optics*, 37:5271. 31, 34

Ramakrishna, S. and Grzegorczyk, T. (2009). *Physics and Applications of Negative Refractive Index Materials*. Taylor & Francis Group, LLC. 3

Raschke, G., Kowarik, S., Franzl, T., Sonnichsen, C., Klar, T. A., Feldmann, J., Nichtl, A., and Kurzinger, K. (2003). Biomolecular recognition based on single gold nanoparticle light scattering. *Nano Letters*, 3:935–938. 29

Rayleigh, J. W. S. (1888). On the remarkable phenomenon of crystalline reflexion described by prof. stokes. *Phil. Mag*, 26:256–265. 121

Ricard, D., Roussignol, P., and Flytzanis, C. (1985). Surface-mediated enhancement of optical phase conjugation in metal colloids. *Optics Letters*, 10:511. 2

Ritchie, R. H. (1957). Plasma losses by fast electrons in thin films. *Physical Review*, 106:874881. 50

Rosberg, C. R., Neshev, D. N., Sukhorukov, A. A., and Kivshar., Y. S. (2005). Tunable positive and negative refraction in optically induced photonic lattices. *Optics Letters*, 30:2293. 122

Rosenblatt, G., Feigenbaum, E., and Orenstein, M. (2010). Circular motion of electromagnetic power shaping the dispersion of surface plasmon polaritons. *Optics Express*, 18:25861. 45

Rotenberg, N., Betz, M., and vanDriel, H. M. (2008). Ultrafast control of grating-assisted light coupling to surface plasmons. *Optics Letters*, 33:2137. 60

Ruppin, R. (2002). Electromagnetic energy density in a dispersive and absorptive material. *Physics Letters A*, 299:309. 48

Russell, J. (1844). Report on waves. *Report of the fourteenth meeting of the British Association for the Advancement of Science*. 25

Russell, P. (2003). Photonic crystal fibers. *Science*, 299:358. 16, 121

Saleh, B. and Teich, M. (2007). *Fundamentals of Photonics*. Wiley. 11

Salgueiro, J. R. and Kivshar, Y. S. (2010). Nonlinear plasmonic directional couplers. *Applied Physics Letters*, 97:081106. 4, 124, 145

Salomon, L., Bassou, G., Aourag, H., Dufour, J. P., DeFornel, F., Carcenac, F., and Zayats, A. V. (2002). Local excitation of surface plasmon polaritons at discontinuities of a metal film: Theoretical analysis and optical near-field measurements. *Physical Review B*, 65:125409. 54

Sapienza, R., Costantino, P., Wiersma, D., Ghulinyan, M., Oton, C., and Pavesi, L. (2003). Optical analogue of electronic bloch oscillations. *Physical Review Letters*, 26:263902. 17

Sarid, D. (1981). Long-range surface-plasma waves on very thin metal films. *Physical Review Letters*, 47:1927. 30, 49

Schmidt, M. A. and Russell, P. S. (2008). Long-range spiralling surface plasmon modes on metallic nanowires. *Optics Express*, 16:13617. 82, 100, 166

Schroter, U. and Dereux, A. (2001). Surface plasmon polaritons on metal cylinders with dielectric core. *Physical Review B*, 64:125420. 82, 100, 166

Schurig, D., Mock, J., Justice, J., Cummer, A., Pendry, J., Starr, A., and Smith, D. (2006). Metamaterial electromagnetic cloak at microwave frequencies. *Science*, 314:977. 3, 124

Segev, M. and Stegeman, G. (1998). Self-trapping of optical beams: spatial solitons. *Physics Today*, 51:42. 25

Seidel, J., Grafstrom, S., and Eng, L. (2005). Stimulated emission of surface plasmons at the interface between a silver film and an optically pumped dye solution. *Physical Review Letters*, 94:177401. 30, 64, 74

Shalaev, V. and Kawata, S. (2007). *Nanophotonics with surface plasmons*. Elsevier. 1, 29

Shalaev, V. M. (2007). Optical negative-index metamaterials. *Nature Photonics*, 1:41–48. 3

Shelby, R. A., Smith, D. R., and Schultz, S. (2001). Experimental verification of a negative index of refraction. *Science*, 292:5514. 124

Shen, Y. (1984). *The Principles of Nonlinear Optics*. John Wiley & Sons. 19, 20

Sirtori, C., Gmachl, C., Capasso, F., Faist, J., Sivco, D. L., Hutchinson, A. L., and Cho, A. Y. (1998). Long-wavelength ($811.5\mu m$) semiconductor lasers with waveguides based on surface plasmons. *Optics Letters*, 23:1366. 58

Skryabin, D. V., Gorbach, A. V., and Marini, A. (2011). Surface-induced nonlinearity enhancement of tm modes in planar subwavelength waveguides. *Journal Of The Optical Society Of America B*, 28:109. 120, 185

Snyder, A. W. and Love, J. D. (1983). *Optical waveguide theory*. Chapman and Hall. 175

Somekh, S., Garmire, E., Yariv, A., Garvin, H., and Hunsperger, R. (1973). Channel optical waveguide directional couplers. *Applied Physics Letters*, 22:46. 122

Sommerfeld, A. (1899). ber die fortpflanzung electrodynamischer wellen lngs eines drahtes. *Ann. Phys. und Chemie*, 67:233290. 2

Stegeman, G. and Seaton, C. (1985). Nonlinear integrated optics. *Journal of Applied Physics*, 58:R57. 122

Stegeman, G. and Segev, M. (1999). Optical spatial solitons and their interactions: Universality and diversity. *Science*, 286:1518. 25

Stegeman, G. I., Seaton, C. T., Ariyasu, J., Wallis, R. F., and Maradudin, A. A. (1985). Nonlinear electromagnetic waves guided by a single interface. *Journal of Applied Physics*, 58:2453–2459. 68, 69, 70

Stegeman, G. I., Wallis, R. F., and Maradudin, A. A. (1983). Excitation of surface polaritons by end-fire coupling. *Optics Letters*, 8:386. 50

Stockman, M. I. (2008). Spasers explained. *Nature Photonics*, 2:327–329. 59

Stratton, J. (1941). *Electromagnetic theory*. McGraw-Hill. 8, 51, 53, 171

Sudarkin, A. N. and Demkovich, P. A. (1989). Excitation of surface electromagnetic waves on the boundary of a metal with an amplifying medium. *Sov. Phys. Tech. Phys.*, 34:764766. 57

Sulem, C. and Sulem, P. (1999). *The Nonlinear Schrodinger Equation: Self-Focusing and Wave Collapse*. Springer. 23

Takahara, J., Yamagishi, S., Taki, H., Morimoto, A., and Kobayashi, T. (1997). Guiding of a one-dimensional optical beam with nanometer diameter. *Optics Letters*, 22:475. 56, 82, 100, 166, 171

Taminiau, T. H., Stefani, F. D., Segerink, F. B., and VanHulst, N. F. (2008). Optical antennas direct single-molecule emission. *Nature Photonics*, 2:234–237. 59

Tong, L. M., Gattass, R. R., Ashcom, J. B., He, S. L., Lou, J. Y., Shen, M. Y., Maxwell, I., and Mazur, E. (2003). Subwavelength diameter silica wires for low-loss optical wave guiding. *Nature*, 426:816–819. 100

Tredicucci, A., Gmachl, C., Capasso, F., Hutchinson, A. L., Sivco, D. L., and Cho, A. Y. (2000a). Single-mode surface-plasmon laser. *Applied Physics Letters*, 76:2164. 58

Tredicucci, A., Gmachl, C., Wanke, M. C., Capasso, F., Hutchinson, A. L., Sivco, D. L., Chu, S. G., and Cho, A. Y. (2000b). Surface plasmon quantum cascade lasers at $\lambda \approx 19\mu m$. *Applied Physics Letters*, 77:2286–2288. 58

Trinh, P., Yegnanarayanan, S., and Jalali., B. (1995). Integrated optical directional couplers in silicon-on-insulator. *Electronics Letters*, 31:2097–2098. 121

Trompeter, H., Krolikowski, W., Neshev, D. N., Desyatnikov, A. S., Sukhorukov, A. A., Kivshar, Y. S., Pertsch, T., Peschel, U., and Lederer, F. (2006a). Bloch oscillations and zener tunneling in two-dimensional photonic lattices. *Physical Review Letters*, 96:053903. 17, 122

Trompeter, H., Pertsch, T., Lederer, F., and Peschel, U. (2006b). Visual observation of zener tunneling. *Physical Review Letters*, 96:023901. 122

Ung, B. and Sheng, Y. (2007). Interference of surface waves in a metallic nanoslit. *Optics Express*, 15:1182. 34, 40, 177

Ung, B. and Skorobogatiy, M. (2011). Extreme nonlinear optical enhancement in chalcogenide glass fibers with deep-subwavelength metallic nanowires. *Optics Letters*, 36:2527–2529. 166

Valentine, J., Li, J., Zentgraf, T., Bartal, G., and Zhang, X. (2009). An optical cloak made of dielectrics. *Nature Materials*, 8:568–571. 124

Vallaitis, T., Bogatscher, S., Alloatti, L., Dumon, P., Baets, R., Scimeca, M., Biaggio, I., Koos, F. D. C., Freude, W., and Leuthold, J. (2009). Optical properties of highly nonlinear siliconorganic hybrid (soh) waveguide geometries. *Optics Express*, 17:17357. 22

Veronis, G. and Fan, S. (2005). Guided subwavelength plasmonic mode supported by a slot in a thin metal film. *Optics Letters*, 30:3359. 50

Veselago, V. (1968). The electrodynamics of substances with simultaneously negative values of permittivity and permeability. *Sov. Phys. Usp.*, 10:509. 3, 124

Vicencio, R. A. and Johansson, M. (2009). Discrete gap solitons in waveguide arrays with alternating spacings. *Physical Review A*, 79:065801. 132

Vincent, R. and Silcox, J. (1973). Dispersion of radiative surface plasmons in aluminum films by electron scattering. *Physical Review Letters*, 31:14871490. 50

Wang, F. Y., Li, G. X., Tam, H. L., Cheah, K. W., and Zhu, S. N. (2008). Optical bistability and multistability in one-dimensional periodic metal-dielectric photonic crystal. *Applied Physics Letters*, 92:211109. 124

Welch, M., K, C., Correa, R., Gerome, F., Wadsworth, W., Gorbach, A., Skryabin, D., and Knight, J. (2009). Solitons in hollow core photonic crystal fiber: Engineering nonlinearity and compressing pulses. *Journal of Lightwave Technology*, 27:1644. 18

Wiederhecker, G. S., Cordeiro, C. M. B., Couny, F., Benabid, F., Maier, S. A., Knight, J. C., Cruz, C. H. B., and Fragnito, H. L. (2007). Field enhancement within an optical fibre with a subwavelength air core. *Nature Photonics*, 1:115–118. 100

Wiederrecht, G. P., Hall, J. E., and Bouhelier, A. (2007). Control of molecular energy redistribution pathways via surface plasmon gating. *Physical Review Letters*, 98:083001. 60

Winter, G., Wedge, S., and Barnes, W. L. (2006). Can lasing at visible wavelengths be achieved using the low-loss long-range surface plasmon-polariton mode? *New Journal of Physics*, 8:125. 74

Wood, R. (1902). On a remarkable case of uneven distribution of light in a diffraction grating spectrum. *Proc. Phys. Soc. London*, 18:269275. 2

Wuenschell, J. and Kim, H. K. (2006). Surface plasmon dynamics in an isolated metallic nanoslit. *Optics Express*, 14:10000. 41

Wurtz, G. A., Pollard, R., and Zayats, A. V. (2006). Optical bistability in nonlinear surface-plasmon polaritonic crystals. *Physical Review Letters*, 97:057402. 2, 82

Wysin, G. M., Simon, H. J., and Deck, R. T. (1981). Optical bistability with surface plasmons. *Optics Letters*, 6:30. 69

Xu, M. Y. and Aitchison, J. S. (2009). Surface plasmon polariton discrete diffraction compensation. *Optics Letters*, 34:350. 124, 144

Yablonovitch, E. (1987). Inhibited spontaneous emission in solid-state physics and electronics. *Physical Review Letters*, 58:2059–2062. 121

Yang, J., Hu, X., Li, X., Liu, Z., Jiang, X., and Zi, J. (2010). Cancellation of reflection and transmission at metamaterial surfaces. *Optics Letters*, 35:16. 124

Yang, J., Sauvan, C., Liu, H. T., and Lalanne, P. (2011). Theory of fishnet negative-index optical metamaterials. *Physical Review Letters*, 107:043903. 124

Yannopapas, V. and Vanakaras, A. (2011). Dirac point in the photon dispersion relation of a negative/zero/positive-index plasmonic metamaterial. *Physical Review B*, 84:045128. 124

Yariv, A. (1985). *Optical Electronics*. HRW. 7, 10, 12, 42

Yatsui, T., Kourogi, M., and Ohtsu, M. (2001). Plasmon waveguide for optical far/near-field conversion. *Applied Physics Letters*, 79:4583. 56, 82, 146, 166

Ye, F., Mihalache, D., Hu, B., and Panoiu, N. C. (2010). Subwavelength plasmonic lattice solitons in arrays of metallic nanowires. *Physical Review Letters*, 104:106802. 3, 124, 175, 182

Ye, F., Mihalache, D., Hu, B., and Panoiu, N. C. (2011). Subwavelength vortical plasmonic lattice solitons. *Optics Letters*, 36:1179. 124

Yin, X. and Hesselink, L. (2006). Goos-hanchen shift surface plasmon resonance sensor. *Applied Physics Letters*, 89:261108. 69

Zabusky, N. and Kruskal, N. (1965). Interaction of "solitons" in a collisionless plasma and the recurrence of initial states. *Physical Review Letters*, 15:240. 25

Zakharov, V. and Shabat, A. (1972). Exact theory of two-dimensional self-focusing and one-dimensional self-modulation of waves in nonlinear media (differential equation solution for plane self focusing and one dimensional self modulation of waves interacting in nonlinear media). *Soviet Physics JETP Letters*, 34:62. 26

Zayats, A. and Richards, D. (2009). *Nano-Optics and Near-Field Optical Microscopy*. Artech House. 2

Zayats, A. V., Smolyaninov, I., and Maradunin, A. (2005). Nano-optics of surface plasmon polaritons. *Physics Reports*, 408:131–314. 68

Zenneck, J. (1907). ber die fortpflanzung ebener elektromagnetischer wellen lngs einer ebenen leiterflche und ihre beziehung zur drahtlosen telegraphie. *Ann. d. Phys.*, 23:846866. 2

Zhang, S., Fan, W., Panoiu, N. C., Malloy, K. J., Osgood, R. M., and Brueck, S. R. J. (2005). Experimental demonstration of near-infrared negative-index metamaterials. *Physical Review Letters*, 95:137404. 124

Zhang, S., Wei, H., Bao, K., Hakanson, U., Halas, N. J., Nordlander, P., and Xu, H. (2011). Chiral surface plasmon polaritons on metallic nanowires. *Physical Review Letters*, 107:096801. 166

Zheludev, N. I., Prosvirnin, S. L., Papasimakis, N., and Fedotov, V. A. (2008). Lasing spaser. *Nature Photonics*, 2:351 – 354. 2, 59

Zhou, H., Chen, X., Hou, P., and Li, C. F. (2008). Giant bistable lateral shift owing to surface plasmon excitation in kretschmann configuration with a kerr nonlinear dielectric. *Optics Letters*, 33:1249–1251. 69